Structures localisées temporelles dans les lasers à semi-conducteur à cavité verticale

Mathias Marconi

UNIVERSITE DE NICE-SOPHIA ANTIPOLIS-UFR Sciences

Ecole Doctorale

Sciences Fondamentales et Appliquées

THESE

pour obtenir le titre de

Docteur en Sciences

de l'Université de Nice - Sophia Antipolis

Discipline : PHYSIQUE

présentée et soutenue par

Mathias MARCONI

Time-Localized Structures in Vertical Cavity Surface-Emitting Lasers

Thèse dirigée par: Massimo GIUDICI

soutenue le 04 Décembre 2014

Jury :

Pr.	Mustapha TLIDI	-	Rapporteur
Pr.	Thorsten ACKEMANN	-	Rapporteur
Pr.	Guy MILLOT	-	Examinateur
Pr.	Pascal BESNARD	-	Examinateur
Dr.	Jean-Marc GAMBAUDO	-	Examinateur
Dr.	Julien JAVALOYES	-	Examinateur
Pr.	Massimo GIUDICI	-	Directeur

Acknowledgements

Tout d'abord un grand merci à Massimo qui
n'aurait pas pu mieux m'encadrer durant ces trois années.
Je me suis toujours senti soutenu et écouté
avec les deux oreilles.
Il a fait preuve d'une patience extrême à mon égard,
a su trouver un dosage parfait entre la rigueur nécessaire
à la production d'un travail acceptable et
la simplicité, l'humour (indispensable) dans nos échanges et
nos "skype" de groupe avec Julien et Salvador.
Ce travail de thèse n'aurait pas pu être fructueux sans l'apport
de nos collaborateurs de Palma de Mallorca.
Julien, "Rouleau specialist", a consacré un temps et une énergie
dingues sur les simulations de nos systèmes expérimentaux et
à chaque fois, boum! les résultats correspondaient.
Quel plaisir d'écrire dans les articles: "our model
very well reproduces the experimental results",
et d'y comprendre finalement quelque chose.
Il fut en permanence disponible, disposé à répondre à mes questions
et à réitérer plusieurs fois la même réponse à la même question...
Salvador aussi a apporté toute son expertise des lasers à semi-conducteurs
et toutes nos discussions ont été très instructives.
Je remercie également Stéphane qui a accompagné mes débuts
sur les premières manip de polarisation de VCSEL (pas les plus faciles),
et grâce à qui je me suis mis à Python, language correspondant très bien
à un "passionné d'informatique" comme moi.
Un grand merci à tous les membres et les anciens membres
de l'INLN et en particuliers aux stagiaires, doctorants et post-doctorants
pour la bonne ambiance entre nous et l'aide que vous m'avez apportée.
Enfin, une pensée pour ma famille, qui m'a poussé à
bien bosser à l'école, à faire des études,
à développer ma curiosité, ce qui m'a donné envie
de découvrir le monde de la recherche.
Je leur dois ces trois belles années de thèse.

Et pour finir: Merci ma chérie !!
Vive la république, et vive la France !
(et vive l'Italie).

Résumé

Structures Localisées Temporelles dans les Lasers à Semi-conducteurs à Cavité Verticale

I - Introduction

Les structures localisées sont des états stables qui apparaissent dans les systèmes dissipatifs spatialement étendus caractérisés par une longueur de corrélation beaucoup plus courte que la taille du système, ce qui permet leur adressage individuel à l'aide d'une perturbation externe. Dans les résonateurs optiques les structures localisées (SL) sont des états où la lumière reste confinée dans la dimension transverse à la propagation du champ (SL spatiales) ou bien dans la dimension longitudinale (SL temporelles) ou bien dans les deux (balles de lumière). La possibilité de les utiliser pour coder des bits d'information a déclenché un fort engouement pour ces structures au cours des vingt dernières années et, en particulier, pour leur implémentation dans les micro-résonateurs à semi-conducteurs qui permettent des temps de réponse rapides, des tailles réduites et un couplage assez naturel avec les systèmes opto-électroniques existants [Lugiato 2003]. Pour pouvoir générer des SL un système optique doit réunir deux conditions: avoir un très grand rapport d'aspect et être dans un régime bistable, où deux solutions sont stables pour les mêmes valeurs de paramètres. Les SL dans les cavités optiques ont été observées dans la section transverse d'un laser à semi-conducteur à cavité verticale (Vertical-Cavity Surface-Emitting Laser, VCSEL). Il s'agit d'un résonateur à un seul mode longitudinal et ayant une section transverse (diamètre $>$ 150 μm) suffisamment étendue pour réaliser la première condition décrite ci-dessus. Nous avons obtenu une réponse bistable du résonateur selon deux types de paradigmes: par injection d'un champ électromagnétique cohérent (morphogenèse passive)[Barland 2002] ou bien par couplage d'un milieu amplificateur avec un absorbant saturable (morphogenèse active)[Genevet 2008]. Les SL créées selon le premier schéma ont été nommées Solitons de Cavité alors que les SL créées dans le cadre de la morphogenèse active ont été nommées Solitons Laser car elles sont

produites par le résonateur actif à partir de l'état du vide, exactement de la même manière qu'une émission laser. La phase des Solitons de Cavité est fixée par le champ injecté alors que les Solitons Laser conservent la symétrie de phase. Dans le domaine temporel, les Solitons de Cavité ont été récemment observés et utilisés pour coder des bits d'information dans un résonateur en fibre optique avec injection [Leo 2010]. Dans cette contribution, nous abordons la possibilité de générer des Solitons Laser Temporels (SLT) à l'aide d'un VCSEL monté en cavité étendue. Dans la direction de propagation du champ la condition de système spatialement étendu se traduit par une longueur de la cavité externe suffisamment importante pour que le temps d'aller-retour dans la cavité (τ) soit beaucoup plus grande que les échelles de temps du VCSEL. Dans cette limite nous montrons l'existence de SLT dans deux montages différents: le premier est basé sur le régime de verrouillage modal passif où le VCSEL est couplé à un miroir absorbant saturable (SAM), le second est basé sur le degré de liberté de polarisation du VCSEL et il génère des SLT vectoriels.

II - Solitons Laser Temporels dans le VCSEL à modes bloqués

Afin d'obtenir le verrouillage modal passif (PML) un amplificateur laser est généralement couplé à un absorbant saturable. Nous montrons que les SLT peuvent être générés dans ce système lorsque: i) la solution nulle est stable et elle coexiste avec la solution à modes bloqués et ii) τ est très grand par rapport au temps de récupération du gain ($\Gamma \approx 1$ns). Le critère de stabilité de Haus pour les pulses PML [Haus 2000] indique que la condition ii) conduirait nécessairement à un verrouillage modal harmonique d'ordre N, avec N pulses circulants dans la cavité comme unique solution stable. Nous montrons que, en dépit de ce critère, dans la limite $\Gamma\tau \gg 1$ et pour des paramètres appropriés, la condition i) peut être vérifiée et une grande quantité de solutions stables devient disponible, chacune caractérisée par un nombre variable d'impulsions (allant de zéro à N) avec des arrangements variables. Cela est montré théoriquement avec l'analyse du diagramme de bifurcation de la solution PML à une seule impulsion en fonction du pompage. Nous montrons que, dans la limite $\Gamma\tau \gg 1$ et pour des paramètres appropriés, cette bifurcation devient sous-critique et qu'elle coexiste avec la solution d'émission nulle. Ce changement de scénario a une conséquence très importante sur les solutions à modes bloqués: la solution PML fondamentale devient stable, même dans la limite $\Gamma\tau \gg 1$ et un grand nombre de solutions à impulsions avec un nombre différent d'impulsions par aller-retour deviennent stables pour les mêmes valeurs de paramètres.

Cette multi-stabilité suggère que la solution de verrouillage modal harmonique d'ordre maximal compatible avec la taille de la cavité externe devient entièrement décomposable, puisque chaque impulsion de cette solution peut être allumée ou éteinte par une perturbation externe. Nous montrons alors que ces impulsions peuvent être utilisées comme des bits d'information, ce qui permet d'implémenter une mémoire tampon tout-optique avec un débit limité par la taille de LS, soit

environ 1 Gb/s pour des paramètres typiques. Les résultats de notre analyse théorique sont confirmés par une expérience où un VCSEL est couplé à un Miroir Absorbant Saturable Résonant (RSAM). Le VCSEL émet à 980 nm et son seuil J_{st} est d'environ 380 mA. Le RSAM présente une réflectivité de 1 % qui augmente à 60 % lorsqu'il est saturé et son temps de relaxation est de 1 ps. Nous appliquons les conditions d'existence des SLT décrites par l'analyse théorique et, en particulier, notre cavité externe est dimensionnée pour avoir τ = 15,4 ns et le VCSEL est pompé en-dessous du seuil $J < J_{st}$. Des impulsions à modes bloqués sont émises à la fréquence de répétition fondamentale de 65 MHz. Pour la même valeur de J, cette émission coexiste avec l'émission nulle et beaucoup d'autres états d'émission, chacun avec un nombre différent d'impulsions (de deux à dix-neuf) par aller-retour. La stabilité de chaque état peut être analysée en balayant le paramètre J, ce qui révèle, en accord avec la théorie, la coexistence de tous ces états et la nature localisée des impulsions qui les composent.

III - Solitons Lasers Temporels Vectoriels

En raison de leur structure symétrique, les VCSELs manquent d'anisotropies assez fortes pour fixer leur polarisation d'émission. Ainsi, la compétition entre les deux états de polarisation linéaires orthogonaux peut être facilement déclenchée par des perturbations optiques anisotropes. Nous avons placé un VCSEL dans une double cavité externe anisotrope. Cette cavité sélectionne un mode de polarisation (LP-Y) et le renvoie au VCSEL selon deux circuits : le premier renvoie la même polarisation LP-Y avec un délai τ_f (feedback sélectif en polarisation, PSF), le second tourne LP-Y en LP-X avant de le renvoyer dans le VCSEL avec un délai τ_r (réinjection de polarisation croisée, XPR). Nous montrons expérimentalement et théoriquement qu'une telle configuration conduit à générer des SLT vectoriels. Il s'agit d'impulsions localisées qui apparaissent en antiphase dans chaque polarisation, mais qui laissent l'intensité totale d'émission constante. L'analyse théorique montre que ces SLT consistent en une rotation complète du vecteur de polarisation sur la sphère de Poincaré. Le bruit présent dans le système induit une diffusion des SLT dans la cavité au fur et mesure que le nombre d'aller-retours progresse, ces trajectoires permettent de distinguer les SLT indépendants des états liés (molécules).

Abstract

Localized Structures (LS) appear in nonlinear dissipative media with large aspect-ratios where one or several solutions coexist in the parameters space. Although LS formation is a general phenomenon, their implementation in semiconductor lasers is of great interest due to the potential of LS for all-optical data processing. In fact, the basic idea consists in using LS as bits of information exploiting their property of addressability in a fast and small-sized medium. In this contribution, I will show the experimental and theoretical results obtained in Vertical Cavity Surface-Emitting Lasers (VCSELs). After a brief historical introduction on spatial LS emerging in the transverse profile of VCSELs, I will describe our method for the generation of temporal LS, that we observed in the frame of passive mode-locking when the VCSEL is coupled to a long external cavity closed by a fast saturable absorber, and vectorial LS, whose formation exploits the polarization degree of freedom of the VCSEL, which is submitted to the actions of a polarization-selective feedback (PSF) and a crossed-polarization reinjection (XPR).

KEY-WORDS : localized structures, surface-emitting semiconductor lasers, passive mode-locking, polarization, feedback.

Contents

1 General introduction **3**
- 1.1 General properties of localized structures . . . 8
- 1.2 Processing information with optical localized structures . . . 10
  - 1.2.1 Localized structures as bits for optical data transmission . . . 10
  - 1.2.2 Localized structures as bits for optical buffer applications . . . 14
- 1.3 Experimental realizations of localized structures in optical resonators. 17
  - 1.3.1 Scalar localized structures . . . 18
    - 1.3.1.1 Spatial and temporal cavity solitons . . . 18
    - 1.3.1.2 Spatial laser localized structures . . . 22
    - 1.3.1.3 Passive mode-locking and dissipative temporal solitons 26
    - 1.3.1.4 Motivations of our work . . . 31
  - 1.3.2 Vectorial localized structures . . . 32
    - 1.3.2.1 Dissipative vector solitons and polarization domains in fiber lasers . . . 32
    - 1.3.2.2 Polarization dynamics in VCSELs . . . 36
    - 1.3.2.3 Motivations of our work . . . 39
- 1.4 Contents . . . 40

2 Passive mode-locking and tilted waves in a broad-area VCSEL **43**
- 2.1 Introduction . . . 43
- 2.2 The experiment . . . 44
  - 2.2.1 The experimental setup . . . 44
  - 2.2.2 The experimental results . . . 47
  - 2.2.3 Discussions on wave vectors selectivity . . . 52
- 2.3 Numerical simulations . . . 55
  - 2.3.1 The model . . . 55
  - 2.3.2 Numerical results . . . 58
- 2.4 Conclusions and perspectives . . . 61

3 How lasing localized structures evolve out of passive mode-locking **63**
- 3.1 Introduction . . . 63
- 3.2 Experimental observations . . . 64
  - 3.2.1 Evidences for temporal localization . . . 64
  - 3.2.2 Writing and moving the localized structures via VCSEL current modulation: preliminary results . . . 68
- 3.3 Theoretical analysis . . . 76
  - 3.3.1 The model . . . 76
  - 3.3.2 From PML pulses to temporal LS: dynamical scenario . . . 76
- 3.4 Conclusions . . . 80

4 Square-wave switching and vectorial localized structures in a small-area VCSEL with delays **81**
4.1 Introduction . . . 82
4.2 Our solitary VCSEL properties . . . 83
4.2.1 Experimental characterization . . . 83
4.2.2 Nonvolatile polarization control of the bistable VCSEL . . . 85
4.2.3 Polarization stability diagram . . . 89
4.3 Robust square-wave polarization switching . . . 90
4.3.1 The setup . . . 91
4.3.2 Experimental results . . . 93
4.3.3 Numerical investigation . . . 98
4.3.3.1 The model . . . 98
4.3.3.2 Numerical results . . . 98
4.3.3.3 Asymmetric sensitivity to feedback . . . 102
4.3.4 Conclusions . . . 103
4.4 Vectorial localized structures . . . 104
4.4.1 Experimental results . . . 104
4.4.1.1 Experimental evidences of vectorial localized structures formation . . . 104
4.4.1.2 Influences of delays in the molecules formation . . . 110
4.4.2 Theoretical analysis . . . 115
4.4.2.1 Vectorial localized structures and molecules . . . 116
4.4.2.2 Vectorial localized structures as polarization kinks and antikinks . . . 120
4.5 Conclusions . . . 123

5 General conclusion **125**

Bibliography **129**

Chapter 1

General introduction

Contents

1.1 General properties of localized structures 8
1.2 Processing information with optical localized structures . . 10
1.2.1 Localized structures as bits for optical data transmission . . . 10
1.2.2 Localized structures as bits for optical buffer applications . . 14
1.3 Experimental realizations of localized structures in optical resonators. 17
1.3.1 Scalar localized structures 18
1.3.1.1 Spatial and temporal cavity solitons 18
1.3.1.2 Spatial laser localized structures 22
1.3.1.3 Passive mode-locking and dissipative temporal solitons 26
1.3.1.4 Motivations of our work 31
1.3.2 Vectorial localized structures 32
1.3.2.1 Dissipative vector solitons and polarization domains in fiber lasers 32
1.3.2.2 Polarization dynamics in VCSELs 36
1.3.2.3 Motivations of our work 39
1.4 Contents 40

The formation of spatial structures from an homogeneous state (morphogenesis) is an ubiquitous phenomenon in nature. For example, patterns can be observed on sand dunes, in the clouds arrangements in the atmosphere (see Fig. 1.1) and on a zebra or a leopard skin. The similarities between these patterns suggest the existence of general principles behind pattern formation that are independent of the detailed physical phenomena responsible for their presence. Typically, morphogenesis arises in nonlinear dissipative systems kept far enough from thermal equilibrium [Turing 1952]. The organization of a quantity towards a pattern in a spatially extended system (independent from any boundaries) is attributed to a coupling between a diffusion mechanism of this quantity and a nonlinearity. Under certain conditions, the diffusion destabilizes a transverse wave vector (modulational instability (MI)) at the origin of the structure formation. Dissipation is necessary for the system to evolve spontaneously from stationary conditions to an asymptotical state. This process is called self-organization, it cannot be observed in conservative systems where structure formation can only evolve out of a pre-existing waveform

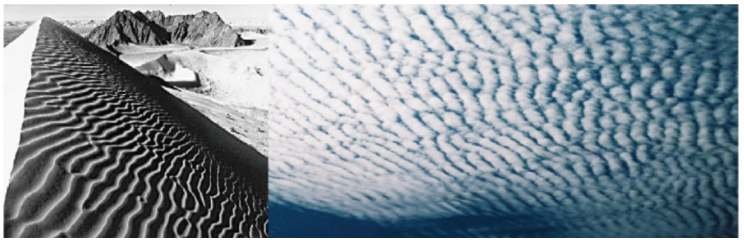

Figure 1.1: Stripes pattern on a sand dune and in the cloud layer in the atmosphere.

through MI. Also, an important effect of dissipation is that the stable pattern amplitude is not arbitrary but has only one or several discrete values prescribed by the balance between gain and losses. Numerically, spatial self-organization is well described by several models, namely the Swift-hohenberg equation for thermal convection [Swift 1977], the reaction-diffusion equations [Liehr 2013] and the complex Ginzburgh-Landau equations (CGLE) [Eckhaus 1965, Segel 1969, Newell 1969] (see [Cross 1993] for a complete review).

In optics we can observe the formation of spatial structures when light (whose propagation in a transparent medium is a conservative phenomenon described by Maxwell equations) is coupled to a nonlinear dissipative medium. Here the spatial coupling is insured by diffraction. When a field is injected from an external source inside a nonlinear medium and the interplay between diffraction and nonlinearities gives rise to a spatial pattern, we are in presence of "passive morphogenesis" [Grynberg 1988, D'Alessandro 1991, Ackemann 1994]. If the nonlinear medium is active (e.g. a laser gain medium) the field experiencing spatial structuration is generated out of vacuum by the system itself, this is "active morphogenesis" [Arecchi 1995].

The spatial patterns obtained from morphogenesis are generally stationary. Nevertheless, it has been shown that progressive one-dimensional patterns can be formed through MI due to the interplay between dispersion of a wave and nonlinearities. This phenomenon was first obtained in conservative deep water systems with boundary conditions [Benjamin 1967]. In this pioneer work it was theoretically prooved and experimentally observed that when a perturbation with a frequency Ω is applied to the progressive Stokes water wave solution of the system (with a frequency ω), the effect of MI is the result of the interaction between the wave at frequency ω and small sidebands at $\omega \pm \Omega$. The amplification of the spectral sidebands after many round-trips eventually leads to the breakup of the progressive Stokes waveform into a progressive train of pulses (see Fig. 1.2) [Zakharov 2009]. Self-modulation has also been observed with electromagnetic waves in nonlinear transmission lines [Ostrovskii 1972]. The effects associated with the instability of traveling electromagnetic waves in lines containing semiconductor diodes are qualitatively similar to the results with Stokes waves. However, in [Ostrovskii 1972] the authors also studied the self-modulation of standing waves occuring in a system of transmission lines forming a nonlinear resonator. In this configuration the instability growth

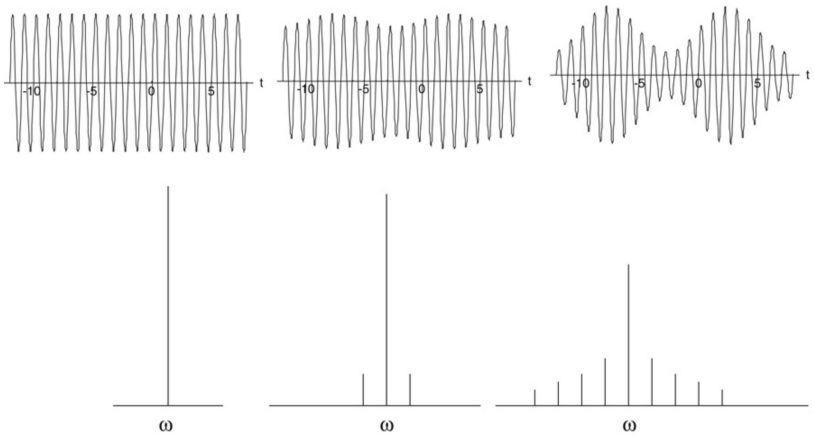

Figure 1.2: Top: evolution of a nonlinear wave train in the course of MI. Bottom: the corresponding evolution of the wave spectrum [Zakharov 2009].

rate is almost the same as in the traveling waves case, but the attenuation in the resonator has to be considered. The effects of dissipation are that self-modulation only develops for discrete values of the perturbation frequency (that depend on the resonator length) and that the amplitude of the perturbation has to exceed a certain threshold value. Modelization of progressive trains of pulses generated out of MI in a conservative system is well achieved via the Nonlinear Schrödinger Equation (NLSE) [Zakharov 2009]. When a dissipative term is added in the model then one ends up with the 1D CGLE which describes progressive patterns.

In optics, the phenomenon of temporal MI has been deeply considered in the frame of conservative light propagation in optical fibers. The first observations of an instability transforming a CW beam into a train of pulses were achieved in the case of the anomalous dispersion regime, when Self-Phase Modulation (SPM) induced by the nonlinearities compensate for dispersion of the pulses [Agrawal 1989]. In the case of normal dispersion however, MI requires the adding or another mechanism called Cross-Phase Modulation (XPM). XPM is the phenomenon that couples two optical beams at different wavelengths or with orthogonal polarizations propagating simultaneously in the fiber. Coupling occurs because the effective refractive index seen by an optical beam in a nonlinear medium depends not only on the intensity of that beam, but also on the intensity of the other copropagating beam. Such a system can be modelized by two coupled NLSE for each beam where both XPM and SPM are taken into account. In this model, MI can occur irrespective from the sign of the Group-Velocity Dispersion (GVD) coefficients (whether in the anomalous or normal dispersion regime) [Agrawal 1989]. Later, MI in the presence of normal dispersion was obtained numerically [Haelterman 1992] and experimentally [Coen 1997] in a system consisting of an externally driven optical cavity made of a single mode Kerr fiber. In this case, besides the effects of dispersion and Kerr nonlinearities, the intracavity light wave undergoes cavity boundary conditions which manifest by an attenuation of the field after each round-trip (dissipation) and by a recurrent coherent superposition with the input beam. MI in a synchronously

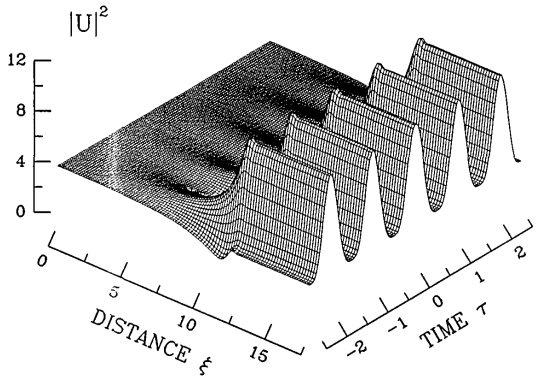

Figure 1.3: Evolution of an initially weakly modulated continuus wave in the cavity. A stable pulse train is generated after $\varepsilon = 10$ which corresponds to a number of round-trips N $= \varepsilon L_d/L = 450$ (L_d is the dispersion length which is large with respect to the cavity, meaning that significant nonlinear and dispersive pulse shaping may only occur after several round-trips). The time unit τ is the input modulation period $T_m = 2\pi/\Omega_m$ [Haelterman 1992].

pumped, dispersive, and nonlinear cavity generates, after some initial transitory period, a stable pulse train with a large and fixed contrast ratio that is independent of the number of round-trips (see Fig. 1.3). This pulse train may be formally viewed as a stable attractor of the dissipative infinite-dimensional dynamical system.

Therefore, in dissipative systems, MI plays an important role in the transition from a motionless state to one varying periodically in space or time. In this thesis a particular attention will be devoted to Localized Structures (LS) which appear in the presence of a subcritical MI in extended systems, i.e. systems led by bulk nonlinearities instead of boundary conditions [Arecchi 1995]. LS are characterized by a correlation length that is much shorter than the system size and, for this reason, they can be individually addressed by a local perturbation.

LS formation has been extensively studied in the spatial domain (spatial LS), whether in the case of active or passive morphogenesis (see sections 1.3.1.1 - 1.3.1.2). Only recently this concept has been extended to the temporal domain in the case of passive morphogenesis [Leo 2010, Herr 2014]. These experimental works are based on models for temporal Kerr frequency combs in optical nonlinear resonators [Haelterman 1992, Matsko 2011, Coen 2013] that can be approximated by a (temporal) Lugiato-Lefever (LL) model, which was first introduced to describe the formation of spatial structures in a nonlinear, passive optical system contained in a cavity, and driven by a coherent plane-wave and stationary beam [Lugiato 1987]. In the active case, and more precisely in the case of lasers, the general Partial Differential Equation (PDE) used to describe the formation of spatial and temporal LS is the cubic quintic CGLE, considering the simple case of a class A laser (where polarization and carriers dynamics are adiabatically eliminated). In fact, the 1D CGLE is used for the modelization of Dissipative Temporal Solitons (DTS) in Passively Mode-Locked fiber lasers [Grelu 2012], while in the 2D case, it can model

a semiconductor laser with large transverse section coupled to a saturable absorber [Rosanov 1992, Aranson 2002] where spatial LS have been observed.

Since the first developments of LS implementation in laser systems, active research has been dedicated to the three-dimensional localization of light (in the transverse plane (2D) and in the axis of propagation (1D)) called Light-Bullets (LB). These objects have been chased in the conservative case since the beginning of '90s [Silberberg 1990]. It was shown that the propagation of an optical pulse in a medium where diffraction and dispersion are compensated by a focusing nonlinearity and anomalous group dispersion is unstable and the pulse collapses to a point if the seeding pulse is not properly set. The integration and management of other nonlinearities as saturation or multiphoton absorption may avoid this collapse on a few diffraction lengths but finally the pulse undergoes a spreading in space and time and/or decay. The most promising results have been obtained recently, showing a spatio-temporal light pulse in a waveguide array propagating for distances longer than the characteristic lengths of linear propagation before decaying [Minardi 2010]. In dissipative systems however, three dimensions LS of light would exist as stable solutions (attractors) towards which the system would spontaneously evolve. Dissipative LB would be robust versus the system parameters and not critically depend on initial conditions. Following original theoretical predictions [Rosanov 1992], promising experimental results have been obtained with a broad-area VCSEL coupled to a saturable absorber in which spatial localization has been demonstrated together with interesting temporal regimes [Genevet 2008]. However the regime of LB has not yet been observed.

In this introduction I will describe the general properties of LS and show that they can be of great interest for optical data processing when generated in optical resonators via active or passive morphogenesis. I will then describe the progress made in spatial localization of laser light achieved in Vertical Cavity Surface-Emitting Laser (VCSEL) transverse profile, and temporal localization in the longitudinal axis of fiber laser resonators, the two devices being widely used as sources in optical telecommunication systems. In the temporal domain, a distinction will be made between the scalar LS observed in the total ouput power of laser systems, and vectorial LS observed in the polarized output.

In the rest of the manuscript, I will present the results obtained during my thesis. My work has been devoted to the generation of time-localized structures out of a system involving a VCSEL placed in nonlinear external cavities. These temporal LS can be either scalar when a broad-area VCSEL is coupled to an external fast saturable absorber or vectorial when polarized light is reinjected inside the VCSEL cavity via several coupled feedback mechanisms. For each type of temporal LS generated, a model has been developed that well-reproduces the experimental observations. Our complete understanding of the mechanisms at the origin of temporal localization in semiconductor lasers with delays represents, to our mind, a new expertise in the field of nonlinear dynamics that is a step towards a future successful implementation of dissipative LB.

1.1 General properties of localized structures

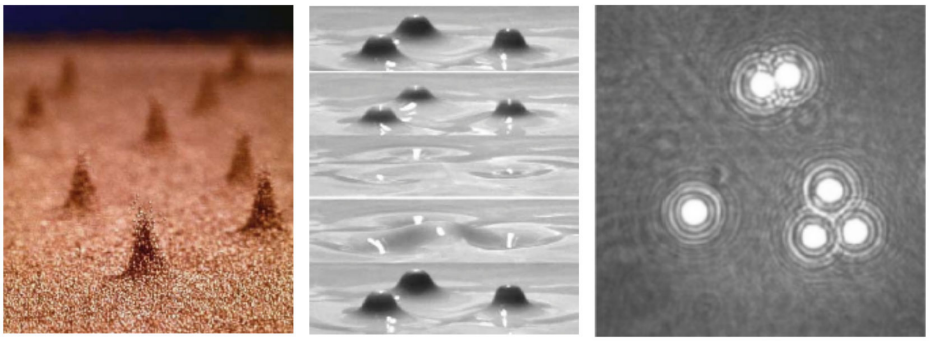

Figure 1.4: Some examples of experimental observations of LS in various systems. Left : vertically vibrated granular medium. Center : vertically vibrated colloids. Right : liquid crystals.

Localized Structures (LS) appear in nonlinear, dissipative and spatially extended systems kept out from thermal equilibrium. These solutions have been observed in a wide variety of physical systems (i.e. binary-fluid convection [Niemela 1990], granular media [Umbanhowar 1996], gas discharge [Astrov 1997], colloidal suspensions [Lioubashevski 1999], liquid crystals valves [Ramazza 2003], Fig. 1.4). Depending on the community, people would also call them Dissipative Solitons (DS) due to their solitary character and the important role played by dissipation in their stabilization [Ramazza 2002, Bode 2002, Purwins 2010]. Since their discovery, LS have attracted a lot of interest owing to their remarkable properties which make them completely different from the conservative solitons observed in lossless media :

- Conservative solitons are spatial or temporal localized solutions of a system that can propagate without modifying their shape due to the balance between a spreading effect (diffraction in space, dispersion in time) and a confining effect such as Kerr nonlinearities [Russel 1844, Zakharov 1972, Hasegawa 1973]. One would need a proper seeding of the initial conditions in order to allow the existence of a conservative soliton in the system (see Fig. 1.5a). The size and shape of the created conservative soliton depend on the characteristics of the input seed.
  Instead, LS (or Dissipative Solitons) are attractors for the physical system and thus they appear as a result of self-organization through the balance between nonlinearities, diffraction, gain and losses (see Fig. 1.5b). The system evolves towards this solution for a wide range of initial conditions which makes LS a robust dynamics. Fauve and thual explain in 1990 that the *"leading-order effect of the dissipative terms is just to select the size of the structure among a family of scale-invariant (conservative) solitons" [Fauve 1990].*

- Whereas integrable conservative solitons cross each other without modifying their shape, LS may repel or attract each other and form clusters with or

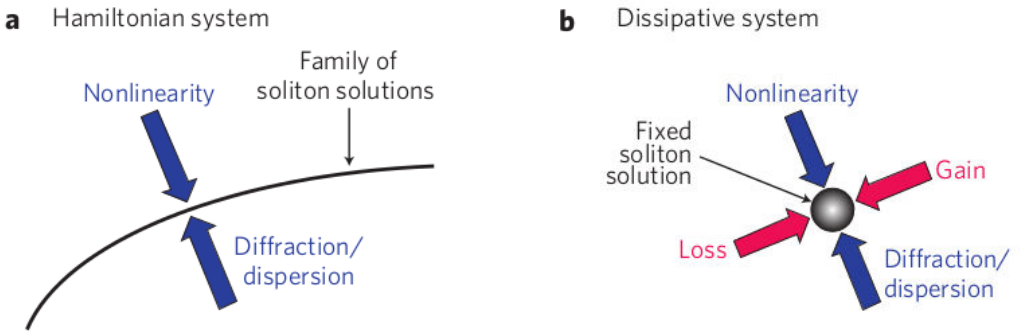

Figure 1.5: Qualitative differences between the solitons in Hamiltonian (a) and dissipative systems (b) [Grelu 2012].

without a well-defined symmetry [Rosanov 1990, Tlidi 1994, Brambilla 1996, Umbanhowar 1996, Astrov 1997, Schäpers 2000]. In the last case, they may form bound states of LS that may evolve as unique particules ([Grelu 2012] and references therein). Therefore, these objects can be called molecules of LS or even crystals when the structure they form fills the entire system size.

- LS appear in a range of parameters where the systems exhibits multistability between at least two stable states : in the simplest case one is the homogeneous solutions of low intensity, the other is a spatially modulated solution of higher intensity. LS can be thus interpreted as a result of connections between the homogeneous background and the higher intensity stable state [Pomeau 1986, Fauve 1990, Coullet 2000a, Coullet 2000b, Coullet 2002]. The shape of LS is related to the spatially modulated solution, whose structure is ruled by the nonlinearities present in the systems and not by the boundaries.

- They are localized solutions of a spatially extended systems, meaning that their size is much smaller than the size of the system and does not depend on the boundary conditions [Coullet 2000b, Burke 2007]. This condition is established in optical systems using the Fresnel number parameter [Arecchi 1993, Arecchi 1995]:

$$\mathcal{F} = a^2/L\lambda, \tag{1.1}$$

where a is the transverse size of the system, L is the longitudinal size and λ is the typical wavelength. When the structures formation is controlled only by the nonlinearities of the medium their typical size does not depend on the value of the Fresnel number. Instead, the size of the structures controlled by boundary conditions follow a law that scales like the square root of $\mathcal{F}$.

- As LS are bistable and local objects, one may be able to switch them on and off by applying into the system a local perturbation [Rosanov 1990, Tlidi 1994, Firth 1996, Coullet 2004a, Coullet 2004b, Clerc 2005]. The property of addressability makes LS potential bits for signal processing.

These are properties arising from theoretical investigations and experimental observations of LS in various physical systems. To sum up, one could therefore define LS as local, multistable, addressable and interacting objects. LS are thus robust and easily controllable, which make them passionating for the laser community [Rosanov 1990, Tlidi 1994, Firth 1996, Brambilla 1997]. Indeed, if one considers that LS can be made of laser light, one could generate ultrafast optical signals or create all-optical buffers with laser LS due to their property of addressability and multistability. As a matter of fact, very shortly after the first discovery of LS in nature, many groups of nonlinear dynamics have been dedicated to the implementation of LS in laser systems for future applications in the domain of optical data transmission.

1.2 Processing information with optical localized structures

1.2.1 Localized structures as bits for optical data transmission

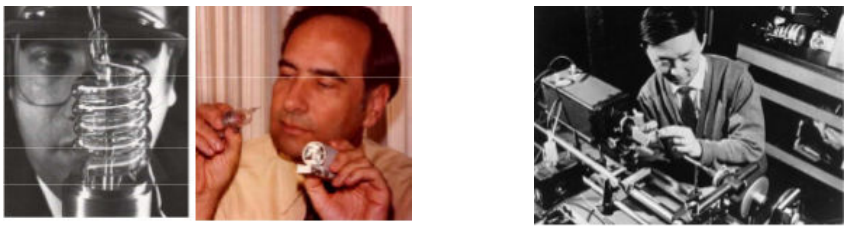

Figure 1.6: Left: 1^{st} laser demonstration : T. Maiman (1960). Right: 1^{st} Low-Loss Fiber Optic Proposal: C. Kao (1966).

The inventions of the laser in 1960 [Maiman 1960] and fiber optics in 1966 [Kao 1966] formed the basis for the telecommunications revolution of the late 20^{th} (see Fig. 1.6). The process of communicating using fiber optics involves the following basic steps : the optical signal is created by a transmitter (a laser or a Light-Emitting Diode (LED)) and is modulated to carry information. The signal is then relayed along the fiber, ensuring that it does not become too distorted or weak. Finally it is received by photodiodes and converted into an electrical signal (see Fig. 1.7).

First developed in the 1970s [Kapron 1970], fiber-based communication systems have revolutionized the telecommunications industry and have largely replaced electric cables for long-haul optical data transmission due to their pronounced advantages (see Fig. 1.8): they are much less heavy than electric cables, the transmission losses can be very low (well below 1 dB/km for the optimum wavelength), fiber connections are immune to electromagnetic interferences and finally, the bandwidth for high-data rates in the wavelength range from 1.3 to 1.6 μm is as large as 43 THz,

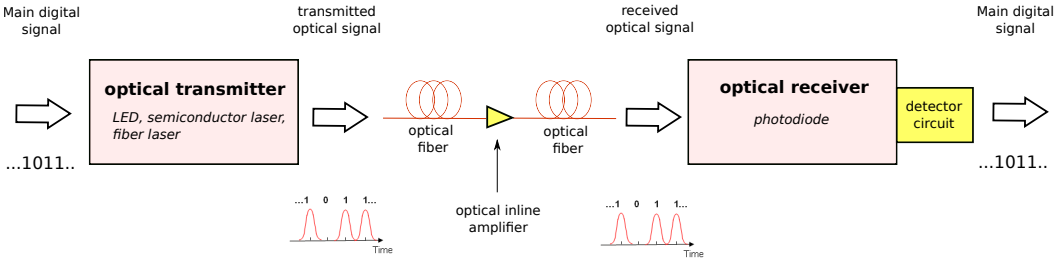

Figure 1.7: schematic representation of an optical fiber communication system.

which is orders of magnitude higher than that of any electrical cable. Within the last 30 years, the transmission capacity of optical fibers has been increased enormously. The rise in available transmission bandwidth per fiber is even significantly faster than e.g. the increase in storage capacity of electronic memory chips, or in the increase in computation power of microprocessors. The transmission capacity of a fiber depends on the fiber length. The longer a fiber is, the more detrimental certain effects such as intermodal or chromatic dispersion are, and the lower is the achievable transmission rate.

For short distances of a few hundred meters or less (e.g. within storage area networks), it is often more convenient to utilize multimode fibers, as these are cheaper to install. Depending on the transmitter technology and fiber length, they achieve data rates between a few hundred Mbit/s and $\approx$ 10 Gbits/s. Single-mode fibers are typically used for longer distances of a few kilometers or more. Current commercial telecom systems typically transmit 2.5 or 10 Gbit/s per data channel over distances of ten kilometers or more. Future systems may use higher data rates per channel of 40 or even 160 Gbit/s, but currently the required total capacity is usually obtained by transmitting many channels with slightly different wavelengths through fibers; this is called Wavelength Division Multiplexing (WDM).

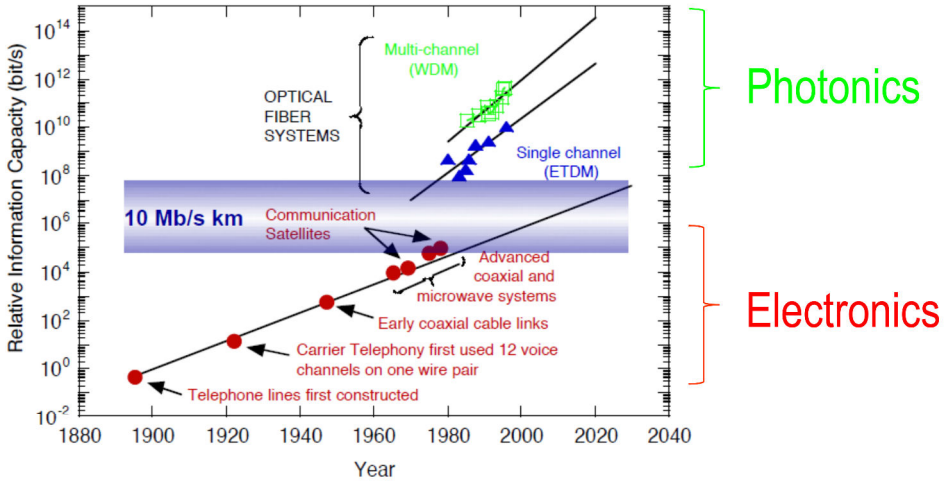

Figure 1.8: Evolution of information transmission capacity.

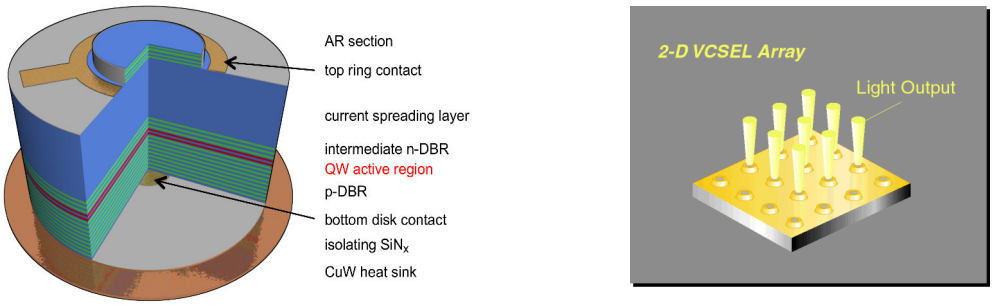

Figure 1.9: Left: internal structure of a VCSEL [Pallmann 2013]. Right: 2-D VCSELs array from the same substrate after the fabrication process.

Nowadays, there is a variety of optical transmitters available on the market or undergoing research and development. The competition is intense in order to reach faster and faster data rates.

For short distances (local area networks), the common and cheapest technique is the direct modulation of semiconductor lasers, which allows to reach up to 10 GHz in bandwidth [Amann 1998, Ramakrishnan 2002, Takagi 2004]. In this context, Vertical Cavity Surface-Emitting Lasers (VCSELs) [Iga 2000, Michalzik 2003] have net advantages over other devices (Fig. 1.9) : they are small-sized, low threshold, single longitudinal and transverse mode devices. Their vertical structure allows to manufacture arrays of devices from the same substrate, which sensibly decreases the fabrication cost (see Fig. 1.9). Their transverse section is circular, therefore the emission profile of a single transverse mode device is gaussian and coupling with a monomode optical fiber is facilitated. However, electrical modulation of semiconductor lasers suffers three major drawbacks. First, the upper frequency for the modulation rate is limited by the impedance of the device (comprising packaging) [Tucker 1985]. Second, for typical high-speed systems, operation with I_{BIAS} at or very near I_{th} is necessary in order to avoid strong noise and distortion of the signal when modulation is resonant with the Relaxation Oscillations (RO) frequency of the laser [Larsson 2004]. This decreases the available Extinction Ratio (ER), which is defined as the pulse one level power divided by the pulse zero level power. Third, directly modulated semiconductor lasers exhibit strong chirp, the laser emission frequency deviates from its equilibrium value due to RO. Therefore, the signal's optical spectrum is broadened and the various frequency components, traveling at different speeds in the fiber, do not arrive simultaneously at the receiving detector. These restricted ER and chirp limit the maximum link distance of those devices to approximately 10 km due to deformation of the pulse, loss of power and growth of the background [Meliga 2004]. A simple and cheap solution for chirp reduction in directly modulated semiconductor was theoretically investigated in [Dokhane 2001] and experimentally demonstrated in [Hachair 2005]. This technique consists in suppressing the RO in the switch-on and switch-off transitions by choosing a shape in the injection current that is capable of compensating for the laser RO, it was named Direct Modulation with Patterned Current Front (DMPCF). Even if this

simple and feasible method showed very good results in improving the speed and quality of off-on and on-off transitions, it has not been retained by the industrial world for optical communication systems.

In order to circumvent the difficulties linked to electrical modulation, a solution may be envisaged using the all-optical generation of localized bits of light in the emission of the VCSELs. Indeed, LS appear as bright and narrow intensity peaks over a low-energy homogeneous background. Their independance, addressability and repetitivity properties would provide high ER, no chirp and fast repetition rates. Moreover, the size and amplitude of the signal emitted by LS is fixed to certain discrete values and the perturbation which is needed to switch them on has to exceed a threshold value. These two properties could be used to restore a noisy or weakly modulated signal since low amplitude values of the input signal could be converted into a LS. As LS are formed over a zero intensity background, the signal-to-noise ratio could be substantially increased. Section 1.3 will depict the already existing techniques and results in the implementation of spatial and temporal localized structures in the output of VCSELs.

Longer distances and high-ends bandwidth applications for fiber data transmission necessitate larger amplitude bits generation. Here the laser source may be operated in the continuous wave (c.w.) regime and the light is modulated by an external device such as a Mach-Zehnder (MZ) interferometer [Tsuzuki 2003] or an Electro-Absorption Modulator (EAM) [Lewen 2004, Fukano 2004]. In contrast with directly modulated semiconductor lasers they can be designed to exhibit both zero chirp and high ER. Today, external modulators are commonly used to achieve 40 GHz data rates.

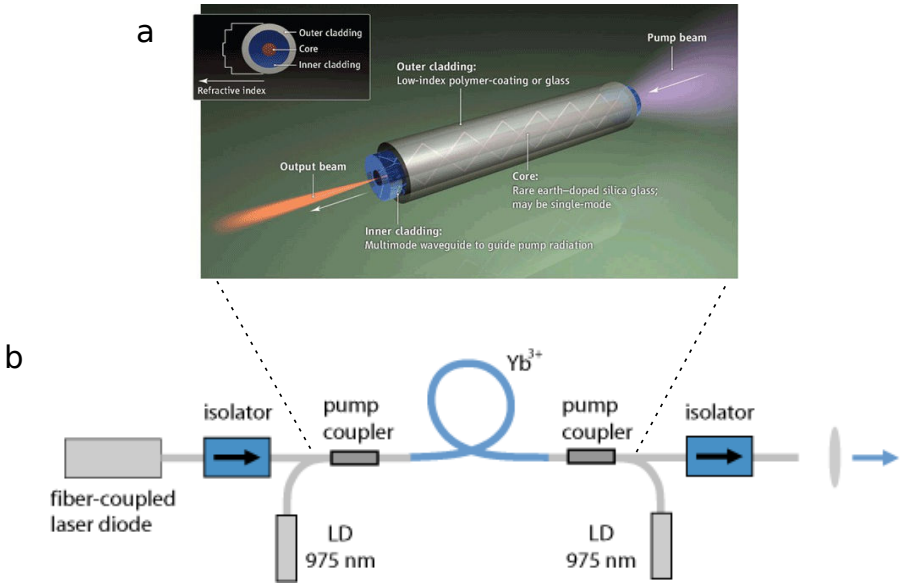

Figure 1.10: a) Fiber laser representation. b) Fiber laser inserted in a MOPA setup.

For applications such as interplanetary or earth-orbiting satellites data transfer, Free-Space Optical communication (FSO) has become more and more interesting as an adjunct or alternative to radio-frequency communications. In order to overcome the various sources of losses and noise in the atmosphere (extinction caused by air and molecules, distortion of the wavefront due to index of refraction turbulences (IRT)), FSO requires high-power transmitters that can accomodate high modulation capabilities with good beam quality. Fiber-based lasers (Fig. 1.10a) offer advantages for spaceborne applications, such as high efficiency, low volume, and mechanical robustness. Output powers now routinely exceed 100 W [Gapontsev 2004, Galvanauskas 2004, Jeong 2004] for continuous wave (CW) fiber lasers and pulsed systems can operate at more than 100-MHz repetition rates with multi-kW peak powers and multi-W average powers [Wright 2007]. Obtaining high modulation quality of the output signal generally leads to master oscillator power amplifier (MOPA) geometries, where the device output modulation, linewidth, and wavelength are determined by the seed laser and the fiber amplifier raises the power to the required level (see Fig. 1.10b). The seed laser can be either a direct-modulated diode laser or an externally modulated CW diode.

In this context also, the generation of temporal LS in the output of fiber lasers could offer a way to increase the repetition rate of bright addressable optical bits. Research in this field is going on, and the next section 1.3 will describe the present results.

1.2.2 Localized structures as bits for optical buffer applications

Whenever two or more optical data packets arrive at a network node at the same time and contend for the same ouptut, external blocking occurs. All packets but one are perceived as superfluous and have to be dealt with. Thus, telecommunication networks need devices capable of temporarily storing light in order to control the time of occurence of events: they are called buffers.

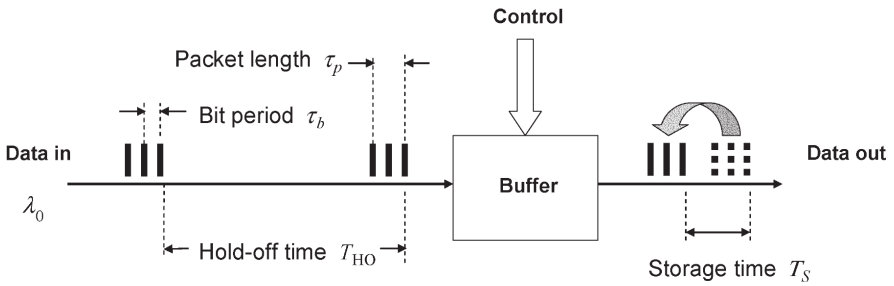

Figure 1.11: Principle of a buffer [Tucker 2005].

An example is given in Fig. 1.11. Two important parameters that characterize the overall performance of the buffer are the storage time T_s and the hold-off time T_{HO}. In Fig. 1.11, the output packet shown with dashed lines represents the input data as it would have emerged from the buffer if it has passed directly

through the buffer without any controlled delay. The storage time is the delay between this and the buffered packet. The difference between a real buffer and a buffer-memory is the accessible range of values for the storage time T_s. While this value is fixed for a buffer-memory, a real buffer can store the data for a controlled amount of time. In Fig. 1.11, the storage time T_s is shown as being larger than the packet length τ_p, but T_s can be smaller than τ_p. The hold-off time is a "dead time" after data have been loaded into the buffer. During T_{HO}, the buffer cannot accept any additional data. This limits the rate at which packets can be loaded into the buffer. We define T_{HO} to be the minimum allowable time between the leading edge of an incoming packet or group of packets that have been stored in the buffer and the leading edge of the following packet or group of packets that are to be stored independently of the first group.

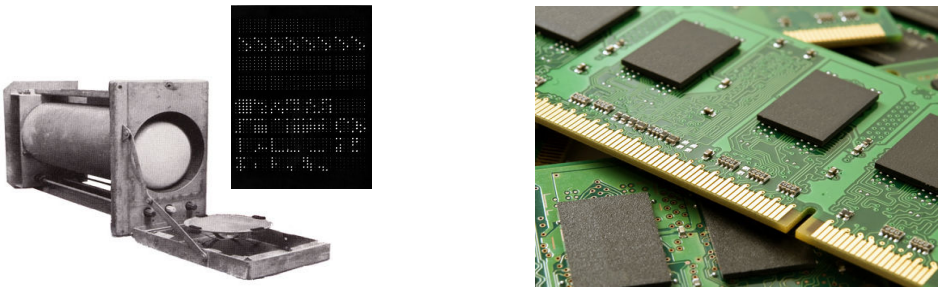

Figure 1.12: Left: Williams-Kilburn's tube. A close-up view reveals dots (ones) and spaces (zeroes) on the face of a tube. The bits had to be refreshed before the dots faded, in less than a second. Right: DRAM.

As electronical telecommunications were the only way to convey information until the 1970s (see Fig. 1.8), electrical buffers have been developed since the invention of the first practical form of Random Access Memory (RAM) called the Williams-Kilburn's tube [Williams 1948](see Fig. 1.12). Memory density has been greatly increased in the early 1970s when Dennard invented the Dynamic Random Access Memory (DRAM) [Dennard 1968] in 1968 (see Fig. 1.12). Data is stored in the tiny capacitance of transistors and had to be periodically refreshed every few millisecond before the charge could leak away. The two main forms of modern RAMs are static RAM (SRAM) and dynamic RAM (DRAM).

With the onset of optical data transmission in the form of packets of light, electrical buffering requires a stage of conversion between photonic information and electrical storing. In this domain, recent research shows that silicon-based Complementary Metal-Oxide-Semiconductor (CMOS) RAM can be used as a storage medium at data rates up to 40 Gb/s. Because bits are stored electronically, such a design offers very long storage times, large capacity, and random access at arbitrary times. However loss and components complexity have limited the design to packets of less than 16 bytes. The restriction on the maximum packet size greatly limits the maximum load of the network. A natural solution envisaged for increasing the data rate storing and the packet size is an all-optical system where electrical con-

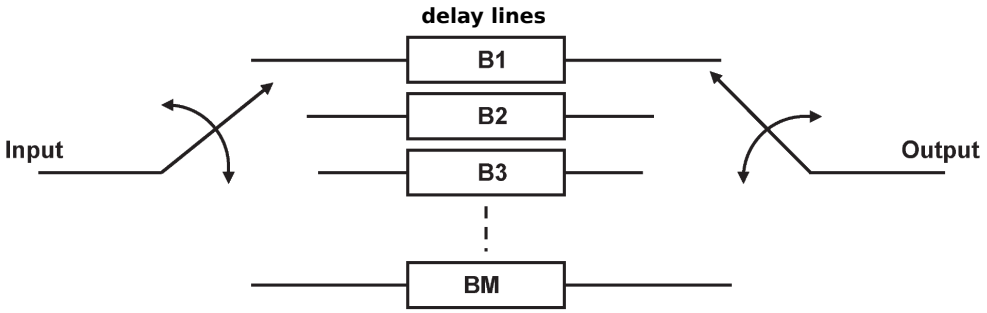

Figure 1.13: Buffer memory [Tucker 2005].

version is avoided. So far, two types of transparent optical buffering approaches have been studied. Both rely on delaying packets by increasing total transmission line, either by decreasing the group velocity (slow-light buffers) or increasing the physical length (delay-line buffers) [Tucker 2005]. The functionality of a fiber delay-line (FDL) memory is essentially different from a traditional electronic RAM. The length of the FDL and the entry time of the packet completely determine when the packet leaves the FDL. Thus, FDL lines hold the information for a fixed amount of time as opposed to RAM where one may retrieve the stored information at any time. Without a controllable change in propagation time, the buffer memory is just a fixed delay that, by itself, does not constitute a buffer. Fig. 1.13 shows how the number of buffer memories B1-BM can be combined in parallel. A RAM buffer can be constructed with this parallel structure using switches at the input and output in order to allow the selection between various storing times. However this technology cannot achieve fast performances and the range of accessible delay values is limited by the number of delay lines that are put in parallel.

Therefore, no optical equivalent to the electrical RAM technology has ever been realized. It may be in the domain of optical buffer systems that the properties of LS appear as the most relevant for great improvements. Indeed, a LS is a stable connection between a low homogeneous background and a higher intensity state. Once a LS is generated via an external perturbation, the on-state is stable and carries on if no other perturbation is applied to the system. Thus the information could be stored for an infinite amount of time without any deformations. We have shown in section 1.1 that LS can also be erased with a suitable perturbation. One could therefore imagine creating an all-optical reconfigurable buffer with LS in VCSELs or fiber lasers. In the next section, we will show how such application for optical LS has already been demonstrated.

1.3 Experimental realizations of localized structures in optical resonators.

The aim of this section is to introduce and precisely define the various types of optical LS experimentally observed both in fiber lasers and VCSELs. We will make a distinction between the LS obtained in the intensity output of lasers and the vectorial LS found in the polarized emission. We will underline the fundamental interests of each LS realization and their potential for applications in the domain of optical data transmission systems.

Scalar LS are observed in the total intensity output of lasers. They were first observed in the transverse section of broad-area VCSELs and therefore were spatial LS [Barland 2002]. The temporal equivalent for these scalar spatial LS were observed a few years ago in fiber lasers [Leo 2010]. They consist of light localization in the axis of propagation (z,t) and therefore look like pulses traveling along the propagation axis of a cavity. Both spatial and temporal scalar LS existence require a mechanism that creates in the system a region of bistability between an homogeneous backgroung and a higher intensity patterned solution.

On the one hand this mechanism can consist of an external beam injecting a passive nonlinear resonator (subthreshold), and the temporal or spatial LS solutions are called Cavity Solitons (CS). In the temporal case, the modelization of the nonlinear fiber resonator consists of a one-dimensional partial differential equation for the intracavity field which takes into account chromatic dispersion, instantaneous Kerr effect, cavity losses, cavity phase detuning and external coherent driving [Matsko 2011]. In the limit of low loss, high finesse cavity (mean-field limit), this model is formally identical to the Lugiato-Lefever model of a diffractive cavity [Lugiato 1987]. In the spatial case, the system under consideration is a driven semiconductor microcavity. Proper models must therefore consider the basic physical mechanisms which govern a semiconductor material, namely, the carrier density dynamics coupled to that of the field and the carrier diffusion which is critically relevant for transverse effects [Brambilla 1997]. Therefore such a model is composed of two 2D partial differential equations for the intracavity field (in the mean-field limit) and carriers. In [Brambilla 1997], spatial CS are found stable either when the laser is pumped below or pumped above transparency (but still below threshold).

On the other hand, when the laser is pumped above threshold and an intracavity saturable absorber induces local bistability, LS can form and constitute independent laser sources (laser solitons) since each structure has the freedom to choose its own phase and frequency ([Rosanov 1992, Vladimirov 1999, Bache 2005] for numerical study, [Genevet 2008, Grelu 2012] for experimental investigations). As in the case of CS, the spatial laser solitons were observed in the transverse section of VCSELs, while temporal equivalents were found in the frame of passively mode-locked fiber lasers.

These spatial and temporal scalar LS are thus a group of LS composed of two subgroups: cavity solitons and laser solitons. The next section will detail the differences between both types of LS. But light is not a scalar quantity, it is a vectorial one. It is an electromagnetic field that has a certain amplitude but also a certain orientation in the transverse plane that is called polarization. In all works cited above the polarization axis of the electric field is fixed, the light orientation degree of freedom is not taken into account.

Both semiconductor and fiber lasers gain media exhibit birefringence (polarization dependent frequency) and dichroism (polarization dependent gain) which allow for the generation of complex polarization dynamics [Agrawal 1989]. In the frame of temporal LS observed in PML fiber lasers (and also in the frame of conservative solitons propagation in fibers), it has been found that the absence of polarizer inside the cavity may allow for the evolution of the polarization orientation of the solitons as they propagate in the anisotropic resonator. These objects are called "Dissipative Vector Solitons" (DVS). This denomination comprises phase-locked DVS, or polarization rotating DVS ([Menuyk 1987, Menuyk 1988, Christodoulides 1988, Afanasjev 1995, Akhmediev 1995] for theoretical predictions, [Tang 2008, Zhao 2009, Zhang 2011, Ouyang 2011] for experimental realizations). In this case, the system can be modelized by a set of coupled CGLE equations (one for each polarization axis) where cross-phase modulation accounts for energy exchange between the two orthogonal axes of polarization. It is important to stress that DVS do not consist in a pure polarization dynamics since a signal can still be obtained while detecting the total intensity output of the system. However another type of vectorial pulses features antiphase dynamics and was observed in fiber lasers where the saturable absorber has been removed [Williams 1997, Zhang 2009, Wabnitz 2009, Lecaplain 2013, Lecaplain 2014]. Here the polarization dynamics can consists in fast polarization flips that are triggered by noise in the system for a specific value of the fiber birefringence. These objects are also called Polarization Domain Wall Solitons (PDWM). As dichroism and birefringence can be managed in fibers via polarization controllers, in [Williams 1997, Lecaplain 2013] authors could also observe the onset of an antiphase square-wave regime as dichroism and losses are increased in the cavity.

1.3.1 Scalar localized structures

In this section we will point out the major differences between the properties of Cavity Solitons and laser LS, both in the temporal and spatial cases.

1.3.1.1 Spatial and temporal cavity solitons

As previously stated in section 1.1, the emergence of LS in optical systems requires a mechanism for bistability and a large aspect-ratio. The first experimental realization of scalar spatial LS was accomplished in 2002 [Barland 2002]. The laser used in this experiment is a broad-area VCSEL (150 μm diameter) that is pumped

above transparency but slightly below threshold (optical amplifier)(Fig. 1.15). The large transverse section of this type of devices allow the center region of the VCSEL to behave independently from the boundaries. In other words, spatial correlation length is much smaller than the transverse size of the device.

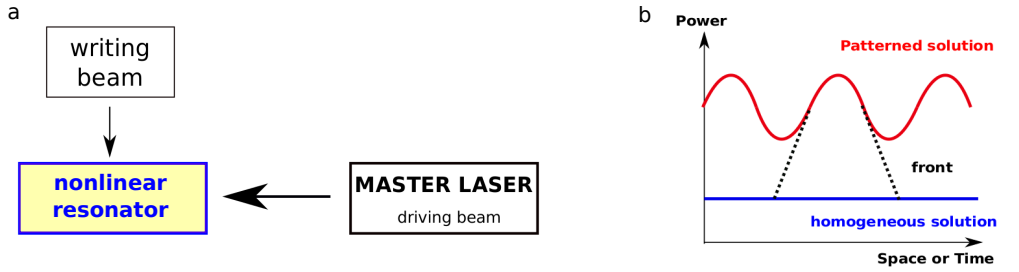

Figure 1.14: a) Schematic of experiments for CS implementation. The nonlinear resonator can be either the transverse section of a VCSEL for spatial localization of light or a fiber laser cavity for temporal localization. The space/time patterned state shown in b) is induced by coherent injection from an external Master beam. The writing beam creates a front connecting the homogeneous stable background with the higher intensity solution.

When this laser is driven via an external coherent beam in resonance with the VCSEL cavity (see Fig. 1.14a), passive morphogenesis of the optical field takes place [Arecchi 1995]. This phenomenon gives rise to a spatial modulation of the field (see Fig. 1.14b). Due to the slight cavity detuning imposed by the VCSEL manufacturing, as the transverse section is scanned along the x-axis, one can pass from an homogeneous zone on the right followed by a spatial modulation in the center and finally another modulation of different frequency on the left (morphogenesis being favored by blue detuning between cavity and holding beam in this case, see Fig. 1.15b). On the line separating the pattern (left) and homogeneous field (right), local values of the cavity resonance meet the conditions for the onset of a pattern-inducing MI. In 2004, the same experiment was renewed with a VCSEL whose cavity resonance gradient was decreased in order to increase the zone where the latter conditions are fulfilled [Hachair 2004].

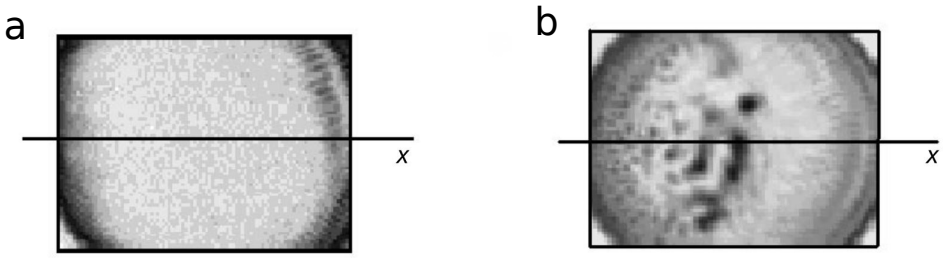

Figure 1.15: Intensity distributions for the solitary laser (a) and the driven VCSEL in b) [Barland 2002].

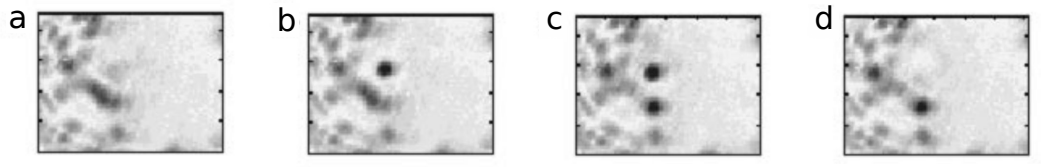

Figure 1.16: Experimental demonstration of independent writing and erasing of CS. The intensity distribution of the output field is shown over a 60 μm * 60 μm region in the sample centre. a) The writing beam (WB) is blocked, b) the WB impinges on the homogeneous region; it induces the appearance of a single high intensity spot (dark in the figure) in a limited region of space, c) a second CS is written, d) the phase of the WB relative to the holding beam is changed by π, and the upper spot disappears [Barland 2002].

Since both homogeneous background and pattern are stable solutions, setting the system in this parameter value does not lead to spontaneous emergence of LS. However, the authors showed that they could apply an external optical perturbation (coherent with the holding beam) into the homogeneous zone and form a high intensity spot with a diameter of about 10 μm (Fig. 1.16b). When they removed the writing beam, the spot remained indefinitely. Yet it could be erased by applying a Π-phase shifted perturbation onto the same spot (Fig. 1.16d), which proved that these structures were bistable and addressable. They finally showed that several spots could coexist in this very zone of the laser and be addressed independently. This is why CS are considered as pixels onto the VCSEL surface. Thus, CS can be used to store and process optical information. Pedaci et al. showed that they could realize a matrix of spatial CS by periodically modulating the phase of the holding beam, this way they managed to spatially organize optical bit storing [Pedaci 2006]. He also proved that the CS can be moved under a phase gradient in the holding beam profile [Pedaci 2008a].

Therefore, [Barland 2002] is of major importance since the authors showed for the first time the experimental realization of LS via passive morphogenesis and modulational instability in an injected nonlinear resonator. The experiment showed that the VCSEL surface under coherent injection is a potential optical array processor with spatial CS as independent pixels. However, the positions of CS on the surface are restricted due to material inhomogeneities of semiconductor media acting as trapping sites [Pedaci 2008b] and the lack of transverse uniformity in the cavity. Consequently, from that discovery on, research has been carried on to avoid these restrictions and make optical LS suitable for applications.

In a Kerr medium, nonlinearities may compensate for diffraction, but also for dispersion of an optical pulse. Actually, if one only considers propagation of light in a cavity and eliminates transverse degree of freedom, then one ends up with a unidimensionnal Kerr nonlinear system susceptible to self-organization phenomena in the longitudinal dimension z [Agrawal 1989]. Eight years after [Barland 2002], the first experimental demonstration of temporal CS in a Kerr cavity was established in [Leo 2010]. In its experiment, a fiber cavity plays the role of the large

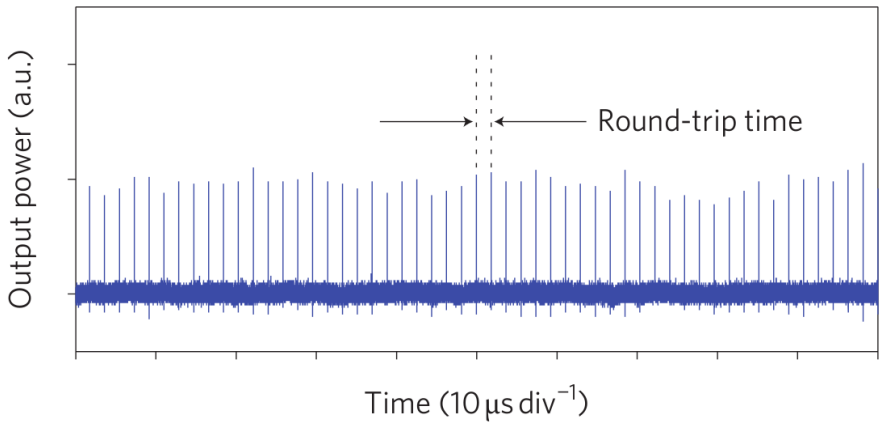

Figure 1.17: Observation of an isolated CS. The delay between subsequent pulses matches the 1.85-μs cavity round-trip time, and confirms the presence inside the cavity of a single persistent pulse circulating repeatedly, only sustained by the c.w. driving beam [Leo 2010].

aspect-ratio nonlinear resonator (Fig. 1.14a). This passive cavity is driven coherently via an external holding beam, providing the mechanism for bistability between an homogeneous c.w. solution and a temporal patterned state of higher intensity. In this range of parameters, when one perturbs the system with a short pulse via an external writing beam, then the response of the system consists of the onset of a pulse after some round-trips that circulates repeatedly in the cavity without modifying its shape (see Fig. 1.17). The authors showed that this pulse is the temporal equivalent of the spatial CS shown in [Barland 2002], since they possess the exact same properties : repetitivity of their size and shape, independence, addressability.

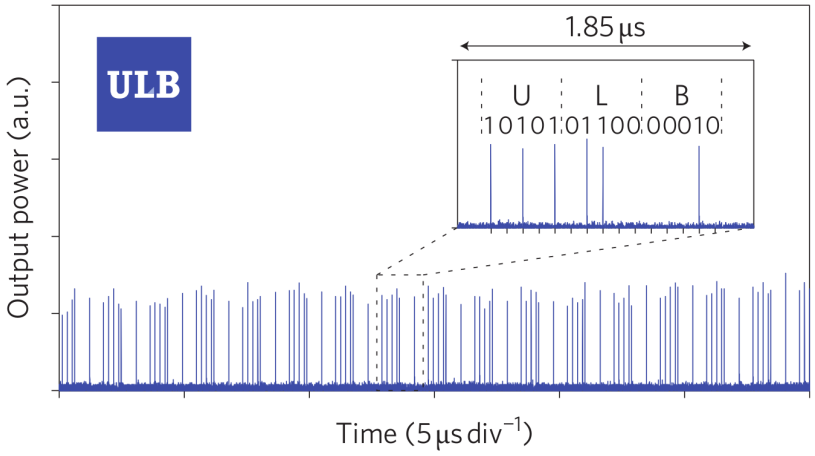

Figure 1.18: The acronym of the ULB institution stored all-optically with temporal CS. ULB (Université Libre de Bruxelles) is encoded as a 15-bit data stream in the passive fibre cavity. Each letter is represented with five bits by its ordinal position in the alphabet (U=21, L=12, B=2) [Leo 2010].

Moreover these temporal pulses possess a serious advantage with respect to their spatial counterpart: since space in Leo's setup is the longitudinal axis of propagation, then its uniformity allows for the generation of temporal CS at any locations within the cavity round-trip. Leo et al. showed that a passive fiber cavity can be used as an array for signal processing and buffer applications where the number of pulses one can address is only limited by the size of the external cavity (the more space, the more pulses allowed) (Fig. 1.18). They showed that they could achieve a bit rate of 25 Gb/s with temporal CS, which is a very competitive result. However lifetime of these pulses is limited by the cavity-length stabilization. In the present work, the temporal LS last for several seconds which surely needs to be improved for useful applications. Besides, following works showed that long-range interaction among CS can be responsible for introducing a minimal distance between LS [Jang 2013b]. This phenomenon is a limitation to the number of pulses allowed within one cavity round-trip.

As a conclusion, CS in the intensity output of lasers have been found both in the spatial and temporal domain. Both methods require an external injection into a passive Kerr medium in order to induce passive morphogenesis. The bistability between the homogeneous state and the space (or time) patterned state allows one to address LS that appear as local surintensity spots (or pulses) over the homogeneous background. However, the use of an external injection decreases the interest for such technologies in potential applications since :

- The setup becomes costy, uneasy to align and to stabilize. In fact, CS can only appear in a very narrow range of frequency detuning between the holding beam and the passive resonator.
- The CS generated out of injected systems are locked in polarization, phase and frequency to the external holding beam. They lose these three degrees of freedom for potential data storing. Moreover, in the case of spatial CS, the frequency locking prevents from multimode oscillations and the observation of interesting CS dynamics. Therefore, ultimately, this setup might not lead to spatio-temporal solitons or self-localized optical light-bullets.

Hence, researchers have been investigating ways to generate LS out of laser systems that do not require an injection beam, which is better suited for monolithic integration and further investigations on LS spatio-temporal dynamics.

1.3.1.2 Spatial laser localized structures

In the field of light-matter interaction, morphogenesis can also emerge actively. In this case the intracavity medium is pumped and gives rise to the emergence a field. This is the case for lasers pumped over threshold. The field being born from the laser nonlinear gain medium, and the laser being unable to self-sustain LS, one has to implement a external mechanism capable of inducing bistablility in order to sustain the so-called Laser Localized Structures (LLS).

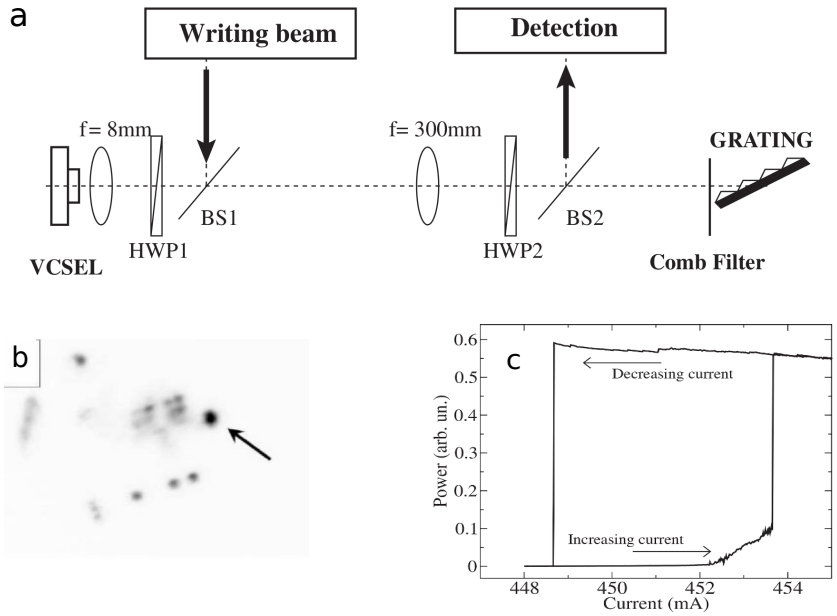

Figure 1.19: a) Experimental apparatus for spatial LLS generation. b) Near-field intensity distribution showing the switching on of a spot with an injected incoherent field (brightest spot, indicated by an arrow). c) Power versus current for a single spot [Tanguy 2008a].

The first Solitons Laser was designed in 2008 [Tanguy 2008a, Tanguy 2008b]. They coupled a broad-area VCSEL (200 μm) to a Frequency-Selective Feedback (FSF) cavity. The FSF is controlled by a grating placed in a littrow configuration and the external cavity is self-imaging so as to provide to the system a high Fresnel number which allows for potential self-localization independent from the boundaries (Fig. 1.19a). The bistability mechanism relies on phase-amplitude coupling and frequency detuning between the solitary laser an the FSF cavity [Henry 1982]. It was first investigated in medium-size VCSELs (80 μm diameter) in similar FSF configurations [Tanguy 2006] where no LLS could be found since the bistable zone was still dependent on boundaries. With such a configuration, Tanguy et al. succesfully managed to create spatial LLS (or microlasers) that are bistable and have the freedom to choose their phase, polarization and frequency (Fig. 1.19b-c). The LLS can be addressed via an external perturbation applied onto the VCSEL top surface with a focused writing beam (WB). Authors also demonstrated the mobility of their LLS by dragging an existing LLS with a WB applied just beside it. They observed a drift of the LLS towards the WB spot probably due to the local increase of refractive index at the WB location [Tanguy 2008b]. These microlasers seem more suitable for communication applications than the spatial CS since they are not sustained with any injection beam. Nevertheless the system suffers some major drawbacks :

- The stability of the structures critically depends on FSF cavity alignment and detuning with respect to the laser. These parameters can be controlled only mechanically which renders the system uneasily exploitable.

- Spatial LLS generated out of this experiment are operating in the continuous regime. A self-pulsing state could only be observed during an on-off transient time of tens of nanoseconds. No further investigations have been led by authors to attempt to generate a stable LLS pulsing dynamics, probably since it would bring to much complexity to their setup.

Another method for the generation of spatial LLS was proposed the same year in [Genevet 2008]. The original idea was first brought by theoreticians in 1992 [Rosanov 1992] (and further developed in [Vladimirov 1999, Fedorov 2000, Rosanov 2002]) who predicted the formation of spatial LLS in a laser with saturable absorber. The motivation for the experimental implementation of Rosanov's idea was to bring to the solitons community a new and compact way for LLS generation and to study likely new features of these objects.

In [Genevet 2008], Genevet et al. proposed to couple a broad-area VCSEL pumped above threshold to the same device kept well below threshold, thus acting as an absorber. In order to maintain a high Fresnel number, a self-imaging configuration is used, which can be made with two or four lenses depending on the size of the cavity (Fig. 1.20a). When the laser frequency is set in resonance with the

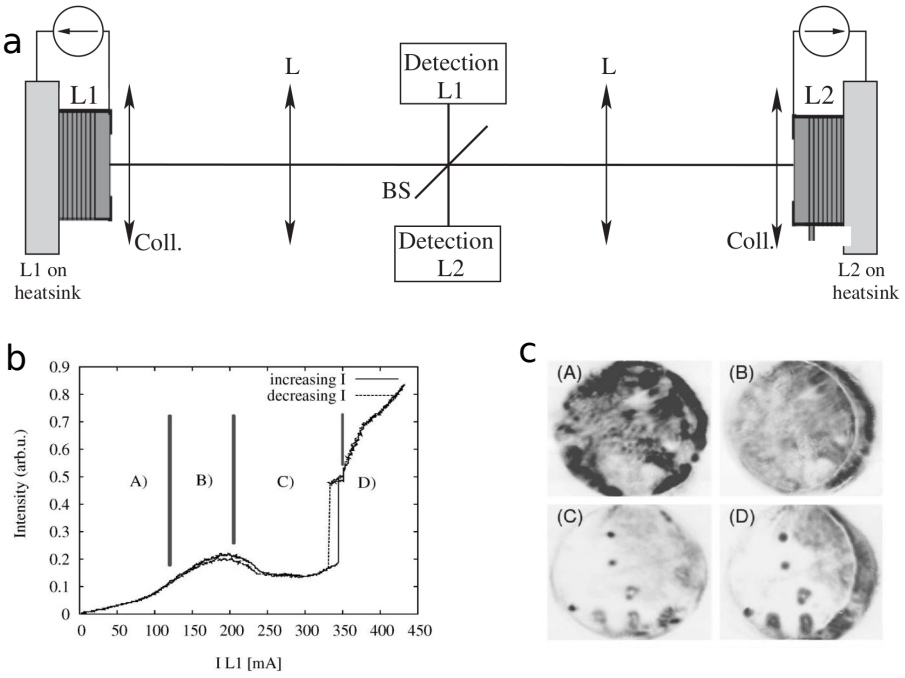

Figure 1.20: a) Experimental setup. L1: Laser above the transparency, L2: laser below the transparency, BS: beam splitter. b) Local intensity output emitted by the system when scanning I_{L1} with all the other parameters kept constant. (A) below threshold, (B) lasing by feedback from L2, (C) absorption by L2, bistable behavior between 330 and 350 mA, (D) pattern formation. c) Near-field of both devices. Dark areas correspond to high intensities. (A), (B) Near-field image of L1 (L2), before the interaction (I_{L1} = 180 mA), (C), (D) Near-field of L1 (L2), in the absorption zone (I_{L1} = 358 mA) [Genevet 2008].

VCSEL absorption peak (zone C in Fig. 1.20b), the system is in the regime of strong absorption and no lasing can possibly occur. In this case, the authors showed that local bistable (with respect to current or temperature scanning) surintensity spots can develop spontaneously in the surface of the VCSEL (Fig. 1.20c). He also showed that he could address these LLS thanks to an external optical perturbation, place several of them within the laser section and proved their mutual independence. He carefully demonstrated the coherence properties of two neighbour structures forming a molecule, and showed that the LLS become incoherent (different frequencies) when sufficiently far from one another. The system possessing a phase degree of freedom, he showed for the first time the formation of vortex localized structures (structures possessing a topological charge [Rosanov 2005]) and composite localized structures that are all multistable in some parameters range.

Thus, he demonstrated the existence of Spatial Laser Localized Structures based on saturable absorption in a system of two coupled broad-area VCSELs and gave proof of the fundamental interest of such a system concerning the coherence properties, mutual interactions and complex structures formation of LLS.

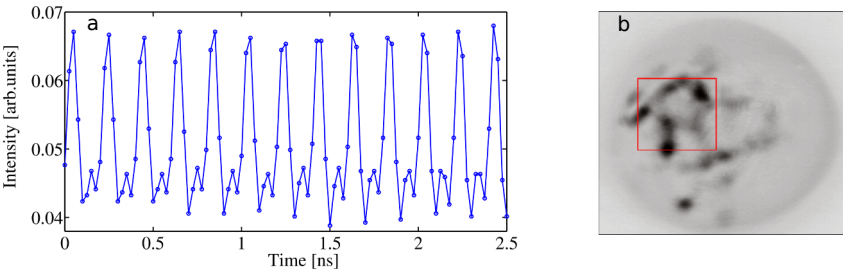

Figure 1.21: a) Periodic train of pulses emitted by the VCSEL when the cavity is not anymore in the self-imaging configuration. The cavity length is about 3 cm. b) Near-Field of the amplifier associated to the temporal trace. The square indicates which zone is pulsing.

Semiconductor (or fiber) lasers coupled to external saturable absorbers have been well-known to develop temporal dynamics consisting of narrow pulses with a period equal to the external cavity round-trip time via a mechanism called Passive Mode-Locking (PML) [Ippen 1994]. Indeed saturable absorbers have the property to create a short temporal window for gain larger than losses which favors a pulsed emission rather than c.w. emission in the laser intensity. Thus, very interestingly, systems coupling lasers with transverse extension to saturable absorbers could develop a dynamics consisting of LLS whose temporal dynamics would be pulses at the external cavity Free Spectral Range (FSR) rate. Such a three-dimensional localization of light in a nonlinear optical resonator with a saturable absorber was predicted in [Vladimirov 1999, Veretonov 2000, Rosanov 2002, Brambilla 2004]. The authors observed a 3D self-organization phenomenon proceeding from the resonator feedback, combined with diffraction and nonlinearities. Their so-called Cavity Light-Bullets (CLB) can be independently excited and erased. Once created, they endlessly survive in the cavity if no appropriate perturbation is applied in order to switch the structures off.

Experimentally, Genevet et al. could only observe a pulsing regime during the switch-on transition or monostable pulsating spatially extending structures (see Fig. 1.21) when the setup was not anymore fulfilling the self-imaging condition. Therefore temporal localization could not by obtained together with spatial LS when two VCSELs are coupled, one providing amplification and the other absorption. Genevet et al. concluded that no light-bullets could be generated out of this experimental setup. Years later, a complex regime of drift-induced excitable LS was identified [Turconi 2013]. In this state, the dynamics of spatial LLS exhibits bursts composed of pulses separated by the round-trip time of the external cavity.

Tanguy and Genevet managed to create Spatial Laser Localized Structures in a broad-area VCSEL. These structures have phase, polarization and frequency degree of freedom (microlasers) since they are not locked to any injection beams as in the case of Cavity Solitons.

But have the LLS ever been observed in the temporal domain ?

1.3.1.3 Passive mode-locking and dissipative temporal solitons

Laser Mode-Locking (ML) is a fascinating self-organized cooperative effect involving a large number of longitudinal modes that was recently linked to out-of-equilibrium phase transitions [Gordon 2002]. From a practical point of view many applications require sources of short pulses like e.g. medicine, metrology and communications [Haus 2000]. Passive ML (PML) is arguably one of the most elegant method to obtain such pulses. It is achieved by combining two elements, a laser amplifier providing gain and a saturable absorber (SA) acting as a pulse shortening element. Under appropriate conditions, the different dynamical properties of the absorption and of the gain favor pulsed emission by creating a limited time window for amplification around an intensity pulse [Haus 1975a, Haus 1975b].

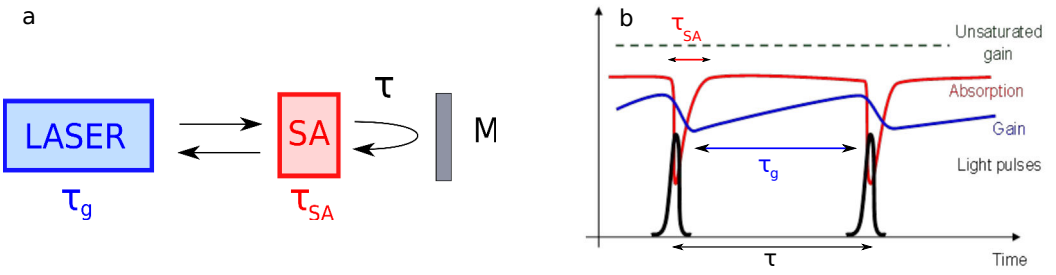

Figure 1.22: a) Scheme for Passive Mode-Locking (PML). b) Time dependence of pulse, loss and gain in the PML regime.

Fig. 1.22a) describes a typical PML setup where the laser, with a gain recovery time τ_g, and the SA, with a loss recovery time τ_{SA}, are inserted in a cavity closed by a mirror with a round-trip time τ. Fig. 1.22b) gives the necessary parameter conditions for the onset of a stable PML regime. When a pulse circulates in the external cavity and interacts with the laser, it induces a depletion in the gain with a certain depth, as depicted in blue line. The same occurs for the losses when the

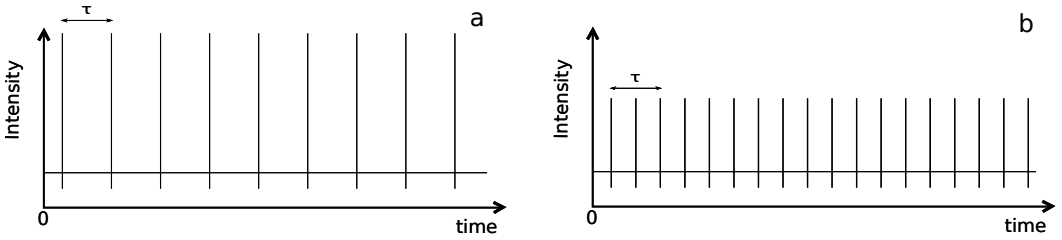

Figure 1.23: a) Fundamental Passive Mode-Locking. b) Harmonic Passive Mode-Locking, the temporal separation between two consecutive pulses is half the external cavity round-trip time.

pulse interacts with the absorber, as shown in red line. The graph demonstrates that a window for net gain around the pulse can be opened only if the modulation of the losses is larger than the modulation of the gain. In other words the SA saturation fluence has to be smaller than the gain saturation fluence. Also, in the interval between two consecutive pulses, the losses have to be larger than the gain in order to provide stability to the background emission (background stability criterion). This imposes a condition between gain and loss recovery times values and the repetition rate such that $\tau_{SA} < \tau < \tau_g$ (when $\tau_{SA} \ll \tau$, the system is in the fast absorption regime). A well-known phenomenon called Harmonic Mode-Locking (HML) (see Fig. 1.23) can occur when the round-trip time becomes much longer than the gain recovery time or when the pumping current is increased. In this case the background stability between two pulses separated by the external cavity round-trip time is lost and a multiple pulsing develops with an equal temporal spacing corresponding to harmonics of the fundamental resonator frequency. This phenomenon can also manifest if the modulation of the gain is very low compared to the modulation of the losses. The harmonic mode-locking regime is thus stabilized to a well-defined value of N_h (N-th order harmonic PML) for a given value of the pump and of the round-trip time. The amplitude of the pulses decreases when HML occurs since the intracavity power is split in more that one pulse per cavity round-trip.

PML can be achieved using artificial SA like e.g. nonlinear polarization rotation [Dorren 2003], Kerr-lens mode-locking [Ippen 1994], Crossed-Polarization [Javaloyes 2006] or Stark-effect modulation [Wilcox 2008]. PML has already been implemented successfully whether in semiconductor lasers or fiber lasers. Yet, the two devices possess very different characteristics:

- The gain recovery time for semiconductor lasers (about 1 ns) is much shorter than the one for fiber lasers (about 10 ms). Therefore semiconductor lasers are used to produce very fast repetition rates thanks to a rapid modulation of the gain.

- Since fiber lasers are optically pumped devices, they exhibit a very shallow modulation of the gain when interacting with a pulse. This effect combined with the large possible extension of external fiber cavities facilitates the onset of the harmonic mode-locking regime. It is often used to produce high

amplitude multi-GHz repetition rates pulses. The only way to achieve low-frequency PML is to operate the fiber laser close to threshold. In the case of semiconductor lasers the fast recovery of the gain prevents from increasing the size of the external cavity while keeping a stable PML regime.

- While the temporal width of semiconductor lasers mode-locked pulses are limited by the photon lifetime in the laser cavity (typically a few picoseconds), in fiber lasers pulses are triggered by the saturable absorber and may be reshaped under the effect of anomalous chromatic dispersion and Kerr nonlinearities while they propagate in the external fiber cavity. This dynamics is called soliton mode-locking, it is used in fiber lasers to achieve femtosecond pulses durations, which can be significantly shorter than the response of the saturation effect [Mollenauer 1984, Kartner 1996].

- In the specific case of VCSELs, the cavity is so small that the device is lasing on a single longitudinal mode. Therefore in a PML scheme, an external cavity must be set to provide the longitudinal degree of freedom for the onset of a mode-locked dynamics. VCSELs having a very high-Q cavity, a regime of gain saturation is rapidly reached when the laser is operating c.w., which unfavors PML dynamics. The way to circumvent that difficulty is to use a "1/2 VCSEL" (a VCSEL whose top DBR layers have been partially removed) in order to prevent the solitary device from lasing. When this device is coupled to an external cavity and feedback from a highly reflective mirror allows to reach laser threshold, the system is called VECSEL (Vertical External-Cavity Surface-Emitting Laser). If one inserts a SA in a VECSEL, PML regime can be obtained either with optically-pumped VECSELs (OP-VECSELs) [Keller 2006], or electrically-pumped VECSELs (EP-VECSELs) [Pallmann 2013].

- The PML dynamics in fiber lasers is very well reproduced in simulations with the Haus Master equation [Haus 2000] which combines the nonlinear Schrödinger equation with dynamical nonlinear gain and losses. In this model, a pulse circulating in a resonator is described with a complex amplitude A(t). While propagating in a nonlinear cavity, the pulse undergoes changes caused by laser gain, optical saturable and unsaturable losses, dispersion and nonlinearities (e.g. Kerr effect). This model assumes small gain and losses and weak saturation which are relevant approximations in the case of fiber lasers. However, semiconductor mode-locked lasers have high gain and losses per cavity round-trip, which invalidates Haus' classical approach. A more general model for semiconductor lasers has been derived in [Vladimirov 2005] which consists of a set of differential equations with time delay for the electric field envelop, carrier density in the gain and absorber section. The only essential assumption that is adopted is a ring cavity geometry with unidirectional lasing.

In fiber lasers, for which the gain and the absorption are respectively much slower and faster than the other variables, the Haus equation can be approximated by the subcritical Cubic-Quintic Complex Ginzburgh-Landau Equation (CQCGLE) where one replaces for simplicity the slowly evolving gain by a constant:

$$i\psi_z + \frac{D}{2}\psi_{tt} + |\psi|^2 = i\delta\psi + i\varepsilon|\psi|^2\psi + i\beta\psi_{tt} + i\mu|\psi|^4\psi - \nu|\psi|^4\psi, \qquad (1.2)$$

Here the optical field envelop is a function of t, the retarded time in the frame moving with the pulse and z is the propagation distance. D is the anomalous (normal) dispersion propagation regime if positive (negative), and ν applies to a quintic Kerr effect; these are conservative terms. δ, ε, β and μ are the coefficients for linear loss (if negative), nonlinear gain (if positive), spectral filtering and saturation of the nonlinear gain (if negative), respectively; they are dissipative terms. Although the quintic Kerr saturation is not reached in most laser materials, it arises in fiber lasers because the lumped laser propagation model of [Haus 2000] is reduced to a distributed model [Ding 2009]. Here the equation 1.2 is written in such a way that if the right-hand side of it is set to zero, one is simply left with the nonlinear Schrödinger equation (NLSE). A complete dynamical analysis of the pulsed solutions of the CQCGLE equation was performed by Fauve and Thual in 1990 [Fauve 1990]. The authors demonstrated that "the dissipative terms in the equation select the size of the structures among a family of scale-invariant solitons (conservative solitons)". The stability of these solitary waves requires a subcritical bifurcation, in other words , it requires a bistability between the LS solution and the homogeneous zero background solution [Soto-Crespo 2001]. It is important to point out that the localized structures can be obtained with this model whether D<0 (anomalous regime [Fauve 1990]) or D>0 (normal regime [Soto-Crespo 1997]). In the first case, the soliton-like solutions are close to the usual NLSE (conservative) solitons. However, in the case of normal dispersion, without gain and losses, the balance between dispersion and nonlinearities can only support dark solitons. The inclusion of cubic nonlinear gain and losses allows to generate bright solitary waves, yet such solitary waves are unstable unless the quintic nonlinear loss (or gain saturation) is also added. A comprehensive study of the stability of these solitary waves in the normal regime is carried out in [Soto-Crespo 1997].

Many nonequilibrium phenomena, such as the generation of spatio-temporal dissipative structures in lasers [Haken 1983, Jakobsen 1992, Harkness 1994], binary fluid convection [Kolodner 1988] and phase transitions [Graham 1975] may be described by the CQCGLE. An extensive theoretical work has been achieved to predict the existence of temporal localized structures in fiber lasers with additive-pulse-mode-locking or nonlinear polarization rotation [Moores 1993, Martinez 1985, Chen 1994, Chen 1995]. It was shown numerically that these structures can form robust bound states via the interaction of initially separated solitons [Akhmediev 1997], in analogy with the physics of matter. This dynamics was experimentally observed in a fiber laser experiment in the regime of anomalous dispersion in [Matsas 1992, Grelu 2002]. Stable soliton pairs have also been found in diverse laser experimental configurations and dispersion regimes [Grelu 2003].

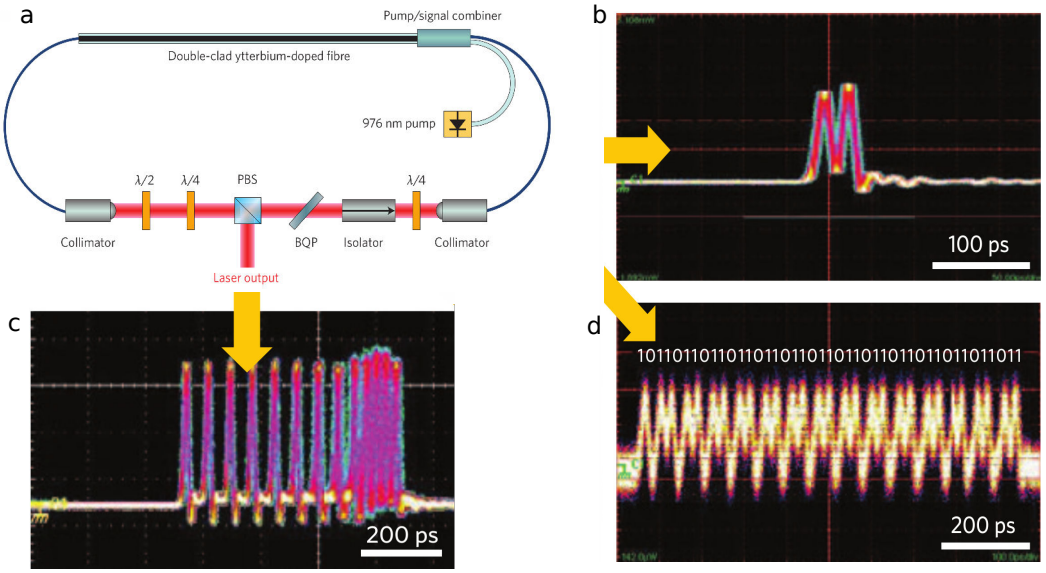

Figure 1.24: a) Experimental setup of an all-normal, dispersion-compensation-free fibre laser cavity operating at a 70 MHz repetition rate and generating 31 nJ pulses. PBS, polarizing beamsplitter; BQP, birefringent quartz plate; $\lambda/4$, quarter-wave plate; $\lambda/2$, half-wave plate. The temporal traces show direct recording of stable self-assembled soliton molecules in the fiber laser experiment: b) a soliton pair, c) an irregularly spaced 13-solitons molecule, d) a $(011)_{N=14}$ macromolecule. The experiment employed a 30 GHz sampling oscilloscope [Grelu 2012].

A direct observation of soliton molecules on an oscilloscope trace is shown on Fig. 1.24 as well as the experimental setup. We can notice that the soliton molecules may possess complicated structures with more than 2 pulses and various temporal intervals between the solitons. [Grelu 2012] (and references therein) also provides a full overview of more complex dynamics such as pulsations, explosions and soliton rains.

Very interestingly these temporal objects have always been named Dissipative Temporal Solitons (DTS) by the authors of experimental observations [Grelu 2012], and not Temporal Localized Structures. This designation is actually justified by two experimental facts. First, one of the properties of LS is their independance if they evolve far enough from each other. Concerning the DTS, no independance has ever been demonstrated. Secondly, in the case of LS, one should be able to prove the multistability between states of multiple structures in the parameters space. As regards DTS, this multistability has been shown theoretically [Soto-Crespo 2001] but not experimentally. For instance people pass from one DTS in the external cavity to a pair of DTS by increasing the pump power, but they have not shown that the two states coexist for the same parameters value. Therefore, the addressability of the DTS seems hard to obtain experimentally, which decreases their interest for potential applications, and it has not yet been evidenced by numerical analysis. The physical origin behind the lack of independence of each

DTS may lie in the slow gain recovery time of fiber lasers. Indeed, $\tau_{g,fiberlaser}$ $\approx$ 10 ms which corresponds to a correlation length of about 3000 km. In the experiment presented in [Grelu 2012], the cavity has a FSR of about 70 MHz, which corresponds to a cavity length of about 2 m. As a matter of fact, two DTS generated within the ring external resonator are de facto correlated by the gain recovery.

1.3.1.4 Motivations of our work

Based on the illustrations of experimental realizations of scalar LS in VCSELs and fiber lasers, we can now show where the interest of our experimental work lies.

The characteristics of DTS observed in fiber lasers are close to the ones of Laser Localized Structures. However the large gain recovery time seems to irreparably act as a coupling parameter between the pulses. So far experiments based on semiconductor lasers coupled to fast saturable absorber have only led to the generation of PML and no temporal localization has ever been observed or even theoretically predicted. For its potential in spatial LS [Genevet 2008] and CS generation [Barland 2002], we choose a broad-area VCSEL as object of our experimental study. Our initial guess was that if this device is coupled to a saturable absorber with a very short recovery time and a large modulation depth we may generate a PML dynamics, as it is currently done in VECSELs coupled to SA in the limit of single transverse mode external cavities. To that aim, we will use a Resonant Saturable Absorber Mirror (RSAM) which fulfills our loss modulation requirements. As gain recovery time of semiconductor does not exceed the nanosecond, we will investigate the evolution of the mode-locking dynamics when the external cavity round-trip becomes larger than τ_g.

The difficulties encountered by Genevet et al. in finding the LB regime originate from the competition between the transverse and longitudinal localization of the laser light. In their experiment, they were using two similar VCSELs facing each other, one acting as an amplifier and the other as an absorber. Transverse localization of light took place in the self-imaging condition for the external cavity, while the pulsed regime shown in Fig. 1.21 was obtained for another configuration which is not detailed in [Genevet 2009]. My work finds itself in a logical evolution of what was described in [Genevet 2009]. Our RSAM being much faster than a VCSEL, we are expecting to observe both spatial and temporal localization of light in the total intensity output of our broad-area VCSEL when the external cavity is set in the self-imaging configuration.

The study of the temporal dynamics arising from such a system is also interesting from a theoretical point of view. In fact, while the CQCGLE is a partial differential equation used for the modelization of DTS in fiber lasers, our VCSEL coupled to an external RSAM is rather modelized by Delay Differential Equations (DDE). DDEs possess the same complexity as PDEs since they both correspond to dynamical systems of infinite dimensionality. Moreover, conceptual links between PDEs and DDEs do exist. It was revealed that a delayed system close to an Andronov-Hopf bifurcation can be described via a GLE [Giacomelli 1996] and recently, a mapping

between a spatially extended laser cavity and an ensemble of coupled Delay Algebraic Equation was developed [Javaloyes 2012, Perez-Serrano 2013]. Finally, in [Marino 2014] the authors have given experimental evidence of dissipative localized structures formation in a delayed optical system based on a bistable semiconductor laser with optoelectronic feedback. Our attempt to generate temporal LLS is a way to obtain an experimental evidence that temporal localization of the electric field can be accomplished in a laser system with all-optical delay.

1.3.2 Vectorial localized structures

As previously said in the introduction of section 1.3, both semiconductor and fiber media are anisotropic, which means that gain and refractive index depend on polarization of light. We are going to give an overview of how polarization dynamics can be generated in both systems. While temporal localization has already been observed in the polarized output of fiber laser, we will explain how such dynamics could be generated in the polarized emission of VCSELs.

1.3.2.1 Dissipative vector solitons and polarization domains in fiber lasers

In 1.3.1.3 a paragraph was dedicated to the formation of Dissipative Temporal Solitons in fiber lasers. We explained that the generation of these pulses requires some saturable absorption mechanism and we named the two common methods, namely nonlinear polarization rotation and the use of a fast saturable absorber.

Nonlinear polarization rotation is the intensity dependent change of polarization orientation of a pulse propagating in an optical fiber that is not polarization maintaining [Hofer 1992, Matsas 1992, Fermann 1993]. If high-intensity light is launched in a fiber with an initial polarization direction oriented at an angle with respect to the slow and fast polarization axes (that we name X and Y), the birefringence will induce rotation of the polarization (via mechanisms called Self-Phase Modulation (SPM) and Crossed-Phase Modulation (XPM)) of the light along the transmission direction of the fiber. The relative phase shift between X and Y components of the light can be expressed as

$$\Delta\Phi_{NL} = (\gamma P L_{eff}/3) cos(2\theta) \tag{1.3}$$

where θ is the angle between the slow axis (X) of the fiber and the light polarization direction, P is the power of the light, γ is the birefringence and L_{eff} is the effective length of the fiber. From this expression we know that for a given distance and input light polarization, the polarization of the output depends on the light power.

The nonlinear polarization rotation mode-locking process uses a ring cavity configuration. A polarizing isolator is placed between two polarization controllers (PC) and acts as the mode-locking element. It plays the double role of a polarizer and an isolator such that light leaving the isolator changes the polarization state to elliptical. The polarization state evolves nonlinearly during the propagation of the

pulse because of SPM and XPM-induced phase shifts imposed on the orthogonally polarized components. The polarization state is non-uniform across the pulse because of the intensity dependence of the nonlinear phase shift. The PC placed before the isolator is adjusted such that it forces the polarization to be linear in the central part of the pulse. Thus, the polarizing isolator lets the central intense part of the pulse pass but absorbs the low intensity pulse wings. The net result is that the pulse is slightly shortened after one round-trip inside the ring cavity, an effect identical to that produced by a fast saturable absorber. This method has become widespread for PML pulses generation in the fiber lasers community. However, only one polarization axis is selected by the intracavity isolator, then one can only form scalar pulses with this technique.

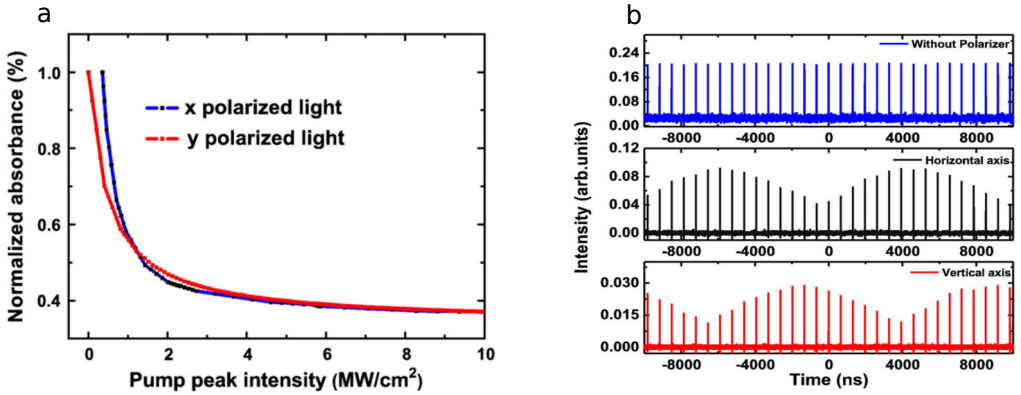

Figure 1.25: a) Polarization resolved saturable absorption curve of graphene-based mode locker, b) Dissipative Vector Soliton operation of the fiber laser. Polarization resolved oscilloscope traces: the soliton is elliptically polarized (phase shift equal to $\pi/2$ between X and Y). When the total ouput is detected (top) the signal appears constant. When one axis is selected for detection (middle and bottom) the signal shows an envelop with a period corresponding to 15 round-trips. The periodic pulse height modulation for each of the orthogonal polarizations is $\pi/2$ out of phase [Zhang 2011].

A fiber laser can also be mode-locked with polarization-independent saturable absorbers such as SEmiconductor Saturable Absorber Mirrors (SESAM) [Jiang 1999, Okhotnikov 2003, Zhao 2009] or even graphene layers [Zhang 2011, Bao 2011]. One can see in Fig. 1.25a) that the absorption of a graphene layer follows the same curve as a function of the pump peak intensity on the two orthogonal polarization axes. Therefore the absorption of these devices is not polarization-sensitive, which allows the polarization of dissipative soliton pulses to evolve freely during propagation in the fiber. Searchers identified the formation of Dissipative Vector Solitons (DVS) consisting of two orthogonal and coupled polarization components. Despite leaving in a birefringent medium, the orthogonal polarizations can copropagate as one unit without splitting (same group velocity) in a low-birefringence fiber due to a strong cross-phase modulation and coherent energy exchange. Then depending on the fiber birefringence, DVS could have either locked

(same phase velocities, [Cundiff 1999, Collings 2000]) or rotating polarization components [Zhang 2008, Zhao 2009, Zhang 2011, Ouyang 2011](Fig. 1.25b). Except their novel vectorial nature, DVS present the same features as the scalar dissipative solitons obtained in experiments involving nonlinear polarization rotation as a mode-locking mechanism. Fig. 1.26 shows that bound states of DVS can be observed as the pump strength is increased. The two DVS coexist in the cavity and the polarizations of the two objects rotate with the same speed. However their polarization orientation is slightly different as the result of gain competition between the two vector solitons.

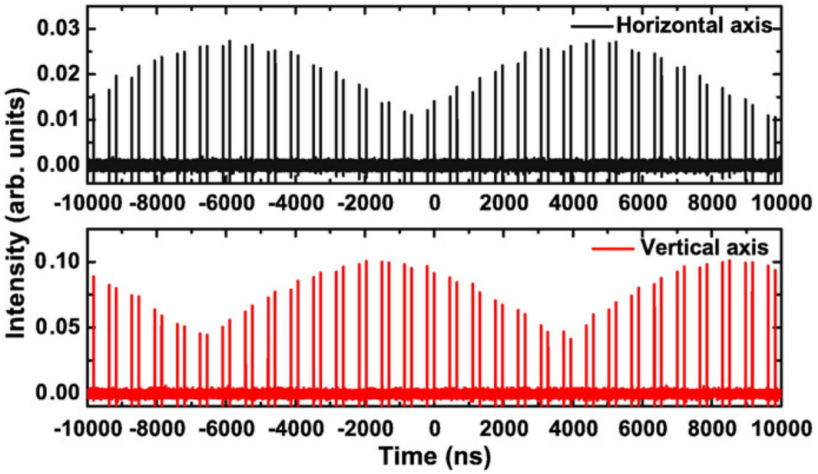

Figure 1.26: A state of two polarization-rotated vector solitons coexisting in the cavity. This state is obtained when the pump power is slightly increased with respect to the value of Fig. 1.25b [Zhang 2011].

To conclude with polarization dynamics in fibers, people have also studied the polarization evolution of a field propagating in a fiber laser where they have removed the saturable absorber element [Williams 1997, Zhang 2009, Lecaplain 2013, Lecaplain 2014] (see Fig. 1.27a). In this case, people have observed the spontaneous formation of fast intracavity polarization dynamics consisting of either square-wave switches or fast polarization flips (see Fig. 1.27b) between the two polarization eigenstates. These dynamics could be very well reproduced via a minimal laser model involving two coupled CGLE:

$$\partial_t U = U + (1+i\beta)\partial_t^2 U - (1-i\alpha)|U|^2 U - (\gamma - i\rho)|V|^2 U, \tag{1.4}$$
$$\partial_t V = V + (1+i\beta)\partial_t^2 V - (1-i\alpha)|V|^2 V - (\gamma - i\rho)|U|^2 V, \tag{1.5}$$

where U(t,τ) and V(t,τ) represent the two orthogonal polarization components of the field in the cavity. The independent variables t and τ are the slow and fast temporal coordinates that describe field variations on the slow time scale of the cavity round-trip and on the fast time scale associated with bandpass filtering and chromatic dispersion. The first term on the right handside represents small-signal

linear gain. The first contribution to the second term describes bandwidth limited gain, and β is associated to group velocity dispersion (GVD). The first contribution to the third term in the right-hand side represents the nonlinear saturation of gain, whereas α is the nonlinear Kerr effect. For the self-focusing nonlinearity of silica fibers, one has $\alpha > 0$. γ and ρ describe nonlinear polarization cross-gain saturation and rotation, respectively. In the absence of nonlinear polarization coupling (i.e., with $\gamma = \rho = 0$), one obtains two independent Ginzburgh-Landau equations.

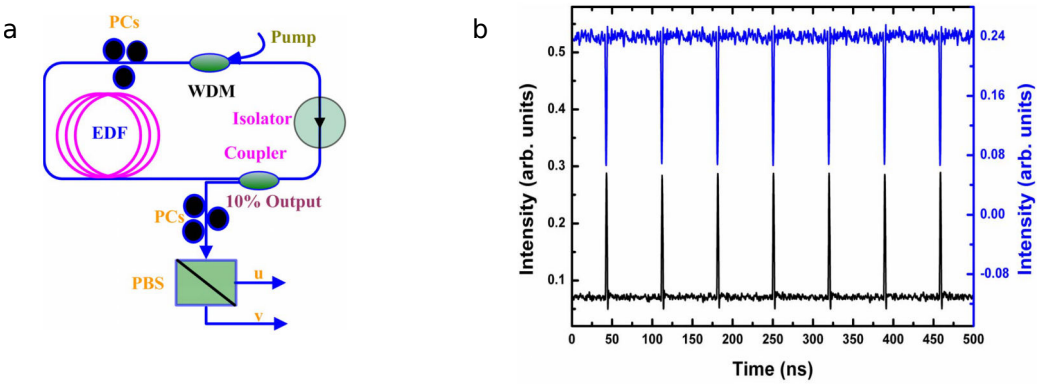

Figure 1.27: a) Experimental setup for PDWS generation. WDM: wavelength-division multiplexer. EDF: erbium-doped fiber. PC: Polarization controller. PBS: Polarization beam splitter. b) PDWS dynamics consisting of antiphased polarization flips between two orthogonal polarization states [Lecaplain 2013].

The fast polarization flips in Fig. 1.27b) were thus interpreted as "localized structures separating domains of two polarization eigenstates", and named as Polarization Domain Wall Solitons (PDWS)". One could pass from squares to pulses by slightly modifying the cavity birefringence. In order to experimentally generate these kinks, birefringence of the fiber cavity must be low enough, but no condition is imposed on the sign of cavity dispersion (PDWs were observed in the normal [Lecaplain 2013] and in the anomalous [Lecaplain 2014] dispersion regimes). These PDWS are triggered due a strong noise background and the authors could observe complexes of PDWS, enhancing the solitary wave nature of these polarization kinks.

To sum up, polarization dynamics automatically develops in anisotropic fiber laser cavities with no polarization controlling elements due to cross-gain saturation and cross-phase modulation. The long fiber lasers cavities makes possible the insertion of polarization controllers that allows to modify the cavity birefringence and study the influence of this parameter on the dynamics. Thanks to that, people have been able to generate polarization structures consisting of narrow antiphase pulses triggered by noise with a repetition time equal to the cavity round-trip time. These so-called PDWS are interesting for applications since they arise due to an interplay between the optical Kerr effect and chromatic dispersions and do not need any extra nonlinear device inserted in the cavity (as opposed to PML) to be

triggered. Nevertheless, the frequency of these self-generated polarization pulses is constrained by the large size of fiber laser cavities. A way to get high repetivity for polarization dynamics would be to use another type of anisotropic lasers : semiconductor lasers. However the small size of these devices does not allow to mechanically control birefringence and dichroism.

1.3.2.2 Polarization dynamics in VCSELs

Polarization dynamics has been an intense subject of research in the semiconductor lasers community. Edge-Emitting Lasers (EEL) or VCSELs gain media exhibit a small birefringence between two orthogonal axes determined by crystalline orientations during material growth in the fabrication process. The major difference between the two concerns their transverse symmetry. While EEL have a rectangular symmetry that enables lasing (gain) only on one polarization axis, VCSELs have a circular symmetry that creates degenerescence between the two polarization eigenstates (Fig. 1.28). Since there is no strong mechanism that selects the polarization axis, VCSELs can exhibit polarization switching and bistability when solitary [Martin-Regalado 1997a, Ackemann 2001, Sondermann 2003, Virte 2014]. Recently, deterministic polarization chaos has been reported from a free-running VCSEL due to a nonlinear coupling between two elliptically-polarized modes [Virte 2013].

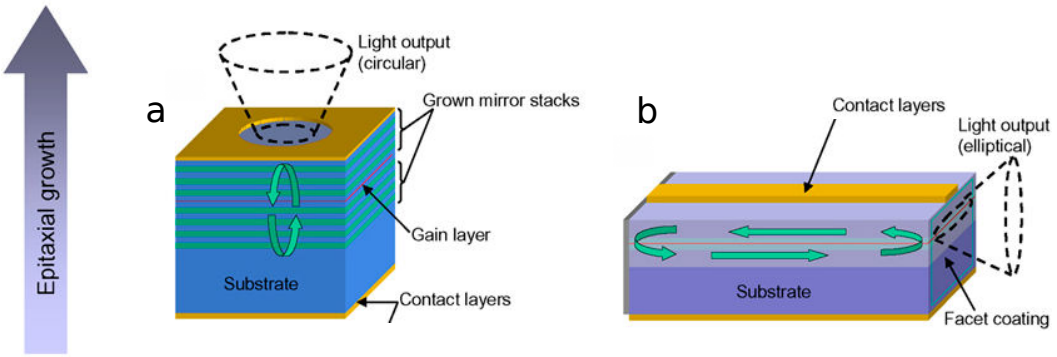

Figure 1.28: a) Schematic diagram of a VCSEL. The light output is indicated in a dashed line and has a circular shape. b) Schematic diagram of an Edge-Emitting Laser. The light output is indicated in a dashed line and has an elliptical shape.

These features are very well reproduced in simulations via the Spin-Flip Model (SFM) [Miguel 1995] that accounts for the vectorial nature of the emission field of VCSELs. The polarization of semiconductor lasers light originates in the spin (angular momentum J) sublevels of the lasing transition between the valence and the conduction band (Fig. 1.29). Considering the case of a surface-emitting quantum well laser, transitions from the conduction to the light-holes band are neglected due to the lower energy of the light-hole sband. Two transitions are thus allowed

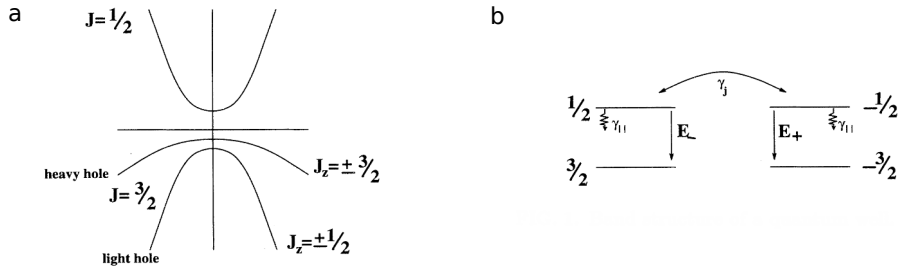

Figure 1.29: Band structure of a quantum well. a) Angular momentum (J) sublevels of the lasing transition between the valence (light holes and heavy holes) and the conduction band. b) Left : transition from J_z=-1/2 to J_z=-3/2 associated with right-circularly polarized light. Right : transition from J_z= 1/2 to J_z= 3/2 associated with left-circularly polarized light. These transitions are coupled via Spin-Flip relaxation rate γ_J [Miguel 1995].

in this model : the one from J_z=-1/2 to J_z=-3/2 associated with right-circularly polarized light and from J_z=1/2 to J_z=3/2 associated with left-circularly polarized light. These transitions are assumed to be coupled via Spin-Flip relaxation processes with a decay rate γ_J [Uenoyama 1990, Damen 1991] which consist of a variety of microscopic interactions. In a quantum well : $\gamma_{||} < \gamma_J < 10^2\gamma_{||}$, where ${\gamma_{||}}^{-1} \approx 1$ ns (gain recovery rate).

With this model, one ends up with a set of four partial differential equations for the evolution of left and right circularly polarized fields, the total population difference between conduction and valence bands, and the difference in population inversions associated with right and left circularly polarized emissions. The model generally predicts linearly polarized laser emission. The stability and dynamical response to fluctuations of the linear states are determined by the parameters of the system such as spin relaxation rate, birefringence, and time scales associated with spontaneous decay. Residual dichroism and birefringence, which are inevitably present, lead to different net gains of the polarization modes, thus slightly favoring one mode over the other at VCSEL threshold. Often single-mode VCSELs show polarization switching when the injection current is scanned. This is due to Joule heating of the VCSEL cavity, which redshifts the gain spectrum at a higher rate than the polarization modes, and more complicated mechanisms, which require more refined models than the pioneer Spin-Flip Model [Martin-Regalado 1997b, Balle 1999].

Taking advantage of VCSELs polarization degree of freedom, a lot of investigations have been performed in order to induce fast regular or chaotic signals in VCSELs under steady conditions of bias current.

When VCSELs are subject to optical feedback, the polarization stability is affected and polarization dynamics appears even in the case of perfectly isotropic feedback [Giudici 1999]. Polarization-rotated optical feedback (where the two linearly polarized components X and Y are fed back into the laser cavity after X is converted into Y and vice-versa) induces a regular polarization dynamics which can be as fast as 9 GHz [Robert 1997, Li 1998].

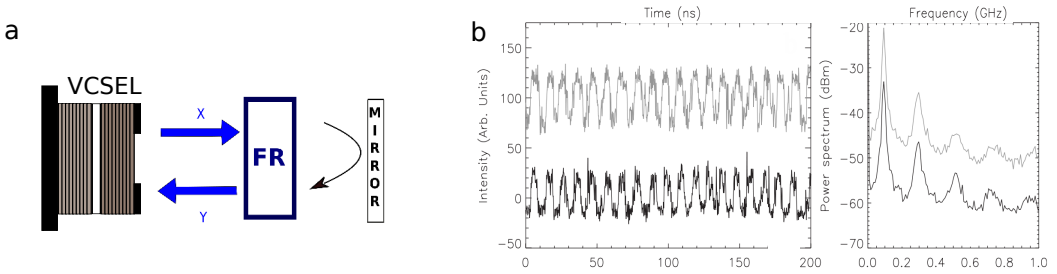

Figure 1.30: a) Schematic representation of XPR principle. b) Antiphased square-wave dynamics on X (grey) an Y (black) polarizations induced by XPR in a large dichroism VCSEL. Right: time traces, left: corresponding RF power spectra [Mulet 2007a].

Another scheme which has been investigated for generating optical pulses is based on Crossed-Polarization Re-injection (XPR) both in edge-emitting devices [Gavrielides 2006] and VCSELs [Mulet 2007a, Sukow 2012]. In such a scheme, the emission from the laser is split into its two linearly polarized components, X and Y, and only one of these components (X, say) is fed back into the laser after being rotated into the orthogonal polarization direction (Y)(Fig. 1.30a). In this way, cross-saturation of the polarization states modifies the photon density in each LP component and may eventually lead to pulsed emission with a fundamental time scale given by the reinjection delay τ_r. When the dichroism in the device is high enough and the emission occurs on a single polarization mode, strong enough XPR leads to square-wave modulation of the power emitted in each of the polarization components with a period close to $2\tau_r$ (Fig. 1.30b). According to the analysis in [Gavrielides 2006], the square-wave regime corresponds to a period-two solution on the slow time scale τ_r that describes a quasistatic orbit between two distinct stages, which appear as intensity plateaus in the polarization-resolved time trace. The former stage (first plateau) corresponds to emission of the only stable polarization in the solitary system, and the latter (second plateau) to amplification of the reinjected light in the orthogonal polarization. Both stages last for a time τ_r that corresponds to the time of flight in the reinjection arm.

In VCSELs, the range of currents where XPR is effective for generating square-wave modulation of the output is limited. In devices that have a low dichroism (hence which may display bistability in some parameters range) the square-wave modulation progressively degrades as the parameters approach the bistable regime and the regularity of the signal is quite sensitive on the working point and strongly affected by small deviations from the optimal parameters values [Mulet 2007a]. On the other hand, when the dichroism is large, square-wave signals can be obtained over large ranges of bias currents, although it was reported in [Sukow 2012] that the quality of the square-wave signal degrades as the current is increased.

Therefore depending on the intrinsic polarization properties of the VCSELs under study, devices response to an optical polarized perturbation may vary. In the case described above, the difference in dichroism and birefringence between various devices is at the origin of discrepancies in polarization dynamics.

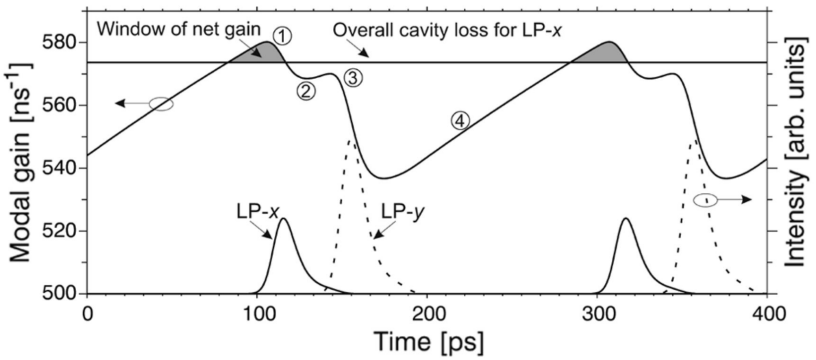

Figure 1.31: Temporal evolution of the gain and overall-cavity loss for X. The loss for Y is out of scale. The labels (1) and (3) depict the positions of the gain depletions, while (2) and (4) stand for gain recovery stages.

Finally, the XPR scheme associated with an external Polarization Selective Feedback (PSF) cavity has already been proposed theoretically for inducing Passive Mode-locking in a VCSEL without using any saturable absorber but directly exploiting the polarization degree of freedom of light. In this approach, the laser amplifier plays a twofold role, i.e. to provide both amplification and the nonlinearities for pulse shortening. PML is achieved by Crossed-Polarization Gain Modulation (XPGM) in the laser amplifier caused by the reinjection of a polarization-rotated replica of the laser output after a time-delay τ_r while a set of longitudinal modes on which the dynamics is decomposed is provided by the PSF cavity [Javaloyes 2006, Mulet 2007b]. Fig. 1.31 shows the evolution of the gain at different stages, and the reference cavity loss for X. The arrival of each pulse induces some amount of depletion at stages 1 and 3. The total gain depletion is the largest when the arrival of the second replica occurs at the gain minimum induced by the arrival of the first pulse, so stage 2 would vanish. The subsequent gain recovery (stage 4) opens a window of net gain after a time T_G and triggers the emission of a new pulse.

1.3.2.3 Motivations of our work

Based on investigations made with a VCSEL submitted to XPR, we are going to develop this scheme by adding a Polarization-Selective feedback cavity as in [Javaloyes 2006]. This scheme is interesting and novel from a fundamental point of view since only recently in optics the influence of multiple delays has been studied, e.g. in the case of the double filtered feedback configuration [Slowinski 2010, Slowinski 2014]. Our motivations for the implementation of such a complex configuration are twofold :

As opposed to fiber lasers, no polarization controllers can be inserted in a VCSEL cavity to slightly change polarization gain and frequencies. Nevertheless, one knows that setting polarized feedback on one axis, one would favor laser emission

on that axis and disable the orthogonal polarization output. Doing so, one has therefore slightly increased the dichroism in the device in an all-optical manner. As a consequence, an implementation of a VCSEL+PSF system coupled to XPR cavity could help generate a robust square-wave output even with of a low dichroism VCSEL.

One could also see these two cavities as two competitive mechanisms. Indeed, if PSF favors emission on one axis, XPR will reinforce emission on the orthogonal one. These effects may be compared (to some extents) to mechanisms of self-phase modulation and cross-phase modulation encountered during light propagation in fiber lasers with low dichroism, which gave rise to PDWS dynamics. Thus, by carefully controlling both XPR and PSF rates, one could expect to observe new and controllable polarization dynamics such as polarization flips in a compact and fast system.

Our experimental implementation of this scheme is therefore promising in terms of polarization dynamics due to the rich amount of nonlinear effects induced by the two coupled and polarized external cavities.

1.4 Contents

In this manuscript I will present the experiments I have developed during these past three years under the supervision of Massimo Giudici at the Institut Non Linéaire de Nice. Each experimental result is reinforced by a theoretical analysis that well reproduces the experimental outcomes and broadens our knowledge on the dynamics we generated. These were carried out by Julien Javaloyes (from the Universitat de les Illes Balears (UIB) in Palma de Mallorca, Spain) and Salvador Balle (from the Instituto Medtirraneo de Estudios Avanzados (IMEDEA) in Palma de Mallorca, Spain). The manuscript is structured as follows:

In chapter 2, we show experimentally and theoretically that an electrically biased 200 μm multi-transverse modes VCSEL can be passively mode-locked via optical feedback from a distant Resonant Saturable Absorber Mirror. This is achieved when one is placed in the Fourier plane of the other. Such non-conventional optical feedback leads to two tilted plane waves traveling in the external cavity with an opposite transverse component and alternating each other at every round-trip. Each one of these plane waves gives birth to a train of mode-locked pulses separated by twice the external cavity round-trip, while the two trains are time-shifted by a round-trip. A large portion of the transverse section of the device contributes to mode-locked emission leading to pulses of approximately 1 W peak power and 10 ps width. We discuss the pinning mechanism of the transverse wave-vector on inhomogeneities in the absorber leading to controllable tilted waves and tunable PML emission over 4 nm.

In chapter 3, we investigate the relationship between passive mode-locking and the formation of time-localized structures in the output intensity of our broad-area

VCSEL. We show experimentally and numerically how the mode-locked pulses generated with the setup described in chapter I transform into lasing localized structures, allowing for individual addressing and arbitrary low repetition rates. Our analysis reveals that this occurs when i) the cavity round-trip is much larger than the slowest medium time scale, namely the gain recovery time, and ii) the mode-locked solution coexists with the zero-intensity (off) solution. These conditions enable the coexistence of a large quantity of stable solutions, each of them being characterized by a different number of pulses per round-trip with various possible arrangements. Then, each mode-locked pulse becomes localized, i.e. individually addressable.

In chapter 4, we study theoretically and experimentally the combined effects of polarization-selective optical feedback and of crossed-polarization reinjection in a small-area single-transverse mode VCSEL. After a detailed analysis of the solitary laser characteristics in terms of polarization stability, we show that the application of polarization-selective optical feedback, which induces an effective dichroism in the system, allows one to generate a robust and regular square-wave output signal in each polarization component. The period of the square-wave signal is determined by twice the reinjection delay. We analyze the regularity of the induced modulation as a function of laser bias current, dichroism, and of the levels and delays of reinjection and feedback, thus revealing the robustness of the square-wave emission in the parameters space. We also show that the feedback is more effective when acting on the long-wavelength polarization mode, which can be traced to the asymmetry of the bistable region of the VCSEL for low dichroism.

Secondly, we show that the nonlinear polarization properties of a VCSEL with PSF and XPR can lead to the formation of vectorial temporal localized structures when the PSF cavity round-trip time is much larger than the laser time scales. These Vectorial LS arise as cycles in the polarization orientation, leaving the total intensity almost constant. They circulate in the cavity by regenerating themselves at every round-trip when interacting with the VCSEL, which size is 10^5 times smaller than the cavity. The large temporal aspect-ratio of the system enables the observation of different states with multiple solitons within the same round-trip . These states, that coexist with the homogeneous solution, encompass either independent or bound solitons, which can be distinguished by their noise-induced motion: while independent solitons exhibit uncorrelated random walks, soliton molecules evolve as rigid bodies. We will present the numerical analysis based on the Spin-Flip model suitably modified for incorporating the effects of PSF and XPR. We will show that far above threshold this system can be reduced to a dynamical system composed of two phases: the orientation phase of the quasi-linear orientation and the optical phase of the field. This model allows to interpret the VLS and square-wave as polarization kinks and antikinks under specific conditions of resonance between the multiple frequencies at play in the system.

Chapter 2

Passive mode-locking and tilted waves in a broad-area VCSEL

Contents

2.1 Introduction 43
2.2 The experiment 44
2.2.1 The experimental setup 44
2.2.2 The experimental results 47
2.2.3 Discussions on wave vectors selectivity 52
2.3 Numerical simulations 55
2.3.1 The model 55
2.3.2 Numerical results 58
2.4 Conclusions and perspectives 61

2.1 Introduction

The PML mechanism has led to the shortest and most intense optical pulses ever generated and pulses in the femtosecond range are produced by dye [Fork 1983], solid-state lasers [Keller 1996] and fiber lasers. However, the large size of these devices and the need for optical pumping strongly limit their application domain. More compact solutions can be envisaged using semiconductor devices. PML is obtained in monolithic edge-emitting semiconductor lasers which have the advantage of being electrically biased and to operate at high repetition rates (1 to 160 GHz) although the peak powers that can be obtained are usually limited because of Catastrophic Optical Damage (COD) [Avrutin 2000]. Large output powers in the Watt range are commonly achieved by coupling Vertical External-Cavity Surface-Emitting Lasers (VECSEL) with a Semiconductor Saturable Absorber Mirror (SESAM) [Rudin 2010, Wilcox 2013]. The external cavity is designed to operate in the fundamental Gaussian mode while a large section of the VECSEL is optically pumped to achieve large power, in this configuration the external cavity length leads to repetition rates from a few to tens of GHz [Keller 2006]. In both monolithic and external-cavity schemes, the presence of higher order transverse modes of the resonator is usually perceived as detrimental for mode-locking stability and it is avoided by cavity design. In fact, when several higher order modes are present,

the emission profile is usually not stationary [Fischer 1996] and even chaotic filamentation may occur [Thompson 1972]. This is due to thermal effects imposing a current-dependent refractive index profile, and to the so-called Spatial Hole Burning (SHB). This phenomenon occurs in regions of high optical intensity, where the local gain (and thus the local carrier density) is depressed by stimulated emission, hence leading to a local increase of refractive index which contributes to strengthen light confinement and to further increase the local field intensity. On the other hand, the possibility of achieving a cooperative effect of transverses modes where they would contribute coherently to longitudinal mode-locking is very attractive for increasing the pulse power, since it would allow to circumvent COD. In this section, we propose a method for taking advantage of the large transverse size of our electrically biased VCSEL in order to generate PML by using a specific external cavity imaging condition.

2.2 The experiment

2.2.1 The experimental setup

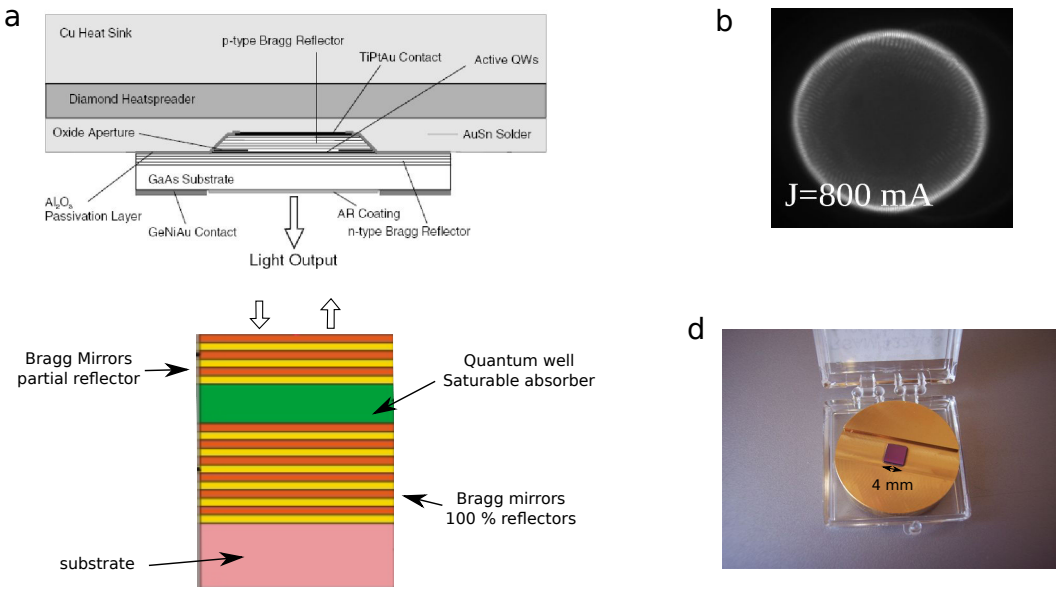

Figure 2.1: a) Scheme of our broad-area VCSEL in the bottom-emitting configuration. b) Near-field of our VCSEL when pumping current is set to 800 mA. We notice that lasing emission occurs on the edge of the section. c) Scheme of a RSAM structure : the absorbing medium is enclosed by two Bragg mirrors, one at the top is partially reflective, the one at the bottom is 100 % reflective. d) Picture of a RSAM mounted onto a brass plate.

The VCSEL is a 980 nm device manufactured by ULM photonics [Grabherr 1998](see Fig. 2.1a) with a diameter of 200 μm. Its standalone threshold (J_{st}) is about 380 mA, though emission is localized only at the external perimeter of the device up to J = 850 mA (Fig. 2.1b) for which a maximum output power

of about 50 mW is reached. When we exceed this value, thermal roll-off starts to occur and the output power decreases.

The 980 nm RSAM (BaTop Gmbh, see Fig. 2.1c-d) has a transverse dimension of 4 mm * 4 mm and it exhibits a low unsaturated reflectivity of 1% that increases up to 60% when saturated. The RSAM saturation fluence is 15 μJ.cm^{-2}. These values are obtained at the RSAM resonant wavelength which can be thermally tuned over 3 nm (between T_1 = 10 °C and T_2 = 50 °C). The Full Width at Half Maximum (FWHM) of the RSAM resonance is around 16 nm and the saturable absorption recovery time is around 1 ps.

The setup is shown in Fig. 2.2a). Both the VCSEL and RSAM are mounted on temperature controlled substrates which allow for tuning the resonance frequency of each cavity; parameters are set for having the emission of the VCSEL resonant with the RSAM at the VCSEL operating current (Fig. 2.2b-c). The FWHM of the VCSEL absorption curve is about 1 nm, which is much smaller than the one of the RSAM.

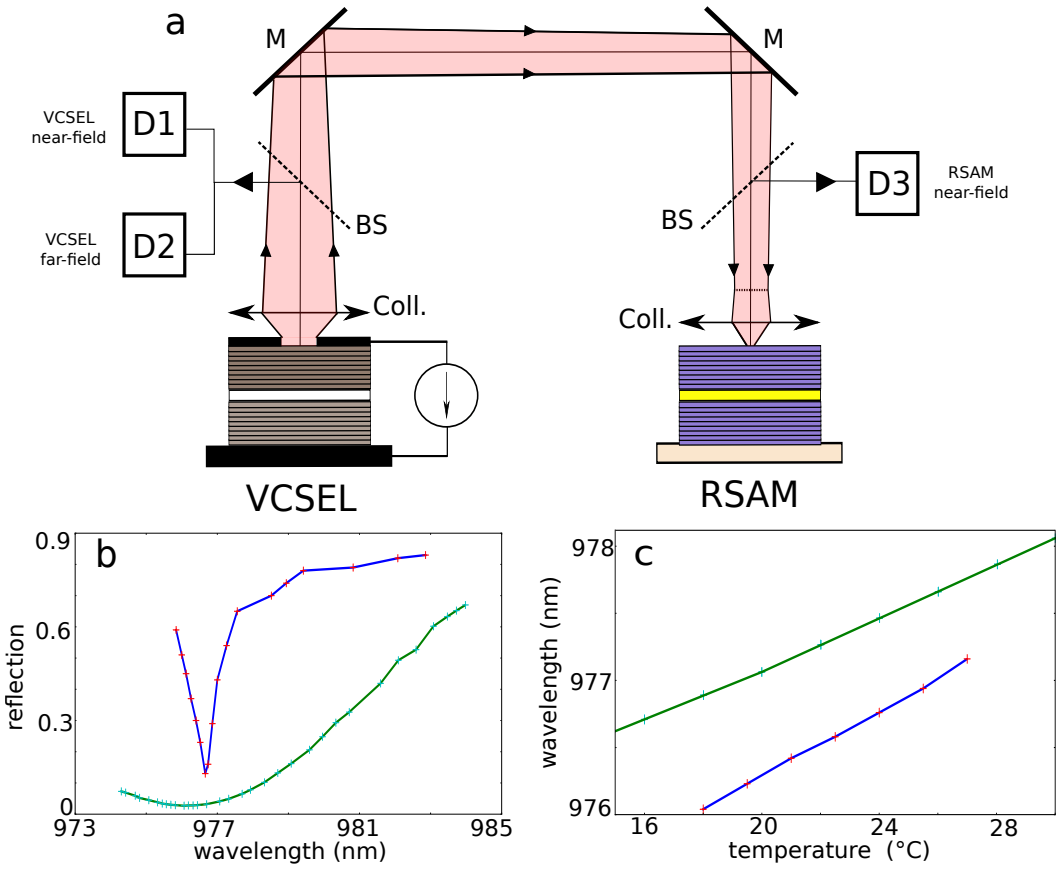

Figure 2.2: a) Experimental setup: temperature-stabilized VCSEL and RSAM. Coll.: Aspheric Lens, BS : Beam Splitter, M: Mirror and D1/D2/D3: Detectors. b) Experimental absorption curves for the VCSEL at J = 0 mA and T_1 = 25 °C (blue) and the RSAM (green) at T_1 = 19 °C when both are at resonance. c) Shift of the resonance wavelength for the VCSEL (blue) and the RSAM (green) as a function of the substrate temperature.

The light emitted by the VCSEL is collected by a large numerical aperture (0.68) aspheric lens and the similar lens is placed in front of the RSAM. Two 10% reflection beam splitters allow for light extraction from the external cavity and to monitor both the VCSEL and the RSAM outputs. The light emitted by the VCSEL is monitored by a 33 GHz scope coupled with a fast 10 GHz detector. Part of the light is sent to two CCD cameras; the first one records the near-field profile of the VCSEL, while the second records the VCSEL far-field profile. A third CCD camera records the light reflected by the RSAM surface. The external cavity length is fixed to L = 30 cm. One of the most important parameters for achieving mode-locking in this setup is the imaging condition of the VCSEL onto the RSAM. We obtain mode-locking when the RSAM is placed in the plane where the exact Fourier transform of the VCSEL near-field occurs.

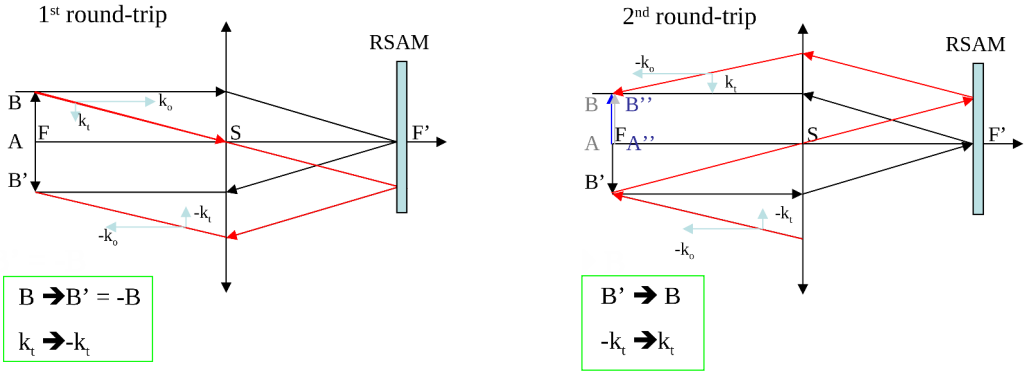

Figure 2.3: Schematic representation of light trajectory after two round-trips in the external cavity. AB is the initial object, A'B' is the intermediate image formed after one round-trip, A"B" is the image of A'B' after a second round-trip.

This working condition is obtained by imaging the VCSEL near-field profile onto the front focal plane of the aspheric lenses placed in front of the RSAM, while the RSAM is placed onto the back focal plane of this lens. We remark that this leads to a non-local feedback from the RSAM onto the VCSEL: if the RSAM were a normal mirror, the VCSEL near-field profile would be inversely imaged onto itself after a cavity round-trip. We obtain that imaging condition by setting $d_{VCSEL-Coll}$ = 8.2 mm, $d_{Coll-Coll}$ = 283.5 mm and $d_{Coll-RSAM}$ = 8.2 mm.

Geometrical optics may be useful to get insights in this scheme. Two rays (one parallel to the optical axis and the other tilted) emitted from the point B of the VCSEL surface are schematically represented in Fig. 2.3. After one round-trip, the near-field of the VCSEL is invertedly self-imaged, the outgoing transverse wave vectors $K_\perp$ return the VCSEL with an opposite sign. When light is reflected by the VCSEL and starts the second round-trip, the image is reinverted and goes back to the VCSEL as the same originally emitted. The same phenomenon holds for the transverse wave vector $K_\perp$. Therefore, all the wave vectors K emitted by any point of the VCSEL are focused onto the same point of the RSAM, saturating it strongly and favoring a well-defined transverse component for the PML regime.

2.2.2 The experimental results

Panel a) in Fig. 2.4 displays the time trace of the VCSEL biased at J = 600 mA in the mode-locking regime which consists of a regular train of pulses with a period equal to the round-trip time in the external cavity $\tau = 2L/c = 2$ ns.

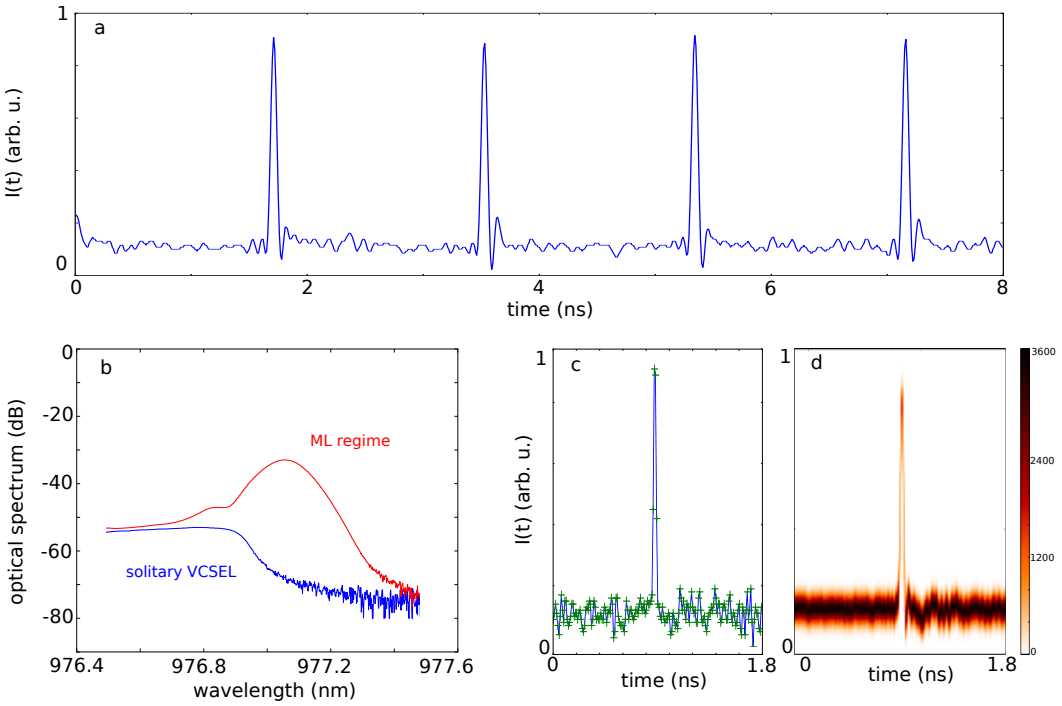

Figure 2.4: Panel a): Temporal trace of the VCSEL in the mode-locked regime. Panel b): Optical spectrum for the solitary laser (blue) and the VCSEL in the mode-locked regime (red). Panel c): Mode-locked pulse acquired with the 42 GHz bandwith detector, the green crosses mark the sampling of the scope (10 ps/point). d) Superposition of the 31,800 pulses contained within one 100 μs acquisition. J = 600 mA.

The pulse width cannot be determined from the oscilloscope trace in Fig. 2.4a, which is clearly limited by our real-time detection system (10 GHz effective bandwidth). However, an estimate of the pulse width can be obtained from the optical spectrum of the output, which exhibits a broad spectral peak whose FWHM is around 0.12 nm that corresponds, assuming a time-bandwidth product of 0.4, to a pulse width of 10 ps FWHM (see Fig. 2.4b) red). Panel b) also shows the optical spectrum for the solitary laser (blue). When the ML regime is reached, the optical spectrum power increases with respect to the blue trace. The pulse was also detected by a 42 GHz detector (Fig. 2.4c), which confirms a pulse width of less than 12 ps FWHM (oscilloscope bandwidth limit). Finally, Fig. 2.4d) shows a superposition of the pulses contained in one time trace, which is about 31 800 in that case. This diagram reveals that the width and amplitude of the pulse remain constant over thousands of round-trip.

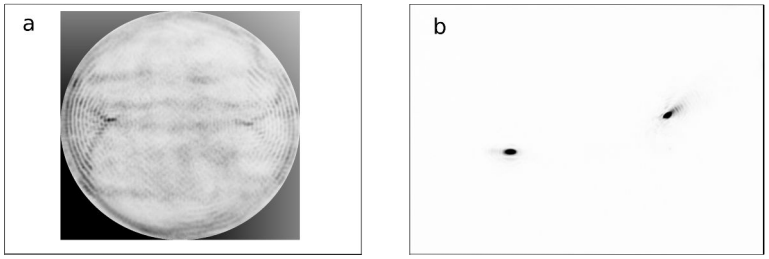

Figure 2.5: a): Near-field emission for the mode-locked VCSEL. b): Corresponding far-field emission from the VCSEL. Intensity grows from white to black. J=600 mA.

Panels a) and b) in Fig. 2.5 show the time-averaged near-field and far-field profiles of the VCSEL, respectively. In addition, we verified that the image of the RSAM surface (not shown) is very similar to Fig. 2.5b), thus revealing that the RSAM is effectively placed in the Fourier plane of the VCSEL near-field. The far-field of the VCSEL exhibits two bright, off-axis spots that indicate the presence of two counter-propagating tilted waves along the cross section of the VCSEL. The transverse wave vector of each of these waves is related in direction and modulus to the position of the spots, and their symmetry with respect to the optical axis indicates that the two transverse wave vectors are one opposite to the other.

Remarkably, however, no interference pattern is visible in the near-field emission. The concentric rings close to the limit of the VCSEL arise from current crowding

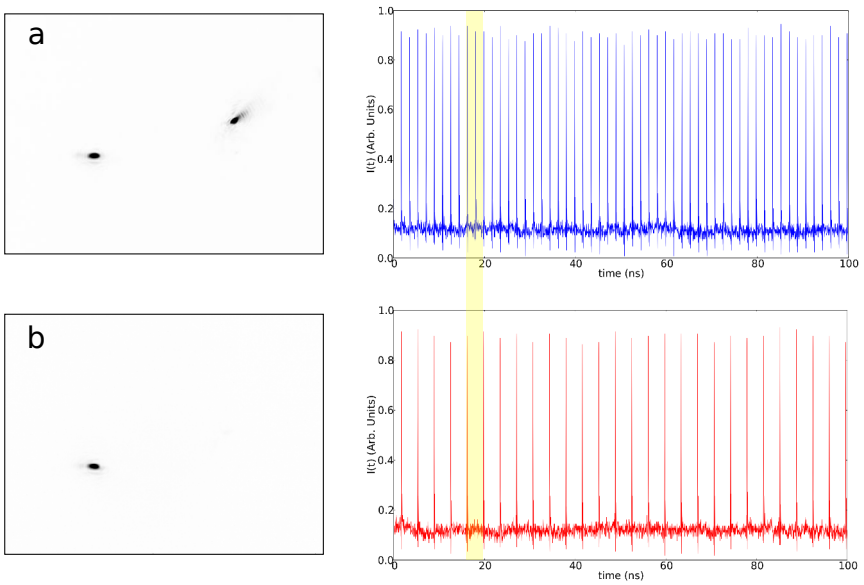

Figure 2.6: Panel a): Time signal of period τ obtained when detecting the two spots of the far-field emission of the VCSEL. Panel b): Time signal of period 2τ obtained when detecting a single spot of the far-field emission of the VCSEL.

[Babushkin 2004] and do not contribute significantly to the bright spots in the far-field, as it was verified by filtering out these rings. The lack of interference pattern between the counter-propagating waves in the time-averaged near-field implies that the transverse waves must not be simultaneously present, exhibiting antiphase dynamics. This is apparent in Fig. 2.6, where the trace from the whole far-field is compared to that from only one of the bright spots. While the emission from the whole far-field has the characteristics discussed above, that emitted by only one of the spots consists also of a periodic train of pulses, but the period is 2τ. Thus the trace from the whole far-field is obtained by interleaving two identical pulse trains of period 2τ with a delay τ of one with respect to the other, each corresponding to a tilted wave with opposite transverse wave vector.

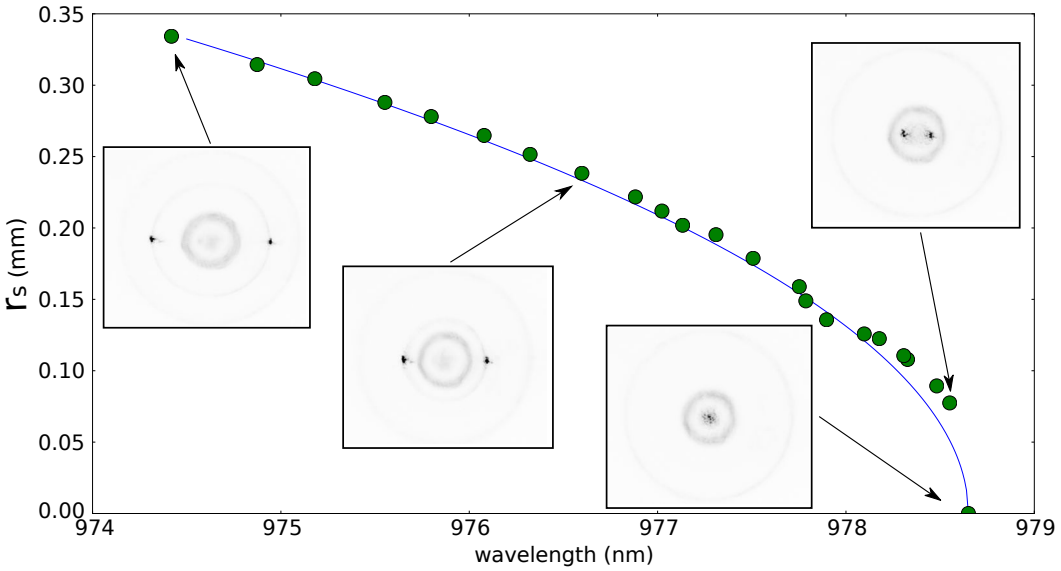

Figure 2.7: Off-axis position of a single spot in the far-field profile as a function of the spectral emission peak of the VCSEL. Far-field profiles are shown for a few points in the graph. VCSEL emission is in the mode-locking regime for all points of the graph while the one at the highest wavelength, where a single on-axis spot appears in the far-field profile, corresponds to very irregular dynamics. VCSEL is biased at 700 mA. The transverse wave vector is selected by laterally shifting the RSAM along the back focal plane of its collimating lens. The large size of the RSAM section (4*4 mm^2) with respect to the far-field size (0.7 mm at most) renders this operation feasible. The blue line has been obtained plotting $r_s = \frac{\lambda_0 f}{2\pi}\sqrt{\lambda^{-2} - \lambda_0^{-2}}$, with λ_0 = 978.65 nm and f = 8 mm.

This mode-locked dynamics does not depend critically on the transverse wave vector value selected by the system. Such value can be modified by shifting the RSAM device laterally (i.e. along the back focal plane of its collimating lens) or slightly displacing the collimating lens off the axis defined by the centers of the VCSEL and the RSAM. The change in selected transverse wave vector is evidenced by the variations in the separation between the two spots on the RSAM mirror,

as shown in Fig. 2.7. The position of each spot on the RSAM with respect to the optical axis is related to the transverse wave vector $\vec{K}_\perp = \vec{K}\text{-}\vec{K}_0$ of the plane wave by

$$\vec{r}_s = \lambda f \frac{\vec{K}_\perp}{2\pi} \tag{2.1}$$

where f is the focal length of the lens in front of the RSAM, λ is the wavelength of the light, $\vec{K}$ is the wave vector emitted by the VCSEL while $\vec{K}_0$ is its component along the cavity axis. Although substantial changes in emission wavelength (over 4 nm tuning) can be induced in this way, it is observed that within a wide parameter range, the temporal characteristics of the pulse train do not change and the spectral bandwith of the mode-locked VCSEL remains equal to 40 GHz. This fact opens very interesting possibilities in terms of wavelength tuning and stirring of the mode-locked beam by controlling the position where the spot on the RSAM appears. The only noticeable effect of varying the position of the spot is a slight reduction of the pulse peak power. We attribute this effect to the increased losses experienced in the external cavity by wave vectors with large $K_\perp$ as a result of the Distributed Bragg Reflectors (DBR) reflectivity angular dependence and/or the finite numerical aperture of the collimating lenses. This point will be further discussed in the theoretical section. Beyond the maximal separation of the two spots on the RSAM shown in Fig. 2.7, mode-locking is suddenly lost. Importantly, mode-locking strongly deteriorates in regularity when the two spots are brought to coincide, even resulting in some cases into c.w. emission. Hence, in our setup, regular mode-locking was not achieved with $K_\perp \approx 0$, i.e. for a plane-wave emission almost parallel to the optical axis of the VCSEL.

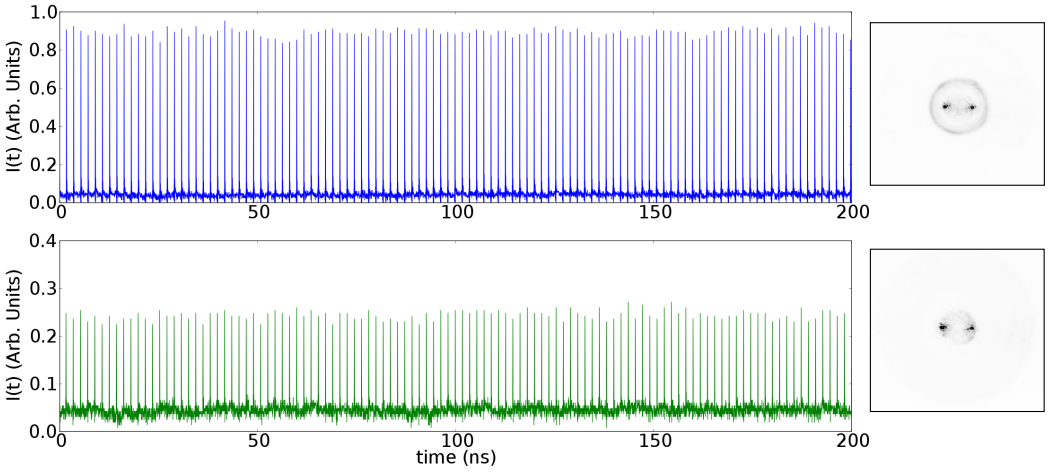

Figure 2.8: VCSEL emission time traces and corresponding far-field emission profiles in the mode-locking regime for two values of the VCSEL bias. Upper panel: J = 703 mA, lower panel: J = 285 mA.

In terms of bias current, the mode-locking regime is stable in a very broad range, namely 285mA < J < 703 mA. If the current is varied in this interval while keeping the alignment, we did not observe any change in the separation between the two bright spots in the far-field profile corresponding to the two tilted waves, see Fig. 2.8. However, the spectral peak corresponding to the mode-locking emission has shifted from 978 nm (J = 703 mA) down to 976 nm (J = 285 mA), thus showing that the selection of $K_\perp$ does not depend on the detuning between the two cavities at least in the range spanned. We also found that, for the external cavity length considered, the PML regime is bistable with the off solution for J < J_{st}. This specific feature will be explained in the next chapter.

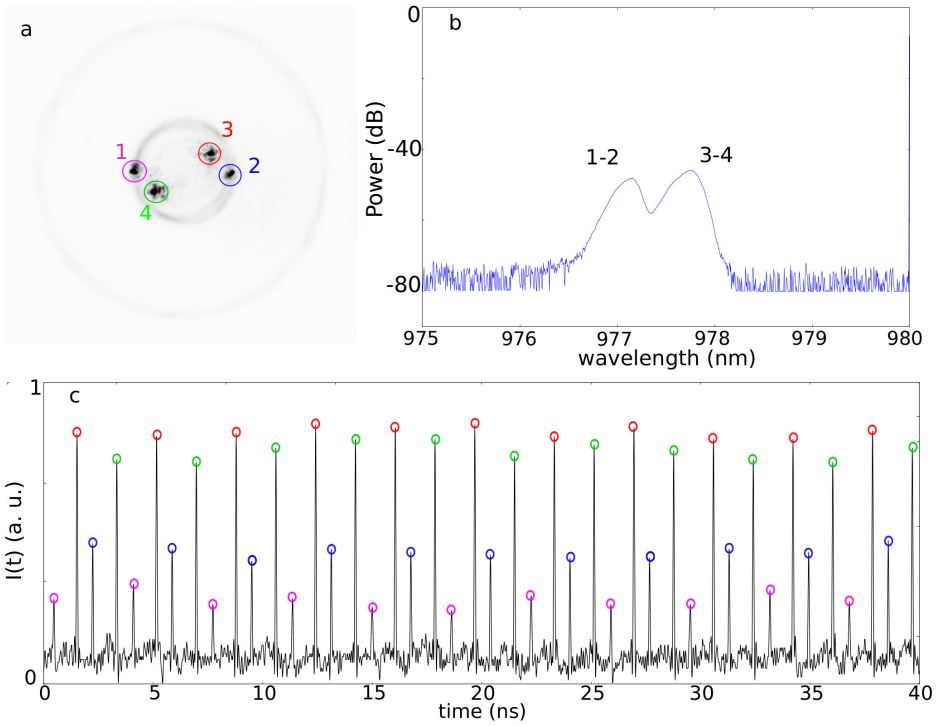

Figure 2.9: Far-field, optical spectrum and temporal trace for a regime consisting of two mode-locked tilted waves with different transverse wave vector components, J = 600 mA. a) The far-field shows two pairs (1-2 and 3-4) of tilted waves where $K_\perp{}^{1-2} > K_\perp{}^{3-4}$. b) The optical spectrum exhibits two peaks corresponding to each tilted wave frequency. They are separated by about 0.7 nm. c) The temporal trace shows the train of pulses emitted by the mode-locked tilted wave 1-2 (purple and blue circles) and 3-4 (red and green circles). The differences in amplitude can be explained by the various coupling efficiency of each tilted wave with the optical fiber.

A very interesting property of this setup is the possibility to generate two couples of mode-locked tilted waves at the same time. An example of such a dynamics is given in Fig. 2.9. In panel a), one can see two pairs of tilted waves (1-2 and 3-4) coexisting in the far-field of the VCSEL. The two pairs have different $K_\perp$ and orientations, a quick look reveals that $K_\perp^{1-2}$ is larger

than $K_{\perp}^{3-4}$. This difference can be appreciated on panel b) where we show the optical spectrum of the tilted waves. One can clearly distinguish two peaks, each corresponding to the pairs of tilted waves in panel a). As $K_{\perp}^{1-2}$ is larger than $K_{\perp}^{3-4}$, the bluest peak is the spectral emission from pair 1-2 and the reddest peak is the one from pair 3-4. Both spectra have a width of about 40 GHz since the VCSEL is operating in the mode-locked regime (see Fig. 2.4). Panel c) shows the time trace of this regime consisting of four periodic trains of pulses, each being attributed a color in order to distinguish each of them. We monitored the dynamics by coupling the entire far-field of the VCSEL to a unique multimode optical fiber. Since all these waves have different wave vectors, their coupling in the fiber is unequal which explains the various amplitudes observed. The colors of the markers in panel c) are associated to the colors of the circles surrounding the spots in the VCSEL far-field in panel a). We were able to link every train of pulses to its corresponding wave vector by blocking successively each spot on the far-field and monitoring which train of pulses disappeared in the temporal trace.

Therefore our spatio-temporal dynamics consisting of mode-locked tilted waves possess very interesting features that may be used for future applications. Indeed from a single experiment, one is able to generate two pulse trains with different wavelength and wave vectors, which allows their separate coupling with optical fibers in data multiplexing applications. Yet, for the moment, addressability of these far-field spots has not been proved and would require an external injection focused onto the RSAM surface. If addressability were evidenced, then this system would consist on a reconfigurable matrix of tunable mode-locked tilted waves.

2.2.3 Discussions on wave vectors selectivity

In this section, we will disclose a possible explanation about the emergence of the mode-locking regime in our system. From the dynamical point of view, mode-locking is favored when the saturable absorber is saturated at a lower fluence than the amplifier [Haus 2000]. In our scheme, this is achieved when the VCSEL emits a tilted plane wave, which imposes a low power density (hence low saturation) in the gain section and, at the same time, a strong local saturation of the RSAM. The reason is that the VCSEL and the RSAM lie one into the Fourier plane of the other, hence any plane wave emitted by the VCSEL yields a spot on the RSAM and vice-versa (see Fig. 2.3). On the other hand, the unsaturated reflectivity of the RSAM is very low ($\approx 1\%$) at resonance, rising up to $\approx 60\%$ when fully saturated. Hence, if the VCSEL emits a pulse in the form of a plane wave with a transverse wave vector $\vec{K}_{\perp}$, all the power will concentrate on a single spot at $\vec{r}_s$ on the RSAM, hereby strongly saturating the RSAM which becomes reflective. The light thus comes back to the VCSEL, where it arrives with a transverse component -$\vec{K}_{\perp}$. Upon amplification and reflection at the VCSEL, the process repeats for this plane wave with opposite transverse wave vectors, which is now imaged onto the RSAM at -$\vec{r}_s$. Thus, after two round-trips the original wave at $\vec{K}_{\perp}$ overlaps with itself, leading to a pulse train at twice the round-trip time for this wave which is

alternating in time with a delay of one round-trip with its replica at -$\vec{K}_\perp$. This explains the observed dynamics, and also the lack of interference pattern in the form of rolls on the VCSEL: even if two tilted waves are then propagating within the VCSEL resonator, they alternate in time with a delay of one round-trip in the external cavity, so they never coexist and do not yield the expected interference pattern; the two spots in the far-field (i.e. over the RSAM) are only an artefact of time-averaging operated by CCD cameras. At variance with tilted waves leading to narrow spots onto the RSAM, the flower mode present on the external frontier of the VCSEL (see Fig. 2.1b) does not contribute to PML. In fact, the Fourier Transform of such flower mode consists in a radial Bessel function of large order $\approx J_m(\mathrm{r})$ with m » 1, which corresponds to an extended ring profile. In this case, the power density on the RSAM remains always below the saturation fluence of the RSAM.

While the above scenario is valid for a large interval of values of the transverse wave vector $\vec{K}_\perp$, experimental results show that the system selects a well-defined value when operating in the PML regime. In principle, this selection may arise from several factors. On the one hand, both the VCSEL and the RSAM are Fabry-Perot cavities defined by Bragg mirrors which complex reflectivity have an angular dependence. Moreover, the reflectivity of a Fabry-Perot cavity depends not only

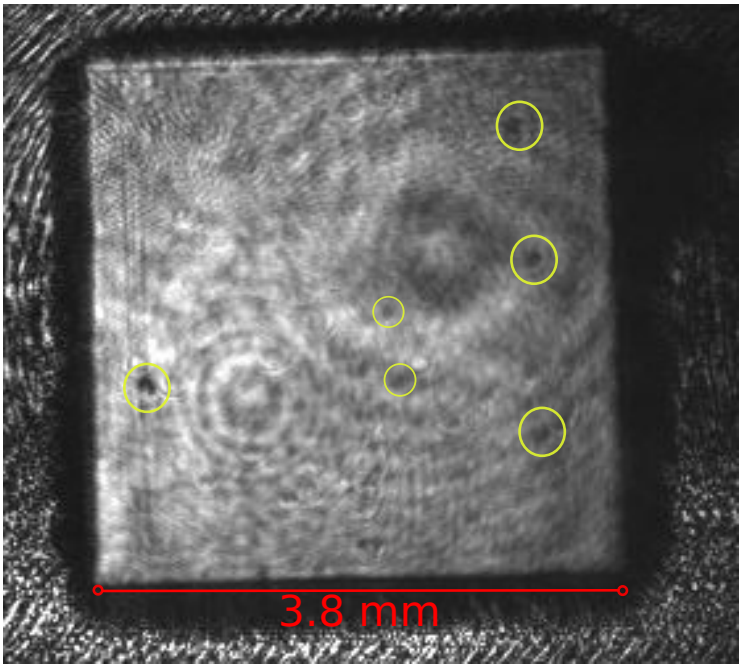

Figure 2.10: Image of the RSAM surface obtained by reflection of a non-resonant laser light. Yellow circles denote the presence of defects on the surface that appear as darks spots. The size of the biggest spots is about 0.1 mm while the RSAM transverse size is 3.8 mm.

on the wavelength but also on the angle of incidence of the light, and the resonant wavelength of the cavity blue-shifts as the incidence angle increases. This effect can be further enhanced in our system due to the compound cavity effect. Nevertheless, experimental evidences shown in Fig. 2.8, where the VCSEL cavity resonance is varied over 2 nm while leaving the transverse wave vector unchanged, seems to indicate that cavities detuning do not play an important role in selecting the value of $\vec{K}_\perp$: this can be understood when considering that the FWHM bandwidth of the RSAM absorption curve (16 nm) is much larger than the VCSEL's one (1 nm).

On the other hand, wave vector selectivity may also arise from any imperfections on the RSAM/VCSEL mirrors that break the spatial invariance. State-of-the-art fabrication process does not fully prevent from formation of small size (a few μm) defects in the transverse plane of semiconductor micro-resonators. These are in general local spatial variations of the semiconductor resonator characteristics [Oudar 1992], which in the case of RSAM would be mainly related to a local variation of unsaturated reflectivity. Visual inspection of the reflection profile of a transversally homogeneous injected monochromatic field onto several used RSAMs has indeed shown the existence of these local variations. Such inhomogeneities on the RSAM surface may correspond to locations where the RSAM exhibits a lower unsaturated reflectivity, hence leading the system to select the tilted wave whose image on the RSAM surface coincides with one of these defect. By laterally shifting the RSAM along the back focal plane of its collimating lens, the position of the defect changes in the far-field plane, thus selecting a tilted wave with another transverse wave vector component. This leads to a continuous scan of the distance between the two spots in the far-field, as shown in Fig. 2.10, and a corresponding change of the emission wavelength, as expected for tilted waves. The experimental evidence of Fig. 2.10 seems to indicate that, in our system, the presence of these inhomogeneities is ruling the selection of the transverse wave vector. The role of small imperfections in the RSAM structure in the transverse wave vector selection is confirmed by the theoretical results presented in the next section.

2.3 Numerical simulations

2.3.1 The model

Our model for the dynamical evolution of the fields E_j and the normalized carrier density N_j in the QW regions of the VCSEL (j = 1) and the RSAM (j = 2) reads :

$$\dot{E}_1 = \left[(1-i\alpha_1)N_1 - 1 + i\Delta_\perp + c_1\Delta_\perp^2\right]E_1 + h_1 Y_1, \tag{2.2}$$
$$\dot{E}_2 = \left[(1-i\alpha_2)N_2 - z + ib\Delta_\perp + c_2\Delta_\perp^2\right]E_2 + h_2 Y_2, \tag{2.3}$$
$$\dot{N}_1 = \gamma_1\left[J_1 - \left(1+|E_1|^2\right)N_1\right] + \mathcal{D}_1\Delta_\perp N_1, \tag{2.4}$$
$$\dot{N}_2 = \gamma_2\left[J_2 - \left(1+s|E_2|^2\right)N_2\right] + \mathcal{D}_2\Delta_\perp N_2, \tag{2.5}$$

where $\Delta_\perp = \partial_x^2 + \partial_y^2$ is the transverse Laplacian and Y_j denotes the field injected in device j. In Eqs. (2.2-2.5) time is normalized to the photon lifetime in the VCSEL κ_1 and space is normalized to the diffraction length in the VCSEL L_d. The complex parameter z is decomposed as $z = a - i\delta$ where a represents the ratio between the photon lifetime in the VCSEL and the RSAM cavities and δ is the scaled detuning between the two cavity resonances. The scaled carrier recovery rates and the bias are denoted γ_j and J_j respectively. We defined the ratio of the saturation intensities of the VCSEL and the RSAM as s. The angular dependence from the DBR reflectivity as well as the one from the Fabry-Perot cavity are contained in the double transverse Laplacian and the parameters $c_{1,2}$. The RSAM being a broadband fast absorber, it is characterized by $J_2 < 0$, $\gamma_2 \gg \gamma_1$, $a \gg 1$ as well as $s \gg 1$.

Injected fields and device coupling

In the case of a self-imaging configuration, the link between the two devices is achieved by expressing the emitted fields O_j as a combination of the reflection of the injection fields Y_j and the self emission E_j, which reads

$$O_j(r,t) = \eta_j E_j(r,t) - Y_j(r,t), \tag{2.6}$$

where we defined $\eta_j = t_1^j / \left(1 + r_1^j\right)$ with t_1^j and r_1^j the transmission and reflection coefficients in amplitude of the emitting DBR from the inside to the outside of the cavity. Considering the propagation delay and the losses incurred by the beam splitter allowing the light extraction, the link between the two devices in ensured by the following two delayed algebraic equations [Javaloyes 2012].

$$Y_1(r,t) = t_{bs}O_2(r,t-\tau_e), Y_2(r,t) = t_{bs}O_1(r,t-\tau_e), \tag{2.7}$$

with t_{bs} a complex number whose modulus and phase model the losses induced by the beam-splitter and the single trip feedback phase, respectively.

However, the image of the VCSEL through its collimator is placed exactly at the object focal plane of the collimator in front of the RSAM. In turn, the RSAM is on

the image focal plane of its collimator. In this configuration, and assuming that the collimators have a large diameter, the field injected in one device is the (delayed) Fourier transform in space of the field coming from the other, which is modelized via Kirchhoff's formula for a lens with focal length f as

$$Y_1(r,t) = t_{bs}\int O_2(r',t-\tau_e)e^{-i\frac{\omega_0}{c}\frac{r\cdot r'}{f}}d^2r' \equiv \mathcal{F}_\tau(O_2) \tag{2.8}$$

$$Y_2(r,t) = t_{bs}\int O_1(r',t-\tau_e)e^{-i\frac{\omega_0}{c}\frac{r\cdot r'}{f}}d^2r' \equiv \mathcal{F}_\tau(O_1) \tag{2.9}$$

and where the beam splitter losses may contain a normalization constant due to the Kirchhoff's integral. It is worth remarking that Eqs. (2.8-2.9) describe the coupling of the two devices to all orders of reflection in the external cavity. They define a delayed map where the field injected into one device returns inverted. This can be seen, for instance, using Eq. (2.6) and saying that the RSAM has an effective reflectivity such that $O_j = r_{eff}Y_j$ and substituting in Eq. (2.8), which yields

$$Y_1(r_\perp,t) = \mu E_1(-r_\perp,t-2\tau) \tag{2.10}$$

where we have used that $\mathcal{F}_\tau \circ \mathcal{F}_\tau[Y_2] = \alpha Y_2(-r_\perp,t-2\tau)$ and $\mu{=}\mathrm{t}_{bs}^2 r_{eff}$ describes the double effect of the beam splitter and of the RSAM reflection. Thus, after one round-trip, Y_1 overlaps with a spatially reversed copy of itself, and it requires a second round-trip to achieve proper overlap.

Parameters

The reflectivities of the DBRs in the VCSEL and the RSAM are taken as $\left(r_1^{(1)}, r_2^{(1)}\right) = \left(\sqrt{0.942}, 1\right)$ and $\left(r_1^{(2)}, r_2^{(2)}\right) = \left(\sqrt{0.59}, 1\right)$ and assume that the single trip in the VCSEL and the RSAM is $\tau = 30\,\mathrm{fs}$ corresponding to an effective length $L_z = 2.6\,\mu\mathrm{m}$ with a index of $n = 3.5$. This gives us $\kappa_1 = 10^{12}\,\mathrm{rad.s}^{-1}$ and $\kappa_2 = 10^{13}\,\mathrm{rad.s}^{-1}$, yielding a FWHM for the resonances of $\Delta\lambda_j = \kappa_j\lambda_0^2/(\pi c)$ of 1 nm and 10 nm respectively. Incidentally, we find that $a = 10$ and $(h_1, h_2) = (2, 20)$. The diffraction lengths is found to be $L_d = \sqrt{L_z q_0^{-1}(1-r_1r_2)^{-1}} = 2\,\mu\mathrm{m}$, hence the numerical domain that is twice the size of the VCSEL and the RSAM is $L_\perp = 200$. The other parameters are $\alpha_1 = 2$, $\alpha_2 = 0.5$, $b = 10^{-2}$,$\gamma_1 = 10^{-3}$, $\gamma_2 = 0.1$, $s = 10$, $t_{bs} = 0.9$, $\mathcal{D}_1 = \mathcal{D}_2 = 10^{-3}$, $c_1 = 10^{-2}$ and $c_2 = 10^{-6}$.

RSAM characteristics

The basic properties of the RSAM can be found assuming an incoming plane wave of amplitude Y at normal incidence and at frequency ω, i.e. $Y_2 = Y\exp(-i\omega t)$. The response of the RSAM is given by

$$\left(z - i\omega - \frac{J_2(1-i\alpha_2)}{1+s|E_2|^2}\right)E_2 \quad = \quad h_2 Y. \tag{2.11}$$

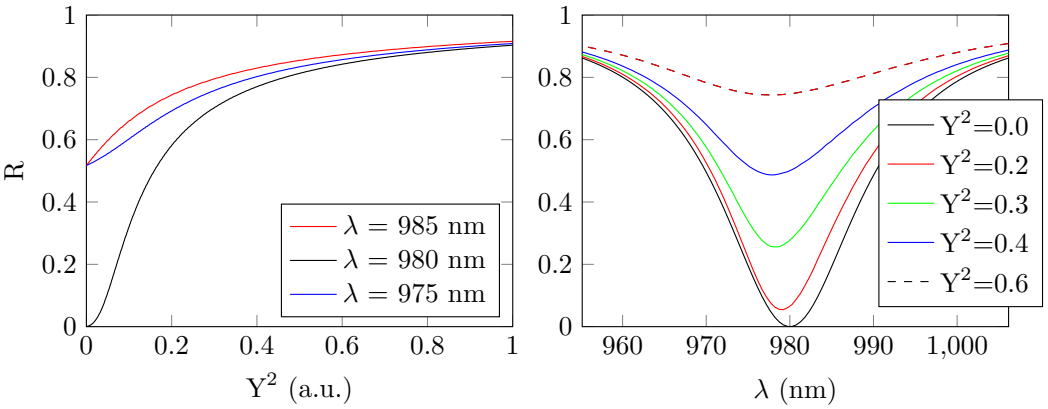

Figure 2.11: Reflectivity of the RSAM as a function of the input field intensity (left) for various values of the wavelength, the resonance being chosen to be $\lambda_0 = 980\,\text{nm}$ and (right) reflectivity as a function of wavelength for increasing input power.

The effective reflectivities are obtained setting $O_2 = rY_2$ that is to say $r = E_2/Y_2 - 1$ yielding the unsaturated and saturated responses

$$r_< = \frac{h_2 - z + i\omega + J_2\,(1 - i\alpha_2)}{z - i\omega - J_2\,(1 - i\alpha_2)}, r_> = \frac{h_2 - z + i\omega}{z - i\omega}. \tag{2.12}$$

By choosing $J_2 = a - h_2$ we obtain a perfectly absorbing RSAM, i.e. $r_< = 0$ at the frequency $\omega = \delta + \alpha\,(a - h_2)$. In between these unsaturated and saturated regimes, the effective reflectivity can be obtained by solving Eq. (2.11) numerically. We represent $R = |r|^2$ in Fig. 2.11.

Defect in the RSAM surface

We assume that the impurity on the RSAM surface has the effect of locally lowering the reflectivity of the top mirror. As such the parameters a and h_2 are allowed to vary in the transverse dimension. A decrease of $r_1^{(2)}$of 0.1 modifies a and h_2 to be $a = 12$ and $h_2 = 24$. We assume a Gaussian profile for such transverse variations.

Numerical considerations

In order to avoid computational difficulties, the theoretical analysis is restricted to a single transverse dimension. We believe that the main spatial feature being lost by such simplification is the description of the non mode-locked two dimensional radial flower mode [Babushkin 2004] on the border of the VCSEL, which has already been qualitatively discussed. Besides, for the sake of simplicity, we used a time delay of $\tau = 200$ ps (instead of 2 ns in the experiment) to avoid the temporal complexity due to long cavities, and to concentrate only on the spatial aspects of the problem. The simulation time is 500 single-trips in the external cavity, i.e. 100 ns.

2.3.2 Numerical results

The bias current is fixed to $J_1 = 0.92$, i.e. below the threshold of the solitary VCSEL but above the threshold of the compound device. We represent in Fig. 2.12, the output time trace for the intensity averaged over the surface of the VCSEL as well as the averaged population inversion in the active region of the VCSEL and in the RSAM. One recognizes the standard PML temporal pattern where the gain experiences depletion during the passing of the pulse followed by an exponential recovery. The same yet inverted pattern is also visible on the RSAM inversion. We found the pulse-width to be of the order of 4 ps somewhat shorter than found experimentally. However, the precise value of the experimental pulse-width is difficult to estimate and could explain the discrepancy.

This averaged representation describes well the experimental situation when the full output of the VCSEL is captured by the photo-detector. Yet it does not disclose

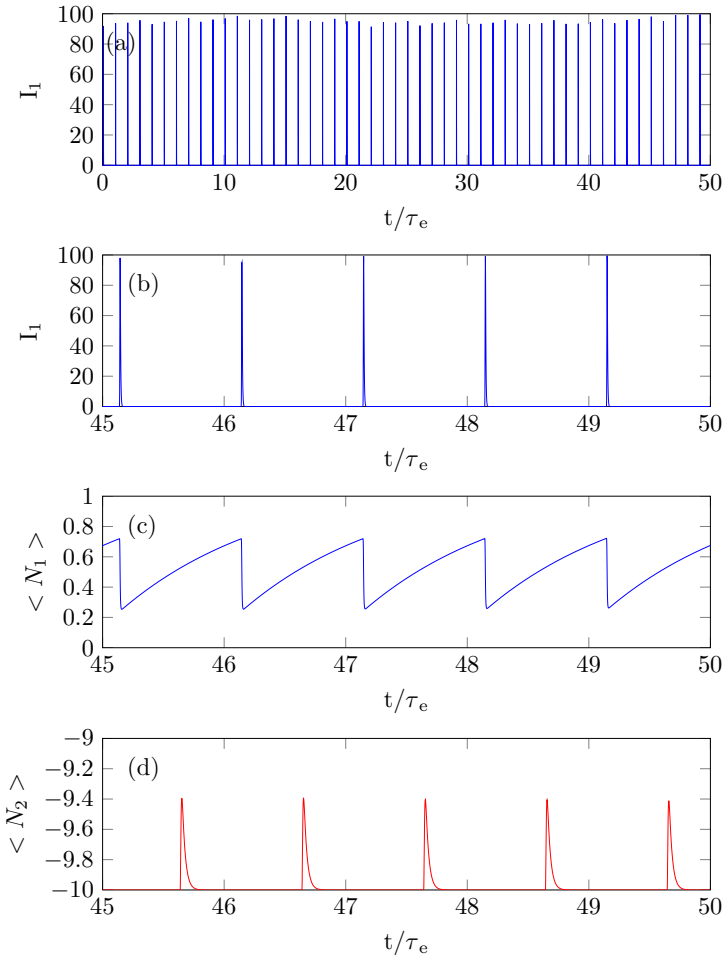

Figure 2.12: Panels a) and b): Averaged intensity profile I_1 as a function of time showing stable PML. Panels c) and d) represent the averaged population inversion in the VCSEL and in the RSAM as a function of time.

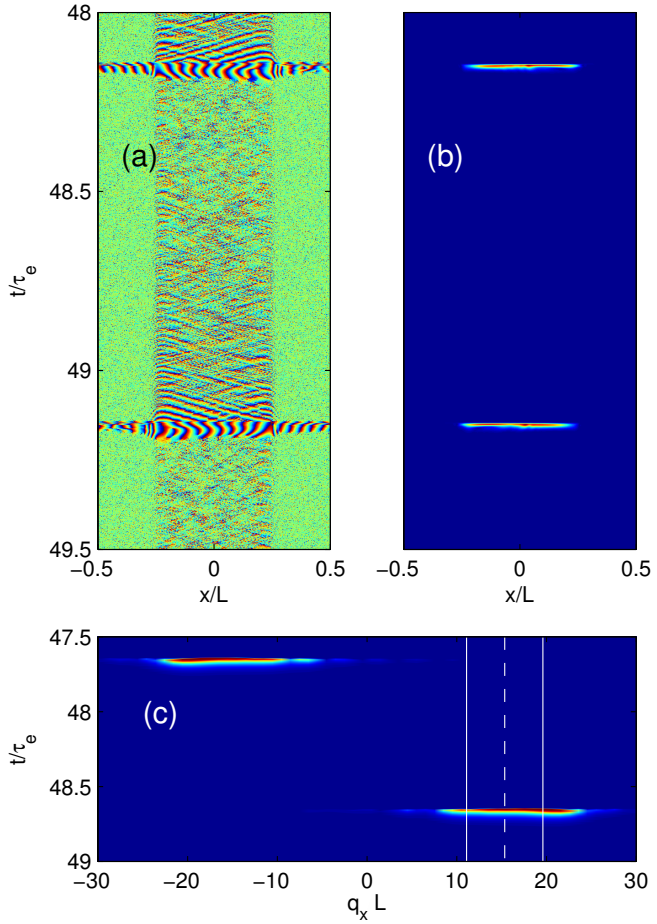

Figure 2.13: Panel a): Phase profile of E_1 as a function of space and time. A tilted wave with alternate wave vector from one round-trip to the next is clearly visible. Panel b) Intensity profile of E_1 showing that the transverse intensity profile is uniform. Panel c): Population inversion in the RSAM. The FWHM size of the population inversion spot is $\approx$ 6 μm and the RSAM is fully saturated locally by the pulse.

the hidden transverse dynamics. We represent in Fig. 2.13 the spatially resolved temporal output of the VCSEL. In Fig. 2.13a) the phase profile $\phi_1 = \arg(E_1)$ discloses the existence of alternate transverse waves while the intensity profile Fig. 2.13b) remains uniform. Such field profile directly impinges the RSAM via its Fourier Transform which explains that the temporal time trace of population inversion in the RSAM (Fig. 2.13c) exhibits two spots at two opposite locations with respect to the center. In Fig. 2.13c) we represented the center of the pinning potential with a dotted line while the two white lines represent the FWHM. The horizontal axis in Fig. 2.13c) is scaled in normalized frequencies. The transverse value of the wave vector here is ~ 16 which corresponds to 8 transverse oscillations along the active region of the VCSEL, i.e. a wavelength of $\sim 25\,\mu$m. We found that by slowly displacing the center of the pinning potential it was possible to tune the

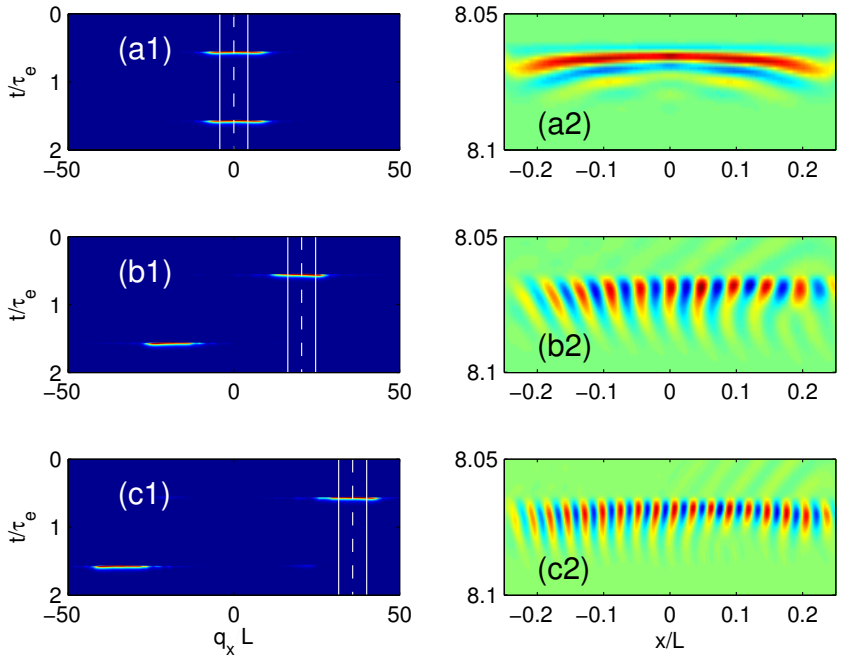

Figure 2.14: Evolution of the transverse wave vector as a function of the position of the pinning potential. Panels a1), b1) and c1) correspond to the population inversion in the RSAM while the panels a2), b2) and c2) correspond to the real part of E_1. The FWHM size of the population inversion spot is ≈ 6 μm and the RSAM is fully saturated locally by the pulse.

transverse wave vector between $q_xL = 0$ and $q_xL = 36$, which corresponds to a minimal wavelength of 11 μm. The associated shift in the emission wavelength is ~ 4 nm around 980 nm, in excellent agreement with the experimental results. Several points along such tuning curve are presented in Fig. 2.14. All cases correspond to stable PML regimes that would seem to be almost identical if one considers only the averaged temporal output like e.g. in Fig. 2.12. Noteworthy, we also found some perfectly regular PML regimes when the inhomogeneity was located at the center of the RSAM. We provide several reasons for such discrepancy between theory and experiment. First, the dissipation of the energy and of the associated heat incurred by the light absorption is doubled when there are two well-separated spots on the RSAM, such thermal effects are not taken into consideration by our model. Second, other spatial inhomogeneities, these ones detrimental to PML, could be located on the sides of the pinning defect favoring PML. When the two spots become less and less separated, the one that is not experiencing the pinning potential (i.e. the left spot in Fig. 2.14b1) will eventually be victim of such detrimental inhomogeneity. At last we note that for instance in the case of the largest value of the transverse wave vector in Fig. 2.14c1) the spot size seems to be quite wider than in Fig. 2.7, however the strong saturation of the CCD camera could explain such difference in the appearance of the spot. In addition, we do represent the population inversion which experiences diffusion that contributes to a broadening of the spot size.

2.4 Conclusions and perspectives

We have shown that electrically biased broad-area VCSELs with optical feedback from a RSAM can be passively mode-locked when the VCSEL and RSAM are placed each at the Fourier plane of the other. In this configuration, the system emits a train of pulses of ≈ 10 ps width with a period equal to the round-trip time of the external cavity τ. In this PML regime the time-averaged VCSEL far-field, which is imaged onto the RSAM plane, exhibits two bright peaks symmetrically located around the optical axis, thus indicating that the VCSEL emits two tilted waves with opposite transverse components. The time traces corresponding to each spot consist of a pulse train with a period 2τ, and the two trains are delayed by one round-trip one with respect to the other. Accordingly, the two tilted waves are alternatively emitted at every round-trip. We have shown that the mechanism leading to wave vector selection is related to the existence of inhomogeneities in the transverse section of the RSAM. Because the RSAM is in the Fourier plane of the VCSEL near-field, a defect may favor a tilted wave emission with a well-defined transverse component. By shifting the RSAM laterally, the defect moves in the Fourier plane, thus selecting another transverse wave vector and allowing for wavelength tuning of the mode-locked emission. With this method we managed to achieve a wavelength detuning of 4 nm while remaining in a stable mode-locked regime.

This section provided a detailed study of the spatio-temporal dynamics in this mode-locked system with transverse degree of freedom for a fixed external cavity round-trip time of about 2 ns. Very surprisingly, we observed that the fundamental mode-locked solution, exhibiting the same spatial features, could be obtained in a cavity where the round-trip time is much larger than the gain recovery time of the broad-area VCSEL; in such configuration, the onset of harmonic mode-locking is expected in order to fulfill the background stability criterion. Noteworthy, we managed to generate a new record of low PML frequency in semiconductor lasers by reaching 65 MHz ($\tau = 15.4$ ns); this record being previously held by Butkus et al. [Butkus 2013]. Thus, in the next section, we will provide an experimental description and a theoretical explanation for the stability of this low-frequency tilted waves PML regime.

Chapter 3

How lasing localized structures evolve out of passive mode-locking

Contents

3.1 Introduction 63
3.2 Experimental observations 64
3.2.1 Evidences for temporal localization 64
3.2.2 Writing and moving the localized structures via VCSEL current modulation: preliminary results 68
3.3 Theoretical analysis 76
3.3.1 The model 76
3.3.2 From PML pulses to temporal LS: dynamical scenario 76
3.4 Conclusions 80

3.1 Introduction

Recent works have addressed the question whether the concept of LS can be extended to the time domain [Leo 2010, Herr 2014, Tlidi 2010, Tlidi 2013] in the case of optically injected cavities. Here we propose to answer to this question considering a phase invariant system, namely our passively mode-locked broad-area VCSEL.

In fiber lasers, for which the gain and the absorption are respectively much slower and faster than all the other variables, the Haus equation can be approximated by the subcritical CQCGLE where one replaces the slowly evolving net gain (which has a typical time scale $\Gamma^{-1} = 10$ ms) by a constant. The PML pulses are interpreted as Dissipative Solitons [Grelu 2012] and they are sometimes studied as perturbed nonlinear Schrödinger conservative solitons [Fauve 1990]. Noteworthy, a similar regime exists in monolithic semiconductor PML lasers in which the cavity round-trip ($\tau \approx 10$ ps) is much shorter than the gain recovery time scale $\Gamma^{-1} = 1$ ns and where the gain weakly evolves around its equilibrium value.

On the other hand, in external cavity configurations [Paschotta 2002, Lorenser 2004], the semiconductor fast time scales allow exploring the transition from the regime $\Gamma\tau \ll 1$ toward $\Gamma\tau \gg 1$, which would be impractical with other active material. In this chapter, we describe both theoretically and experimentally how lasing LS form out of a PML semiconductor laser during the transition from the

regime $\Gamma\tau \ll 1$ toward $\Gamma\tau \gg 1$, thus clarifying in which conditions the pulses become localized and can be used as independent bits for storing information. We show that LS require two conditions to be fulfilled: i) the trivial off solution must be stable and coexist with the mode-locked solution and ii) the cavity round-trip must be much longer than the slowest medium time scale (i.e. the semiconductor gain). While condition ii) usually implies the violation of the background stability criterion for fundamental mode-locking and leads to a high-order harmonic mode-locked solution ($N_h \gg 1$) as the unique stable solution, we show that, if condition i) is verifed, the background automatically becomes stable. This enables the coexistence of a large quantity of stable solutions, each of them being characterized by a different number of pulses per round-trip (ranging from zero to N_h) with different arrangements. In this situation, the PML pulses become LS that can be addressed as independent bits.

3.2 Experimental observations

3.2.1 Evidences for temporal localization

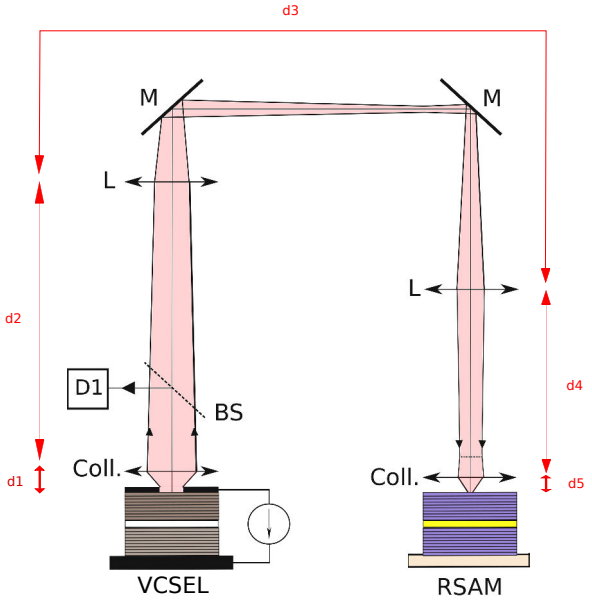

Figure 3.1: Experimental setup: temperature-stabilized VCSEL and RSAM. Coll.: aspheric lens, BS : beam splitter, M: mirror, L: lens and D1: detector. The cavity length is 2.3 m, the two 30 cm converging lenses are placed so as to image the far-field of the VCSEL surface onto the RSAM surface.

The experimental setup is the same as in Chapter 2 (see Fig. 2.2). In order to match the conditions for observing LS, we set the cavity round-trip to τ = 15.4 ns, corresponding to a FSR of 65 MHz and to $\tau \approx 50\Gamma^{-1}$. This is technically realized by inserting two 30 cm focal length lenses inside the cavity placed in such a way to create the image of the VCSEL in the focal plane of

the collimating lens placed in front of the RSAM (f = 8 mm). Thus the exact Fourier transform of the VCSEL near-field is imaged onto the RSAM surface when this last is set at 8 mm from the collimator, see Fig. 3.1. In order to find the right distances between each lens in the setup we used the same technique as the one described in the annexe of [Genevet 2009]. The condition we impose in our geometrical calculations is that the image of the VCSEL has to return inverted after one round-trip in the external cavity and that d1 = d5 = 8 mm and d2 = d4, which is the simplest configuration. We end up with d2 = 737 mm and d3 = 810 mm.

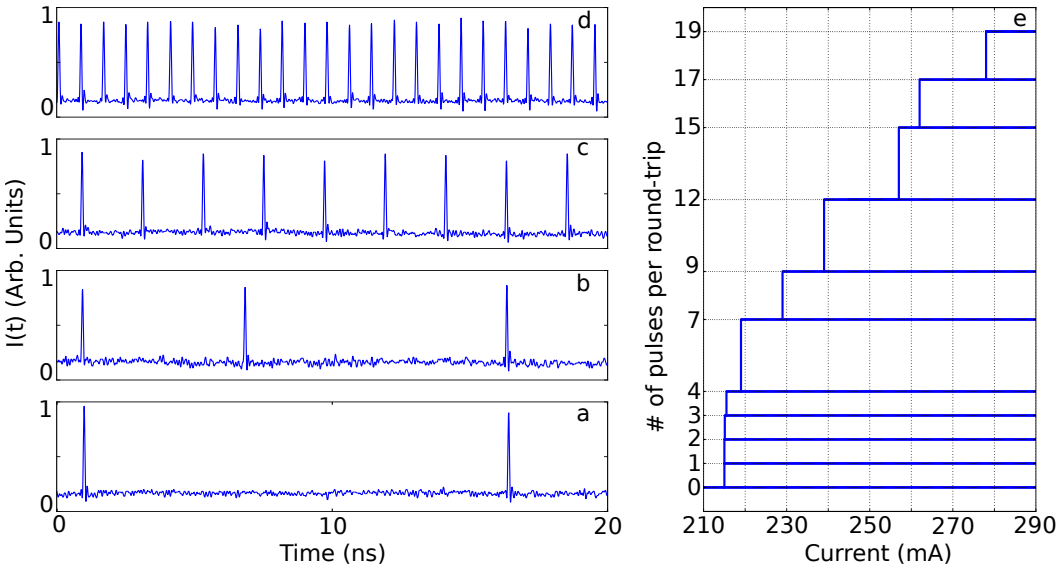

Figure 3.2: Panels a), b), c) and d): coexisting time output traces (J = 290mA). Panel e): experimentally obtained bifurcation diagram for the number of pulses per round-trip. The stability of each solution is indicated by the solid horizontal lines.

In this situation narrow laser pulses are regularly emitted at the fundamental repetition rate of 65 MHz (see Fig. 3.2a) which is, to the best of our knowledge, the smallest repetition rate ever obtained with a PML semiconductor laser. The pulse width is below the limit of our detection system but the corresponding spectral emission consists of a peak with 0.12 nm bandwidth (FWHM), thus indicating a pulse width of approximately 12 ps. The width of the pulse being the same as the one obtained with a shorter cavity (see chapter 2), it is therefore independent from the size of the cavity. Several emission states coexist for the same values of bias current, as shown in Fig. 3.2a-d). The system may remain in the off-state that corresponds to the lower value between pulses or emit a pulse train with different number of pulses (from one up to nineteen) per round-trip. In these emission states, the individual pulses may appear grouped (Fig. 3.2b) or equally separated (Fig. 3.2c,d).

All these regimes coexist for a wide range of the VCSEL current J. The multi-stability of our system is depicted in Fig. 3.2e) where we classify the different solutions in terms of the number of pulses per round-trip. It is important to

remember that, for a given number of pulses, an arbitrary number of different arrangements of these pulses within the round-trip was found, corresponding to an arbitrary number of different solutions. Fig. 3.2e) is obtained increasing the parameter J from J = 210 mA, where only the steady off solution is stable, up to the value where it loses its stability (J = 600 mA) and then sweeping it down until a periodic emission with 19 pulses per round-trip appears (Fig. 3.2d), which probably corresponds to the highest order harmonic mode-locking solution that can be fitted in our cavity round-trip (Fig. 3.1). As J is decreased this solution loses its stability and the number of pulses per round-trip reduces progressively, until only one remains (Fig. 3.2a), thus leading to the bifurcation scenario shown in Fig. 3.2e). Each solution is spontaneously appearing as J is scanned downward and, once a new solution is found, we increase J to explore the stability of this solution up to J = 290 mA. As long as the system remains on the same branch there are no changes in the arrangement of the pulses; even if several arrangements are possible, a given arrangement of N pulses/round-trip is stable versus parameters variation.

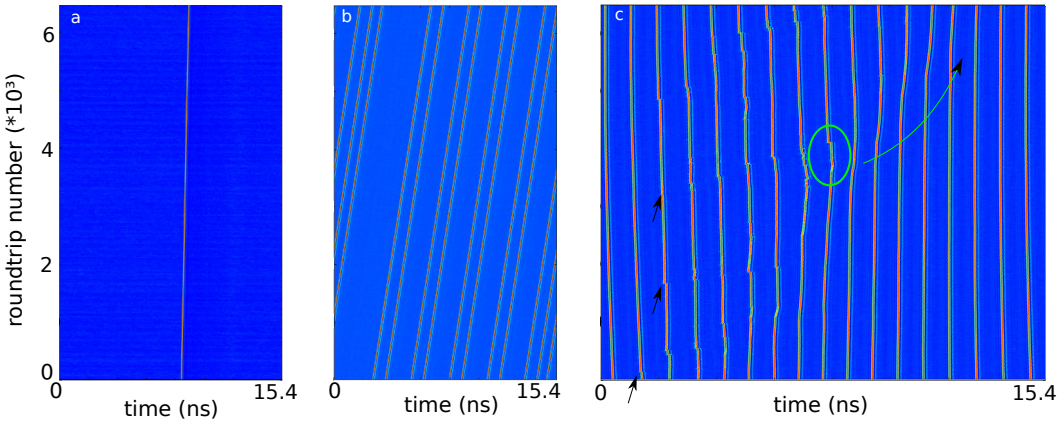

Figure 3.3: Space-time like diagrams for multiple arrangements of temporal LS in the cavity, J = 280 mA. a) A single LS. b) 11 LS coexisting in the cavity, the left-most LS seem to form a group of 3, while the 8 others are forming pairs of LS with a unique interval between each. c) Propagation of a perturbation through transmission among the 17 LS present in the cavity. The speed of one LS is affected by the displacement of the previous one, and then it transfers this speed variation to the next.

In Fig. 3.3 we show several of these arrangements using the so-called space-time diagram representation where the temporal traces are folded at the cavity round-trip period in order to follow the pulse evolution in the external cavity as a function of the round-trip number. This is a generic method for representing the time evolution of temporal localized structures in a delayed system [Arecchi 1992]. Panel a) shows the trajectory of a single LS in the external cavity. This diagram clearly evidences that the size of the pulse is small compared to the one of the cavity, and the evolution is then independent from the boundaries. Quite surprisingly, the pulse does not visibly jitter and seems to follow a straight line without being sensitive to the surrounding

noise. This main fact is attributed to the action of the saturable absorber. As previously explained, the RSAM opens a very short window of net gain around the pulse, which allows amplification only for the LS. The rest of the background dynamics is absorbed by the RSAM so that no noise can influence the LS temporal evolution. In fact, in the three panels, the background is completely homogeneous (blue surface) and corresponds to zero emission. Panel b) represents a dynamics consisting of multiple LS coexisting in the cavity (11 in this case), the coexistence of several LS within the cavity boundaries is allowed by the large temporal aspect-ratio of our system. Since no pinning potential in the background can fix the locations of the LS, the intervals between the LS seem to take any possible values. On the right, the LS seem to form a group of three close peaks, while the 8 other LS seem to be coupled in four pairs. The absence of noise in this system prevents us from studying the interactions between the structures present in the cavity and from distinguishing between independant and bound states of LS. Also, the space-time diagram reveals that all the LS drift at the same speed with respect to the cavity reference frame. We note that this speed is higher than the one of the single structure in a). Finally, panel c) demontrates that close enough LS coexisting in the cavity can interact [Grelu 2012, Jang 2013b]. The bottom black arrow indicates that, at round-trip 100, the second LS undergoes a small perturbation, resulting in a forward kink on its trajectory. One can note that this kink actually propagates by successive transmissions from one LS to the next. This first perturbation seems to finally vanish after about 2000 round-trips, which may be due to a finite interaction length between LS. However, a second and a third one appear respectively at round-trips 1500 and 3000. These two propagate at different speeds in the cavity and their action combine in the zone marked by the green circle. As a consequence the LS reaction to the perturbation gets amplified, which results in large variations of LS speed which propagates from one LS to the next, as a domino effect (following the green arrow). The fact that their stability is recovered after hundreds of round-trips reveals that vibrational energy is rapidly dissipated and that LS mutual interactions act as a damping mechanism.

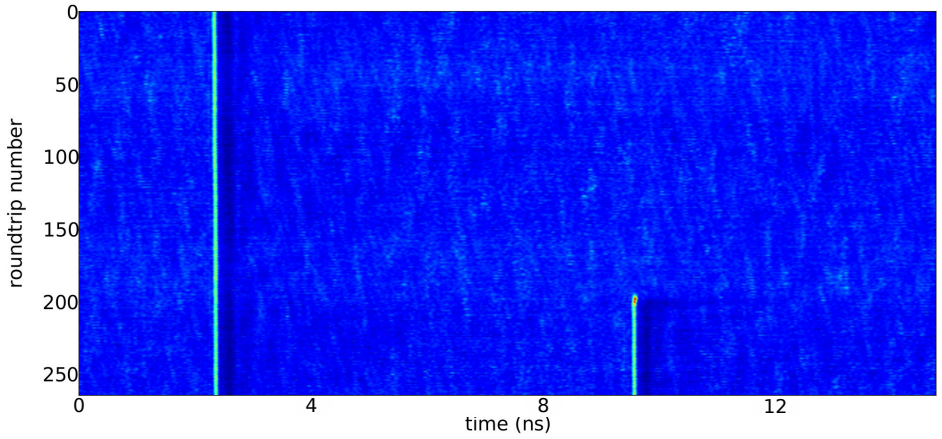

Figure 3.4: Spontaneous switch-on of a LS while another one is present in the cavity.

The diagrams of Fig. 3.3 give experimental evidences that our pulses possess the multi-stability property of temporal LS. Fig. 3.4 shows the spontaneous switch-on of a temporal structure while another is already present in the cavity. This switch-on is characterized by high amplitude peaks during the five first round-trips (red dot on the diagram) which then stabilize to the value of the other LS. In this example, the second LS is formed at a distance $\tau_f/2$ from the first one.

Therefore, relying on this crucial property, our objects may be potentially utilized as bits for all-optical information processing, though individual addressing of the LS is beyond our experimental capabilities. A best way to realize this would be to inject ps-pulses from an external generator in order to provide a temporal local perturbation in our system as realised in [Leo 2010]. Unfortunately, we do not possess such a source of short optical pulses. Another option would consist in implementing a second mode-locked VCSEL with saturable absorber that would serve as a writing beam. Realizing such a system requires more time and will be the main topic of further research in the addressing of the temporal localized structures.

With time and material in my possession, I have simply started to analyze the effects of current modulation on the control and addressing of the structures. This is presented in the next subsection.

3.2.2 Writing and moving the localized structures via VCSEL current modulation: preliminary results

As demonstrated in the previous chapters, our delayed system is a temporal LS generator based on active morphogenesis via fast saturable absorption. One remarkable property is the translational invariance of the "pseudo-space" created by our external cavity in which the LS propagate. Thus, one may be able to shift the living-LS position by imposing a gradient of potential in the external cavity or to address a LS with a suitable external perturbation at any location within the external round-trip.

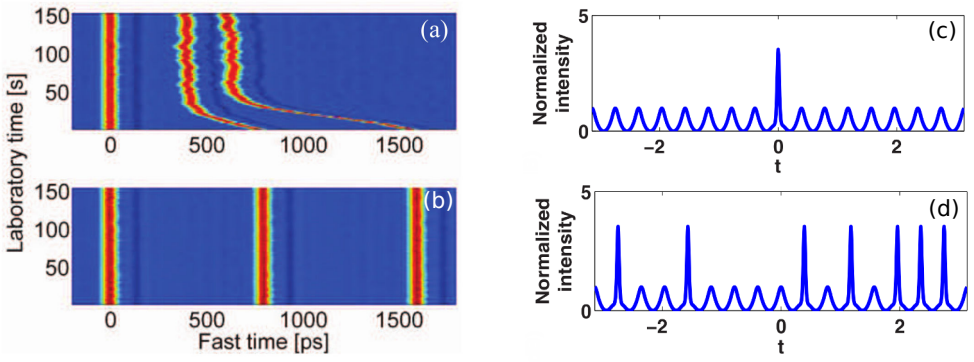

Figure 3.5: Evolution of three CS initially separated by 800 ps without (a) and with (b) phase modulation [Jang 2013a]. c) Single CS on top of a stationary low-intensity pattern [Hansson 2014]. d) coexistence of multiple injected CS on top of the pattern [Hansson 2014].

Imposing such a gradient all-optically is made possible when the LS are generated from passive morphogenesis in injected lasers cavities. For example, people could make spatial cavity solitons drift [Firth 1996, Pedaci 2008a] by setting a spatial phase gradient in the holding beam. They showed that the CS move towards the maxima of potential and acquire a velocity proportional to the gradient strength. The same type of control has been demonstrated for temporal cavity solitons. It was shown that acoustic-induced long-range interactions of temporal CS in a fiber cavity [Jang 2013b] could be suppressed by a sinusoidal phase modulation of the driving beam [Jang 2013a]. Fig. 3.5a) shows acoustic-induced interactions between three CS with no phase modulation. They are initially separated by 800 ps. Their temporal separations slowly shift under the interaction force until they stabilize at specific time intervals. Fig. 3.5b) shows the CS evolution when the driving beam undergoes a 5 GHz phase modulation. The separation between adjacent CS is now locked to a multiple of 200 ps (period of the modulation). This clearly demonstrates that phase modulation effectively counters attracting long-range interactions. Thus, CS can be moved under the action of a temporal or spatial phase gradient. Very recently, a new way to control the respective positions of multiple temporal CS in a microresonator cavity with bichromatic pumping has been theoretically investigated [Hansson 2014]. The dual-pump configuration is shown to support CS formation and has also the potential benefit to suppress interactions between them. In fact, the pumping of two modes that are separated by multiples of the free spectral range introduces a low-intensity temporal pattern in the cavity. When a pulse is injected in the cavity, it will locate on a maximum of this pattern (see Fig. 3.5c). Consequently, when multiple pulses coexist in the cavity, the temporal separation is fixed by integer multiples of the period of the low-intensity pattern (see Fig. 3.5d).

In the experiments described in Chapter 2-3, the VCSEL is mounted in a Thorlabs head which allows external coupling to fast current modulation (up to 500 MHz). We therefore provide current modulation to our laser by connecting the laser head to a waveform generator (HP E4421B). In order to ensure sufficent amplitude

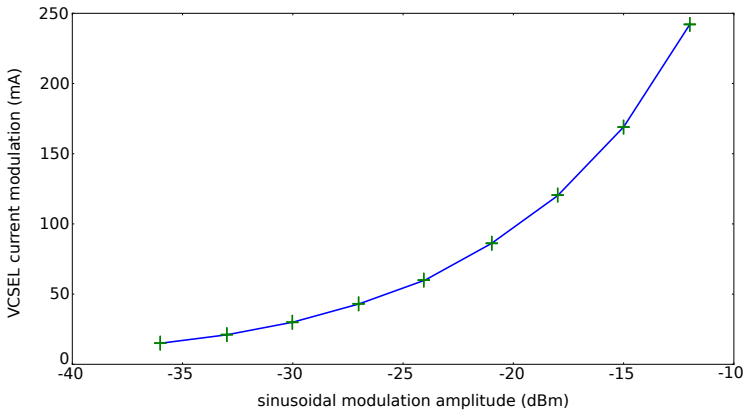

Figure 3.6: Peak to peak current modulation of the VCSEL as a function of the output electrical sine from the waveform generator after the 20 dB stage of amplification.

for the modulation, the signal is sent to a 20 dB amplifier (10 MHz - 4.2 GHz) just before the VCSEL input. Fig. 3.6 shows the evolution of the VCSEL current modulation as the generator waveform amplitude is increased. The maximum input power the amplifier can support is 0 dBm. Depending on the DC current value on which we superpose our sinusoidal current modulation, this mechanism may induce two types of phenomena. First, if gain periodically exceeds the value for which LS exist as stable solutions over a zero background (J = 215 mA, see Fig. 3.2), then one may be able to observe a LS emerging only in the zone of maximal gain. Secondly, if one sets the DC current value in a zone of multi-stability between different LS number and the modulation is set to a low value, one may induce some drift of the LS present in the cavity due to the weak gradient of gain.

As a first result, modulation of the current allowed to create an arbitrary pulse-pattern generator. Indeed, in a first experiment, we set the pumping current value far below threshold (J = 150 mA). When no modulation is applied, the laser is in the off-state and no LS can emerge spontaneously, which is in agreement with Fig. 3.2e). When we use a sinusoidal modulation of the current with a frequency corresponding exactly to the FSR of the cavity (ν_{FSR} = 67 665 700 Hz) and a large enough amplitude (-23.16 dBm), we notice the emergence of a LS just before the maximum modulation value (whiter zone in the background, see Fig. 3.7a). From that state, as the modulation amplitude is increased we observe the emergence of

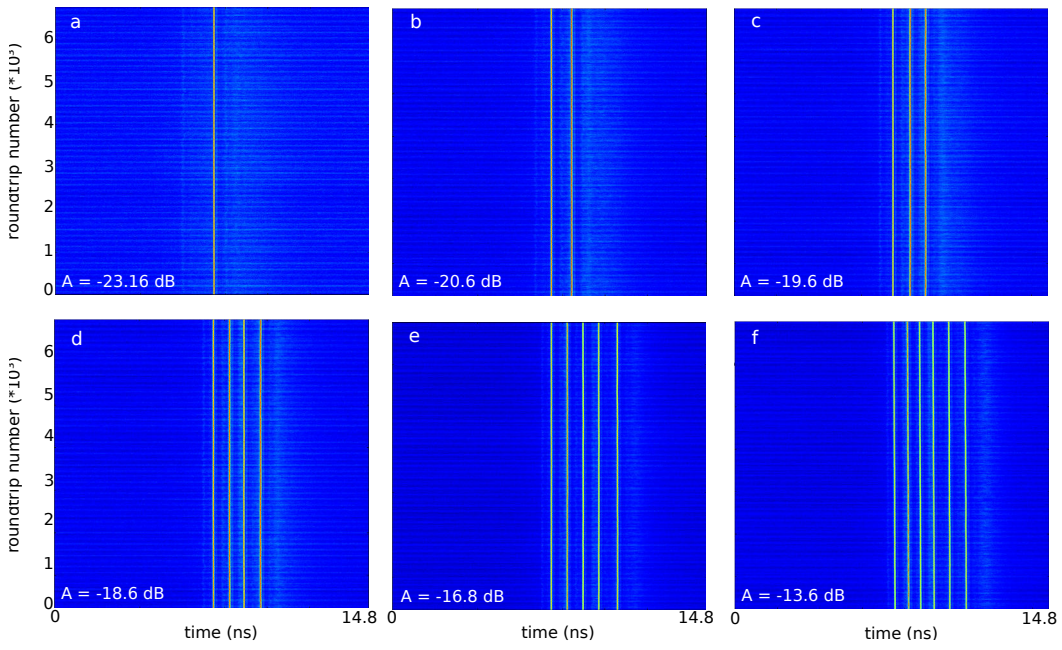

Figure 3.7: Modulation can be used to write the temporal LS in the cavity. I = 150 mA, τ_f = 14.8 ns, $\nu_{mod} = 1/\tau_f$. As A is increased (from a) to f)) the number of pulses increments by 1 on top of the modulation for specific values of A. The maximum number of LS that we achieved is 6 (f). The same occurs when A is decreased but the values for which LS disappear are lower than the ones for which they appeared.

multiple LS where the amplitude of the sine is the highest. We reached a maximum of 6 LS coexisting in the cavity as shown in Fig. 3.7f). We note that the distances between the LS are not fixed as it can be appreciated in panels c) and f). We can also remark that the amplitudes of the LS decrease as the number of LS increases (red color in the diagrams denote the points of maximum amplitude). This can be well understood by the fact that each temporal LS depletes the available gain of the system. Very importantly, the opposite behaviour is observed when we decrease the modulation amplitude from the modulation in panel f). However the amplitude values for which LS switch off are all lower than the ones for which they appeared, thus evidencing a bistable character of these structures with respect to pumping.

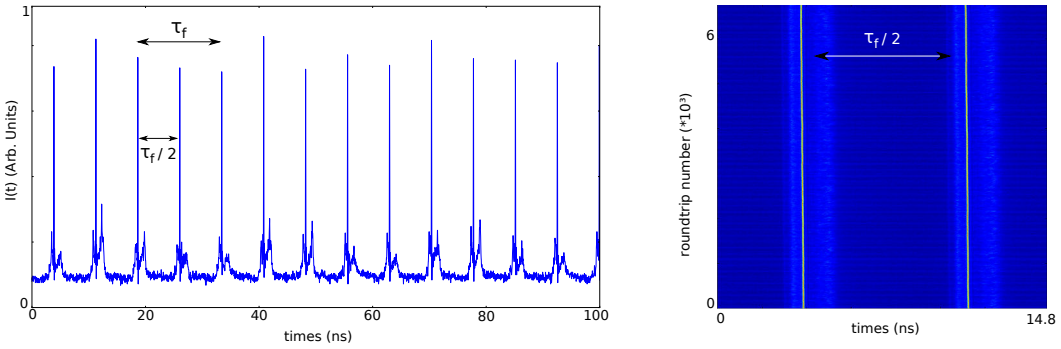

Figure 3.8: Writing the LS is possible even when τ_{mod} is $\tau_f/2$. I = 150 mA and τ_f = 14.8 ns. Left: temporal trace showing the LS pulses on top of maxima of gain. Right: space-time diagram representation.

Therefore with such an experiment, we demonstrated the possibilty to write our LS in a most simple and practical way. Indeed, to each LS writing and erasing events corresponds a value of modulation amplitude, providing that the modulation frequency is fixed to the FSR of the external cavity. This resonant condition is in fact crucial as it seems to trigger the apparition of the first LS by destabilizing the homogeneous background solution. Then the more gain is brought by increasing the modulation amplitude, the more LS can coexist. This interpretation is confirmed by the result shown in Fig. 3.8. Here the modulation frequency is twice the FSR of the external cavity. We see that a LS appears on every maximum of gain in the cavity. To obtain this regime, the amplitude of the modulation has to be about -10 dBm, which is larger than in panel f) of Fig. 3.7. The DC current value is still 150 mA. When a pulse is emitted, the space-time diagram clearly evidences that it takes about one nanosecond for the gain to fully recover. As the frequency of the sine modulation is increased, the gain window for which the emergence of a LS can occur gets narrower. Both facts may explain why we were not able to observe multiple LS on each modulation maximum.

It is important to point out that for the results of Figs. 3.7-3.8, once the modulation is switched off, the structures do not survive in the cavity as it is the modulation of the gain that sustains their existence. Indeed, as the pumping current was fixed

to 150 mA the laser without modulation is not able to support the existence of a LS. In order to allow the LS to remain once modulation is cancelled, we may set the pumping current value very close to the threshold for the bifurcation diagram depicted in fig 3.2e), e.g. 215 mA.

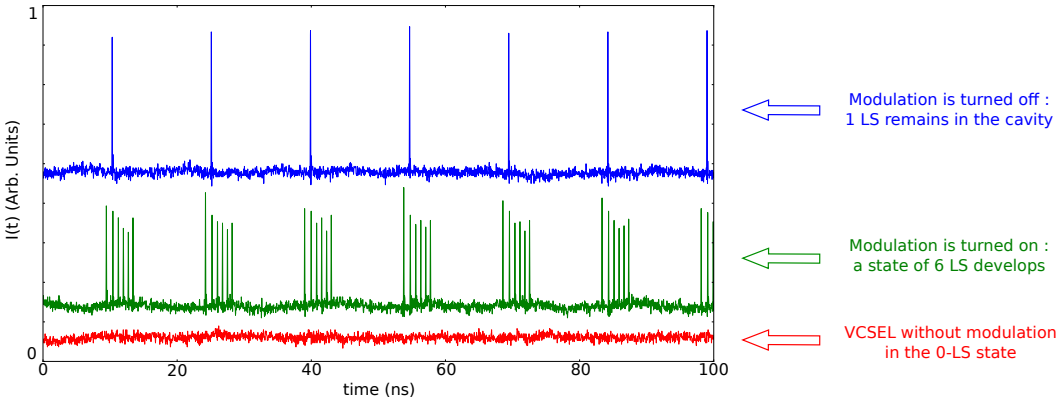

Figure 3.9: Time traces showing the experimental process for LS generation via current modulation. First the laser is in the 0-LS state without modulation (red), J = 215 mA. Second, modulation is applied with -30 dBm amplitude, 6 LS suddenly arise on top of the modulation (green). When we switch-off current modulation, only 1 LS remains in the cavity.

In this pumping current condition, our system is able to sustain the existence of only 1 or 0 LS in the cavity. As one can remark from Fig. 3.2e), the range of current for which this bistability is true is tiny, almost inexistent (about 0.1 mA) and the system may spontaneously become multi-stable with the 2,3,4,5 and 6-LS states. The experimental process is summarized in Fig. 3.9. First, the laser without modulation is set to the 0-LS state (red trace). We then apply our current modulation at resonance with the external feedback cavity. The amplitude is set as low as possible in order to induce the minimal effect onto the laser dynamics. Here the value is -30 dBm, which corresponds to a current modulation of about 20 mA. The green trace shows the emergence of a 6-LS state once the modulation is applied. This dynamics persists as long as modulation is acting. Once this last is removed, we are left with only 1 LS in the cavity that perpetually propagates. We point out that this operation has been repeated many times and always gave the same result.

The results presented so far revealed the possibility to use current modulation as a mechanism allowing to write temporal LS in the cavity when the DC current is below the LS regime threshold. Now let us see if we can make the LS drift via gain modulation when placing the DC current value above that threshold.

An example of the effects induced by pumping current modulation in this case is given in Fig. 3.10. We first set the system so as to leave only two LS in the external cavity when modulation is off (τ_f = 14.8 ns). To do so, we progressively decrease the pumping current from a situation where more than 2 LS coexist, as

shown in Fig 3.2e), to a value of 220 mA. Blue trace shows that the two LS coexist with a temporal interval of about 4.15 ns between the first and the second LS in the temporal trace. We then apply a sinusoidal current modulation with a frequency matching perfectly the free spectral range of the external cavity and an amplitude of -25 dBm (about 50 mA). We end up with the signal shown in green, where the two pulses are closer to each other (2.80 ns interval). We willingly superposed the first pulse to the blue one in order to compare the distances between LS in each pair. The migration of the right pulse is attributed to the need for the pulse to drift towards larger gain zones in time. Besides, the amplitude of the right green pulse has increased compared to the right blue one since it experiences more gain. In order to confirm that behaviour, the modulation amplitude is further increased to -23 dBm. The corresponding time trace appears in red, the right peak is now on top of the modulation and the temporal separation is only 1.76 ns. We remark that the amplitude of the right peak has not varied between the two last conditions. However its position change in the cavity is noticeable; we therefore attribute that to a drift of the LS provoked by the gain gradient imposed via current modulation. Noteworthy, for any given modulation amplitude value, the time inteval between the two LS remains constant as the number of round-trip goes (the LS trajectories remain parallel in a space-time representation). This would not be the case if the gradient imposed by our modulation were the only force acting on our LS. We are thus in presence of a repelling force as well that stabilizes the LS position. A careful look at the post-pulse dynamics reveals that gain logically experiences depletion for a time of about 1 ns. This effect imposes a minimal delay between two consecutive LS and depending on the gradient strength, it may more or less counteract the drift of the pulse generated by the gain gradient. This might be why the two LS get closer when the modulation amplitude gets larger.

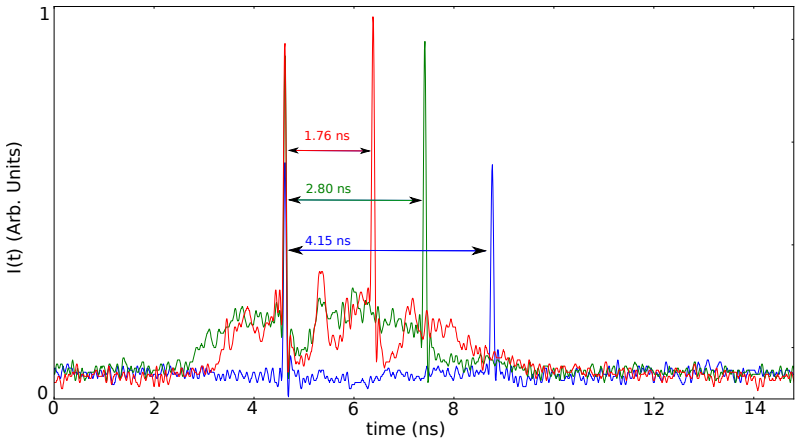

Figure 3.10: Temporal traces showing two LS coexisting in the external cavity. The trace goes from 0 to 14.8 ns, which is the round-trip time in the external cavity. This graph shows the dynamics when no current modulation is applied (blue trace). A small modulation (-25 dBm) tends to confine the two LS on top of the gain peak, which decreases their time separation (green). This effect is enhanced as modulation is increased to -23 dBm (red).

Another example of the effect of an electrical modulation resonant with the external cavity is given in Fig. 3.11. Here J = 250 mA and the cavity round-trip time is 14.8 ns. In this pumping current condition the maximum number of LS one can obtain in the cavity is 12, as shown in Fig. 3.2e). We start from a dynamics with 12 LS equally separated in the external cavity when no modulation is applied (not shown). When a weak modulation is turned on (-31 dBm), we see in Fig. 3.11a) that the LS get confined in the region where current is larger. Temporal intervals between the peaks are not fixed to any value and the LS have kept the same intensity before and after modulation is triggered. When modulation amplitude is increased (-17 dBm), three phenomena take place (panel b)): first the LS are further confined, the minimum time interval is about 250 ps. Second, additionnal LS spontaneously emerge on top of the modulation, here LS number has raised up to 19. Third, all LS amplitudes have increased to about the same value. Here the minimal distance between LS does not seem to be limited by the gain recovery after the pulse. We may envisage that the pumping current being larger than in the situation described in fig. 3.10, a LS can be triggered before the gain has fully recovered.

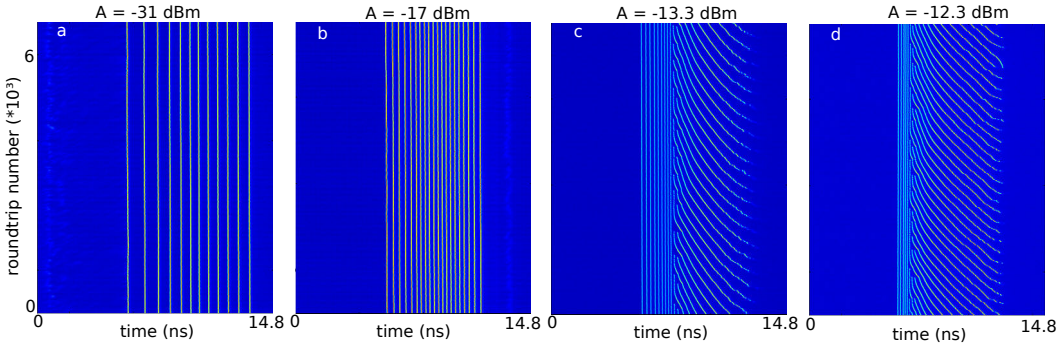

Figure 3.11: Effects of current modulation as modulation amplitude A is increased, starting from a dynamics consisting of 12 coexisting LS with equal temporal separations when the modulation is off. I = 250 mA, τ_f = 14.8 ns, $\nu_{mod} = 1/\tau_f$. See the text for a complete description of each panel.

Panels c) and d) illustrate an unexpected and interesting phenomenon. When we set modulation amplitude to an even larger value (-13.3 dBm), the dynamics of our LS becomes more complicated. In c), part of the LS (9) are localized on the front edge of the modulation and keep a constant position in the cavity. The confinement is such that the minimum temporal separation is now 150 ps. The rest of the LS are born on the opposite edge of the modulation, at about 12.5 ns. Once created, they undergo a drift towards the modulation peak and LS amplitude increases. The maximum speed LS reach is about 70 μm/ns. As they get closer to the fixed pack of LS they progressively slow down and their amplitude decreases until they stop next to the right-most LS in the pack. They stabilize for a few hundreds of round-trips and are generally killed by the one arriving just after. What is striking in this regime is the periodicity in the formation of the LS, in fact they are born every 315 round-trips (4.6 μs). When the modulation amplitude is

increased again (-12.3 dBm), panel d) shows that the LS dynamics is qualitatively the same, except that the left pack confinement is larger (the minimum time interval between two LS is about 100 ps) and the birth period of LS on the right is now 260 round-trips (3.8 μs). We therefore report a spontaneous formation of a periodic flow of temporal LS induced by an interplay between our cavity resonant gain gradient and conditions for the appearence of a LS in the cavity. Such a phenomenon has already been observed in the context of spatial cavity solitons [Caboche 2009], where a periodic flow of CS emerged from the interplay between a constant gradient in the holding beam phase and hosting VCSEL surface defects. Via an experimental and numerical analysis, they showed that the switching period T of a spatial CS is strongly influenced by the value of the bias current J. In fact, as J was approaching a critical lower value, they observed a divergence of T, which was interpreted as a critical slowing down in a bistable system [Mitschke 1989]. In our case, the system shows quite similar behaviour since the switching time of LS is increased as A is decreased. However more experimental analysis and a numerical study are to be carried out in order to shed some light on the complex effects of gain modulation in the onset of that regime.

We thus disclosed for the first time a drift of temporal LS induced by a modulation of the gain amplitude in resonance with the external cavity. The mechanisms at the origin of this drift are not very well understood. In comparison with what has been observed for spatial CS motion [Pedaci 2008a], the LS seem attracted by the maximum gain region in the cavity. Their speed then decreases and they finally stabilize in a region where gain is just enough for them to survive in the cavity. It seems to occur on the front edge of the gain modulation. When the amplitude of the modulation is weaker (panels a) and b)) the effect is simply to confine static LS. Once a steady-state with fixed LS in the cavity is reached, the system can persist in this regime as long as no parameter is modified.

To conclude this section, modulation can be used as a temporary perturbation for the creation of temporal laser LS. We also proved that current modulation induces a drift of LS in some specific experimental conditions. Some further investigations may be led on the influence of modulation frequency and modulation phase on the LS dynamics. The use of a sinusoidal function is for us the simplest way to demonstrate that LS can be written via an external perturbation. A full addressability (writing and erasure) of LS via electrical perturbation of the gain seems very hard to achieve due to the high multi-stability of our system versus parameters value. It would require the injection in our VCSEL of electrical pulses of the order of ten picoseconds, which we cannot realize with material in our possession. The addressing property may only be provided with a local optical perturbation.

3.3 Theoretical analysis

3.3.1 The model

We describe the PML laser using the generic delay differential equation model of [Vladimirov 2005] which generalizes Haus' model as it encompasses both the pulsating and the steady regimes. Denoting by A the amplitude of the optical field, G the gain, and Q the saturable absorber losses, the model reads :

$$\frac{\dot{A}}{\gamma} = \sqrt{\kappa}\exp\left[\frac{(1-i\alpha)\,G_\tau - (1-i\beta)\,Q_\tau}{2}\right]A_\tau - A, \tag{3.1}$$

$$\dot{G} = g_0 - \Gamma G - e^{-Q}\left(e^{G}-1\right)|A|^2, \tag{3.2}$$

$$\dot{Q} = q_0 - Q - s\left(1-e^{-Q}\right)|A|^2, \tag{3.3}$$

where time has been renormalized to the SA recovery time, α and β are the linewidth enhancement factors of the gain and absorber sections respectively, κ is the fraction of the power remaining in the cavity after each round-trip, g_0 is the pumping rate, Γ is the gain recovery rate, q_0 is the value of the unsaturated losses which determines the modulation depth of the SA, s is the ratio of the saturation energy of the SA and of the gain sections and γ is the bandwidth of the spectral filter. In Eq. 3.1 the subscript τ denotes a delayed value of the variable, $x_\tau = x(t\text{-}\tau)$. This delay renders the dynamical system infinitely-dimensional and it describes the spatial boundary conditions of a cavity closing onto itself. As such it governs the fundamental repetition rate of the PML laser. We use standard parameter values : $\kappa = 0.8$, s = 3, q_0=0.3, Γ^{-1}= 25 and γ=10. Importantly we stress that the dynamical scenario presented in this manuscript is mostly independent of the phase-amplitude couplings. Hence we choose $\alpha = \beta = 0$ for the sake of simplicity. The lasing threshold is determined by the pump level g_0 for which the off solution (A,G,Q)=(0,$\Gamma^{-1}g_0$,q_0) becomes linearly unstable; in our case it is given by g_{th}=ΓG_{th}=$\Gamma(q_0\text{-}\log(\kappa))$. Above threshold, $g_0 > g_{th}$, a stable continuous wave (c.w.) solution bifurcates from the off state, but rapidly becomes unstable as g_0 is further increased. At that point, a pulsing solution emerges from it leading to PML through an Andronov-Hopf bifurcation.

3.3.2 From PML pulses to temporal LS: dynamical scenario

The common settings for achieving PML in semiconductor lasers usually consider a SA with a relatively large modulation depth ($q_0 \approx 0.3$) and a cavity round-trip shorter than the gain recovery time $\tau \ll \Gamma^{-1}$. With these two conditions, the fundamental PML solution appears above the solitary laser threshold and exhibits a single pulse per round-trip. As the pump or the cavity length is increased, the so-called regime of harmonic mode-locking develops at the expense of the fundamental PML solution, as shown in Fig. 3.12a,b).

Such transition can be understood via the background stability criterion. Harmonic mode-locking appears when this condition is not verified anymore for the

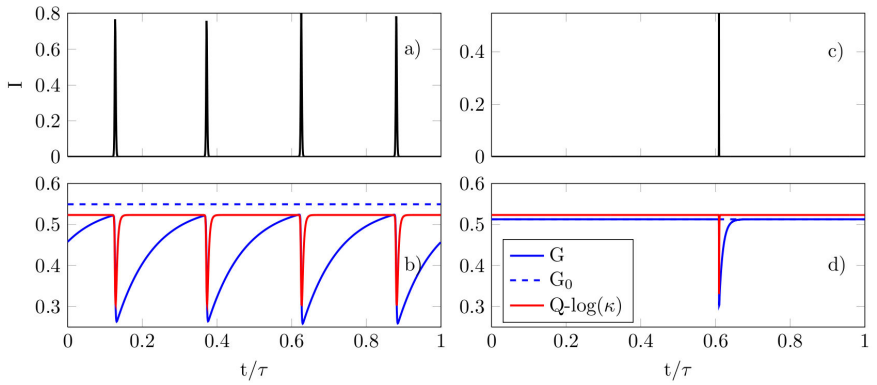

Figure 3.12: Intensity of the field (a,c), gain and total losses (b,d). For short delay $\tau = 10\Gamma^{-1}$ and $G_0 = 1.1G_{th}$ (a,b) the intensity and the absorption (I,Q) reach an equilibrium between pulses but not the gain that remains far from the equilibrium value G_0. For $\tau = 100\Gamma^{-1}$ and $G_0 = 0.98G_{th}$ (c,d) all the variables reach equilibrium and the solution becomes localized.

fundamental regime. The increases of the pumping current or of the cavity length lead to an increasing number of pulses N_h in a single round-trip, such that the new-found value of N_h becomes again compatible with the background stability criterion. In Fig. 3.12a-b), $N_h = 4$. One notices in Fig. 3.12b) that the gain (blue line) that tends to G_0 (dotted line) never surpasses the losses (red line). It is useful to stress that, for a given value of pumping current and τ, only one of these harmonic PML solutions is usually stable [New 1974, Vladimirov 2005] notwithstanding a small region of bistability between operation at harmonic number N_h and N_h+1.

The scenario described above radically changes for a long cavity, still choosing a SA with a strong modulation depth.

We analyzed in Fig. 3.13 the PML bifurcation scenario with DDEBIFTool [Engelborghs 2001]. For a relatively short cavity, see Fig. 3.13a), fundamental PML still occurs as a supercritical Andronov-Hopf bifurcation on the dominant c.w. lasing mode and PML exists only above its bifurcation point up to a pump level where it becomes unstable against the harmonic PML solution $N_h = 2$ (not shown). Yet, for longer cavities, see Fig. 3.13b), the Andronov-Hopf bifurcation that originates the PML state becomes subcritical, hence the PML solution may exist below its bifurcation point, where it coexists with the c.w. solution. For even longer cavities, the breadth of the folded fundamental PML solution may very well extend below the lasing threshold, where it coexists with the off solution, see Fig. 3.13c). Interestingly, during this folding phenomenon the fundamental PML branch eventually disconnects from the c.w. solution. It entails that PML appears for long delays as a saddle-node bifurcation of limit cycles instead of a nascent Andronov-Hopf bifurcation of the c.w. solution making this scenario out of the reach of any weakly nonlinear analysis. The change in dynamical scenario that occurs in Fig. 3.13c) has a profound consequence on the mode-locked solutions, as it can be seen in Fig. 3.12c-d): the fundamental PML solution becomes stable even in the limit $\Gamma\tau \gg 1$ and the

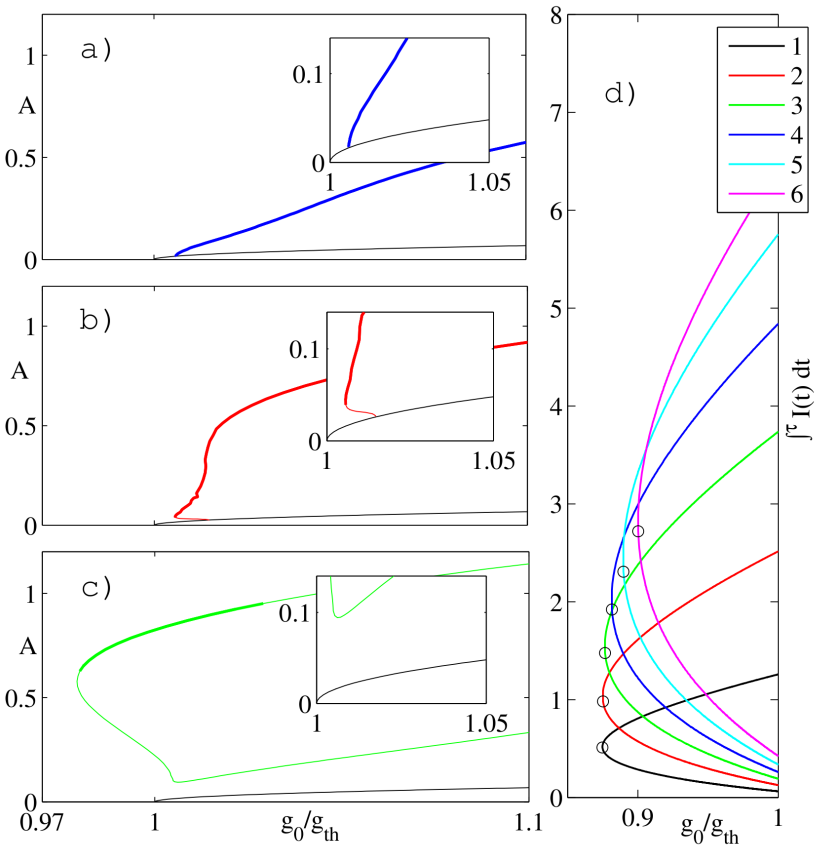

Figure 3.13: Panels (a-c) depict the bifurcation scenario as a function of the gain for different values of the delay: a) τ=1.2Γ^{-1}, b) τ=2Γ^{-1} and c) τ=4Γ^{-1}. For short delays, the PML periodic solution (in colors) appears as a supercritical Andronov- Hopf bifurcation of the dominant c.w. mode (thin black line). The stability of the PML solution is indicated by thick lines while the stability of the c.w. mode is omitted. Panel d) shows, for τ=16Γ^{-1}, the folding of the several PML solutions having a different number of equally separated pulses per round-trip while the folding point g_{sn} is represented by a circle.

pulse, whose duration becomes dominated by the gain recovery time ($\tau_p \approx 3\Gamma^{-1}$), becomes temporally localized in the same limit. Moreover, a very large number of pulsing solutions with different number of pulses per round-trip and different arrangements become stable for the same parameter values.

We reconstructed analytically some of these solutions using New's approximation [New 1974] for $\tau = 16\Gamma^{-1}$ and restricting our analysis to equally spaced pulses solutions, see Fig. 3.13d). Clearly, all these branches of solutions extend well below the laser threshold, where they stably coexist among them and with the off solution, although New's approximation of neglecting spectral filtering leads to an overestimation of the breadth of the PML region below threshold. We calculated the expression of the folding point g_{sn} shown in Fig. 3.13d). Such expression, in the long delay limit $\Gamma\tau \gg 1$ and for large saturation s $\gg$ 1, reads

$$\frac{g_{sn}}{g_{th}} = \frac{\kappa - 1}{\kappa(q_0 - log(\kappa))} W_{-1}[-exp(\frac{q_0\kappa}{s(\kappa - 1)} - 1)], \tag{3.4}$$

with $W_k(z)$ the Lambert function. When $g_{sn}/g_{th} < 1$, PML becomes stable below the unsaturated laser threshold, and the region of coexistence between the off and the PML solutions increases when q_0 and s increase and/or in the good cavity limit $\kappa \longrightarrow 1$, for which we simply have $g_{sn} = g_{th}/s$. Here, for the parameters in Fig. 3.13d) one finds $g_{sn} = 0.89 g_{th}$; in good agreement with the value calculated numerically (shown in Fig. 3.13d)).

The multi-stability evidenced by Fig. 3.13d) suggests, in analogy to spatial LS [Coullet 2000a, Coullet 2004a], that the harmonic mode-locked solution of maximal order that exists below threshold becomes fully decomposable, since essentially any pulse of this solution can be set on or off. We give evidence of this property by imposing an arbitrary sequence of pulses within the laser cavity and examining the stability of the resulting configuration. The addressing is realized by setting the system on the off solution and sending short light pulses inside the resonator. Following the tradition of [Leo 2010], the bit sequence corresponds, in our case, to the letters "UIB-INLN" encoded over bytes of five bits. Each pulse optically injected triggers the emission of a lasing LS, whose shape stabilizes after a short transient. A single localized pulse is not affected by a neighbor one, provided that their time separation is suffciently large, i.e. $\Delta_p \gtrapprox \tau_p$. As can be seen in Fig. 3.14, the sequence remains stable, and the device acts as an all-optical buffer with a bit rate limited by the size of the LS, i.e. approximately 1 Gb/s for typical semiconductor parameters. Erasing and writing the bits can in principle be done incoherently via cross-gain modulation in the gain and the SA sections, respectively, but this necessitates a more complex dynamical model like e.g. [Javaloyes 2010, Javaloyes 2011] and will be the topic of further studies.

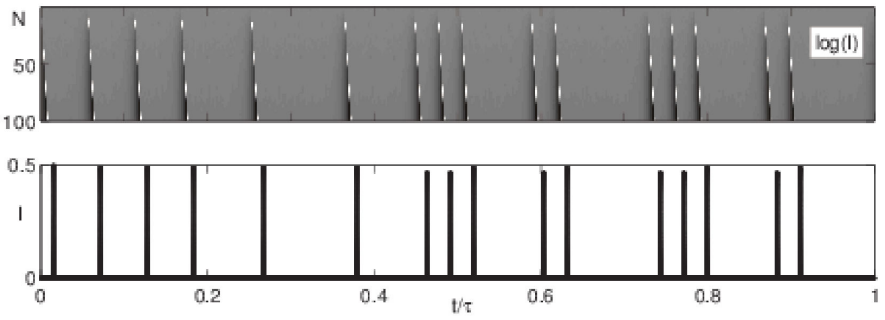

Figure 3.14: Evolution over N = 100 round-trips of a bit pattern written optically by injecting 1 ps pulses in the cavity (top) and detail over a single period (bottom). Parameters as in Fig. 3.12 with $\tau = 200\Gamma^{-1}$. The bit sequence is 10101010010001001110011000111001100.

3.4 Conclusions

We have shown theoretically and experimentally that a PML laser with large temporal aspect-ratio, i.e. having a cavity round-trip much larger than the other system time scales, can display multi-stability among the off solution and a large ensemble of different pulsing solutions. In such conditions, each pulse can be independently addressed, which allows to interpret them as lasing temporal LS.

Our observations generalize to lasing systems the all-optical buffer based on temporal CS in an injected Kerr fiber resonator [Leo 2010, Herr 2014]. Systems based on lasing LS have the advantage of avoiding the use of an injection beam and bypassing the associated tuning problems. Besides, the phase invariance of our system opens the way to exploit the phase degree of freedom for additional encoding of information. In terms of applications, semiconductor devices as support of phase invariant all-optical buffers are very attractive allowing for fast time scale and scalability. Exploiting lasing LS in an arbitrarily long cavity results in laser pulses at an arbitrarily low repetition rate, with a reconfigurable pulse pattern, which may be very useful for applications that necessitate pulses on demand like e.g. broadband spectroscopy, telecommunications and astronomy.

Our system consisting of a broad-area VCSEL coupled to a RSAM via a Fourier transform long external cavity imaging configuration is therefore a tilted waves temporal localized structures generator. All the spatial properties of our PML regime described in chapter 2 such as wave vector selectivity with RSAM impurities or wavelength tuning hold with the long cavity setup. We could therefore generate multiple trains of temporally localized laser light with frequencies spanning over 4 nm, which is of great potential for optical telecommunications applications.

Chapter 4

Square-wave switching and vectorial localized structures in a small-area VCSEL with delays

Contents

4.1 Introduction . . . 82
4.2 Our solitary VCSEL properties . . . 83
4.2.1 Experimental characterization . . . 83
4.2.2 Nonvolatile polarization control of the bistable VCSEL . . . 85
4.2.3 Polarization stability diagram . . . 89
4.3 Robust square-wave polarization switching . . . 90
4.3.1 The setup . . . 91
4.3.2 Experimental results . . . 93
4.3.3 Numerical investigation . . . 98
4.3.3.1 The model . . . 98
4.3.3.2 Numerical results . . . 98
4.3.3.3 Asymmetric sensitivity to feedback . . . 102
4.3.4 Conclusions . . . 103
4.4 Vectorial localized structures . . . 104
4.4.1 Experimental results . . . 104
4.4.1.1 Experimental evidences of vectorial localized structures formation . . . 104
4.4.1.2 Influences of delays in the molecules formation . . . 110
4.4.2 Theoretical analysis . . . 115
4.4.2.1 Vectorial localized structures and molecules . . . 116
4.4.2.2 Vectorial localized structures as polarization kinks and antikinks . . . 120
4.5 Conclusions . . . 123

4.1 Introduction

In this chapter, we will study how we can generate and control polarization dynamics with a transverse and longitudinal monomode VCSEL submitted to Crossed-Polarization Reinjection (XPR) and Polarization-Selective Feedback (PSF).

Firstly we will perform the complete experimental characterization of our solitary device in terms of optical spectrum, polarized L/J-curve and frequency shift versus pumping current. Thanks to the SPM model and the characteristics of our device, we will depict the polarization stability diagram over the whole current range accessible. We will also report the first experimental evidence of nonvolatile all-optical memory operation using the two linear polarization states emitted from our VCSEL. The two polarization states coexist in a large range of pumping currents and substrate temperatures, and they can be controlled all-optically by exposing the device to PSF, to XPR or by injection from an external laser. The active polarization state is recovered after powering off and on the VCSEL, while memory is lost if the substrate temperature is varied. The time scales of such induced polarization switchings are of the order of the second and we believe that they are induced by temperature dependent mechanical stress in the device.

Secondly, we will show that the combined effects of PSF and XPR can lead to a robust square-wave (SW) polarization switching whose period is determined by twice the XPR delay. We will study the dynamics theoretically and experimentally and show that the application of PSF induces an effective dichroism in the VCSEL, while XPR induces polarization switching. We also show that the PSF is more effective when acting on the slow polarization mode, which can be traced to the asymmetry of the bistable region of the low dichroism VCSEL.

Finally, when the PSF delay is set much longer than the laser internal time scales the nonlinear polarization dynamics can lead to the formation of short antiphase pulses in the polarized output of the VCSEL. Thanks to a detailed analysis of the dynamics, we demonstrate that these vectorial pulses are temporal LS that regenerate every PSF round-trip. This property makes possible the formation of LS molecules and complexes whose formation and interaction depend on the delays. This dynamics is well reproduced theoretically via the SFM model modified so as to incorporate PSF and XPR effects. We show that this model can be reduced to a dynamical model composed of two phases : the orientation phase of the quasi-linear polarization and the optical phase of the field. In this framework our Vectorial LS arise as polarization orientation kinks and antikinks.

I forcefully stress that the regimes of robust SW swicthing and vectorial LS have been obtained with the VCSEL showing polarization memory, and also with a VCSEL without memory effect. However this second device developed a transverse multimode operation (Laguerre-Gaussian TEM 01) when the current exceeded J = 6*J_{th}, which rendered our study more difficult. Thus we focused on the monomode transverse device with memory since the time scale for this effect (about the second) has nothing in common with the physical effects at the origin of the SW and the fast polarization flips dynamics that are of the order of tens of picoseconds.

4.2 Our solitary VCSEL properties

4.2.1 Experimental characterization

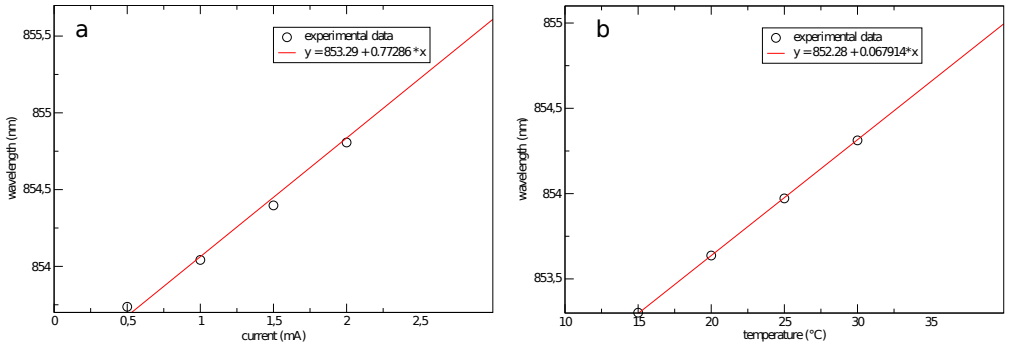

Figure 4.1: a) Wavelength as a function of the pumping current. b) Wavelength as a function of the substrate temperature. Circles represent the experimental data. The red trace is the linear regression.

Our VCSEL is an oxide-confined GaAs device fabricated by ULM-photonics and lasing at 850 nm. It is a single transverse mode device with a suppression ratio larger than 10 dB in the current region between 0 and 3 mA. The VCSEL is powered by a current driver having an accuracy of 1 μA while its substrate temperature is stabilized by using a thermo-controlled laser mount (up to 1 m°C). We have measured the wavelength drift of the laser emission as a function of the injection current J and of the temperature substrate T (see Fig. 4.1). We have obtained a linear dependence of λ as a function of T which allows to infer that $\frac{\partial\lambda}{\partial T} = 28GHz/°C$ (Fig. 4.1b). Concerning the dependence of λ as a function of J we can comfortably approximate it to a linear dependence in the range 0.5 mA $<$ J $<$ 3 mA where $\frac{\partial\lambda}{\partial J} = 320GHz/mA$ (Fig. 4.1a). These coefficients allow to estimate that the variation of the refractive index in the active medium is varied of the same quantity either by a current increase of 0.9 mA or a T increase of 30 °C. We have also remarked that, when adjusting T, the beam emission is stirred horizontally of 4.10^{-3} degrees and vertically of 8.10^{-4} for T varying from 15 °C to 45 °C.

In Fig. 4.2, we show the polarization resolved L/J curves of the VCSEL output for different substrate temperatures. At T = 40°C, in the neighborhood of threshold, two linear and orthogonal polarizations are active but one (that we call LP-X) takes over rapidly and it is stable in the entire current range explored. When T is decreased, it appears that the VCSEL starts to lase at threshold on a single polarization (that we call LP-Y) orthogonal to LP-X. Besides, for some value of current depending on T, we observe a polarization switching to LP-X. For T = 25°C this switch occurs at J = 1.1 mA and, as T is decreased, it occurs at higher current values until, for T lower than 20°C, it disappears and the VCSEL emits on LP-Y in the whole range of scanned J. T is then increased upward and this situation, where LP-Y dominates for the entire range of current explored, is maintained till the highest value of T available in our setup (40°C). We note that the situation

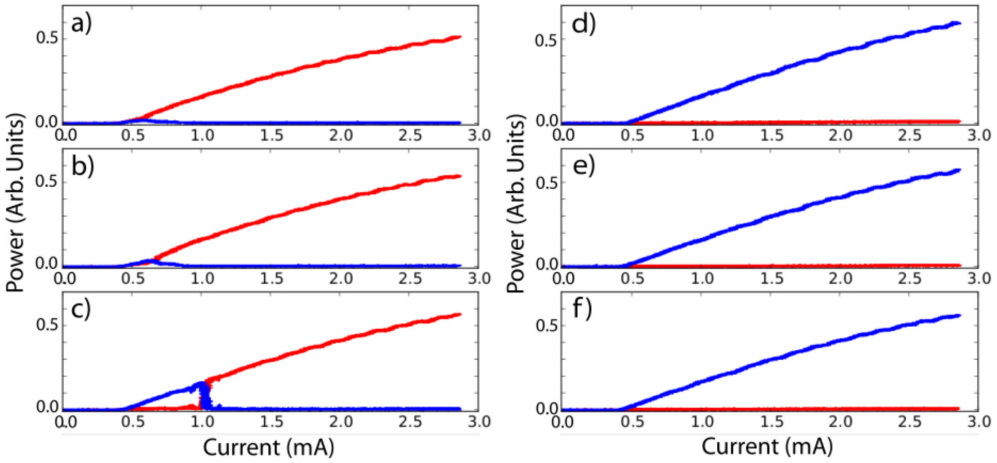

Figure 4.2: Polarization resolved L/J curves versus T (red trace LP-X, blue trace LP-Y). a) T = 40°C and then T is decreased to T = 30°C (b), T = 25°C (c) and to T = 15°C (d) then T is increased to T = 25°C (e) and T = 40°C (f).

of Fig. 4.2a) cannot be re-established by increasing T (in the limit of the values experimentally accessible). As we will show in the following results, this situation can be instead restored by a proper optical perturbation of the VCSEL. Fig. 4.2 shows that, for a large interval of currents and temperatures, LP-X and LP-Y coexist and, therefore, it should be possible to optically perturb the VCSEL to control its polarization emission. Spectral measurements reveal that LP-Y is 7.5 GHz blue detuned with respect to LP-X. We also notice that the two different situations observed in the polarization-resolved L/J curves for the same value of T (Figs. 4.2c) and 4.2e), for example) lead to the very same total (non polarization-resolved) L/J curve.

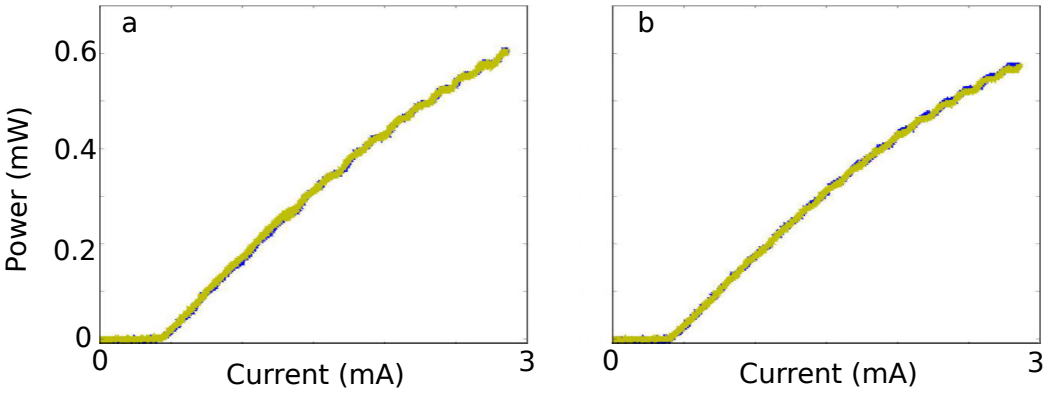

Figure 4.3: Light output versus pumping current for different substrate temperatures T and for different situations of the polarization resolved L/J curve. a) T = 25°C: the blue trace corresponds to the situation shown in Fig. 4.2c), the green trace corresponds to the situation shown in Fig. 4.2e). b) T = 40°C: the blue trace corresponds to the situation shown in Fig. 4.2a), the green trace corresponds to the situation shown in Fig. 4.2f).

The total L/J curve emission corresponding to two coexisting situations for the polarization resolved L/J curves (like the one shown in Fig. 4.2) are shown in Fig. 4.3. Both curves are superposed indicating that there is no difference in the total intensity output when passing from one dominant polarization to the other one. The curves described in Fig. 4.2 and 4.3 are obtained scanning the current of the VCSEL from 0 to 3 mA in 45 ms.

4.2.2 Nonvolatile polarization control of the bistable VCSEL

As shown in Fig. 4.4 , the VCSEL output is collimated and split by a polarization preserving beam splitter. One part of the output beam undergoes polarization splitting along its two orthogonal directions and is used for monitoring. The other part of the output is used for controlling the polarization state.

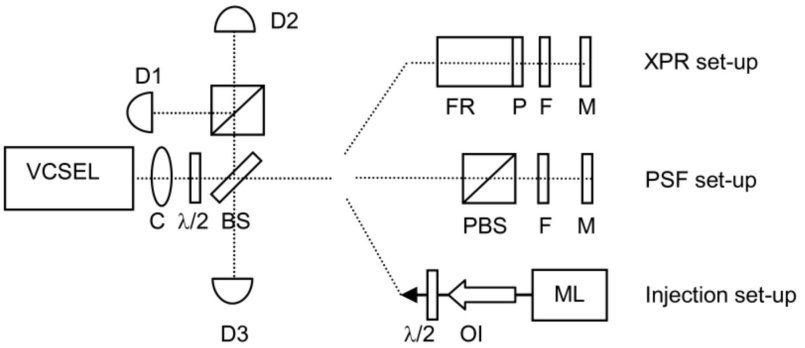

Figure 4.4: Experimental setup with the three different schemes used for controlling the polarization. C: collimator, $\lambda/2$: half-wave plate, D: Detector, BS: Polarization preserving beamsplitter, PBS: Polarizing beam splitter, FR: Faraday rotator, P: Polarizer, F: Variable neutral density filter, M: Mirror, OI: Optical Isolator, ML: Master Laser.

Control of the polarization state of our VCSEL has been achieved implementing three different methods. The first one is based on XPR, where only one polarization component (LP-X, say) is rotated into the orthogonal polarization direction (LP-Y) and then is injected back into the VCSEL. If LP-X is the active component, XPR depletes the carriers available for it and eventually it brings LP-X below threshold, thus favoring the activation of LP-Y. Since LP-Y does not experience XPR, and the VCSEL is in the bistable regime, a polarization switch occurs. The LP component used for XPR must be the active one and it can be selected by adjusting the wave-plate at the VCSEL output. In this way a switch from LP-X to LP-Y and vice versa can be obtained.

In Fig. 4.5 we show the polarization switching obtained by using this method. In panel a) LP-Y is initially active (the monitored polarization LP-X is off). We apply XPR for about 1.3 s and, when XPR is removed, the VCSEL has switched to the LP-X state. If the VCSEL is exposed to XPR for shorter times, it returns to emitting in the LP-Y state when XPR is removed. The XPR rate chosen is the minimal one able to induce a polarization switching but no significant reduction of

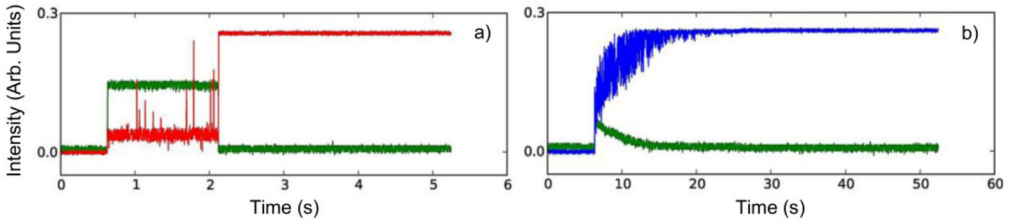

Figure 4.5: LP-X (red trace), LP-Y (blue trace) polarization intensities and XPR signal injected into the VCSEL (green trace), T = 30°C, J = 2.1mA, XPR rate = 2%.

the times required is observed when increasing this rate. In panel b) we show the situation where the VCSEL is emitting in the LP-X mode (the monitored LP-Y mode is off). Even in this case the minimal time of exposure to XPR inducing a switch is extremely long compared with semiconductor time scales. We also remark that the exposure to XPR induces polarization dynamics which are different if XPR is using the LP-Y or the LP-X component. In the first case (panel a)), XPR induces an almost stationary elliptical polarization state with sporadic upward intensity spikes. In the second case (panel b)), XPR induces a slow increase of the LP-Y intensity at the expense of the LP-X intensity (and thus of the XPR signal). This envelope contains fast dynamics whose amplitude decreases as the switching to a pure LP-Y emission is completed. Polarization emission control using XPR has been obtained in the whole bistable domain shown in the polarization-resolved L/J curve. Required XPR exposure times vary with J and T and their orders of magnitude span from 0.2 s to several seconds.

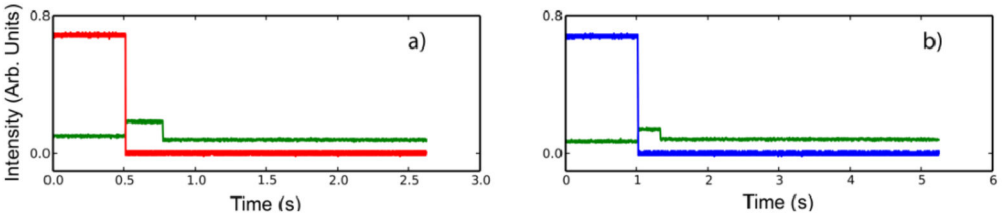

Figure 4.6: LP-X (red trace), LP-Y (blue trace) polarization intensities and PSF signal injected into the VCSEL (green trace), for clarity green trace is shifted vertically of 0.1 units. T = 30°C, J = 2.9mA.

Another method for controlling the polarization state is based on PSF. In this scheme an external cavity with a polarizing element admitting only the inactive LP mode is placed in front of the VCSEL. PSF selectively decreases the losses of this mode, thus effectively changing its dichroism and, above a critical rate, it leads to polarization switching. The control sequence of the polarization state by PSF is shown in Fig. 4.6. The PSF rate required is as low as 0.044% (for inducing polarization switching from LP-X to LP-Y, panel a)) and as low as 0.017% (for switching from LP-Y to LP-X, panel b)). Polarization switch occurs immediately after the PSF is applied and, at the same time, a feedback

signal (green trace) is detected. Nevertheless, in order to induce a permanent switch, i.e. surviving upon PSF removal, it is necessary to apply PSF for time windows of several hundreds of milliseconds. As for XPR, these times change depending on VCSEL current, but their order of magnitude is considerably larger than semiconductor time scales. Polarization emission control using PSF has been obtained in the whole bistable domain shown in the polarization resolved L/J curves.

The last method we used to control the polarization emission is based on external optical injection. This method has been already successfully implemented by the Kawaguchi group [Sakaguchi 2010, Katayama 2011] and it consists of addressing the inactive LP mode by injecting a coherent electromagnetic field linearly polarized with the same orientation as the addressed LP mode and tuned to the same frequency. This method allows us to control the polarization emission in the whole bistability range of the VCSEL with very small injection intensities. On the other hand, as for the other methods implemented, we noticed that long exposure times to optical injection are required to induce a switching. The lowest injection levels required are obtained when the injected field is resonant with the addressed LP mode.

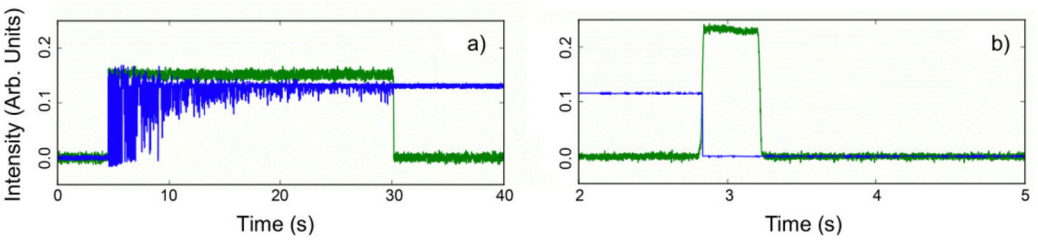

Figure 4.7: LP-Y polarization (blue trace) and injected external signal (green trace). In panel b) the green trace is magnified vertically of a factor of 30 with respect to panel a). J = 2.1 mA, T = 30°C.

This implies that, because of the birefringence, the injected field frequency must be adjusted for inducing switching from LP-X to LP-Y and vice versa. Fig. 4.7 has been obtained in these resonant conditions and the injected powers are of 80 nW for panel a), where we induce the switching from LP-X to LP-Y, and 4 nW for panel b) where we induce the switching from LP-Y to LP-X. In the first case a minimum injection time of 25 s is required, in the second case this time is less than 0.2 s. As in Fig. 4.5, we note that the switching from LP-X to LP-Y is accompanied by fast polarization dynamics, while the reverse switching occurs abruptly.

While performing polarization control experiments we realized that after powering off the VCSEL, it always recovered the last polarization state upon being powered on again. We performed systematic measurements to analyze this phenomenon. In Fig. 4.8 the VCSEL is periodically switched on and off by modulating J with a rectangular signal and we monitor the LP-X polarization. The

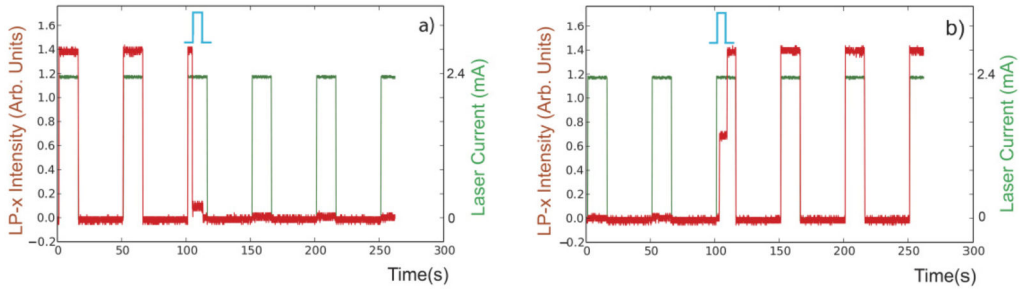

Figure 4.8: Laser driving current (green curve, right axis) and LP-X polarization intensity (red curve, left axis), T = 30°C, exposure to XPR is indicated by the blue pulse.

current modulation drives the laser periodically at J = 0 mA for 35 s and at J = 2.36 mA for 15s. As shown before, for T = 30 °C and J = 2.36 mA the VCSEL exhibits polarization bistability. In panel a), initially the VCSEL is emitting on the LP-X polarization and surprisingly this state is recovered whenever it switches on. During the third cycle, when the VCSEL is on, we apply PSF to induce a polarization switching to LP-Y. When PSF is removed, the VCSEL has switched to LP-Y (LP-X is now off) and thereafter the VCSEL recovers this polarization state whenever is switched off and on. In panel b) the VCSEL is initially emitting LP-Y mode (LP-X is off) whenever it switches on until, at the third cycle, we apply PSF in order to induce polarization switching to LP-X. Once XPR is removed, the VCSEL emits on LP-X and thereafter it recovers this polarization state after any current cycle.

We have performed other tests where the VCSEL was switched off (also with the electrical contact short-circuited) during several hours and still, when driving the VCSEL in the bistable current range, it recovered the polarization state which was active before being powered off. This result was conditioned to leaving the substrate temperature T stabilized at the same value during the entire experiment. If T is varied during the time the laser is off, the polarization memory is lost, thus indicating that some parameter depending on T is at the origin of this memory effect. This can also explain why bistability can be disclosed in the polarization resolved L/J curves by scanning T. It is worth pointing out that this parameter is not affected by active region temperature variations induced by variations of J via Joule heating.

Different mechanisms can influence polarization stability through T. It is well known that polarization dichroism depends on mechanical stress on the laser chip [Panajotov 2000]; it is possible that a change in T may induce some mechanical stress in the laser structure and that this stress has a hysteresis behavior versus T, thus explaining the result of Fig. 4.2 and the memory effect of the polarization state. This hypothesis is supported by the observation of an output beam steering in the VCSEL far-field of 0.004° horizontally and 0.0008° vertically when T is varied from 15°C to 45°C. This steering may be a consequence of the T-dependent mechanical stress in the laser structure. It is important to point out that beam steering was

not found when varying J and it was not observed in correspondence with a polarization switching. Whether of mechanical origin or not, the question of how this T-dependent mechanism might also be influenced by very weak optical perturbations is still unsolved. It is possible that optical perturbations activate the depressed polarization via the intracavity field and/or the semiconductor carrier with a fast time scale and that, if the addressed polarization is kept activated long enough, it may induce some change in the laser structure such as the one provoked by T. More work is to be carried out to clarify this point.

4.2.3 Polarization stability diagram

In order to theoretically study the polarization behaviour of our solitary VCSEL, we use the so-called Spin-Flip Model (SFM). It is important to stress that this model does not take into account the memory property described in the previous subsection due to its very slow time scale. This assumption is reinforced by the fact that temperature will be kept constant during the oncoming dynamical results.

Although the natural basis for the SFM is that of the circularly polarized components of the field, $E_{\pm} = (X \pm iY)/\sqrt{2}$, the simplest way to express the model is in terms of the linearly polarized components (X,Y). In this base, the model reads :

$$\dot{X} = (1+i\alpha)\left[(N-1)X + inY\right] - (\gamma_a + i\gamma_p)X, \tag{4.1}$$

$$\dot{Y} = (1+i\alpha)\left[(N-1)Y - inX\right] + (\gamma_a + i\gamma_p)Y, \tag{4.2}$$

$$T\dot{N} = \mu - N(1+|X|^2+|Y|^2) - in(X^*Y - XY^*), \tag{4.3}$$

$$T\dot{n} = -n(\gamma_s + |X|^2 + |Y|^2) - iN(X^*Y - XY^*), \tag{4.4}$$

where N(n) is the scaled total (difference of) carrier densities in the two spin channels. In equations (4.1-4.4), time has been scaled to the cavity decay rate κ, $T = \kappa/\gamma_e$ represents the scaled carrier lifetime and γ_s/T is decay rate of the spin-difference. The scaled density of carriers injected per unit time into the active region due to the bias current is μ. In addition, α stands for the linewidth enhancement factor [Henry 1982] and $\gamma_a(\gamma_p)$ describes the linear dichroism (birefringence) of the VCSEL cavity. Finally, we have added to the time evolution independent Langevin sources $\left(F_X(t), F_Y(t), F_{D_+}(t), F_{D_-}(t)\right)$, describing noise due to spontaneous emission and current fluctuations. The scaled spontaneous emission noise variance is $\xi \sim 10^{-4} - 10^{-3}$. We assume typical values $\alpha = 2$, $T = 150$ and $\gamma_s = 75$ which — taking $\kappa = 300\,\mathrm{ns}^{-1}$ — correspond to a carrier lifetime of 0.2 ns and a spin-difference decay time of 6.6 ps, respectively.

The polarization switchings in the SFM have been exhaustively analyzed in the literature [Martin-Regalado 1997c, Erneux 1999]; in this model, the VCSEL displays large ranges of bistability when dichroism and birefringence are small [Erneux 1999]. We choose $\gamma_p = +5.24\ 10^{-2}$, which means that we denote by LP-X the reddest mode. For this ensemble of parameters, the stability diagram of the solitary VCSEL as a function of the bias current and of the dichroism is depicted in Fig. 4.9.

For small $|\gamma_a|$, the range of bistability extends over large intervals of bias current. For instance, when $|\gamma_a| = 2.6.10^3$, the VCSEL is monostable on the blue polarization

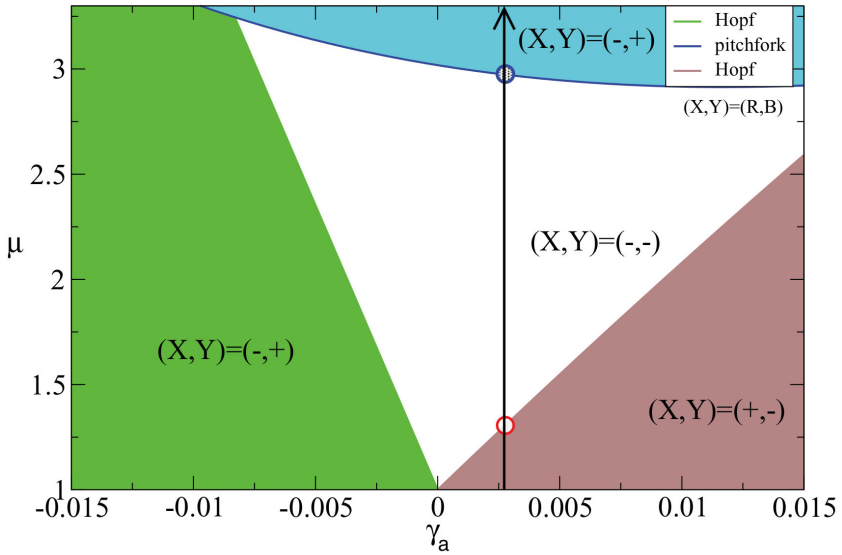

Figure 4.9: Stability diagram of the solitary VCSEL for $\gamma_p > 0$, i.e., the LP-Y mode being the bluest. Modal stability is indicated as (X,Y)=(a,b), where a negative value denotes stable and vice versa. The vertical line depicts a current scan in the bistability diagram. In the case shown (LP-Y mode selected at threshold), the red (blue) circle at low (high) value of μ represents the critical value of the current $\mu_h(\mu_\varepsilon)$, where the LP-X (LP-Y) mode gains (loses) stability via a subcritical Hopf (supercritical pitchfork) bifurcation; see [Mulet 2001] for details.

from $\mu_{th}^{Y} = 1 - \gamma_a$ to $\mu_h \approx 1.3$ and then bistable until $\mu_\varepsilon \approx 2.9$; similarly, for $\gamma_a =$ -2.6.10 $^{-3}$, the red polarization is only stable between $\mu_{th}^{X} = 1 + \gamma_a$ and $\mu_h \approx 1.7$ and then bistable until $\mu_\varepsilon \approx 3.1$. Note, however, that in practice this range can be reduced due to Joule heating as current is increased: the subsequent redshift of the gain curve relative to the mode spectrum favors the reddest mode [Choquette 1995]. Since we are mainly interested in analyzing the effects of PSF and XPR on the dynamics in the bistable regime, we disregard any changes in dichroism as current is varied.

4.3 Robust square-wave polarization switching

In this section, we propose an experimental scheme that allows one to generate square-wave signals from VCSELs with weak dichroism where XPR alone would not work. We show experimentally and theoretically that the application of PSF decreases the losses of the selected polarization, and can be seen as an external mechanism for controlling the effective dichroism in the device. As such, PSF can effectively bring the device into a monostable regime, hereby reinforcing the effectiveness of XPR for the generation of a very regular square-wave emission which turns out to be very robust versus parameter changes.

4.3.1 The setup

The setup used for the robust square-wave generation is described in Fig 4.10. The light emitted from a thermally stabilized VCSEL (±0.001 °C) driven with a low-noise current source (±1 μA) is collimated and sent to a 50:50 polarization-preserving beam splitter (BS) after passing through a half-wavelength waveplate ($\lambda/2$) that allows one to align the VCSEL polarization axes to the horizontal and vertical directions with respect to the optical table.

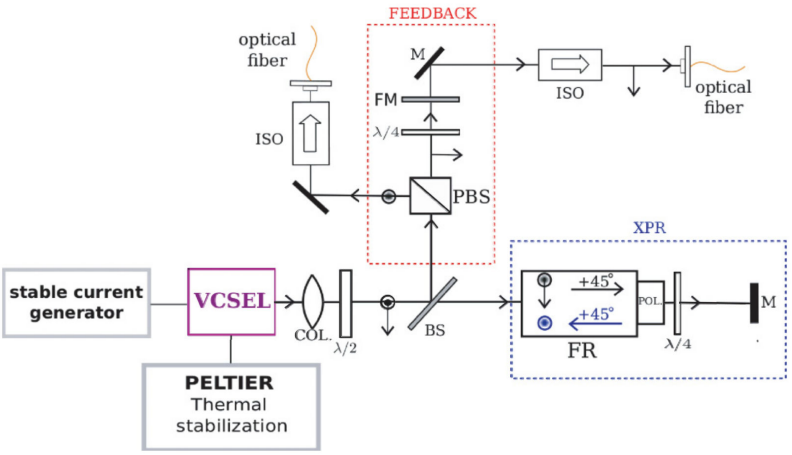

Figure 4.10: Experimental setup. COL: collimator. $\lambda/2$: half-wavelength waveplates. $\lambda/4$: quarter-wavelength waveplates. BS: polarization-preserving beam splitter. PBS: polarizing beam splitter. FR: faraday rotator. POL: polarizer. FM: feedback mirror. M: mirror. ISO: optical isolator.

The BS divides the beam in two, both having the same intensity. The beam deflected by the BS passes through a Glan-Taylor polarizing beam splitter (PBS) and a partially reflecting mirror (FM) which sends the beam back into the VCSEL, thus providing PSF. The PBS is set to transmit the polarization component parallel to the optical table while deflecting the orthogonal one. Thus the optical feedback circuit returns the same polarization after a delay $\tau_f = 2L_{PSF}/c$, L_{PSF} being the optical path length from the VCSEL to the feedback mirror. The XPR arm is realized by placing a 45° Faraday Rotator (FR) with an exit polarizer (i.e., an optical isolator where the input polarizer has been removed) on the path of the beam transmitted by the BS. Upon reflection on a mirror (M), only one of the LP components of the light is reinjected back into the VCSEL, after experiencing a 90° rotation of its polarization orientation. The FR axes with their exit polarizer are oriented such that the LP component that passes through the XPR circuit and which is rotated 90° before being reinjected into the VCSEL is the same selected by the PSF arm, i.e., the polarization component parallel to the optical table. The delay in the XPR circuit is given by $\tau_r = 2L_{XPR}/c$, L_{XPR} being the optical path length from the VCSEL to mirror M.

In order to quantify the maximum rates of PSF and XPR, we measure the fraction of the emitted power that is returned back to the VCSEL along the corresponding circuit somewhere between the $\lambda/2$ placed at the VCSEL output and the polarization preserving BS. These measurements are performed checking that the VCSEL is emitting in a single linear polarization; moreover, in order to avoid interactions of these returned beams with the VCSEL and thus altering the measurement of rates, the returned beams were slightly misaligned with respect to the optical axis. The maximum rates for XPR and PSF achievable in our setup are of 17% and of 5%, respectively. A quarter-wavelength waveplate ($\lambda/4$) placed before each of the mirrors used for closing the PSF and XPR circuits finally allows for independent fine-tuning of the PSF and XPR rates.

Polarization-resolved detection of the VCSEL emission is performed on the feedback circuit by monitoring both the beam transmitted through the semireflecting feedback mirror and the beam deflected by the Glan-Taylor PBS. We use two photodiode detectors (8 GHz bandwidth) connected to a 6 GHz digital scope and a 20 GHz power spectrum analyzer.

We have tested two VCSELs from ULM-photonics lasing at 850 nm (ULM.850-PMTNS46FOP). They are single mode with a suppression ratio larger than 10 dB at the rated power of 1 mW. Both devices exhibit a birifringence of 7.5 $\pm$ 0.5 GHz and both emit linearly polarized light. Their threshold is around 0.5 mA with the bluest polarization mode, that we call LP-Y, appearing at threshold. Both devices may exhibit a polarization switch at a current value J_{switch} depending on substrate temperature. In the first device, the one described in the previous section in details, $J_{switch} \approx 1.3$ mA at T = 20 °C; however, J_{switch} decreases as temperature is increased and, at T = 30 °C, it cannot be distinguished from the laser threshold. In the second device, J_{switch} is much closer to threshold at ambient temperature, and we need to cool down the device to less than T = 10 °C for clearly distinguishing a polarization switching.

Polarization bistability property of the first device is largely detailed in section 4.2.3. Nevertheless this bistability is "weak" since an external operation has to be applied to the device in order to induce a polarization switch, and this cannot happen spontaneously. In the second device, it is possible to induce the same switch from the two polarization states when applying PSF (or XPR) which also occurs abruptly when the PSF (or XPR) rate exceeds a given value; in this case, however, the VCSEL emission comes back to LP-X a short time after PSF (or XPR) is removed. Thus the two devices show weak bistable behavior over a large current range. Since both device have the same birefringence, the numerical polarization stability diagram in section 4.2.3 holds for both of them. All the dynamics investigated in the next sections were obtained with the memory device. In fact, it possesses the advantage of remaining single transverse mode over the whole range of pumping current accessible whereas the second device without memory effect displays a higher order transverse mode when biased too far from threshold.

4.3.2 Experimental results

We focus now on the dynamics obtained when the VCSEL is submitted to XPR and PSF. The results we show depend on the polarization component that is selected to pass through the feedback circuit and the Faraday Rotator.

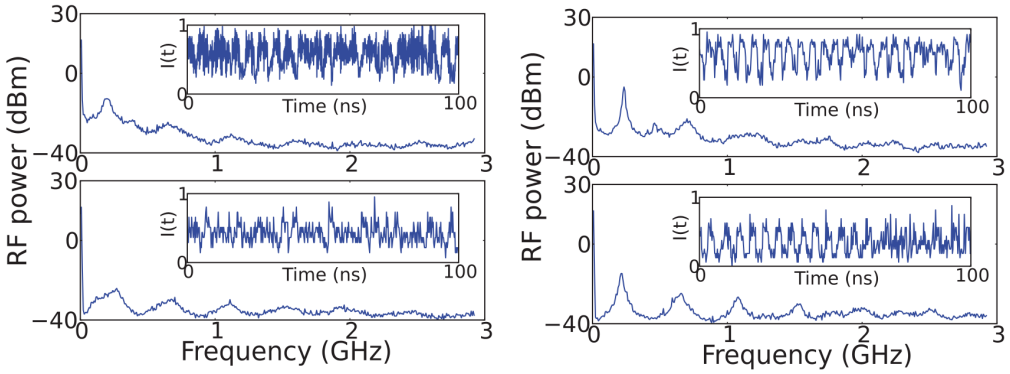

Figure 4.11: Upper panels: power spectra and corresponding time signals (inset) of the LP-Y output of the first device when J = 0.85 mA, T = 30 °C, and the VCSEL is submitted to XPR only (rate 17%) of the LP-Y component (left column) and both to XPR (rate 17%) and PSF (rate 0.15%) on LP-Y (right column). Lower panels: power spectra and corresponding time signals (inset) of the LP-Y output when J = 0.55 mA and the VCSEL is submitted to XPR only (rate 17%) of the LP-X component (left column) and both to XPR (rate 17%) and PSF (rate 0.15%) on LP-X (right column). In all cases, L_{XPR} = 33 cm and L_{PSF} = 58.8 cm.

The bistable character of the VCSEL under test does not allow one to obtain a square-wave signal in any configuration when only XPR is acting, as shown in the left column of Fig. 4.11 at T = 30°C. Let us consider the case of LP-Y selected by the XPR circuit (top panel). If VCSEL parameters are such that emission is on LP-Y, the power in LP-Y decreases (and that in LP-X component increases) almost linearly as the XPR rate is increased. When the XPR rate is raised above 0.5%, an abrupt increase of the LP-X component and an abrupt decrease in the LP-Y component are observed, but the VCSEL is emitting stationarily in a mixed polarization state. If the XPR is further increased, an instability appears in both polarization components, their dynamics being out of phase. At the highest achievable XPR rate, the power spectrum exhibits a first peak at $\nu = c/4L_{XPR} = (2\tau_r)^{-1}$ and only odd harmonics of this fundamental frequency are present, as previously observed in [Mulet 2007a]. Nevertheless, the peaks are broad and shallow, and indeed the regular square-wave emission observed in [Mulet 2007a] could not be observed in our VCSEL for any parameter set: the most regular situation is obtained for J = 0.85 mA, as shown in Fig. 4.11, upper panel. If we set XPR selecting LP-X and we set the XPR rate at the highest level, a power spectrum with odd harmonics of the fundamental frequency appears only for currents very close to laser threshold, J = 0.55 mA, but the time trace reveals a poor quality of the square waveform (Fig. 4.11, lower panel in left column).

Our VCSEL, then, does not produce good-quality square-wave signals by XPR only, which is not surprising considering its bistable behavior [Mulet 2007a]; in fact, as discussed in [Mulet 2007a], the bistability of the VCSEL is detrimental for the formation of a square-wave signal.

In order to improve the quality and robustness of the square-wave signals generated by the VCSEL, we provide PSF on the same polarization component that is allowed to pass through the XPR circuit. PSF is expected to change the effective dichroism between LP states, hereby breaking polarization bistability and helping the development of the square-wave oscillation. Indeed, we observe a qualitative improvement of the regularity of the signal in both cases, either selecting LP-Y (Fig. 4.11, right column, upper panel) or LP-X (Fig. 4.11, right column, lower panel). In order to explore the existence and robustness of a regular square-wave signal when using both XPR and PSF, we perform an analysis versus the system parameters.

The time behavior of LP-Y component when the VCSEL is submitted to both XPR and PSF selecting LP-X is shown in Fig. 4.12 for different rates of PSF. The length of the external cavity providing PSF is set to L_{PSF} = 98 cm and the length of the XPR circuit is set to L_{XPR} = 49 cm; thus the optical feedback delay corresponds to twice the delay for XPR. The rate of XPR is the maximum (17%), and when increasing the feedback level, we observe the sequence shown in Fig. 4.12.

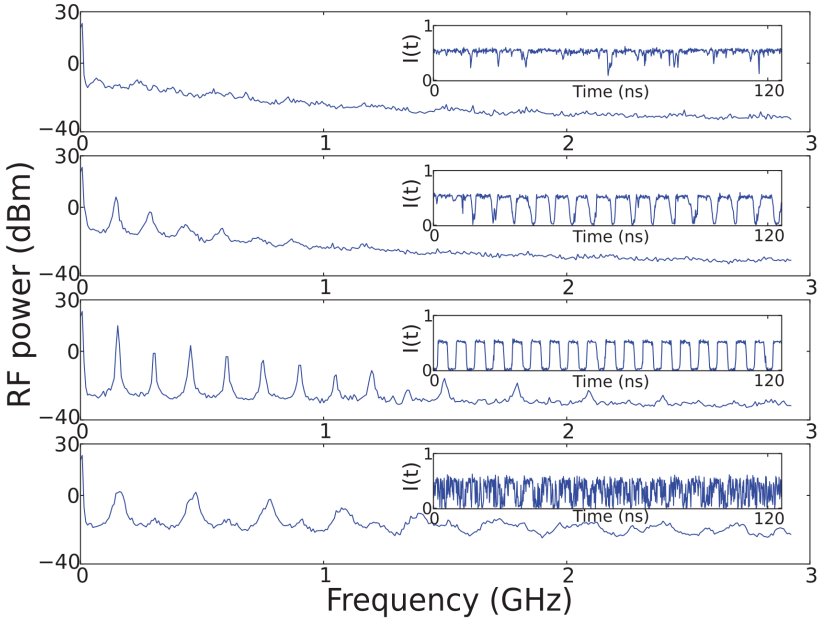

Figure 4.12: Power spectra and time traces (inset) of the LP-Y signal when the VCSEL is submitted to both XPR and PSF of the LP-X component for J = 3 mA, T = 30 °C, L_{PSF} = 98 cm, and L_{XPR} = 49 cm. The XPR rate is 17% and the PSF rates are, from top to bottom, 0.03%, 0.05%, 0.44%, and 2.5%, respectively.

For a very small feedback rate, the signal is noisy and its power spectrum shows excess noise at the harmonics of the main peak given by $c/4L_{XPR}$. As the feedback level is increased, a regular square-wave signal develops and settles down for a feedback strength of 0.12%. For a feedback level of 0.44% the regularity is maximized, and its power spectrum displays narrow peaks at the harmonics of the fundamental frequency $\nu_r \approx c/4L_{XPR} = (2\tau_r)^{-1}$; the odd harmonics clearly dominate the spectrum, the even harmonics being suppressed by more than 10 dB with respect to the preceeding odd harmonics. However, when the PSF level is above $\approx 1\%$, the output signal becomes irregular again, and the square waveform eventually disappears.

The robustness of this square signal has been assessed also versus pumping current. In Fig. 4.13 we show how the dynamics evolves when changing J.

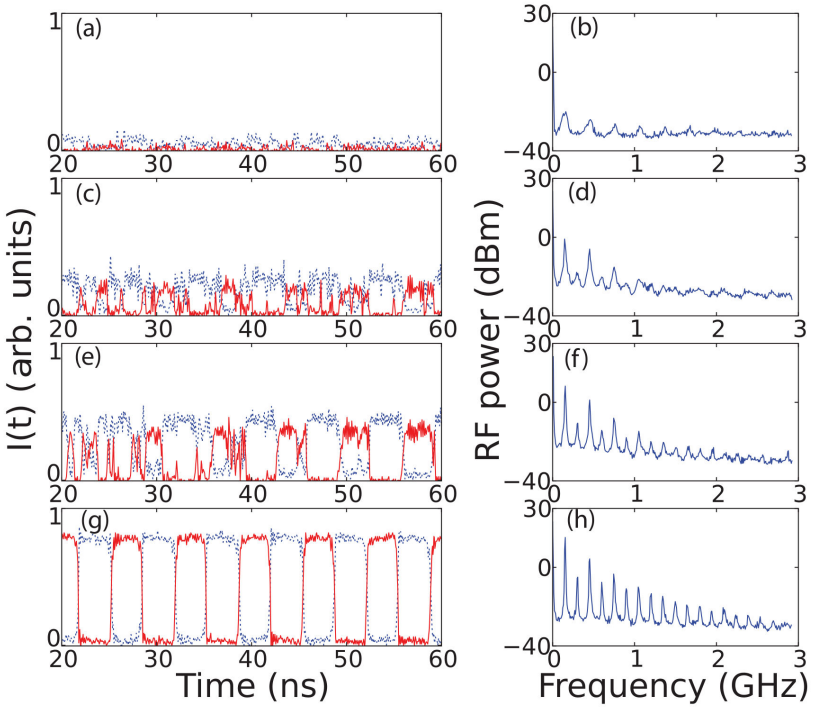

Figure 4.13: Left column: power of the LP-Y (blue dotted trace) and LP-X (red trace) components when the VCSEL is submitted to both XPR and PSF of the LP-X component for L_{PSF} = 98 cm, L_{XPR} = 49 cm, T = 30°C, PSF = 0.4%, and XPR = 17% for J = 0.5 mA (a), J = 1.0 mA (c), J = 1.5 mA (e), and J = 3.0 mA (g). Right column: corresponding power spectra of the LP-Y component.

For a wide current range 2 mA < J < 3 mA, the square signal appears regular with the same characteristics shown in the optimal parameter set of Fig. 4.12. When the current is decreased down to 1 mA the regularity is lost. Synchronous and balanced acquisition of the two polarization components reveals that, for 2 mA < J < 3 mA, the square-wave oscillations in the two polarizations are in antiphase and have the same amplitude as can be observed in Fig. 4.13, thus leading to a constant total intensity output of the VCSEL. In the most regular situation,

obtained in Fig. 4.13 for J = 3 mA, the full width at half maximum of the first peak is of 200 kHz, while the suppression of the first even harmonic peak over the fundamental peak is larger than 20 dB.

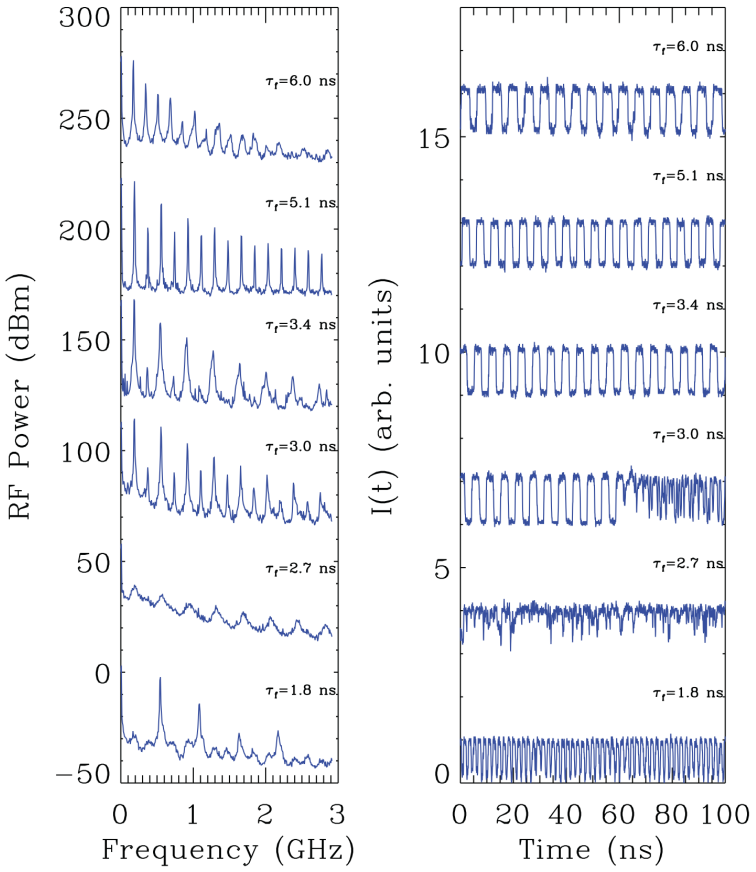

Figure 4.14: Power spectra (left panel) and temporal signals (right panel) of the LP-Y polarization when the VCSEL is submitted to both XPR (rate 17%) and PSF (rate 0.1%) of the LP-X component, for different values of τ_f as indicated. τ_r = 2.6 ns and J = 2.5 mA; T = 30 °C. For clarity, the spectra have been vertically offset by 55 dB and the time traces have been shifted by 3 units.

We remark that the regularity of this square signal is quite sensitive to the XPR rate; in fact, if the rate of XPR is decreased below 16%, the regularity is rapidly lost and a noisy signal is found. This is in agreement with the existence of a minimum threshold for the rate of XPR yielding squares, as discussed in [Mulet 2007a]; unfortunately, this value is very close to the maximum level of XPR attainable in our setup. We have also characterized the square signal versus the ratio of delays, τ_f/τ_r. As discussed above, the first peak in the power spectrum and the repetition rate of the square signal are given by $\nu_r \approx c/4L_{XPR} = (2\tau_r)^{-1}$. If XPR is removed, the power spectrum exhibits peaks at integer multiples of $\nu_f = c/2L_{PSF} = {\tau_f}^{-1}$, the inverse of the round-trip time in the external feedback cavity.

Fig. 4.14 shows that the existence of the square signal depends on the ratio of the delays. For a XPR delay of $\tau_r = 2.6$ ns and varying τ_f by steps of 200 ps we have observed that the square signal appears for 3.4 ns $< \tau_f <$ 5.4 ns, which in terms of delay ratio means $1.3 < \frac{\tau_f}{\tau_r} < 2.1$. In this range, the regularity of the square signal is maximum in the range $1.7 < \frac{\tau_f}{\tau_r} < 2.1$, and the square wave is not sensitive to the feedback phase. The only effect of the feedback phase in the range of cavity lengths explored is to modify the noise on the square-wave signal, increasing by a few dB the noise floor level in the square-wave power spectrum.

When τ_f is decreased below this range, the regularity is progressively lost; bursts of irregular behavior appear for $\tau_f = 3$ ns and get more and more dominant in time as τ_f is decreased, until, for $\tau_f = 2.7$ ns ($\frac{\tau_f}{\tau_r} \approx 1$), the signal is completely irregular. Further decreasing $\frac{\tau_f}{\tau_r} \approx 0.7$ leads to an oscillating signal whose power spectrum exhibits only peaks at integer multiples of the third harmonic of ν_r (Fig. 4.14 for τ_f = 1.8 ns). When τ_f is further decreased the signal becomes again very irregular and its power spectrum shows excess noise at several frequencies that can be associated to multiples of ν_r and multiples of ν_f. Instead, for $\tau_f > 6$ ns (i.e., for $\frac{\tau_f}{\tau_r} > 2.3$) the regularity is rapidly degraded and the peaks in the power spectra broaden showing a substructure with smaller peaks that can be associated to ν_f and multiples.

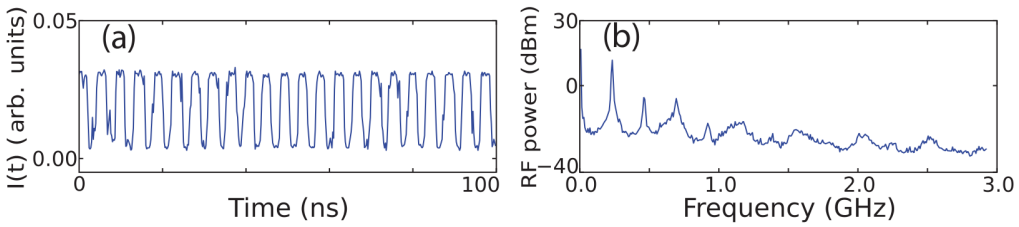

Figure 4.15: LP-X output emission (a) together with LP-X power spectrum (b) when the VCSEL is submitted to both XPR and polarization-selective optical feedback. Both XPR and optical feedback circuits are set to select LP-Y and all parameters are optimized to obtain the most regular square signal. L_{PSF} = 58.8 cm, L_{XPR} = 69.8 cm, PSF = 0.15%, XPR = 17%, J = 2.8 mA, and T = 30 °C.

The results presented up to now correspond to the case where LP-X polarization is selected for PSF and XPR. When LP-Y is selected for feedback and reinjection, qualitatively similar phenomena are obtained. In this case, however, although the presence of PSF increases significantly the regularity of the output signal obtained with XPR only, we were unable to observe a square-wave signal as regular as the one observed when selecting LP-X. In Fig. 4.15 we show the most regular signal we were able to obtain selecting LP-Y. This signal was obtained by optimizing the delay times and levels of XPR and PSF, as well as the laser pumping current. The square-wave modulation obtained by using LP-Y for XPR and PSF is stable in a much narrower parameter region than when using LP-X. The square-wave signal is now stable only over 0.5 mA in pump current and, in terms of delays ratio, there is only a sharp interval where the regularity is preserved.

4.3.3 Numerical investigation

4.3.3.1 The model

In order to reproduce the dynamics obtained experimentally, we use the SPM (see section 4.2.3), suitably modified for incorporating the effects of both PSF and XPR. In the linearly polarized base the model reads :

$$\begin{aligned}
\dot{X} &= (1+i\alpha)\left[(N-1)X+inY\right]-(\gamma_a+i\gamma_p)X \\
&+ \eta e^{-i\Omega}[aX(t-\tau_f)+bY(t-\tau_r)], \qquad (4.5)\\
\dot{Y} &= (1+i\alpha)\left[(N-1)Y-inX\right]+(\gamma_a+i\gamma_p)Y \\
&+ \beta e^{-i\theta}[aX(t-\tau_r)+bY(t-\tau_f)], \qquad (4.6)\\
T\dot{N} &= \mu - N(1+|X|^2+|Y|^2)-in(X^*Y-XY^*), \qquad (4.7)\\
T\dot{n} &= -n(\gamma_s+|X|^2+|Y|^2)-iN(X^*Y-XY^*), \qquad (4.8)
\end{aligned}$$

The terms X(t - $\tau_{f,r}$) and Y(t - $\tau_{f,r}$) in the evolution equations for the X and Y components describe the effects of PSF and of XPR, which have strengths η and β, respectively, with time delays τ_f and τ_r, respectively. a and b describe which LP component experiences feedback and reinjection: when LP-X experiences PSF and is reinjected turned into LP-Y, then a = 1 and b = 0, and vice versa.

4.3.3.2 Numerical results

In this subsection we present results for the numerical simulation of the extended SFM in Eqs. (4.5-4.8), which, as will be discussed later, are in excellent agreement with the experimental results. If not otherwise stated, the PSF and the XPR rates are chosen to be real, i.e., $\Omega = \theta = 0$, while the delays are $\tau_r = 900$ and $\tau_f = 2\tau_r$, which correspond to 6 ns and 12 ns, respectively, if a standard cavity decay rate $\kappa = 300$ ns^{-1} is considered. For definiteness, we take $\gamma_a = 2.6.10^{-3}$ and (a,b) = (0,1), i.e., the LP-Y component is selected for PSF and used for XPR.

We show in Fig. 4.16 both a short segment of the time traces and the power spectra of the LP-Y component of the VCSEL under the action of XPR ($\beta = 0.3$) as the level of PSF is increased. There is a critical value of the feedback rate $\eta_c \approx 0.01$ below which no dynamics can be observed. The existence of a minimum PSF level η_c for developing the square-wave signal can be understood as the level of feedback required to drive the system, via the effective dichroism due to PSF, into the monostable parameter regimes (see Fig. 4.9). Above η_c, a square-wave signal develops and its quality improves with the feedback level for some range, but eventually it degrades since too large values of η allow many modes of the external cavity to compete for the gain, hereby creating a complex oscillation instead of a clean plateau.

The optimal value of the PSF rate has to be defined with respect to a somewhat arbitrary criterion. If we consider the suppression of the even harmonics and the

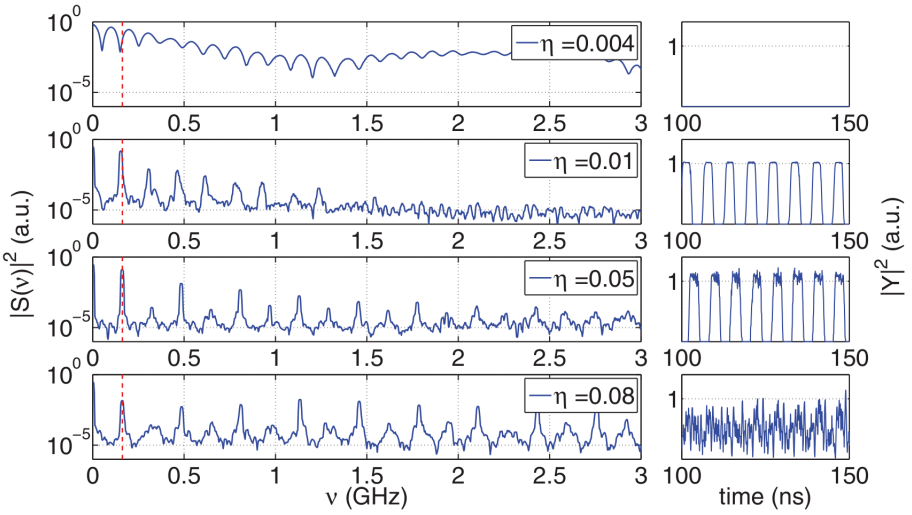

Figure 4.16: Power spectra (left) and temporal traces (right) of the intensity of the LP-Y component of the VCSEL for increasing values of the PSF rate η with $\mu = 2$ and $\beta = 0.3$. For too small values of η, the system operates on the stable LP-X polarization, and there is an optimal feedback value $\eta \approx 0.01$ above which the regularity of the square-waves deteriorates. The vertical red line in the spectra marks the frequency spacing of the external cavity modes.

similarity of the power spectrum to that of an ideal square-wave signal (which has power ratios $|a_k/a_0|^2 = 1/k^2$ for the odd harmonics k = 1,3,5, . . .) then the optimal value for these working conditions is in between $\eta \approx 0.03$ and $\eta \approx 0.06$.

Within this regime, we did not notice an influence of the feedback phase Ω on the square-wave dynamics, only on the amount of noise present on the signal. This can be understood from the fact that during the second plateau of the square-wave, the LP-Y feedback is reinjected into an "off" laser (i.e., LP-X emitting), and the feedback intensity has simply to be sufficient to expel the system from the basin of attraction of the LP-X mode allowing one to restart another cycle of the square-wave.

Instead (see Fig. 4.17) the value of the PSF delay τ_f compared to the XPR delay τ_r has a paramount influence on the dynamics. The analysis of plateaux in [Gavrielides 2006] indicates that PSF will help in regularizing the square-wave signal if the PSF onto the LP-Y arrives close to the end of the second plateau, since this will accelerate the transition from LP-X into LP-Y emission, i.e., for PSF delays that verify $\tau_f \approx 2n\tau_r$ with n an integer. Indeed, the numerical simulations in Fig. 4.17 show that good quality square-waves are obtained for $1.5\tau_r < \tau_f < 2.5\tau_r$. An alternative assessment of the quality of the square-wave signal in this range can be obtained by looking at the power spectrum of the signal and comparing it with that of a perfect square-wave signal, which as discussed before contains only the odd harmonics of the fundamental frequency, with power decreasing as the square of the harmonic index. Indeed, we observe (see Fig. 4.18) that power of the second harmonic has a minimum and that power in third harmonic is about one-tenth

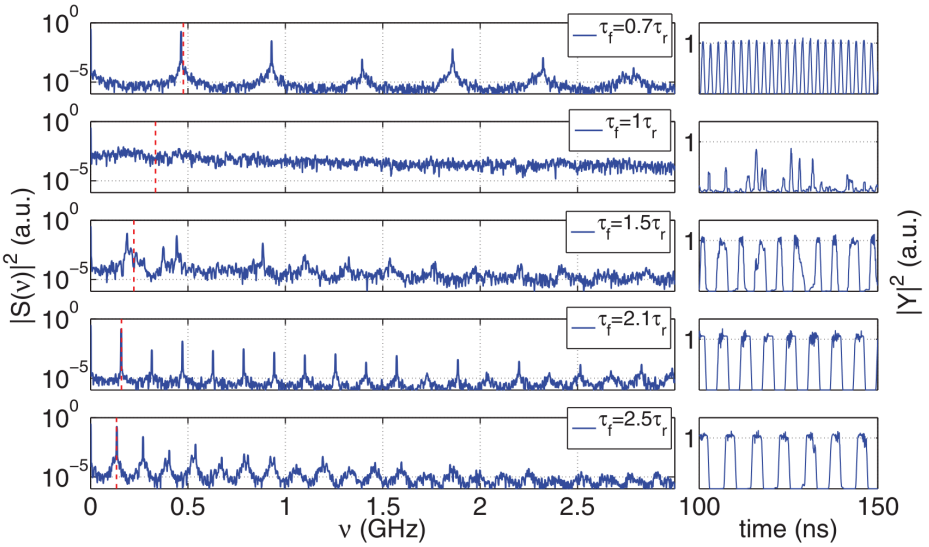

Figure 4.17: Power spectra (left panel) and traces (right panel) of the intensity of the LP-Y component of the VCSEL for increasing values of the PSF delay τ_f, with $\eta = 0.03$, $\mu = 2$, and $\beta = 0.3$. The vertical red line in the spectra marks the spacing of the external cavity modes.

of that in the first harmonic for $\tau_f = 2\tau_r$. Around this region, a good-quality rectangular signal is still obtained, but the duty-cycle progressively deviates from 50%, hence increasing the power in the second harmonic. For feedback cavities shorter $\tau_f/\tau_r \approx 0.8$, the power in each component exhibits fast oscillations with a dominant frequency that roughly corresponds to the third harmonic of the fundamental frequency of the squares and to the fundamental frequency

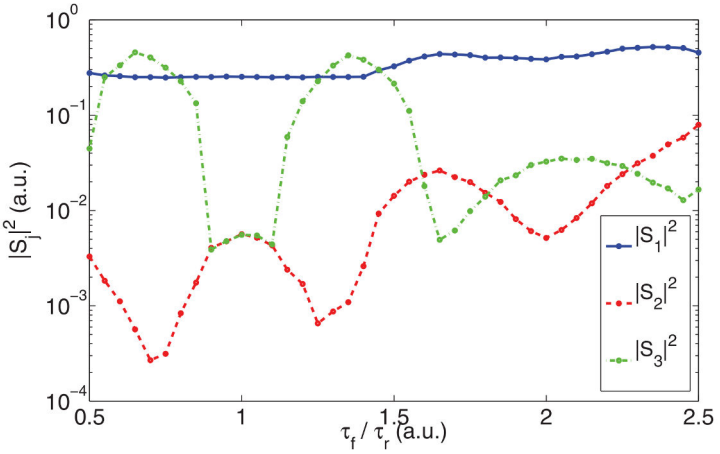

Figure 4.18: Peak power in the first (solid blue), second (dashed red), and third (dash-dotted green) harmonic of the square-wave signal as a function of the delay in the PSF arm normalized to the XPR delay.

of the PSF delay. For long cavities, the excitation of multiple external cavity modes destroys the square-wave, at least in the range of cavity lengths explored here.

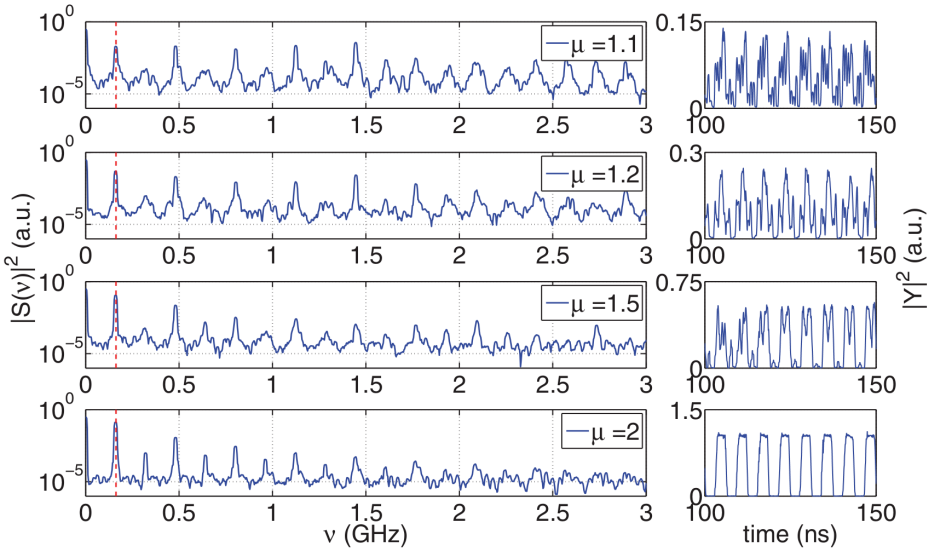

Figure 4.19: Power spectra (left) and temporal traces (right) of the intensity of the LP-Y components of the VCSEL for increasing values of the bias current μ, with $\eta = 0.03$, $\Omega = 0$, $\mu = 2$, and $\beta = 0.3$ in the optimal case where $\tau_f = 2\tau_r$. The quality of the square-wave oscillation is strictly increasing with the bias current since no bistability is encountered along the way.

We conclude our analysis by studying the effect of the bias current on the square-wave quality. In the optimal case depicted in Fig. 4.19, where τ_f=$2\tau_r$, one can see that square-waves are present from close to threshold up to three times the threshold. We found that the quality of the square-wave oscillation as inferred from the spectra in Fig. 4.19 steadily increases with the bias current; see, for instance, bottom panel of Fig. 4.19 obtained with $\mu = 2$. This is at variance with the analysis developed in [Mulet 2007a] where it was shown that there is an optimal bias current value above which the square-wave oscillation deteriorates. It was shown in [Mulet 2007a] that XPR has the side effect of rendering the Hopf bifurcation of the LP-Y mode supercritical instead of subcritical, which has the effect of anticipating bistability (see Fig. 9 of [Mulet 2007a]). As a consequence, when the bias current approaches this regime, the vicinity of the limit cycle distorts the orbit imposed by XPR, thus destroying the waveform regularity. It is worth remarking that this deterioration is mitigated here due to the presence of PSF, and that the combination of XPR and PSF allows one to largely increase the parameter space domain (both with respect to the XPR strength and bias current) where the square-signal output exhibits a high degree of regularity.

4.3.3.3 Asymmetric sensitivity to feedback

The numerical results in the previous subsection have been obtained in the case where PSF and XPR select the LP-Y component, i.e. the mode with the highest optical frequency and the lowest threshold, and γ_a= 2.6.10^{-3}. Qualitatively similar results are obtained when PSF and XPR select LP-X, but it is observed that, in this second case, the levels of PSF needed to achieve good-quality square-waves were systematically lower than in the first case.

This remarkable asymmetry between the two cases regarding the quality of the square-wave signal is obtained independent of the value of γ_a, as exemplified in Fig. 4.20. For the sake of definiteness, we assume here that γ_a = -2.6.10^{-3} and γ_p = 5.24.10^{-2}, i.e. the solitary VCSEL is dominantly emitting LP-X (the reddest polarization component) and it operates on the left part of the bistable region; see Fig. 4.9 with μ = 2 and γ_a= -2.6.10^{-3}. Due to the bistability, the square-wave cannot be obtained using only XPR. Since dichroism in our devices is rather small, minute quantities of (resonant) feedback should be sufficient to destroy the bistability since the system is close to the region where the red mode (the green area in Fig. 4.9) is the only one stable. Hence we use η = 0.005, which indeed yields a regular square output, as seen in Fig. 4.20a).

Oppositely, an identical amount of feedback in the bluest polarization component (LP-Y) does not allow for square-waves as the system enters more deeply into the bistable region. Here, the minimal value needed is close to η = 0.02, which allows reaching the brown region where the LP-Y is the only stable mode. One can see in Fig. 4.20b) that the square-signal regularity is clearly worse than in the previous case in spite of all the system parameters being identical except for the polarization component selected for PSF and XPR.

The different effectiveness of PSF for the different LP components can be qualitatively understood when considering the effect of the PSF as a modification of the effective dichroism and making reference to the asymmetry of the bistable region; see Fig. 4.9. For small values of the dichroism (as the ones considered here),

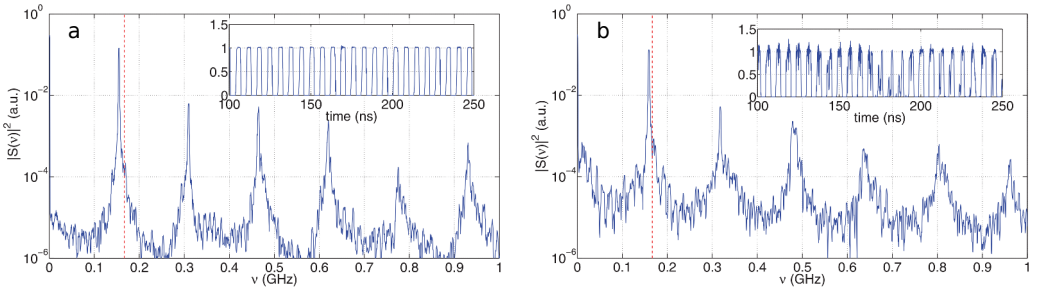

Figure 4.20: Power spectra and time traces (inset) of : a) The LP-X polarization when the LP-X is fed back and re-injected turned into LP-Y. The parameters are γ_a = -2.6.10^{-3}, μ = 2, and β = 0.15. The feedback rate is η = 0.005. b) The LP-Y polarization when the LP-Y is fed back and re-injected turned into LP-X. The parameters are γ_a = -2.6.10^{-3}, μ = 2, and β = 0.15. The feedback rate is η = 0.02.

the higher slope of the border on the $\gamma_a < 0$ side implies that, in general, a lower PSF strength is required to leave the bistability region when selecting LP-X instead than LP-Y.

For a given rate of PSF, the system can be driven into a polarization monostable region. If PSF is applied on LP-X, it is pushed deeper into the green left region than if the same amount of PSF is applied on LP-Y. In this case, the system is pushed into the brown right region but it lies closer to the bistable region than in the former case. Hence the vicinity of the bistable region leads to a less regular and robust square-wave signal. The higher minimal value of the feedback required in the latter case implies a larger number of active external cavity modes that eventually lead to more complex and irregular dynamics. Conversely, in the case of positive values of dichroism (yet such that the VCSEL is in the bistable range), the situation would be reversed.

4.3.4 Conclusions

We have studied theoretically and experimentally the generation of square-wave signals from bistable VCSELs submitted both to XPR and to weak PSF. The presence of PSF decreases the losses of the selected polarization providing a mechanism which effectively increases the dichroism and that reinforces the effectiveness of XPR for the generation of a very regular square-wave emission which is very robust versus parameter changes. For high enough feedback levels, the VCSEL is effectively driven into a regime where only one polarization state can exist, and the square-wave signal develops. Interestingly, the impact of PSF in such a process is different for each LP component, as evidenced both theoretically and experimentally, due to the asymmetry of the bistability region with respect to dichroism. The proposed scheme allows one to generate square-wave signals from VCSELs with weak dichroism where XPR alone would not work.

4.4 Vectorial localized structures

In this section we focus on a dynamics consisting of short antiphased polarization pulses obtained with the same setup for a thin range of parameters. Since the total signal remains constant, the dynamics is only vectorial similarly to the robust square-wave regime. Thus, the relevant time scale of the bulk system is much faster than the gain recovery time and large aspect-ratios can be obtained with nanosecond external cavity round-trips.

We first give the experimental evidences that these pulses are vectorial LS, and therefore possess the general properties of localized structures, namely robustness, multi-stability, independence and interaction. These vectorial LS circulate in the external cavity and regenerate every PSF cavity round-trip when interacting with the VCSEL gain medium. We show that our setup allows to pin the position of the multiple LS coexisting in the cavity via the difference in XPR and PSF delays.

In this scheme for LS formation, nonlinearities and dispersion are localized in space. The system is thus modeled via the Delay Differential Equations (DDE) already used in section 4.3. Remarkably, this model can reduce to a phase model where the whole dynamics of the system only consists of polarization reorientation between two polarization eigenstates. We show an excellent agreement between theory and experiment since the model reproduces the solitonic behaviour of the pulses and also the pinning mechanism or the solitons respective positions in the cavity.

4.4.1 Experimental results

4.4.1.1 Experimental evidences of vectorial localized structures formation

The whole experimental setup is the same as the one used for the robust square-wave generation (see Fig. 4.10). It is important to underline that the linear polarization component favored by the PSF cavity and used for XPR must be the dominant component appearing at threshold of the solitary laser, equivalently in our case LP-Y, the bluest one. We also stress that all the experimental results given in this section can either be obtained with the VCSEL with memory or the other, as in the case of the square-wave regime. Here, and for the whole oncoming experimental results, the temperature of the VCSEL is fixed at 30 °C and the pumping current at J = 3 mA (well-above threshold).

When setting PSF rate at around 0.5% and XPR rate around 1%, one ends up with the typical dynamics shown in Fig. 4.21a). The traces are acquired with two 10 GHz detectors coupled to a 33 GHz oscilloscope.

The VCSEL emits a train of pulses that are separated by the PSF delay τ_f. These pulses are upward on a low intensity background on LP-X (red) and downward from a high level intensity on LP-Y (blue). We verified that during this regime the total signal remains constant, thus revealing the vectorial character of our pulses. The pulse-width shown on the trace is not fully resolved with the 10

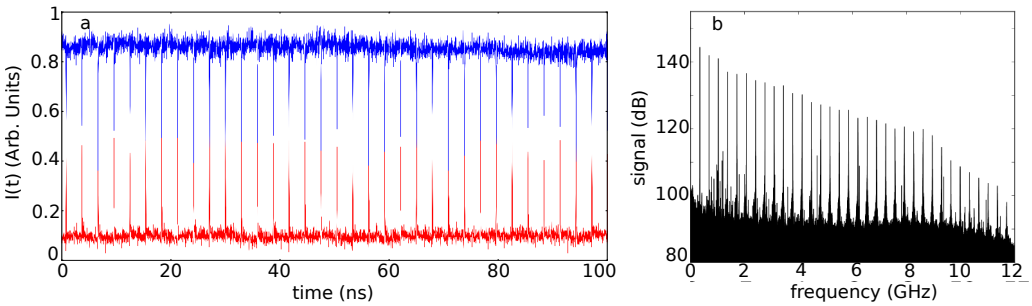

Figure 4.21: a) Time signal of the LP-Y (blue) and LP-X (red) outputs when the VCSEL is submitted to XPR (rate 1.4%) and PSF (rate 0.6%). T = 30 °C, J = 3.0 mA, τ_f = 2.9 ns, τ_r = 3.3 ns. b) Calculated RF power spectrum for the LP-X trace of a).

GHz detector. We verified with a 42 GHz detector that the pulse-width is about 70 ps. In Fig. 4.21b) we show the calculated RF power spectrum for the LP-X trace of panel a). This reveals that a large number of PSF cavity modes are involved in the dynamics. It also prooves that the pulses are not fully resolved with the 10 GHz detector since the RF is limited in bandwidth (decay after 9 GHz). We are thus dealing with periodic vectorial pulses. But are these pulses localized structures ?

In order to further characterize our dynamics and give an answer to that issue, we are performing statistical analysis over our data to study the robustness, mobility, multi-stability, independence and interactions of our pulses. If they satisfy all of these conditions, then they are localized structures and could be potentially addressable. LS are supposed to keep a constant shape over successive round-trips, but visual inspection of the time serie in Fig. 4.21a) indicates that the pulses fluctuate in amplitude. Statistical analysis over a long time series spanning 34,000 round-trips reveals that the amplitude fluctuations are limited $\approx$ 10% around the mean value (see Fig. 4.22a). Moreover, the shape of the pulse is robust and

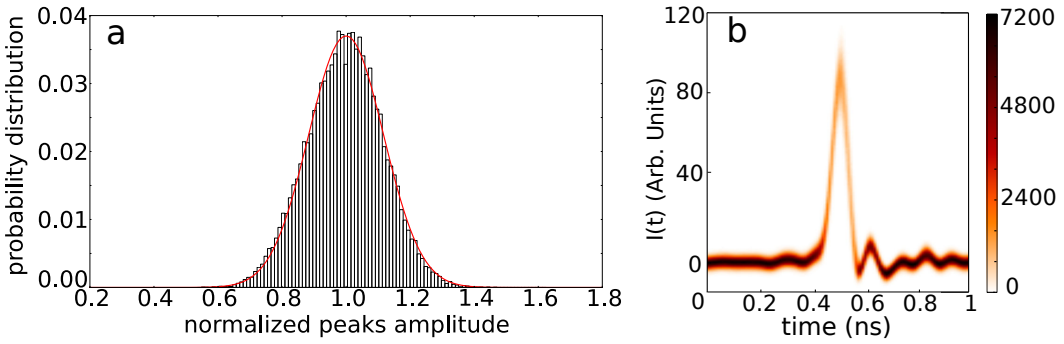

Figure 4.22: Panel a): Probability distribution for the amplitudes of the pulses in Fig. 4.21a) on LP-X. Panel b): Histogram (in color grade persistence) resulting from the superposition of 34,000 pulses in the LP-X polarization obtained using the same trace as Fig. 4.21a).

stable from one round-trip to the other, as evidenced by the reproducibility of the fine structure of the pulse (see Fig.4.22b)). We conclude that these amplitude fluctuations originate from both the limited bandwidth and sampling rate of our detection system and from the various noise sources present in the experiment (namely spontaneous emission from the laser, shot noise of the fast photodiode, mechanical stability of the mounting). Therefore the robustness property of LS is fulfilled by our vectorial pulses.

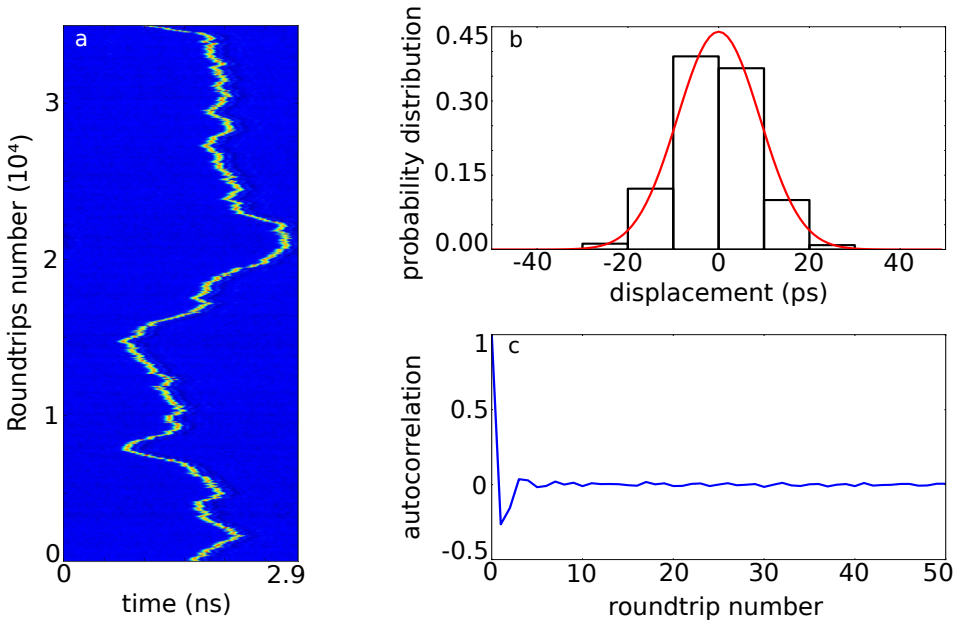

Figure 4.23: Statistical analysis for the motion of a single pulse in the cavity. Panel a): Space-time like diagram of a single pulse obtained using the LP-X trace of Fig. 4.21a). Panel b): Probability distribution of the residual $R_n = \Delta_n - \Delta_{n-1}$ calculated from the LP-X trace in Fig. 4.21a) with Δ_n the position of the pulse at round-trip n in a). Panel c): Autocorrelation of R_n.

The dynamics within an external cavity can be usefully described in terms of space-time like diagrams where the time trace is folded over itself at intervals τ_f, so that the round-trip number becomes the pseudo-time discrete variable while the pseudo-space variable corresponds to the timing of the vectorial LS modulo τ_f (see chapter 3)[Giacomelli 1996, Arecchi 1992]. This representation pictures the pulse position Δ_n within the external cavity as a function of the round-trip number [Jang 2013b]. When applied to the LP-X polarization trace of Fig. 4.21a), it reveals that Δ_n fluctuates noticeably over a typical time scale of the order of a hundred of cycles, suggesting that the noise present in the system acts upon the pulse as a Langevin force over a free particle, leading to a Brownian-like motion of the pulse within the external cavity as a function of the round-trips covered (see Fig. 4.23a). Indeed, the analysis of the time series for Δ_n indicates that this variable is described by a first order autoregressive model, $\Delta_n = \Delta_{n-1} + R_n$, with R_n a random term which is distributed as a Gaussian of zero mean and a standard deviation $\sigma_r = 11$ ps,

as shown in Fig. 4.23b). Moreover, the autocorrelation of R_n (Fig. 4.23c)) falls-off very rapidly (a few round-trips) indicating that the sequence of Δ_n corresponds to the regular sampling of an one-dimensional stochastic process.

The analogy between unidimensional random motion of a free particle and the drift of the pulse position in the external cavity can be traced back on the temporal translational invariance of our dynamical system. It is worth noting that this action of noise could not be observed in spatial systems where the translational invariance is often broken by the inhomogeneities of the hosting devices [Bödeker 2003]. At the same time the small duration of the pulses as compared to τ_f indicates that our system may have a large temporal aspect-ratio. If this were the case, several independent pulses could coexist within the same PSF cavity round-trip.

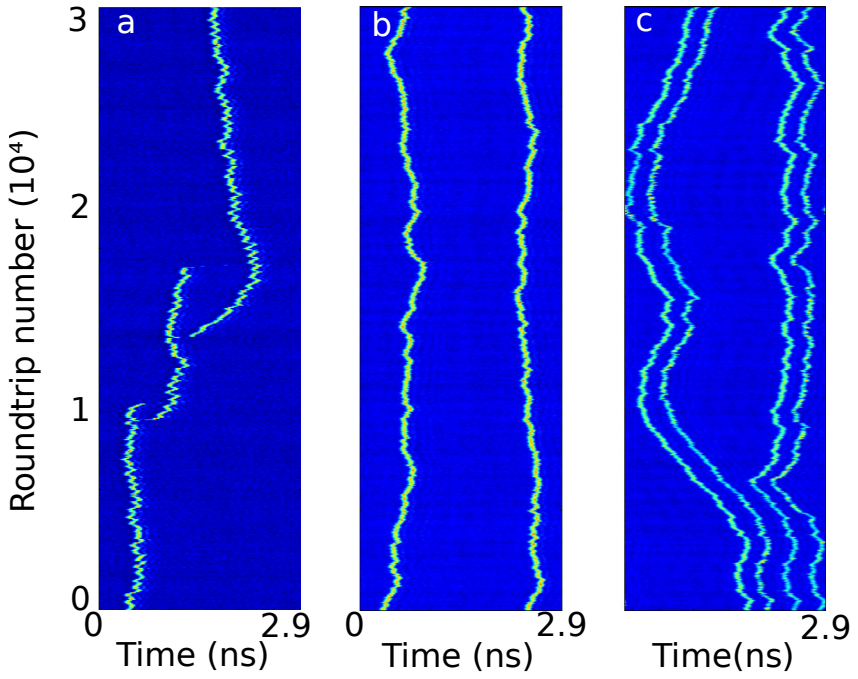

Figure 4.24: Space-time like diagrams of different states of multiple pulses coexisting in the same external cavity round-trip for the same parameters value. a) Switch-on and switch-off of pulses. b) Two independent pulses, c) Two independent pairs of pulses composed by two bounded pulses. Pairs are independent until round-trip 25,000 where they get closer to each other and start forming a molecule of four bounded pulses that evolves as a unique particle.

Fig. 4.24 shows space-time diagrams for different ensembles of pulses that coexist within the same round-trip. These different states coexist in the same parameter space with the homogeneous background. The system may evolve from one to another in response to perturbations or parameter sweeps, in the latter case displaying a large degree of hysteresis.

Fig. 4.24a) shows how different pulses can nucleate spontaneously from the c.w. solution. We clearly see that two pulses can coexist in the cavity and that switch-on, switch-off and trajectories of both pulses are totally independent. In Fig. 4.24b) we

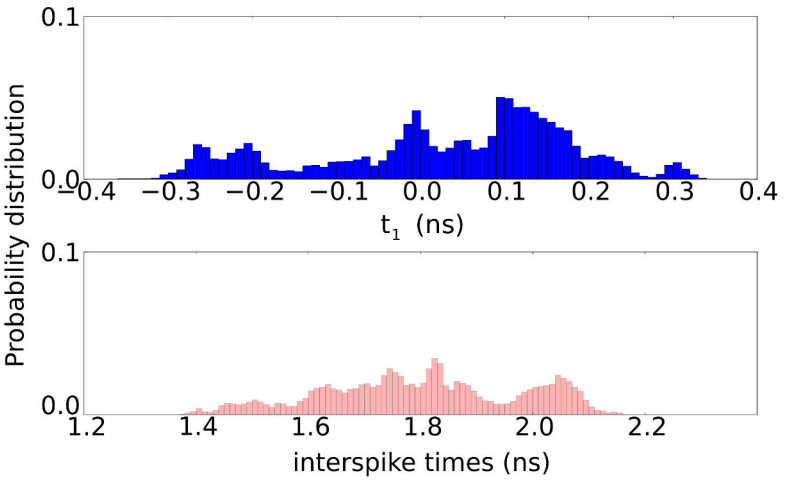

Figure 4.25: Statistical analysis of the two independent pulses trajectories in Fig. 4.24b). top: we plot the PDF of the position of the first pulse within the external cavity. bottom: we plot the PDF of the time intervals between the first and the second one.

show a dynamics where the two pulses have noise-induced trajectories that seem uncorrelated, evidencing that they are independent. A statistical analysis of the distances between the two pulses may provide more quantitative indications about their interaction. In Fig. 4.24b), we call t_1 the temporal position of the first peak of the molecule within the external cavity delay time, t_2 the temporal position of the second peak. In Fig. 4.25, we plot the Probability Distribution Function (PDF) of t_1 (top) and the PDF of t_2 - t_1 (bottom). The PDF of t_1 indicates that the pulse jitters within the external delay on a wide time interval with no preferred position. The time separations between the two pulses also follows a very broad PDF, showing that the two pulses have uncorrelated trajectories.

It is worth remarking that the correlation or uncorrelation of the noise-induced motion of pulses in these space-time diagrams is a valuable tool for discriminating between independent and bounded pulses. Indeed, if noise were absent from our system, then no way to distinguish between the two would exist.

Instead Fig. 4.24c) shows a rather different situation with four pulses in the same round-trip. The trajectories of these pulses are highly correlated by pairs: the two left-most pulses move like a rigid body, keeping an almost constant seperation, and so do the two right-most pulses. PDFs of the time intervals between pulses in each pair (not shown) exhibit two peaks at 400 ps and 500 ps, meaning that the time separation must be somehow imposed by a background modulation of the order of 10 GHz. This could either correspond to birefringence or RO frequency. However, the motion of one pair is uncorrelated with that of the other. Thus, this state with four pulses can be interpreted as two molecules formed by two pulses each. Surprisingly, after 25,000 round-trips the two molecules approach and form a bound state with four peaks that move as a single structure, i.e. a molecule of four pulses.

For the same parameter values, we have also obtained several kind of pulses complexes, namely one of three peaks, one of six peaks and one of seven peaks. Their time traces are shown in Fig. 4.26a) while in the panels b), c) and d) we plot the evolution of these structures in the space-time like diagrams. These diagrams indicate clearly that each one of these structures behaves as a unique one and thus

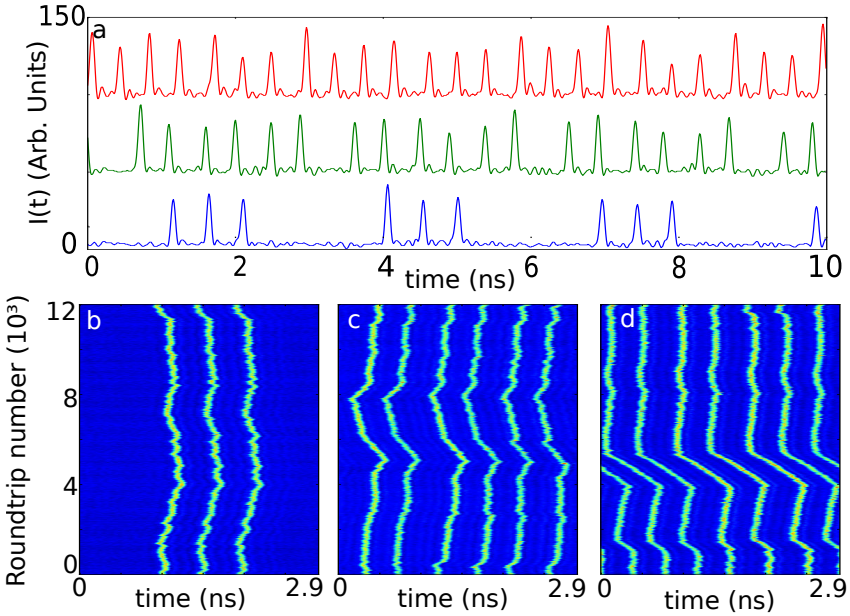

Figure 4.26: Panel a): (blue) LP-X time trace showing a three-peaks molecule, (green) a six-peaks molecule, (red) a seven-peaks molecule. The two last traces have been shifted vertically for clarity. Panel b): Space-time like diagram for the 3-peaks molecule, panel c) for the 6-peaks molecules, panel d) for the 7-peaks molecule.

is a molecule. The largest structure observed (not shown) is composed of eight pulses and fills the entire round-trip, forming a "crystal" of pulses. The PDF of the intervals are shown in Fig. 4.27. In a) we see that the time separations of the peaks in Fig. 4.27b) are characterized by a probability distribution very peaked around 480 ps (the standard deviation is less than 20 ps), indicating that the second and the third peak follow the jitter of the first one. In Fig. 4.27b) we show the statistics for the peaks of the molecule of 6 pulses. The PDF of t_2 - t_1 shows a narrow peak centered around 400 ps. The PDF of the other temporal separations, for example t_3 - t_2, reveals a bipeaked distribution with a separation of the two peaks corresponding to approximately 100 ps. As previously shown for the situation in Fig. 4.24c), the separation between the elements of the molecules can undergo sudden shifts which are always 100 ps, thus revealing the existence of an underlying structure.

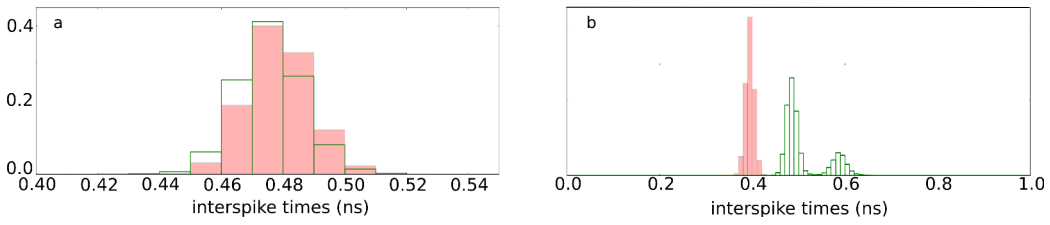

Figure 4.27: Statistical analysis of the intervals between pulses in the molecules. a) for the 3-peaks molecules, t_2 - t_1 (pink) and t_3 - t_2 (green). b) for the 6-peaks molecule, t_2 - t_1 (pink) and t_3 - t_2 (green).

To conclude, we observed the emergence of a dynamics consisting of vectorial pulses with a repetition time τ_f when our small-area VCSEL is submitted to PSF and XPR selecting the bluest polarization axis. A statistical analysis made over our data reveals that our vectorial pulses possess the properties of robustness, noise-induced motion, multi-stability and coexistence with the homogeneous state, independence and interaction when two structures are close enough to each other. Noise in our system allows to distinguish between independent and bounded structures. Therefore, this set of properties allows us to call our vectorial pulses Vectorial Localized Structures (VLS).

Such dynamics is very different from the concept of intensity solitons since in this case it purely consists in a polarization reorientation that does not involve a strong exchange of energy between the light and the active medium. Hence the addressing speed of these VLS should not be limited by the time scales governing the evolution of the gain. The fast time scales involved in the dynamics make this system promising for all-optical information processing where information bits can be stored in the form of VLS.

By studying the separation times between VLS in molecules, we noticed that discrete bond distances are favored in our system. We recall that in our experiment τ_r - τ_f = 3.3 - 2.9 = 0.4 ns. Very interestingly this value is equal to the interpeak distances found for the molecules studied in this section. Therefore, it seems that a direct link can be established between the number of pulses that can coexist in the external cavity and the difference between XPR and PSF delays.

4.4.1.2 Influences of delays in the molecules formation

We proved in the previous section that our pulses are VLS. As a consequence, their shape or conditions of existence should not be dependent on the length of the external PSF cavity, which determines the repetition rate of the VLS. We verify this assumption by implementing in our setup a much larger external PSF cavity. It is important to remark that due to the size of the elements in our experimental setup we cannot reach a size of the PSF cavity that is smaller than 1.5 ns, which is still much larger than the size of one VLS.

The PSF cavity length is now fixed at 10.8 ns and the XPR length is 11.1 ns. We define $\Delta_\tau = \tau_r$ - $\tau_f \pmod{\tau_f}$. Here Δ_τ = 11.1 - 10.8 = 0.3 ns, we fixed Δ_τ close to the value of the previous section so as to only modify the absolute values of both external cavities round-trip times and not the relative ones. Fig. 4.28 shows the space-time diagrams for different VLS dynamics. In Fig. 4.28a) we can see a single VLS propagating in the external cavity. The width of the structure is still about 80 ps, which proves that the size of the VLS does not depend on the cavities lengths. The structure exhibits some noise-induced drifts. However these are less obvious than the ones shown in the previous section since the PSF cavity is more than 3 times larger. By inspecting closely the space around the pulse, one can distinguish an embossed design located 0.3 ns behind the pulse. This interval corresponds to Δ_τ and we interpret this phenomenon as a XPR echo of the pulse traveling in the feedback caviy. The echo appears as a dark shadow on the polarization-resolved

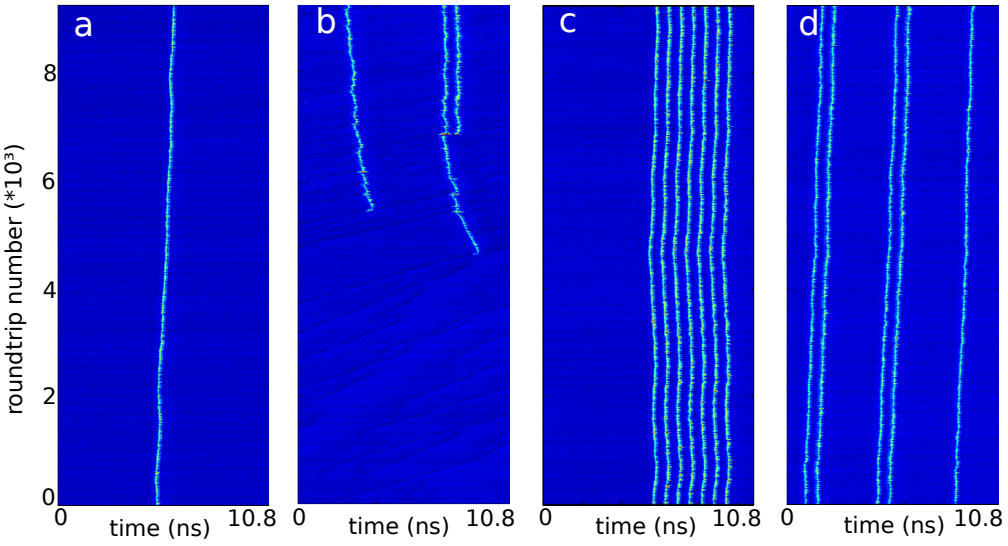

Figure 4.28: Space-time diagrams showing different dynamics of VLS in a long cavity of 10.8 ns, XPR is fixed at 11.1 ns. a) One VLS circulating in the cavity. b) Spontaneous VLS switch-ons and formation of a pair of VLS. c) 7-VLS molecule with a single binding distance between each element. d) Coexistence of two pairs of VLS with a single VLS.

time trace. The complete understanding of this phenomenon will come from the theoretical study of our system. Fig. 4.28b) shows that the VLS solution coexists with the homogeneous background and that the VLS can interact and form bound states. Indeed, at round-trips 5000 and 5500, two independent VLS appear and follow uncorrelated trajectories. At round-trip 7000, a third VLS is born and forms a pair with the right-most VLS. The two have a constant binding distance of 0.6 ns, which is equal to $2\Delta_\tau$. Fig. 4.28b) also gives some important details about the switch-on dynamics of VLS. One can notice from the figure that the two first VLS apparitions seem to result from the collisions of small dark structures that drift in the cavity with a much higher speed than the bright VLS. These dark structures coexist with the VLS and collide with them due to their different speed. Every collision seems to destabilize the VLS and provokes an amplification and broadening of the pulses. The creation of the third VLS seems to follow such destabilization of the first-born pulse. Again, a theoretical study is necessary to determine the origins of such dark structures. Fig. 4.28c) shows a molecule of 7 VLS with a binding distance still equal to $2\Delta_\tau$. The whole structure evolves as a rigid body, as already evidenced in Fig. 4.26d). Nevertheless, whereas the seven-peaks structure in Fig. 4.26d) was filling up the entire cavity, here the molecule lies quite far from the "pseudo-boundaries" imposed by our representation. This discriminates the possibility that the six-peaks and seven-peaks molecules of Fig. 4.26 can be somehow modeled with an effect due to the boundaries of our system. Finally, Fig. 4.28d) shows the coexistence of correlated and uncorrelated structures in the cavity, as compared with Fig. 4.24c). Two pairs of correlated VLS evolve in the cavity together with a single VLS. The three objects have uncorrelated motions since they travel with a large distance between them.

Therefore, the dynamics presented in this last figure suggest that the VLS can exist in very large external cavities. Their properties do not depend on the size of the external cavities. The study of their binding distances reveals again a close link with the difference of PSF and XPR delays Δ_τ. In order to confirm this assumption, we now leave the PSF cavity as it is and only modify the XPR cavity size. As such, Δ_τ will increase, which should change the binding distances between VLS.

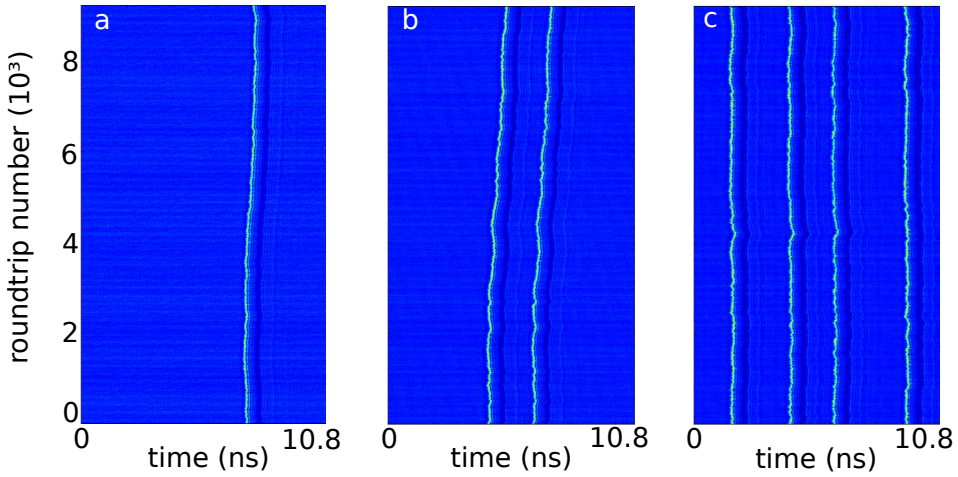

Figure 4.29: Space-time diagrams showing different dynamics of VLS in a long cavity of 10.8 ns, XPR is fixed at 11.5 ns. a) One VLS circulating in the cavity. b) Pair of VLS. c) 4-VLS molecule with three different binding distances between each element.

Now we set τ_r = 11.5 ns, and so $\Delta_\tau = \tau_r$ - τ_f = 11.5 - 10.8 = 0.7 ns. Fig. 4.29 clearly shows the binding mechanisms for the VLS molecules. In the space-time diagram of Fig. 4.29a), a single VLS is in the cavity. The dark shadow is visible and positioned at a distance Δ_τ behind the VLS. In this configuration for the delays, we can identify a second and a third shadow respectively located at $2\Delta_\tau$ and $3\Delta_\tau$ behind the VLS. Their intensity decreases as they get farther from the VLS. We interpret these second and third relieves respectively as the shadow of the first shadow and the shadow of the second shadow. Fig. 4.29b) shows two VLS in the cavity with correlated motions. Both VLS present the same features as the one observed in a). This diagram makes clear that the right VLS is fixed at a distance $3\Delta_\tau$ behind the left VLS. Therefore the post-VLS dark shadows seem to act as a pinning mechanism for the VLS in the cavity. This is confirmed by Fig. 4.29c) that shows four VLS in the cavity with three different time intervals. From left to right, the diagram reveals that the distances are $4\Delta_\tau$, $3\Delta_\tau$ and $5\Delta_\tau$ between the VLSs. We notice that the fourth VLS trajectory on the right does not experience the small kink located at round-trip 4000 and visible on the other VLS trajectories. This VLS being weakly bounded to the previous one, its trajectory seems to be less correlated to the others.

These observations are of paramount importance since our system contains a non-local pinning mechanism which can be experimentally controlled by modifying the size of the XPR cavity. We can explain the existence of such binding distances to the small kink generated in the wake of the VLS by the replica arriving after time

intervals Δ_τ. We noticed also that several exponentially decreasing replica at times $n\Delta_\tau$ exist and generate a weak binding force and several equilibrium distances for the molecules.

One has to recall that our VLS propagate in a cavity that is a ring and that has periodic boundary conditions. Therefore, if we set a value of Δ_τ such that the distance between the n^{th} visible dark replica and the VLS is larger than the PSF round-trip time, we can expect to observe molecules with intervals corresponding to non-integer values of Δ_τ.

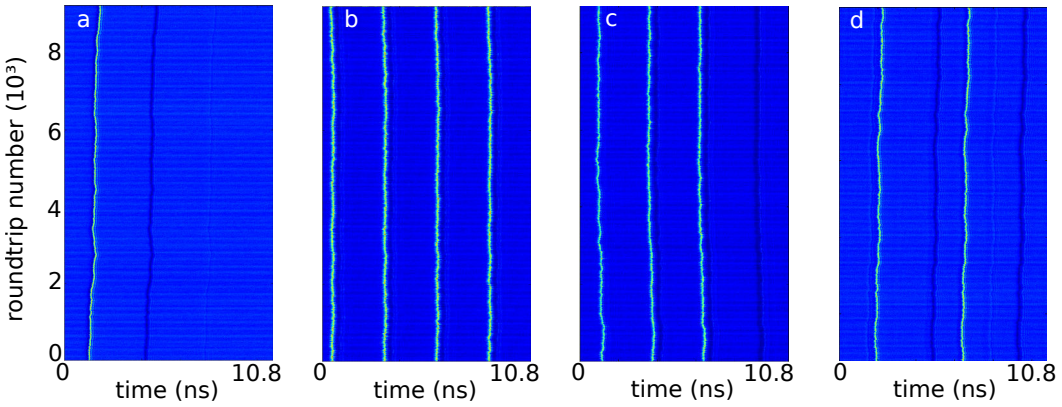

Figure 4.30: Space-time diagrams showing different dynamics of VLS in a long cavity of 10.8 ns, XPR is fixed at 3.05 ns. a) One VLS circulating in the cavity. b) 4-VLS molecule with a single binding distance between each elements. c) 3-VLS molecule with the same binding distance as b). d) Pair of VLS .

We investigate an experimental situation where $\tau_r = 3.05$ ns, which gives $\Delta_\tau = 3.05$ - 10.8 (mod 10.8) = 3.05 ns. The space-time diagrams of Fig. 4.30 evidence new mechanisms that fix the binding distances between VLS. Fig. 4.30a) shows the VLS and the exponentially decreasing dark replica located at integer multiples of Δ_τ. The third shadow is present but is too weak to be perceived in this representation. Fig. 4.30b) shows a 4-VLS molecule with a unique value for the binding distances between the pulses. One can observe that each pulse has been pinned by the first replica of the previous one. Whereas $\frac{\tau_f}{\Delta_\tau} = 3.54$ is not an integer value, the VLS seem to adapt their position in the cavity in order to impose a unique interval between them. Indeed, the distance between the VLS is $\tau_f/4 = 2.7$ ns and is slightly smaller than Δ_τ. From these observations, we can infer that our external cavity is comparable to a ring since the trajectory of the right-most VLS is correlated to the one of the left-most VLS. It is also important to remark that these periodic structures have nothing to do with some kind of harmonic mode-locking imposed by the cavity. Indeed Fig. 4.30c) shows the exact same structure except that no VLS has emerged next to the right-most shadow. As a consequence, the first VLS on the left is not linked to any dark replica. This dynamics clearly demonstrates that each VLS is independent and that the pinning structure in the cavity is only imposed by the difference of delays. Last but not least, Fig. 4.30d) exemplifies another type

of pinning mechanism. Here the two VLS are separated by a distance $\delta = 4.5$ ns, which corresponds to $\frac{3\Delta_\tau}{2}$. This is easily explained considering the relative values of Δ_τ and τ_f. In our parameter conditions, we remark that $\frac{2\tau_f}{\Delta_\tau} \approx 7$. This means that XPR actually imposes a set of pinning points in the cavity that are located every $\Delta_\tau/2$. This periodic relief in the round-trip is striking on Fig. 4.30d). Consequently, for this set of delays the maximum number of pulses that could coexist in the cavity is 7, unfortunately such dynamics has never been observed.

The diagrams of Fig. 4.30b-c) show two types of pinning mechanisms at play for the determination of the positions and number of pulses allowed within one cavity round-trip for a given set of exernal cavity delays. We assume that the competition between both is one of the reasons for the multi-stability of our system and the weak robustness of each configuration.

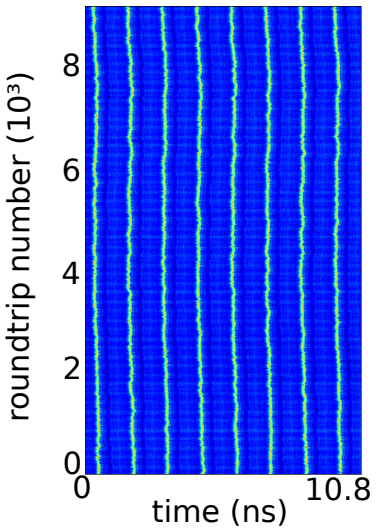

Figure 4.31: Space-time diagram showing a crystal of VLS in a long cavity of 10.8 ns, XPR is fixed at 7.23 ns. The crystal is composed by 8 VLS in the cavity.

To conclude with the pinning mechanisms, Fig. 4.31 illustrates how both effects described in Fig. 4.30 can actually collaborate to give rise to a crystal-like structure. Here $\tau_r = 7.23$ ns while τ_f remains unchanged, thus $\Delta_\tau = 7.23$ ns. In our configuration, $\frac{\tau_f}{\Delta_\tau} \approx 1.50$ is not an integer number. The molecule is composed of 8 VLS and the time interval between them is $\delta = 1.35$ ns. We verify that $\frac{\tau_f}{\delta}$ is equal to 8, which is the number of pulses that we observe. As in Fig. 4.30b), the VLS seem to live in the cavity alongside a dark shadow. However this time, the dark shadow corresponds to the replica of a pulse located 7.23 ns before. $\frac{\Delta_\tau}{\delta} = 5.355$ which means that the XPR imposes a set of pinning points in the cavity that are located about every $\Delta_\tau/5$, as previously explained in the analysis of Fig. 4.30d). Therefore, the VLS adapts its position with respect to the shadow in order to find an equilibrium between two balancing effects : pinning imposed by XPR and integer number of intervals within one round-trip. In this case, the equilibium is obtained for a number of pulses in the cavity equal to 8.

4.4.2 Theoretical analysis

The theoretical analysis uses the same model as the one previously computed for the robust square-wave switching implementation (4.5,4.6,4.7,4.8). It is the SPM modified for incorporating the effects of XPR of LP-Y onto LP-X and PSF of Y onto Y, identical with the experimental situation. In a mixed description in terms of linearly polarized components of the field X and Y where XPR and PSF are easily expressed, and circularly polarized components $E_\pm = (X \pm iY)/\sqrt{2}$ where the SFM is naturally expressed, the model reads :

$$\begin{aligned}
\dot{X} &= (1+i\alpha)\,[\frac{G_+E_+ + G_-E_-}{\sqrt{2}} - X] - (\gamma_a + i\gamma_p)X \\
&+ \beta e^{-ia} Y(t-\tau_r), \qquad (4.9) \\
\dot{Y} &= (1+i\alpha)\,[\frac{G_+E_+ - G_-E_-}{i\sqrt{2}} - Y] + (\gamma_a + i\gamma_p)Y \\
&+ \eta e^{-i\Omega} Y(t-\tau_f)], \qquad (4.10) \\
T\dot{N}_\pm &= \mu - D_\pm - G_\pm |E_\pm|^2 \mp \frac{\gamma_J}{\gamma_e}(N_+ - N_-), \qquad (4.11)
\end{aligned}$$

where $N_\pm$ is the scaled carrier density in each spin channel and $G_\pm = N_\pm(1-(\varepsilon_g/2)|E_\pm|^2)$ is the gain for each circularly polarized component including gain saturation. The origin of ε_g will be further discussed in 4.4.2.2. PSF and XPR have strengths η and β, phases Ω and a, and time delays τ_f and τ_r. In the three equations time has been scaled to the cavity decay rate κ, $T = \kappa/\gamma_e$ is the scaled carrier lifetime and γ_J is the decay rate of the spin difference.

The vectorial LS so far observed in fiber lasers where gain, losses, dispersion and nonlinearities are distributed along the resonator, are usually described by coupled nonlinear Partial Differential Equations (PDE) for the two orthogonal polarization axes. Instead, in our system the nonlinearities are concentrated in a single point (the VCSEL) and the VLS we generate are more properly described by Delay Differential Equations (DDE) rather than PDE. We demonstrate in this section the first temporal localization based on coupled DDEs. We establish a criterion for localization based on the degeneracy of the Floquet exponents.

Via this model, we managed to reproduce the polarization antiphase dynamics and we analysed it using the Stokes parameters representation. This last enabled us to decouple the effects of PSF and XPR and understand their respective role in the polarization flip mechanism. A further analysis revealed that the model can be reduced to a phase model for the polarization orientation, where the VLS are described as kinks of a reminiscent Sine-Gordon equation [Dodd 1984].

Lastly, even if we proved that we created vectorial LS with our experiment, the weak stability of our regime and the difficulties in implementing a controlled temporal perturbation prevented us from experimentally addressing these structures. Therefore, the advantage of the numerical study lies in the possibility of addressing the VLS by applying a local perturbation in the system. We demonstrate the robustness of the dynamics by writing a complete set of vectorial bits which suggests that our VLS can be used for information processing.

4.4.2.1 Vectorial localized structures and molecules

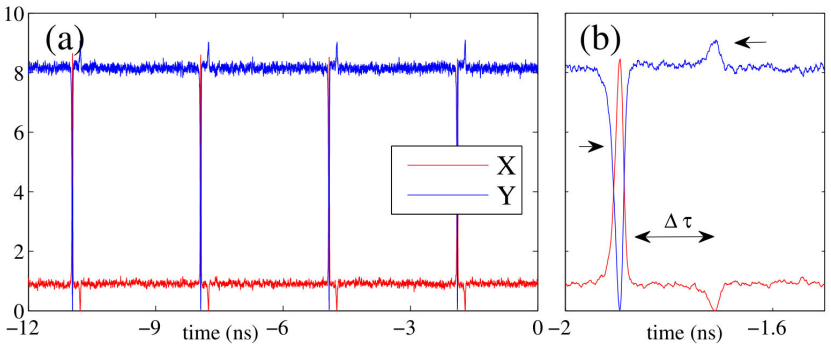

Figure 4.32: Theoretical temporal trace for a single vectorial LS (a) created by perturbing the phase of PSF and zoom on the pulse detail (b): the antiphase dip is followed by a small inverted kink after a time delay Δ_τ corresponding to the re-injection of Y into X after a longer time τ_r. Other exponentially decreasing replica of this secondary kink (not visible) follow at time intervals $n\Delta_\tau$.

The parameters values used in the simulation in order to recreate the VLS dynamics are guided by the experimental situation. XPR and PSF rates are set respectively to $\beta = 0.06$ and $\eta = 0.09$ while Ω = a = 0. We assume typical values $\alpha = 2$, $\varepsilon_g = 2{*}10^{-2}$, $\gamma_a = 0$, $\gamma_p = 5{*}10^{-2}$, μ=10, T = 500 and $\gamma_J = 60\gamma_e$ which, taking $\kappa^{-1} = 2$ ps, correspond to a carrier lifetime ${\gamma_e}^{-1} = 1$ ns, a spin difference decay time ${\gamma_J}^{-1} = 16.6$ ps, a frequency splitting $\gamma_p\kappa/\pi \approx 8$ GHz and a relaxation oscillation frequency $\nu_r = (2\pi)^{-1}\sqrt{2(\mu-1)\gamma_e\kappa} \approx 15$ GHz.

Fig. 4.32a) shows a dynamical state for the 1-VLS case in good agreement with the experiment: the intensity of each linearly polarized component displays localized antiphase pulsations separated by the PSF time ($\tau_f = 3$ ns), followed by a small inverted kink after a time $\Delta_\tau = \tau_r$ - $\tau_f = 0.2$ ns (with $\tau_r = 3.2$ ns), see Fig. 4.32b). We predict an almost 100 % antiphase as well as pulse-widths of the order of ≈ 30 ps which is compatible with the experimental results taking into account the bandwidth limitations. Importantly, such regime coexists with a c.w. solution and in-between pulses (or in the absence of them), the emission consists in a quasi-linearly polarized mode whose orientation is neither X nor Y. The polarization orientation is governed by a complex interplay between the dichroism, the birefringence, the PSF and the XPR rates as well as the two delays, see [Javaloyes 2014] for details. Typically, the suppression ratio between I_y=I_x can be tuned between 20 and 5.

In addition to isolated LS, we reproduce the coexistence of multiple independent solitons, see Fig. 4.33a). Here $\tau_r = 3.6$ ns and $\Delta_\tau = 0.6$ ns in order to better visualize the shadow of the pulse. The presence of the inverted kink in the experimental data can be appreciated in Fig. 4.33a) as a dark shadow following the LS at a distance Δ_τ. Also, similarly to the experiment, one may barely notice the existence of a second shadow following the LS at a distance of $2\Delta_\tau$. We already revealed in the experimental part that any "strong enough" shadow could act as a pinning defect in the longitudinal space of propagation. Therefore we need to address a second

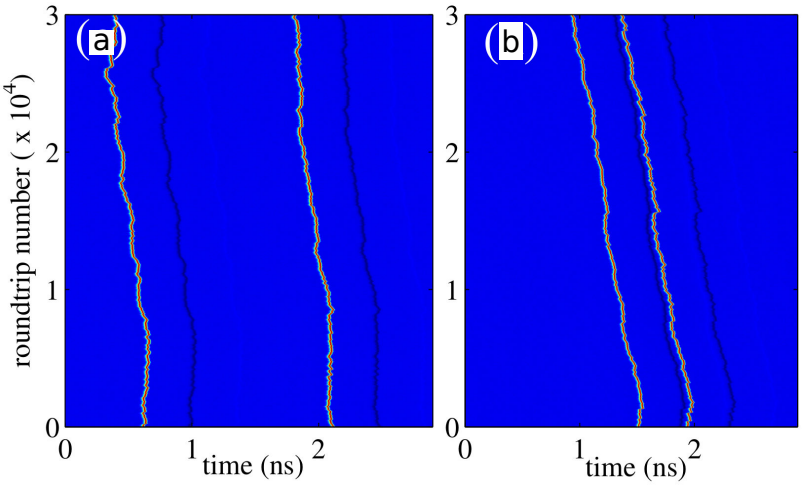

Figure 4.33: Folded space-time representations: the shadow following the LS corresponds to the inverted dip at Δ_τ. In (a) the second LS was created far from the first one yielding two independent objects as evidenced by their uncorrelated motion. Conversely, if the second LS is nucleated at some precise closer distance, one obtains a bounded state (b) where the two solitons exhibit correlated motion. The period of the solutions is slightly superior to τ_f, such secular drift being due to the finite response time of the VCSEL.

VLS far from the first-born one in order to escape from any binding force. The second VLS is created at a distance d $> 3\Delta_\tau$ and one can appreciate that this second VLS exhibits a motion independent on the right VLS. This second VLS is also accompanied by two ghosts at Δ_τ and $2\Delta_\tau$. Additional LS can be written at arbitrary positions without perturbing the already present localized structures. The bound states are accounted for as well, which can be appreciated in Fig. 4.33b). We explain the existence of a specific binding distance to the small kink generated in the wake of the vectorial LS by the replica of the main LS impinging the VCSEL a second time after a time interval Δ_τ, in agreement to the experimental results.

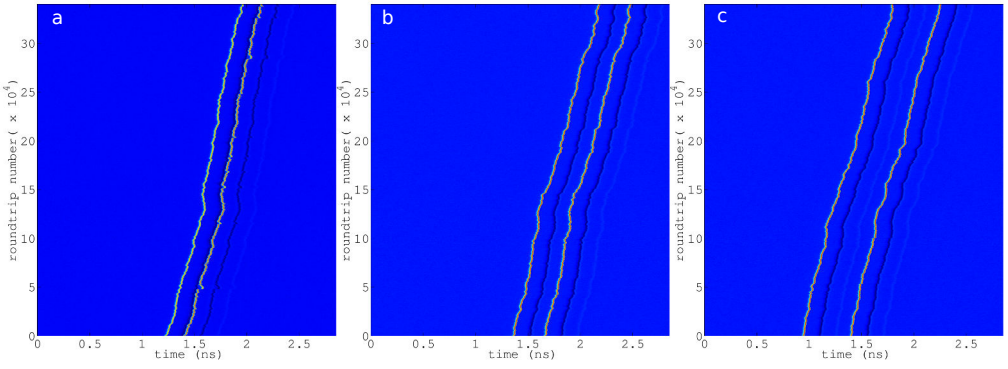

Figure 4.34: Several stable equilibrium distances are found and correspond to multiples of Δ_τ: a) Δ_τ, b) $2\Delta_\tau$ c) $3\Delta_\tau$). The larger the distance, the weaker the binding force as indicated by the larger amount of fluctuation between the two elements of the molecule.

Fig. 4.34 shows that the exponentially decreasing replica of VLS at times $n\Delta_\tau$ (here Δ_τ is the same as in Fig. 4.32) can generate a weak binding force that pins the distances between VLS in a molecule. This is in fantastic agreement with the experimental results exposed in Fig. 4.29 since, as the VLS interval increases (from a) to c)) the motions become less and less correlated. Such effect is similar to the ultra-weak interaction of DS in fibers with sound waves shown in [Jang 2013b].

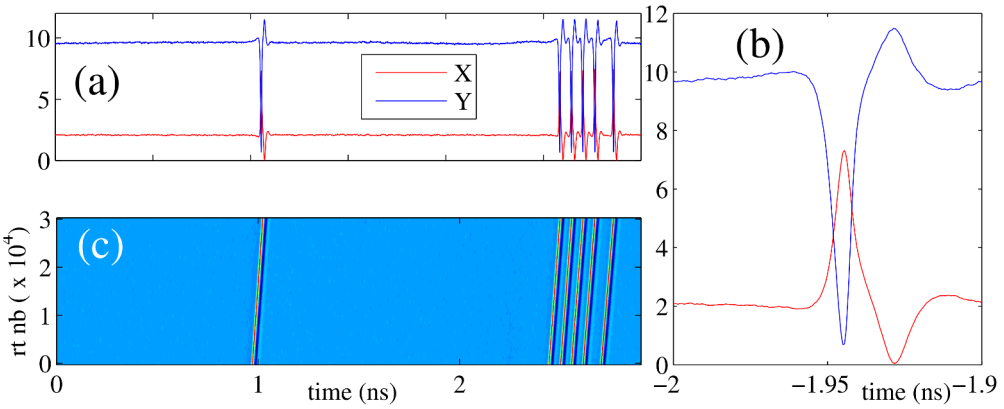

Figure 4.35: Temporal time trace (a) with $\gamma_p = 0.1$ (corresponding to a frequency splitting of 15 GHz), $\tau_f = 3$ ns and $\tau_r = \tau_f + 18$ ps. The full orbit considering the oscillatory tail represented in (b) is around 25 ps. A complex bit sequence is represented in (c) over many round-trips signaling the stability of the setup to store information as polarization encoded bit sequences.

However, with the perspective of applications in mind, such multiple binding distances can be a hindrance and the value of Δ_τ can be reduced as much as the time corresponding to the VLS time-width. Here, the secondary kink would be located at a very close distance, thereby negating this multiplicity of binding distances. This is easily realized numerically, and by setting $\Delta_\tau = 18$ ps (with $\tau_r = 3.018$ ns) we end up with the temporal trace shown in Fig. 4.35a). Here 6 VLS coexist in the cavity, Δ_τ is so small that no replica can be observed onto the background. Thus no binding distance is imposed and two VLS can coexist with a time interval of about 70 ps. Fig. 4.35c) represents the space-time diagram corresponding to the temporal trace. In this configuration, a maximum of $\tau_f/\Delta_\tau \approx 40$ VLS can be independently addressed which makes this system potential for fast information processing. For all the results of Fig. 4.35, the birefringence has been raised to about 15 GHz (2 times the real value) and the consequence is described in Fig. 4.35b). We show an enlarged representation of one of the pulses in panel a). The pulse width is now about 10 ps (instead of 30 ps for a birefringence of 7.5 GHz) and the full orbit considering the oscillatory tail is around 25 ps. This result demonstrates that the birefringence is the parameter that controls the pulse width in our system; it is logic since we are dealing with a pure antiphase dynamics where the carrier lifetime may not be the time scale limit regarding the pulse-width.

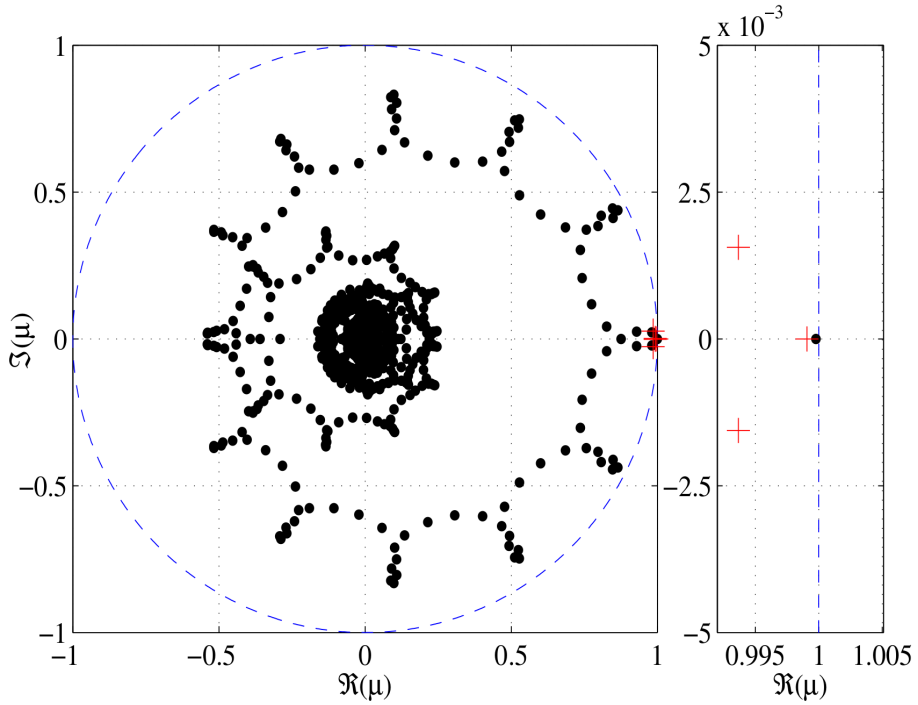

Figure 4.36: Floquet multipliers μ (black circles) of the single LS solution showed in Fig. 4.32a). All the multipliers have a modulus smaller than unity, as expected for a stable solution. A zoom in the vicinity of $\mu = 1$ allows to find a single multiplier as expected for a periodic solution in a time-independent dynamical system. For the case of N = 3 LS, we represent for clarity only the right-most multipliers (red crosses): we notice the existence of not one but three quasi-degenerate Floquet multipliers that have no equivalent with the single LS case, demonstrating the existence of N degenerate neutral modes that correspond to independent translational motion of the various LS. The fact that the three multipliers are not exactly equal to unity is a consequence of the ultra-weak residual interactions between distant LS. Such residual interaction implies that multiple LS are not totally independent for any finite values of the delay.

As a proof of the independence of the LS, we performed the analysis of the Floquet multipliers considering the LS as periodic solutions of a high-dimensional dynamical system. The results of our analysis are depicted in Fig. 4.36 for the case of one and three LS. With three LS, we notice in the vicinity of $\mu = 1$ the existence of not one but three quasidegenerate Floquet multipliers. We analyzed the eigenvectors associated with these neutral modes and found that they correspond to relative translations of each LS, further confirming, beyond the observation of correlated or uncorrelated motion in Fig. 4.32c-d), their independence and defining mathematically the concept of temporal localization within the framework of delayed systems. Interestingly, the analysis of bound states yielded a single multiplier $\mu = 1$ confirming that the ensemble moves as a single entity. Finally, the presence of many weakly damped oscillatory modes in Fig. 4.36 explains the variations of pulse heights and the sensitivity of the system to noise.

4.4.2.2 Vectorial localized structures as polarization kinks and antikinks

The experimental and theoretical results presented previously are obtained when the laser is biased well above threshold (about 10 times in both cases). In this pumping current range, one expects the dynamics that involves the relaxation oscillations (RO) between the total emitted power and the carrier reservoir to play only a minor role. Typically, when J $\approx$ 10*J_{th}, the RO frequency experimentally measured is about 12 GHz. The strong damping of the RO that we observe renders our VCSEL almost a class-A laser. Standard unsaturated rate equations and the SFM model do not reproduce this regime of strong damping and so in our model we included a nonlinear saturation for the gain that we express here in the circular basis :

$$G_{\pm} = D_{\pm}(1 - \frac{\varepsilon_g}{2}|E \pm|^2), \tag{4.12}$$

Several physical effects can contribute to the gain compression parameter ε_g like, for instance, spatial hole burning in the transverse plane of the VCSEL, spectral hole burning due to saturation of the individual intra-band transitions, as well as carrier heating. In the following, we assumed that ε_g is a real number which is consistent with a situation dominated by spatial hole burning, i.e. inter-band saturation.

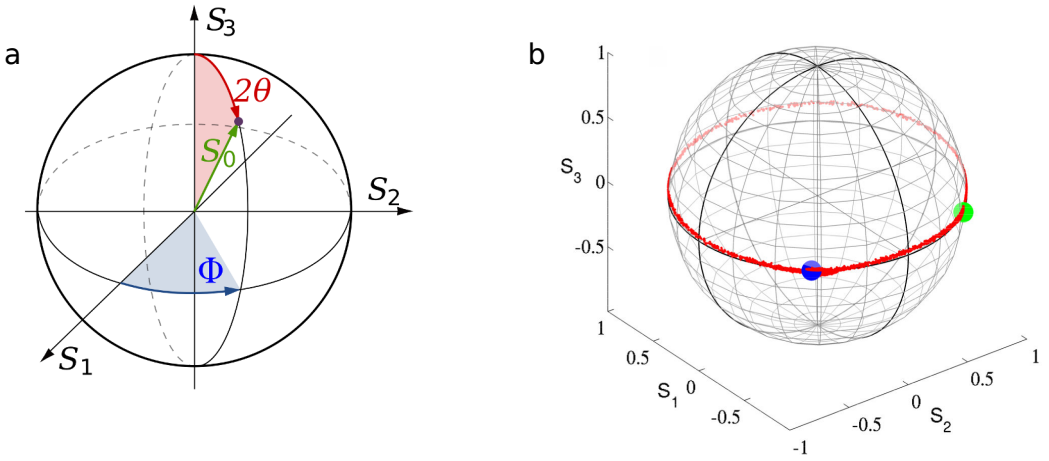

Figure 4.37: a) Angular representation of the VCSEL dynamics onto the Poincaré sphere. b) Stokes representation of the VLS polarization dynamics.

Far from threshold, the fluctuations of the total intensity die out rapidly and the dynamics is confined on a Poincaré sphere with a radius given by twice the total intensity 2I. Without external perturbations, one may not expect any complex residual dynamics since the reduced dynamics is only two-dimensional. It consists of the polarization angle Φ and the ellipticity parameter θ, the optical phase being decoupled from the rest, see Fig. 4.37a). We recall that the normalized Stokes parameters read:

$$S_0 = |E_-|^2 + |E_+|^2 = 2I \quad , \quad S_1 = 2\Re\left(E_-^\star E_+\right) = S_0 sin(2\theta)cos(\Phi)$$
$$S_2 = -2\Im\left(E_-^\star E_+\right) = S_0 sin(2\theta)sin(\Phi) \quad , \quad S_3 = |E_-|^2 - |E_+|^2 = S_0 cos(2\theta).$$

In addition, strongly elliptical states would incur a large energetic penalty due to the induced imbalance between the two carrier reservoirs. This further confines the residual dynamics to the vicinity of the equatorial plane, i.e. $\theta = \pi/4$. As such, the dynamics takes place over an invariant circle corresponding to the intersection between the equatorial plane and the Poincaré sphere.

We show in Fig. 4.37b) the temporal trace during the vectorial LS regime using the Stokes representation. It is found that the orbit proceeds essentially along the equator of the sphere ($|S3| \approx 0$). The system starts form the stable quasi-linearly polarized state represented by a green circle and performs a full clockwise rotation to reach the blue circle. Because these two polarizations are degenerate in a representation based solely upon the intensity dynamics of X and Y, one would think having reached the initial point. Yet, it is only after receiving the second delayed perturbation after an additional time delay Δ_τ that the polarization cycle is closed. Incidentally, this explains why the secondary kink in Fig. 4.32a-b) is upward since one must pass through the pure Y emission state (S1 = -1) during this secondary plateau.

Such phase-kinks are reminiscent of the Sine-Gordon phase equation which is know to give topological kinks and anti-kinks solutions. In our case the phase must be interpreted as the orientation of the polarization Φ. After applying a multiple time scales analysis to Eq. (4.9-4.11) considering the relaxation oscillations as a smallness parameter (since we are far from threshold, see [Javaloyes 2014] for more details), we obtain a phase model for the orientation, i.e. the difference between the two circular components of the field $\psi_\pm$, $\Phi = \psi_+ - \psi_-$ (with $(\cos\Phi, \sin\Phi)=(S_1, S_2)$). The global optical phase is represented conveniently by the half sum $\Sigma = (\psi_+ + \psi_-)/2$. The reduced model with PSF and XPR, which is valid only far from threshold, reads

$$\begin{aligned}
\dot{\Sigma} &= (\alpha\gamma_a - \gamma_p)\cos\Phi - \bar{\eta}\sin\frac{\Phi^{\tau_f}}{2}\sin\frac{\Phi}{2}\sin\left(u+\Omega+\Sigma-\Sigma^{\tau_f}\right) \\
&+ -\bar{\beta}\cos\frac{\Phi}{2}\sin\frac{\Phi^{\tau_r}}{2}\sin\left(u+a+\Sigma-\Sigma^{\tau_r}\right), \qquad (4.13)\\
\frac{\dot{\Phi}}{2} &= (\gamma_a + \alpha\gamma_p)\sin\Phi + \bar{\eta}\sin\frac{\Phi^{\tau_f}}{2}\cos\frac{\Phi}{2}\cos\left(u+\Omega+\Sigma-\Sigma^{\tau_f}\right) \\
&+ -\bar{\beta}\sin\frac{\Phi}{2}\sin\frac{\Phi^{\tau_r}}{2}\cos\left(u+a+\Sigma-\Sigma^{\tau_r}\right) \qquad (4.14)
\end{aligned}$$

with $\left(\bar{\eta},\bar{\beta}\right) = \left(\bar{\eta},\bar{\beta}\right)\sqrt{1+\alpha^2}$ and $u = \arctan\alpha$. It is worthwhile to notice that these two phases Φ and Σ are of very different nature: while the optical phase precise value (Σ) is irrelevant due to the phase invariance in an autonomous system, the orientation phase (Φ) value is a meaningful quantity due to the broken rotational invariance imposed by the dichroism and the birefringence of the VCSEL cavity.

In the case of a monochromatic solution, the orientation of the quasi linear polarization Φ reaches a fixed point while the half sum $\Sigma \sim \omega t$ drifts at the frequency of the mode under consideration. The modal structure of Eqs. (4.13,4.14) is a

complex problem and is reported in [Javaloyes 2014]. In the case of the LS presented in this manuscript, hundreds of such monochromatic solutions defined by doublets $[\omega, \Phi(\omega)]$ exist.

The analysis of such modes is useful for explaining the LS in the sense that we identified that some modes verify the resonance condition $u + \Omega + \omega\tau_f = n\pi$ and $u + a + \omega\tau_r = m\pi$. In this case, by writing $\Sigma = \omega t + \delta$ with $\delta \ll 1$, one can decouple the fluctuations of the optical phase δ dynamics from the orientation dynamics and reduce the dynamics to a single equation for Φ:

$$\frac{\dot{\Phi}}{2} = (\gamma_a + \alpha\gamma_p)\sin\Phi + \bar{\eta}\sin\frac{\Phi^{\tau_f}}{2}\cos\frac{\Phi}{2}\cos\left(u + \Omega + \Sigma - \Sigma^{\tau_f}\right) - \bar{\beta}\sin\frac{\Phi}{2}\sin\frac{\Phi^{\tau_r}}{2}, \tag{4.15}$$

The results of our reduced model is in quantitative agreement with the results of the full model and was indeed used to generate Fig. 4.38.

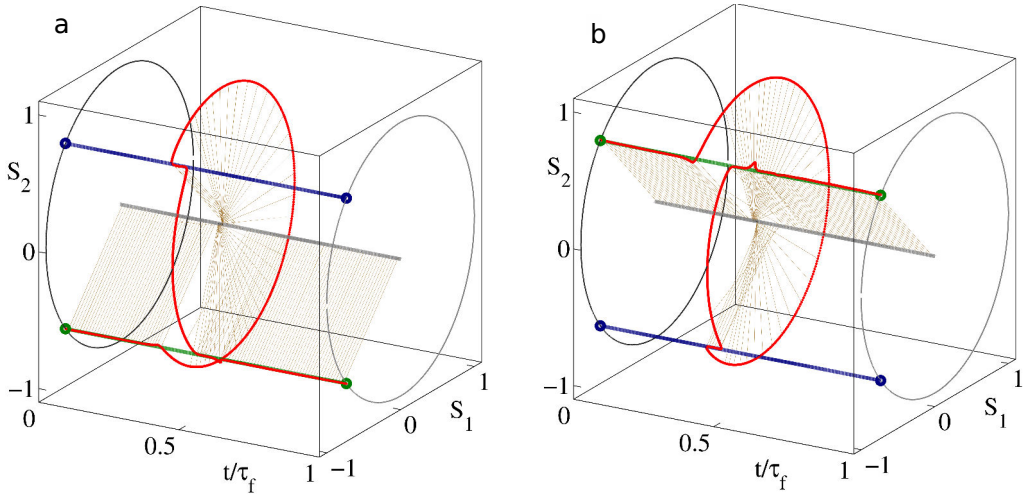

Figure 4.38: A single orbit unfolded in time is presented in (a). Here, one notices the existence of two plateaus corresponding to the antiphase dip followed by the small inverted kink replica after a time $\Delta\tau$. A stable anti-kink was generated in (b) by inverting the phase of the XPR, i.e. setting $\beta \to -\beta$.

In Fig. 4.38a), one can clearly identify two plateaus corresponding to the antiphase dip followed by the small inverted kink replica after a time Δ_τ. We were able to find LS as short as 25 ps both in the full and in the simplified model. Since the phase dynamics proceeds along the equator of the Poincaré sphere or, equivalently, because the polarization remains always linear, there is no imbalance between the two population reservoirs indicating that the spin-flip time scale could not be the ultimate limiting factor regarding the pulse-width.

Also, exploiting the symmetry properties (Φ,β) $\to$ (-Φ, -β), we deduce the existence of anti-kinks solutions, which are depicted in Fig. 4.38b). More complicated kinks and anti-kinks that do not correspond to entire rotations also exist and will be the topic of further studies.

In summary, we demonstrated the existence of vectorial localized structures and molecules in a VCSEL enclosed in a double external cavity. A simple theoretical model was found to reproduce the main experimental features and the pulse shadow was identified as the pinning mechanism allowing the creation of molecules. The proof of independence was given experimentally by the study of the LS random motion and theoretically by the analysis of the Floquet multipliers. We interpreted the LS as rotations along the equatorial plane of the Poincaré sphere and a multiple time scale analysis allowed us to reduce the dynamics to a single delayed equation for the polarization orientation.

4.5 Conclusions

The double delays setup with competitive reinjection mechanisms has induced very rich polarization dynamics. Due to the weak anisotropy of VCSELs, PSF and XPR can temporarily modify the polarization state of the laser emission. Their effect depends on the polarization axis on which they are acting, this is due to the asymmetric polarization stability diagram of the solitary VCSEL. PSF and XPR respective frequencies and rates allow to generate and control fast polarization switchings, which consist either in robust square-wave dynamics or fast polarization flips.

The origin of the SW can be understood as an interplay between XPR, responsible for the onset of a square-wave dynamics, and PSF as a mechanism that increases the dichroism of the device. The SW frequency is thus ruled by the XPR delay, and the ratio between XPR and PSF delays plays a crucial role in the stability of the dynamics. Therefore, it is important to underline that the robust and fast square-wave polarization switchings do not represent temporal localized structures since their duration are fully set by boundary conditions imposed by our double-cavity setup.

If one decreases the XPR rate, then one can set the system in a continuous regime where the two orthogonal linear polarization axes are slightly rotated with respect to the original axes. From that dynamical state on, a small perturbation can provoke the onset of short antiphased pulses in the polarized output of the VCSEL that regenerate after a round-trip in the PSF cavity. Our statistical analysis over the pulses trajectories revealed that noise in the system acts on the pulses as a Langevin Force on free particules, which results in a brownian motion of the pulses. They are therefore independent from any boundary conditions due to the large aspect-ratio between the pulse size and the PSF cavity length : a change in the PSF cavity length does not modify the vectorial pulses temporal width. This large aspect-ratio allows to observe multiple pulsing within the cavity round-trip and noise in our system enables to distinguish between bound states of pulses and independent ones. We thus disclosed for the first time a regime of vectorial localized structures in semiconductor lasers. A theoretical analysis based on the Stokes parameters helped understand the respective roles of PSF and XPR in the

formation of the pulse. While PSF allows the linear polarization to perform a cycle on the Poincaré sphere, the rotation is fully closed and the system reaches the initial point only after a time correponding to XPR delay. The intervention of XPR is also responsible for the generation of a small secondary kink that acts as a pinning mechanism for the creation of another vectorial structure in the cavity. Therefore, at variance with the SW dynamics, it is the difference between the two delays (and not the ratio) that has a seminal importance in the VLS formation and stabilization.

Chapter 5

General conclusion

In this work, I have shown how we can generate scalar and vectorial time-localized structures in the output of a VCSEL.

In chapters 2 and 3 of this manuscript, we experimentally and theoretically studied a situation where a broad-area VCSEL and a RSAM are both located at the Fourier plane of the other. We demonstrated that this non-conventional feedback can induce passive mode-locking of two tilted plane waves traveling in the cavity with an opposite transverse component and alternating each other at every round-trip. These plane waves emitted by the VCSEL appear as spots on the RSAM surface. We observed that these spots are actually pinned by defects on the RSAM, that we interpret as local regions of lower reflectivity where saturation is more efficient. Consequently, it was possible for us to generate two couples of passively mode-locked plane waves with different transverse wave vectors values, their number depending on the number of impurities present on the VCSEL far-field. These defects have been interpreted as local reductions of the RSAM surface reflectivity. Moreover the spots in the far-field can be stirred by displacing the RSAM surface or shifting the position of the collimator in front of the RSAM. We remarked that modifying the transverse wave vector value of the tilted waves induces a spectral shift that can be as large as 4 nm. At last, local changes of reflectivity could also be induced by an external injection beam focused onto the RSAM surface. We strongly believe that we may be able to address the mode-locking regime with a careful tuning of the injection beam frequency and power. Demonstrating such a control of our spatio-temporal dynamics could have very interesting applications in the future and would bring our experimental results very close to the generation of a new type of light-bullets where spatial localization would not take place in the near-field but in the far-field of the VCSEL.

The mode-locked dynamics born from our setup is very robust. We were able to preserve the mode-locking regime for cavities longer than 15 ns (65 MHz) and we actually set a new low-frequency mode-locking record in semiconductor devices. However, in the context of mode-locking, when the cavity length becomes much longer than the gain recovery time of the VCSEL (about 1 ns), harmonic mode-locking usually takes place in order to satisfy the background stability criterion. In our system the harmonic solution exists but it is not the only stable one, it coexists with the fundamental solution and the homogeneous background. We deduced that this long cavity configuration allowed us to disclose a regime where the PML pulses become localized, and therefore a large quantity of stable solutions coexist, each of them being characterized by a different number of pulses per round-trip. As these pulses are scalar localized structures over a stable homogeneous background, one

may be able to address them as independent bits with an external writing beam. Our theoretical analysis on this dynamics brought confirmation that addressing is possible, and we provided some preliminary experimental observations on the effects induced by a sinusoidal modulation applied to the VCSEL pumping current set in resonance with the external cavity FSR. Depending on the DC value of the current and on the modulation amplitude, we disclosed several effects imposed by modulation of the current (inducing modulation of gain in the cavity) such as LS switch-on and switch-off or LS drift. In the near future we plan to obtain a full addressability by locally perturbing our system with an external pulsed laser source in order to turn our system into an all-optical signal processor and buffer.

As VCSELs are devices prown to develop fast polarization dynamics due to their weak anisotropy, we also performed some investigations on the temporal dynamics we could generate taking advantage of their polarization degree of freedom. This work has been presented in chapter 4. In order to simplify our study, we took a small-area VCSEL so as to get rid of transverse modes. Basing ourselves on a theoretical implementation of passive mode-locking [Javaloyes 2006], we submitted our laser to two kinds of polarized feedback mechanisms: one is a polarization-selective feedback (PSF), the other is crossed-polarization reinjection (XPR). We showed that these two effects induce polarization competition for the gain, which leads to two kinds of temporal dynamics in the polarized output of the laser: one is a robust square-wave polarization switching whose period is governed by XPR, the other is a fast polarization reorientation consisting of antiphased pulse with a repetition rate governed by PSF. We demonstrated that this last dynamics is the first experimental observation of temporal vectorial localized structures in semiconductor lasers. Very interestingly, in this scheme only the laser gain medium provides both the mechanism responsible for light amplification and the nonlinearities for light localization, the light experiencing only diffraction in ambient air when propagating in the external cavities. Our theoretical approach, based on the Spin-Flip model, well reproduces the experimental results and shows that such vectorial LS can be addressed via local perturbation, which renders the system potential for applications in data processing. A detailed theoretical analysis also showed that far from threshold, the dynamics can be reduced to a phase dynamics, where the phase is the polarization orientation of the output emission of the VCSEL. In this context, the vectorial LS are a new type of topological structures, which can be compared to the solutions of a Sine-Gordon equation for the linear polarization orientation.

Both scalar and vectorial temporal LS that we obtained represent the first experimental observations of such objects realized in semiconductor lasers with delays. We believe that these results are of major importance since they involve very simple setups (no injection) and fast time scales, which are crucial properties for a future implementation in optical data processing and buffering systems. The independence of LS existence with respect to boundaries offers a wide range of accessible repetition rates for LS, spanning over hundreds of MHz. In addition, we think that our results are a significant progress towards light-bullets (LB) generation.

In fact, coupling a broad-area VCSEL and a saturable absorber medium has already shown to induce spatial LS formation when the absorber is slow (1 ns) and the cavity is self-imaging [Genevet 2008]. In our case, temporal localization is obtained when the absorber is fast (1 ps) and the Fourier transform of the VCSEL near-field is imaged on it. Thus, in this last configuration, the system is supposed to be unable to support both spatial and temporal localization of light at the same time. Therefore, in order to implement LB, more research is to be carried out using the same devices (VCSEL and RSAM) and setting the cavity in the self-imaging configuration. As we were trying to obtain light-bullets, we first performed experiments with a short external cavity (about the ns), for which magnification (the ratio between the VCSEL transverse size and its image on the RSAM) could not be larger than 2, which prevented us from saturating the RSAM. To our minds, and refering to previous works [Genevet 2009], the cavity had to be short in order to allow the onset of a mode-locked dynamics. Our detailed study of the system, and the proof we brought for the existence of a regime of temporal localization when the external cavity is long, makes us think of further investigating the spatio-temporal dynamics in the long self-imaging cavity condition. Indeed, the more we increase the cavity length, the larger is the magnification we can possibly set. We deduce from the results presented in chapter 2 that the size of the VCSEL image onto the RSAM should be approximately 10 μm, which corresponds to a magnification of about 20 in order to saturate our absorber. In this situation we may have to face some technical problems since the transverse size of the intra-cavity beam may increase a lot, which requires large and good optics in order to prevent too important dissipation of light. A possible way to avoid this difficulty could consist in using a "half-VCSEL" instead of a VCSEL for amplification. Indeed, due to the high-Q of its cavity, the VCSEL usually saturates faster than the RSAM which unfavors the onset of a PML dynamics. Removing part of the top Bragg reflectors of the VCSEL would decrease the lifetime of light in the VCSEL cavity and prevent saturation of the device. The modulation of the gain being decreased this way, the required modulation of losses for the onset of a stable PML regime is diminished as well. As a consequence, the RSAM could be only weakly saturated which means that the magnification of the external cavity could be many times smaller than 20 for the emergence of a PML regime. The so-called Vertical External Cavity Surface-Emitting Laser (VECSEL) consisting of a "half-VCSEL" coupled to a SESAM has been used for the generation of passive mode-locking [Keller 2006], but in these schemes the external cavity is designed to operate in the fundamental Gaussian mode in order to stabilize the PML regime and reach high-power pulsations. A prospect for our study would consist in implementing such a system using an electrically biased broad-area VECSEL where the external cavity would be closed by a RSAM and set in the self-imaging configuration. We believe that a dynamics consisting of pulsing spatial localized structures could develop out of this experimental scheme.

At last, a second method one could investigate in order to make spatial LS pulse would take advantage of our results on polarization dynamics. Indeed, our method for generating vectorial LS could be implemented in a broad-area VCSEL. One could imagine obtaining spatial LS following the experimental realization of Genevet et al. [Genevet 2008] in which two broad-area VCSELs, one acting as an amplifier and one as an absorber, are coupled via a self-imaging external cavity. Once this regime is reached, an external XPR mechanism could be implemented on a single spatial LS in order to generate a robust square-wave switching if XPR rate is high or a vectorial LS dynamics if XPR rate is low.

Bibliography

[Ackemann 1994] T. Ackemann and W. Lange. *Non- and nearly hexagonal patterns in sodium vapor generated by single-mirror feedback.* Phys. Rev. A, vol. 50, pages R4468–R4471, 1994. (Cited on page 4.)

[Ackemann 2001] T. Ackemann and M. Sondermann. *Characteristics of polarization switching from the low to the high frequency mode in vertical-cavity surface-emitting lasers.* Appl. Phys. Lett., no. 78, page 3574, 2001. (Cited on page 36.)

[Afanasjev 1995] V. V. Afanasjev. *Soliton polarization rotation in fiber lasers.* Optics Letters, vol. 20, pages 270–272, 1995. (Cited on page 18.)

[Agrawal 1989] G. P. Agrawal. In Nonlinear fiber Optics. Academic Press, San Diego, 2^{nd} edition, 1989. (Cited on pages 5, 18 and 20.)

[Akhmediev 1995] N. N. Akhmediev, A. V. Buryak, J. M. Soto-Crespo and D. R. Andersen. *Phase-locked stationary soliton states in birefringent nonlinear optical fibers.* Journal of the Optical Society of America B, vol. 12, pages 439–439, 1995. (Cited on page 18.)

[Akhmediev 1997] N. N. Akhmediev, A. Ankiewicz and J. M. Soto-Crespo. *Multisoliton solutions of the complex Ginzburg–Landau equation.* Physical Review Letters, vol. 79, pages 4047–4051, 1997. (Cited on page 29.)

[Amann 1998] M.-C. Amann. *Tunable Laser Diodes.* 685 Canton Street, Norwood, MA 02062: Artech House, Inc., 1998. (Cited on page 12.)

[Aranson 2002] Igor S. Aranson and Lorenz Kramer. *The world of the complex Ginzburgh-Landau equation.* Review of Modern Physics, vol. 74, page 99, 2002. (Cited on page 7.)

[Arecchi 1992] F. T. Arecchi, G. Giacomelli, A. Lapucci and R. Meucci. *Two-dimensional representation of a delayed dynamical systems.* Physical Review A, vol. 45, pages 4225–R4228, 1992. (Cited on pages 66 and 106.)

[Arecchi 1993] F. T. Arecchi, S. Boccaletti, P.L. Ramazza and S. Residori. *Transition from boundary to bulk-controlled regimes in optical pattern formation.* Physical Review Letters, vol. 70, pages 2277–2280, 1993. (Cited on page 9.)

[Arecchi 1995] F. T. Arecchi. *Optical morphogenesis : pattern formation and competition in nonlinear optics.* Physical D : Nonlinear phenomena, vol. 86, pages 297–322, 1995. (Cited on pages 4, 6, 9 and 19.)

[Astrov 1997] Yu. A. Astrov and Yu. A. Logvin. *Formation of Clusters of Localized States in a Gas Discharge System via a Self-Completion Scenario.* Physical Review Letters, vol. 79, pages 2983–2986, Oct 1997. (Cited on pages 8 and 9.)

[Avrutin 2000] E. A. Avrutin, J. H. Marsh and E. L. Portnoi. *Monolithic and multi-GigaHertz mode-locked semiconductor lasers: Constructions, experiments, models and applications.* IEEE Proceedings Opto-Electronics, vol. 147, pages 251–278, 2000. (Cited on page 43.)

[Babushkin 2004] I. V. Babushkin, N. A. Loiko and T. Ackemann. *Eigenmodes asymmetry selection mechanisms in circular large-aperture vertical-cavity surface-emitting laser.* Physical Review E, vol. 69, page 066205, 2004. (Cited on pages 49 and 57.)

[Bache 2005] M. Bache, F. Prati, G. Tissoni, R. Kheradmand, L.A. Lugiato, I. Protsenko and M. Brambilla. *Cavity soliton laser based on VCSEL with saturable absorber.* Applied Physics B, vol. B, no. 81, pages 913–920, 2005. (Cited on page 17.)

[Balle 1999] S. Balle, E. Tolkachova, M. San Miguel, J. Tredicce, J. Martin-Regalado and A. Gahl. *Eigenmodes asymmetry selection mechanisms in circular large-aperture vertical-cavity surface-emitting laser.* Optics Letters, vol. 24, page 1121, 1999. (Cited on page 37.)

[Bao 2011] Qiaoliang Bao, Han Zhang, Zhenhua Ni, Yu Wang, and Zexiang Shen Lakshminarayana Polavarapu, Qing-Hua Xu, Dingyuan Tang and Kian Ping Loh. *Monolayer graphene as a saturable absorber in a mode-locked laser.* Nano Research, vol. 4, pages 297–307, 2011. (Cited on page 33.)

[Barland 2002] S. Barland, J. R. Tredicce, M. Brambilla, L. A. Lugiato, S. Balle, M. Giudici, T. Maggipinto, L. Spinelli, G. Tissoni, Thomas Knoedl, M. Miller and R. Jager. *Cavity solitons as pixels in semiconductor microcavities.* Nature, vol. 419, pages 699–702, 2002. (Cited on pages iii, 17, 18, 19, 20, 21 and 31.)

[Benjamin 1967] T. Brooke Benjamin and J. E. Feir. *The disintegration of wave trains on deep water.* J. Fluid. Mech., vol. 27, pages 417–430, 1967. (Cited on page 4.)

[Bode 2002] M. Bode, A.W. Liehr, C.P. Schenk and H.-G. Purwins. *Interaction of dissipative solitons: particle-like behaviour of localized structures in a three-component reaction-diffusion system.* Physica D, vol. 161, pages 45–66, 2002. (Cited on page 8.)

[Bödeker 2003] H. U. Bödeker, M. C. Röttger, A. W. Liehr, T. D. Frank, R. Friedrich and H.-G. Purwins. *Noise-covered drift bifurcation of dissipative solitons in a planar gas-discharge system.* Physical Review E, vol. 67, page 056220, 2003. (Cited on page 107.)

[Brambilla 1996] M. Brambilla, L. A. Lugiato and M. Stefani. *Interaction and control of optical localized structures.* Europhysics Letters, vol. 34, no. 2, page 109, 1996. (Cited on page 9.)

[Brambilla 1997] M. Brambilla, L. A. Lugiato, F. Prati, L. Spinelli and W. J. Firth. *Spatial Soliton Pixels in Semiconductor Devices.* Physical Review Letters, vol. 79, pages 2042–2045, Sep 1997. (Cited on pages 10 and 17.)

[Brambilla 2004] M. Brambilla, Tommaso Maggipinto, Giuseppe Patera and Lorenzo Columbo. *Cavity Light Bullets: Three-Dimensional Localized Structures in a Nonlinear Optical Resonator.* Physical Review Letters, vol. 93, page 203901, Nov 2004. (Cited on page 25.)

[Burke 2007] John Burke and Edgar Knobloch. *Homoclinic snaking: Structure and stability.* Chaos, vol. 17, page 037102, 2007. (Cited on page 9.)

[Butkus 2013] M. Butkus, E. A. Viktorov, T. Erneux, C. J. Hamilton, G. Maker, G. P. A. Malcolm and E. U. Rafailov. *85.7 MHz repetition rate mode-locked semiconductor disk laser: fundamental and soliton bound states.* Optics Express, vol. 21, pages 25526–25531, 2013. (Cited on page 61.)

[Caboche 2009] E. Caboche, S. Barland, M. Giudici, J. Tredicce, G. Tissoni and L. A. Lugiato. *Cavity-soliton motion in the presence of device defects.* Physical Review A, vol. 80, page 053814, Nov 2009. (Cited on page 75.)

[Chen 1994] C.-J. Chen, P. K. A. Wai and C. R. Menyuk. *Stability of passively mode-locked fiber lasers with fast saturable absorption.* Optics Letters, vol. 19, page 198, 1994. (Cited on page 29.)

[Chen 1995] C.-J. Chen, P. K. A. Wai and C. R. Menyuk. *Self-starting of passively mode-locked lasers with fast saturable absorbers.* Optics Letters, vol. 20, page 350, 1995. (Cited on page 29.)

[Choquette 1995] K. D. Choquette, R. P. Schneider, K. L. Lear and R. E. Leibenguth. *Gain-dependent polarization properties of vertical-cavity lasers.* IEEE J. Sel. Top. Quantum Electron., vol. 1, pages 661–666, 1995. (Cited on page 90.)

[Christodoulides 1988] D. N. Christodoulides and R. I. Joseph. *Vector solitons in birefringent nonlinear dispersive media.* Optics Letters, vol. 12, pages 53–55, 1988. (Cited on page 18.)

[Clerc 2005] M. G. Clerc and C. Flacon. *Localized Patterns and hole solutions in one-dimensional extended systems.* Physica A: Statistic mechanics and its applications, vol. 356, page 48, 2005. (Cited on page 9.)

[Coen 1997] S. Coen and M. Haelterman. *Modulational Instability Induced by Cavity Boundary Conditions in a Normally Dispersive Optical Fiber.* Physical Review Letters, vol. 70, page 4139, 1997. (Cited on page 5.)

[Coen 2013] Stéphane Coen, Hamish G. Randle, Thibaut Sylvestre and Miro Erkintalo. *Modeling of octave-spanning Kerr frequency combs using a generalized*

mean-field Lugiato–Lefever model. Optics Letters, vol. 38, page 37, 2013. (Cited on page 6.)

[Collings 2000] B. C. Collings, S. T. Cundiff, N. N. Akhmediev, J. M. Soto-Crespo, K. Bergman and W. H. Knox. *Polarization-locked temporal vector solitons in a fiber laser: experiment.* J. Opt. Soc. Am. B, vol. 17, pages 354–365, 2000. (Cited on page 34.)

[Coullet 2000a] P. Coullet, C. Reira and C. Tresser. *Qualitative Theory of Stable Localized Structures in One Dimension.* Progress of Theoretical Physics, vol. 139, page 46, 2000. (Cited on pages 9 and 79.)

[Coullet 2000b] P. Coullet, C. Reira and C. Tresser. *Stable Static Localized Structures in One Dimension.* Physical Review Letters, vol. 84, page 3069, 2000. (Cited on page 9.)

[Coullet 2002] P. Coullet. *Localized patterns and fronts in nonequilibrium systems.* International journal of bifurcations and chaos, vol. 11, pages 2445–2457, 2002. (Cited on page 9.)

[Coullet 2004a] P. Coullet, C. Reira and C. Tresser. *A new approach to data storage using localized structures.* Chaos, vol. 14, page 193, 2004. (Cited on pages 9 and 79.)

[Coullet 2004b] P. Coullet, C. Toniolo and C. Tresser. *How much information one can store in a nonequilibrium medium ?* Chaos, vol. 14, pages 839–844, 2004. (Cited on page 9.)

[Cross 1993] M. C. Cross and P. C. Hohenberg. *Pattern formation outside of equilibrium.* Reviews of Modern Physics, vol. 65, page 851, 1993. (Cited on page 4.)

[Cundiff 1999] S. T. Cundiff, B. C. Collings, N. N. Akhmediev, J. M. Soto-Crespo, K. Bergman and W. H. Knox. *Observation of Polarization-Locked Vector Solitons in an Optical Fiber.* Physical Review Letters, vol. 82, pages 3988–3991, 1999. (Cited on page 34.)

[D'Alessandro 1991] G. D'Alessandro and W.J. Firth. *Spontaneous Hexagon formation in a nonlinear optical medium with feedback mirror.* Physical Review Letters, vol. 66, pages 2597–2600, 1991. (Cited on page 4.)

[Damen 1991] T.C. Damen, L. Vina, J.E. Cunningham, J. Shah and L.J. Sham. *Subpicosecond spin relaxation dynamics of excitons and free carriers in GaAs quantum wells.* Physical Review Letters, vol. 67, pages 3432–3435, 1991. (Cited on page 37.)

[Dennard 1968] R.H. Dennard. *Field-effect transistor memory DRAM.* Patent, vol. 3,387,286, 1968. (Cited on page 15.)

[Ding 2009] E. Ding and J. N. Kutz. *Operating regimes, split-step modeling, and the Haus Master Mode-Locking Model.* Journal of the Optical Society of America B, vol. 26, pages 2290–2300, 2009. (Cited on page 29.)

[Dodd 1984] R. K. Dodd, J. C. Eilbec, J. D. Gibbon and H. C. Morris. Solitons and nonlinear wave equations. London: Academic Press, 1984. (Cited on page 115.)

[Dokhane 2001] N. Dokhane and Lippi. G. L. *Chirp reduction in semiconductor lasers through injection current patterning.* Applied Physics Letters, vol. 78, page 3938, 2001. (Cited on page 12.)

[Dorren 2003] H. Dorren, D. Lenstra, Y. Liu, M. Hill and G.-D. Khoe. *Nonlinear polarization rotation in semiconductor optical amplifiers: theory and application to all-optical flip-flop memories.* IEEE Journal of Quantum Electronics, vol. 39, pages 141–148, 2003. (Cited on page 27.)

[Eckhaus 1965] W. Eckhaus. Studies in nonlinear stability theory. Springer, Berlin, 1965. (Cited on page 4.)

[Engelborghs 2001] K. Engelborghs, T. Luzyanina and G. Samaey. In Dde-biftool v. 2.00: a matlab package for bifurcation analysis of delay differential equations. Technical report. Department of Computer Science, K.U.Leuven, Belgium, 2001. (Cited on page 77.)

[Erneux 1999] T. Erneux, J. Danckaert, K. Panajotov and I. Veretennicoff. *Two-variable reduction of the San Miguel–Feng–Moloney model for vertical-cavity surface-emitting lasers.* Physical Review A, vol. 59, page 4660, June 1999. (Cited on page 89.)

[Fauve 1990] S. Fauve and O. Thual. *Solitary waves generated by subcritical instabilities in dissipative systems.* Physical Review Letters, vol. 64, pages 282–284, Jan 1990. (Cited on pages 8, 9, 29 and 63.)

[Fedorov 2000] S. V. Fedorov, A. G. Vladimirov, G. V. Khodova and N. N. Rosanov. *Effect of frequency detunings and finite relaxation rates on laser localized structures.* Physical Review E, vol. 61, pages 5814–5824, 2000. (Cited on page 24.)

[Fermann 1993] M. E. Fermann, M. J. Andrejco, Y. Silberberg and M. L. Stock. *Passive mode locking by using nonlinear polarization evolution in a polarization-maintaining erbium-doped fiber.* Optics Letters, vol. 18, pages 894–896, 1993. (Cited on page 32.)

[Firth 1996] W. J. Firth and A. J. Scroggie. *Optical Bullet Holes: Robust Controllable Localized States of a Nonlinear Cavity.* Physical Review Letters, vol. 76, pages 1623–1626, Mar 1996. (Cited on pages 9, 10 and 69.)

[Fischer 1996] I. Fischer, O. Hess, W. Elsasser and E. Gobel. *Complex spatiotemporal dynamics in the near-field of a broad-area semiconductor laser.* Optoelectronics, vol. 35, pages 579–584, 1996. (Cited on page 44.)

[Fork 1983] R. Fork, C. Shank, R. Yen and C. Hirlimann. *Femtosecond optical pulses.* IEEE Journal of quantum electronics, vol. 19, pages 500–506, 1983. (Cited on page 43.)

[Fukano 2004] H. Fukano, T. Yamanaka, M. Tamura, H. Nakajima, Y. Akage, Y. Kondo and T. Saitoh. *40 Gbit/s electro absorption modulators with 1.1 V driving voltage.* Journal of Lightwave Technology, vol. 40, pages 1144–1146, 2004. (Cited on page 13.)

[Galvanauskas 2004] A. Galvanauskas and B. Samson. *Large Mode Area Fibers.* OE magazine, pages 15–17, 2004. (Cited on page 14.)

[Gapontsev 2004] D. Gapontsev. *Recent Progress on High Power Fiber Lasers.* Diode and Solid State Laser Technology Review, 2004. (Cited on page 14.)

[Gavrielides 2006] A. Gavrielides, T. Erneux, W. S. Sukow, B. Guinevere, T. McLachlan, J. Miller and Amonette J. *Square-wave switching by crossed-polarization gain modulation in vertical-cavity semiconductor lasers.* Optics Letters, vol. 76, pages 2006–2008, 2006. (Cited on pages 38 and 99.)

[Genevet 2008] P. Genevet, S. Barland, M. Giudici and J. R. Tredicce. *Cavity Soliton Laser Based on Mutually Coupled Semiconductor Microresonators.* Physical Review Letters, vol. 101, page 123905, Sep 2008. (Cited on pages iii, 7, 17, 24, 31, 127 and 128.)

[Genevet 2009] P. Genevet. *Laser à Solitons et Vortex Localisés.* PhD thesis, Université de Nice Sophia Antipolis, 2009. (Cited on pages 31, 65 and 127.)

[Giacomelli 1996] G. Giacomelli and A. Politi. *Relationship between delayed and spatially extended dynamical systems.* Physical Review Letters, vol. 76, pages 2686–2689, 1996. (Cited on pages 31 and 106.)

[Giudici 1999] M. Giudici, S. Balle, T. Ackemann, S. Barland and J. R. Tredicce. *Polarization dynamics in vertical-cavity surface-emitting lasers with optical feedback: experiment and model.* J. Opt. Soc. Am. B, vol. 16, no. 11, pages 2114–2123, Nov 1999. (Cited on page 37.)

[Gordon 2002] A. Gordon and B. Fischer. *Phase transition theory of many-mode ordering and pulse formation in lasers.* Physical Review Letters, vol. 89, page 103901, 2002. (Cited on page 26.)

[Grabherr 1998] M. Grabherr, R. Jager, M. Miller, C. Thalmaier, J. Herlein, R. Michalzik and K. Ebeling. *High-power mixsel, an integrated ultrafast semiconductor laser with 6.4 W average power.* IEEE Photonics Technology Letters, vol. 10, pages 1061–1063, 1998. (Cited on page 44.)

[Graham 1975] R. Graham. Fluctuations, instabilities and phase transitions. Berlin, Springer, 1975. (Cited on page 29.)

[Grelu 2002] Ph. Grelu, F. Belhache, F. Gutty and Soto-Crespo. *Phase-locked soliton pairs in a stretched-pulse fiber laser.* Optics Letters, vol. 27, pages 966–968, 2002. (Cited on page 29.)

[Grelu 2003] Ph. Grelu, J. Beal and J. M. Soto-Crespo. *Soliton pairs in a fiber laser: from anomalous to normal average dispersion regime.* Optics Express, vol. 11, pages 2238–2243, 2003. (Cited on page 29.)

[Grelu 2012] P. Grelu and N. Akhmediev. *Dissipative solitons for mode-locked lasers.* Nature Photonics, vol. 6, pages 84–92, 2012. (Cited on pages 6, 9, 17, 30, 31, 63 and 67.)

[Grynberg 1988] G. Grynberg, E. Le Bihan, P. Verkerk, P. Simoneau, J.R.R. Leite, D. Bloch, S. Le Boiteux and M. Ducloy. *Observation of instabilities due to mirrorless four-wave mixing oscillation in sodium.* Optics Express, vol. 11, pages 2238–2243, 1988. (Cited on page 4.)

[Hachair 2004] Xavier Hachair, Stéphane Barland, Luca Furfaro, Massimo Giudici, Salvador Balle, Jorge R. Tredicce, Massimo Brambilla, Tommaso Maggipinto, Ida M. Perrini, Giovanna Tissoni and Luigi Lugiato. *Cavity solitons in broad-area vertical-cavity surface-emitting lasers below threshold.* Physical Review A, vol. 69, page 043817, Apr 2004. (Cited on page 19.)

[Hachair 2005] X. Hachair, S. Barland, J. R. Tredicce and Gian Luca Lippi. *Optimization of the switch-on and switch-off transition in a commercial laser.* Applied Optics, vol. 44, page 4761, 2005. (Cited on page 12.)

[Haelterman 1992] M. Haelterman, S. Trillo and S. Wabnitz. *Additive-modulation-instability ring laser in the normal dispersion regime of a fiber.* Optics Letters, vol. 17, page 745, 1992. (Cited on pages 5 and 6.)

[Haken 1983] H. Haken. Synergetics. Berlin, Springer, 1983. (Cited on page 29.)

[Hansson 2014] T. Hansson and S. Wabnitz. *bichromatically pumped microresonator frequency combs.* Physical Review A, vol. 00, page 003800, 2014. (Cited on pages 68 and 69.)

[Harkness 1994] G. K. Harkness, W. J. Firth, J. B. Geddes, J. V. Moloney and E. M. Wright. *Boundary effects in large-aspect-ratio lasers.* Physical Review A, vol. 50, page 4310, 1994. (Cited on page 29.)

[Hasegawa 1973] A. Hasegawa and F. Tappert. *Transmission of stationary nonlinear optical pulses in dispersive dielectric fibers. I. Anomalous dispersion.* Applied Physics Letters, vol. 23, page 142, 1973. (Cited on page 8.)

[Haus 1975a] H. A. Haus. *Theory of Mode-locking with a fast saturable absorber.* Journal of Applied Physics, vol. 46, pages 3049–3058, 1975. (Cited on page 26.)

[Haus 1975b] H. A. Haus. *Theory of Mode-locking with a slow saturable absorber.* IEEE Journal of Quantum Electronics, vol. 11, pages 736–746, 1975. (Cited on page 26.)

[Haus 2000] H. A. Haus. *Mode-locking of lasers.* IEEE Journal of Selected Topics Quantum Electronics, vol. 6, pages 1173–1185, 2000. (Cited on pages iv, 26, 28, 29 and 52.)

[Henry 1982] C. H. Henry. *Theory of the linewidth of semiconductor lasers.* IEEE Journal of Quantum Electronics, vol. 18, page 259, 1982. (Cited on pages 23 and 89.)

[Herr 2014] T. Herr, V. Brasch, J. D. Jost, C. Y.Wang, N. M. Kondratiev, M. L. Gorodetsky and T. J. Kippenberg. *Temporal solitons in optical microresonators.* Nature Photonics, vol. 8, page 145, 2014. (Cited on pages 6, 63 and 80.)

[Hofer 1992] M. Hofer, M.H. Ober, F. Haberl and M.E. Fermann. *Characterization of ultrashort pulse formation in passively mode-locked fiber lasers.* Quantum Electronics, IEEE Journal of, vol. 28, page 720, 1992. (Cited on page 32.)

[Iga 2000] Kenichi Iga. *Surface-emitting laser: Its birth and generation of new optoelectronics field.* IEEE Journal of Selected Topics in Quantum Electronics, vol. 6, pages 1201–1215, 2000. (Cited on page 12.)

[Ippen 1994] E.P. Ippen. *Principles of passive mode locking.* Applied Physics B, vol. 58, pages 159–170, 1994. (Cited on pages 25 and 27.)

[Jakobsen 1992] P. K. Jakobsen, J.V. Moloney, A.C. Newell and R. Indik. *Space-time dynamics of wide-gain-section lasers.* Physical Review A, vol. 45, page 8129, 1992. (Cited on page 29.)

[Jang 2013a] J. K. Jang, M. Erkintalo, S. G. Murdoch and S. Coen. *Suppression of temporal cavity soliton interactions by phase modulation of the driving beam.* Lasers and Electro-Optics Europe (CLEO EUROPE/IQEC), 2013 Conference on and International Quantum Electronics Conference, page 1, 2013. (Cited on pages 68 and 69.)

[Jang 2013b] J. K. Jang, M. Erkintalo, S. G. Murdoch and S. Coen. *Ultraweak long-range interactions of solitons observed over astronomical distances.* Nature Photonics, vol. 7, pages 657–663, 2013. (Cited on pages 22, 67, 69, 106 and 118.)

[Javaloyes 2006] J. Javaloyes, J. Mulet and S. Balle. *Passive mode locking of lasers by crossed-polarization gain modulation.* Physical Review A, vol. 97, page 163902, 2006. (Cited on pages 27, 39 and 126.)

[Javaloyes 2010] J. Javaloyes and S. Balle. *Quasiequilibrium time-domain susceptibility of semiconductor quantum wells.* Physical Review A, vol. 81, page 062505, 2010. (Cited on page 79.)

[Javaloyes 2011] J. Javaloyes and S. Balle. *Anticolliding design for monolithic passively mode-locked semiconductor lasers.* Optics Letters, vol. 36, pages 4407–4409, 2011. (Cited on page 79.)

[Javaloyes 2012] J. Javaloyes and S. Balle. *Multimode dynamics in bidirectional laser cavities by folding space into time delay.* Optics Express, vol. 20, pages 8496–8502, 2012. (Cited on pages 32 and 55.)

[Javaloyes 2014] J. Javaloyes, M. Marconi and M. Giudici. *Phases dynamics in VCSELs with delayed optical feedback and cross re-injection.* Physical Review A, vol. submitted, 2014. (Cited on pages 116, 121 and 122.)

[Jeong 2004] J. Jeong, J. K. Sahu, D. N. Payne and J. Nilsson. *Yb-Doped Large Core Fiber Laser with 1 kW CW Output Power.* Advanced Solid State Photonics, 2004. (Cited on page 14.)

[Jiang 1999] M. Jiang, G. Sucha, M. E. Fermann, J. Jimenez, D. Harter, M. Dagenais, S. Fox and Y. Hu. *1.5-μm monolithic GaInNAs semiconductor saturable-absorber mode locking of an erbium fiber laser.* Optics Letters, vol. 24, pages 1074–1076, 1999. (Cited on page 33.)

[Kao 1966] K. C. Kao and G. A. Hockham. *Stimulated Optical Radiation in Ruby.* Proceedings of the Institution of Electrical Engineers, vol. 113, pages 1151–1158, 1966. (Cited on page 10.)

[Kapron 1970] F. P. Kapron, D. B. Keck and R. D. Maurer. *Radiation losses in glass optical waveguides.* Applied Physics Letters, vol. 17, pages 423–425, 1970. (Cited on page 10.)

[Kartner 1996] F.X. Kartner, I.D. Jung and U. Keller. *Soliton mode-locking with saturable absorbers.* Selected Topics in Quantum Electronics, IEEE Journal of, vol. 2, pages 540–556, 1996. (Cited on page 28.)

[Katayama 2011] T. Katayama, A. Yanai, K. Yukawa, S. Hattori, K. Ikeda, S. Koh and H. Kawaguchi. *All-optical flip-flop operation at 1-mA bias current in polarization bistable VCSELs with and oxide confinement structure.* IEEE Photonics Technology Letters, vol. 23, pages 1811–1813, 2011. (Cited on page 87.)

[Keller 1996] U. Keller, K. J. Weingarten, F. X. Kartner, D. Kopf, B. Braun, I. D. Jung, R. Fluck, C. Honninger, N. Matuschek and J. Aus der Au. *Semiconductor saturable absorber mirrors (SESAM) for femtosecond to nanosecond pulse generation in solid-state lasers.* IEEE Journal of Selected Topics in Quantum Electronics, vol. 2, pages 435–453, 1996. (Cited on page 43.)

[Keller 2006] U. Keller and A.C. Tropper. *Passively modelocked surface-emitting semiconductor lasers.* Physics Reports, vol. 429, pages 67–120, 2006. (Cited on pages 28, 43 and 127.)

[Kolodner 1988] P. Kolodner, D. Bensimon and C. M. Surko. *Onset of Oscillatory Convection in a Binary Fluid Mixture.* Physical Review Letters, vol. 60, page 1723, 1988. (Cited on page 29.)

[Larsson 2004] A. Larsson, Carlsson C., J. Gustavsson, A. Haglund, P. Modh and J. Bengtsson. *Direct high-frequency modulation of VCSELs and applications in fibre optic RF and microwave links.* New Journal of Physics, vol. 6, page 176, 2004. (Cited on page 12.)

[Lecaplain 2013] C. Lecaplain, Ph. Grelu and S.Wabnitz. *Polarization-domain-wall complexes in fiber lasers.* Journal of the Optical Society of America, vol. 30, page 211, 2013. (Cited on pages 18, 34 and 35.)

[Lecaplain 2014] C. Lecaplain, Ph. Grelu and S.Wabnitz. *Dynamics of the transition from polarization disorder to antiphase polarization domains in vector fiber lasers.* Physical Review A, vol. 00, page 003800, 2014. (Cited on pages 18, 34 and 35.)

[Leo 2010] F. Leo, S. Coen, P. Kockaert, S. P. Gorza, P. Emplit and M. Haelterman. *Temporal cavity solitons in one-dimensional Kerr media as bits in an all-optical buffer.* Nature Photonics, vol. 4, page 471, 2010. (Cited on pages iv, 6, 17, 20, 21, 63, 68, 79 and 80.)

[Lewen 2004] R. Lewen, S. Irmscher, U. Westergren, L. Thylen and U. Eriksson. *Segmented transmission-line electroabsorption modulators.* Journal of Lightwave Technology, vol. 22, pages 172–178, 2004. (Cited on page 13.)

[Li 1998] H. Li, A. Hohl, A. Gavrielides, H. Hou and K. D. Choquette. *Polarization modulation dynamics of vertical-cavity surface-emitting lasers with an extended cavity.* Applied Physics Letters, vol. 72, page 2255, 1998. (Cited on page 37.)

[Liehr 2013] A. W. Liehr. *Dissipative Solitons in Reaction Diffusion Systems. Mechanism, Dynamics, Interaction.* 2013. (Cited on page 4.)

[Lioubashevski 1999] O. Lioubashevski, Y. Hamiel, A. Agnon, Z. Reches and J. Fineberg. *Oscillons and Propagating Solitary Waves in a Vertically Vibrated Colloidal Suspension.* Phys. Rev. Lett., vol. 83, pages 3190–3193, Oct 1999. (Cited on page 8.)

[Lorenser 2004] D. Lorenser, H. J. Unold, D. J. H. C. Maas, A. Aschwanden, R. Grange, R. Paschotta, D. Ebling, E. Gini and U. Keller. *Towards wafer-scale integration of high repetition rate passively mode-locked surface-emitting semiconductor lasers.* Applied Physics B, vol. 79, page 927, 2004. (Cited on page 63.)

[Lugiato 1987] L. A. Lugiato and R. Lefever. *Spatial dissipative structures in passive optical systems.* Physical Review Letters, vol. 58, page 2209, 1987. (Cited on pages 6 and 17.)

[Lugiato 2003] L.A. Lugiato. *Introduction to the Special Issue on Cavity Solitons.* IEEE J. Quantum Electron., vol. 39, page 193, 2003. (Cited on page iii.)

[Maiman 1960] T. H. Maiman. *Stimulated Optical Radiation in Ruby.* Nature, vol. 187, pages 493–494, 1960. (Cited on page 10.)

[Marino 2014] Francesco Marino, Giovanni Giacomelli and Stephane Barland. *Front Pinning and Localized States Analogues in Long-Delayed Bistable Systems.* Physical Review Letters, vol. 112, page 103901, 2014. (Cited on page 32.)

[Martin-Regalado 1997a] J. Martin-Regalado, J. L. Chilla, J. J. Rocca and P. Brusenbach. *Polarization switching in vertical-cavity surface emitting lasers observed at constant active region temperature.* Applied Physics Letters, vol. 70, page 3350, 1997. (Cited on page 36.)

[Martin-Regalado 1997b] J. Martin-Regalado, F. Prati, M. San Miguel and N. Abraham. *Polarization properties of Vertical Surface-Emitting Lasers.* IEEE J. Quantum Electron., vol. 33, page 765, 1997. (Cited on page 37.)

[Martin-Regalado 1997c] J. Martin-Regalado, F. Prati, M. San Miguel and N.B. Abraham. *Spiral wave activity: a possible common mechanism for polymorphic and monomorphic ventricular tachycardias.* IEEE Journal of Quantum Electronics, vol. 33, pages 765–783, 1997. (Cited on page 89.)

[Martinez 1985] O. E. Martinez, R. L. Fork and J. P. Gordon. *Theory of passively mode-locked lasers for the case of a nonlinear complex-propagation coefficient.* J. Opt. Soc. Am., vol. 2, page 753, 1985. (Cited on page 29.)

[Matsas 1992] V.J. Matsas, T.P. Newson and M.N. Zervas. *Self-starting passive mode-locked fibre ring laser exploiting non-linear polarisation switching.* Optics Communications, vol. 92, pages 61–66, 1992. (Cited on pages 29 and 32.)

[Matsko 2011] A. B. Matsko, A. A. Savchenkov, W. Liang, V. S. Ilchenko, D. Seidel and L. Maleki. *Mode-locked Kerr frequency combs.* Optics Letters, vol. 36, page 2845, 2011. (Cited on pages 6 and 17.)

[Meliga 2004] M. Meliga, C. Coriasso and R. Paoletti. *Uncooled lasers for datacom and telecom applications.* LEOS-04, pages 92–93, 2004. (Cited on page 12.)

[Menuyk 1987] Curtis R. Menuyk. *Stability of solitons in birefringent optical fibers. I: Equal propagation amplitudes.* Optics Letters, vol. 12, page 614, 1987. (Cited on page 18.)

[Menuyk 1988] Curtis R. Menuyk. *Stability of solitons in birefringent optical fibers. II. Arbitrary amplitudes.* Journal of the Optical Society of America B, vol. 5, page 392, 1988. (Cited on page 18.)

[Michalzik 2003] R. Michalzik and K. J. Ebeling. *Operating principle of VCSELs.* In Vertical-Cavity Surface-Emitting Laser Devices, , volume 6, pages 53–98. Springer Berlin Heidelberg, 2003. (Cited on page 12.)

[Miguel 1995] M. San Miguel, Q. Feng and J. V. Moloney. *Light-polarization dynamics in surface-emitting semiconductor lasers.* Physical Review A, vol. 52, page 1728, 1995. (Cited on pages 36 and 37.)

[Minardi 2010] S. Minardi, F. Eilenberger, Y. V. Kartashov, A. Szameit, U. Röpke, J. Kobelke, K. Schuster, H. Bartelt, S. Nolte, L. Torner, F. Lederer, A. Tünnermann and T. Pertsch. *Three-Dimensional Light Bullets in Arrays of Waveguides.* Physical Review Letter, vol. 105, page 263901, 2010. (Cited on page 7.)

[Mitschke 1989] F. Mitschke, C. Boden, W. Lange and P. Mandel. *Exploring the dynamics of the unstable branch of bistable systems.* Optics Communications, vol. 71, pages 385–392, 1989. (Cited on page 75.)

[Mollenauer 1984] L. F. Mollenauer and R. H. Stolen. *The soliton laser.* Optics Letter, vol. 9, pages 13–15, 1984. (Cited on page 28.)

[Moores 1993] J. D. Moores. *On the Ginzburg-Landau laser mode-locking model with fifth-order saturable absorber term.* Optical Communications, vol. 96, page 65, 1993. (Cited on page 29.)

[Mulet 2001] J. Mulet, C. R. Mirasso and M. San Miguel. *Polarization resolved intensity noise in vertical-cavity surface-emitting lasers.* Physical Review A, vol. 64, page 023817, 2001. (Cited on page 90.)

[Mulet 2007a] J. Mulet, M. Giudici, J. Javaloyes and S. Balle. *Square-wave switching by crossed-polarization gain modulation in vertical-cavity semiconductor lasers.* Physical Review A, vol. 76, page 043801, October 2007. (Cited on pages 38, 93, 94, 96 and 101.)

[Mulet 2007b] J. Mulet, J. Javaloyes and S. Balle. *Mode-Locking of VECSELs by Crossed-Polarization Gain Modulation.* Quantum Electronics, IEEE Journal of, vol. 43, pages 786–793, September 2007. (Cited on page 39.)

[New 1974] G. New. *Pulse evolution in mode-locked quasi-continuous lasers.* IEEE Journal of Quantum Electronics, vol. 10, page 115, 1974. (Cited on pages 77 and 78.)

[Newell 1969] A.C. Newell and J.A. Whitehead. *Finite bandwidth, finite amplitude convection.* J. Fluid Mech., vol. 38, page 279, 1969. (Cited on page 4.)

[Niemela 1990] Joseph J. Niemela, Guenter Ahlers and David S. Cannell. *Localized Travelling Wave States in Binary-Fluid Convection.* Physical Review Letters, vol. 64, page 1365, 1990. (Cited on page 8.)

[Okhotnikov 2003] O. G. Okhotnikov, T. Jouhti, J. Konttinen, S. Karirnne and M. Pessa. *1.5-μm monolithic GaInNAs semiconductor saturable-absorber mode locking of an erbium fiber laser.* Optics Letters, vol. 28, pages 364–366, 2003. (Cited on page 33.)

[Ostrovskii 1972] L. A. Ostrovskii and L. V. Soustov. *Self-modulation of electromagnetic waves in nonlinear transmission lines.* Izvestiya VUZ, Radiofizika, vol. 15, page 242, 1972. (Cited on page 4.)

[Oudar 1992] J. Oudar, R. Kuszelewicz, B. Sfez, J. Michel and R. Planel. *Prospects for further threshold reduction in bistable microresonators.* Optical and Quantum Electronics, vol. 24, pages 193–207, 1992. (Cited on page 54.)

[Ouyang 2011] Chunmei Ouyang, Honghai Wang, Ping Shum, Songnian Fu, Jia Haur Wong, Kan Wu, Desmond Rodney Chin Siong Lim, Vincent Kwok Huei Wong and Kenneth Eng Kian Lee. *Properties of a vector soliton laser passively mode-locked by a fiber-based semiconductor saturable absorber operating in transmission.* Optics Communications, vol. 284, pages 619–624, 2011. (Cited on pages 18 and 34.)

[Pallmann 2013] W. P. Pallmann, C. A. Zaugg, M. Mangold, I. Dahhan, M. Golling, B. W. Tilma, B. Witzigmann and U. Keller. *Ultrafast Electrically Pumped VECSELs.* IEEE Photonics Journal, vol. 5, pages 435–453, 2013. (Cited on pages 12 and 28.)

[Panajotov 2000] K. Panajotov, B. Nagler, G. Verschaffelt, A. Georgievski, H. Thienpont, J. Danckaert and I. Veretennicoff. *Impact of in-plane anisotropic strain on the polarization behavior of vertical-cavity surface-emitting lasers.* Applied Physics Letters, vol. 11, no. 7, pages 1590–1592, 2000. (Cited on page 88.)

[Paschotta 2002] R. Paschotta, R. Haring, A. Garnache, S. Hoogland, A. C. Tropper and U. Keller. *Soliton-like pulse-shaping mechanism in passively mode-locked surface-emitting semiconductor lasers.* Applied Physics B, vol. 75, page 445, 2002. (Cited on page 63.)

[Pedaci 2006] F. Pedaci, P. Genevet, S. Barland, M. Giudici and J. R. Tredicce. *Positioning cavity solitons with a phase mask.* Applied Physics Letters, vol. 89, page 221111, 2006. (Cited on page 20.)

[Pedaci 2008a] F. Pedaci, E Barland S.and Caboche, P. Genevet, M. Giudici, J.R. Tredicce, T. Ackemann, A.J. Scroggie, W.J. Firth, G.L. Oppo, G. Tissoni and R. Jäger. *All-optical delay line based on semiconductor cavity solitons.* Applied Physics Letters, vol. 92, page 011101, 2008. (Cited on pages 20, 69 and 75.)

[Pedaci 2008b] F. Pedaci, G. Tissoni, S. Barland, M. Giudici and J. Tredicce. *Mapping local defects of extended media using localized structures.* Applied Physics Letters, vol. 93, page 111104, 2008. (Cited on page 20.)

[Perez-Serrano 2013] A. Perez-Serrano, J. Javaloyes and S. Balle. *Spectral delay algebraic equation approach to broad area laser diodes.* Journal of Selected Topics in Quantum Electronics, vol. 1, page 99, 2013. (Cited on page 32.)

[Pomeau 1986] Y. Pomeau. *Front motion, metastability and subcritical bifurcations in hydrodynamics.* Physica D: Nonlinear Phenomena, vol. 23, pages 3–11, 1986. (Cited on page 9.)

[Purwins 2010] H.-G. Purwins, H. U. Bodeker and Sh. Amiranashvili. *Dissipative solitons.* Adv. Phys., vol. 59, pages 485–701, 2010. (Cited on page 8.)

[Ramakrishnan 2002] A. Ramakrishnan, G. Steinle, D. Supper, C. Degen and G. Ebbinghaus. *Electrically pumped 10 Gbit/s MOVPE grown monolithic 1.3 μm VCSEL with GaInNAs active region.* Electronics Letters, vol. 38, pages 322–324, 2002. (Cited on page 12.)

[Ramazza 2002] P.L. Ramazza, E. Bentler, U. Bortolozzo, S. Boccaletti, S. Ducci and F. T. Arecchi. *Tailoring the profile and interactions of optical localized structures.* Physical Review E, vol. 65, page 066204, 2002. (Cited on page 8.)

[Ramazza 2003] P.L. Ramazza, S. Boscaletti, Bortolotto U. and F.T. Arecchi. *Control of localized structures in an optical feedback interferometer.* Chaos, vol. 13, page 335, 2003. (Cited on page 8.)

[Robert 1997] F. Robert, P. Besnard, M. Chares and G. Stephan. *Polarization modulation dynamics of vertical-cavity surface-emitting lasers with an extended cavity.* IEEE J. Quantum Electron, vol. 33, page 2231, 1997. (Cited on page 37.)

[Rosanov 1990] N. N. Rosanov and G.V. Khodova. *Diffractive autosolitons in nonlinear interferometers.* J. Opt. Soc. Am. B, vol. 7, pages 1057–1065, 1990. (Cited on pages 9 and 10.)

[Rosanov 1992] N. N. Rosanov and . S.V. Fedorov. Optics and Spectroscopy, vol. 72, page 782, 1992. (Cited on pages 7, 17 and 24.)

[Rosanov 2002] N.N. Rosanov. Spatial hysteresis and optical patterns. Springer, 2002. (Cited on pages 24 and 25.)

[Rosanov 2005] Nikolay N. Rosanov, Sergey V. Fedorov and Anatoly N. Shatsev. *Curvilinear Motion of Multivortex Laser-Soliton Complexes with Strong and Weak Coupling.* Physical Review Letters, vol. 95, page 053903, Jul 2005. (Cited on page 25.)

[Rudin 2010] B. Rudin, V. J. Wittwer, D. J. H. C. Maas, M. Hoffmann, O. D. Sieber, Y. Barbarin, M. Golling, T. Sudmeyer and U. Keller. *High-power mixsel, an integrated ultrafast semiconductor laser with 6.4 W average power.* Optics Express, vol. 18, pages 27582–27588, 2010. (Cited on page 43.)

[Russel 1844] J. S. Russel. *Report on waves.* Report of the 14^{th} meeting of the British Association for the Advancement of Science, page 331, 1844. (Cited on page 8.)

[Sakaguchi 2010] J. Sakaguchi, T. Katayama and H. Kawaguchi. *All-optical memory operation of 980-nm polarization bistable VCSEL for 20-Gb/s PRBS RZ and 40-Gb/s NRZ data signals.* Optics Express, vol. 18, pages 12362–12370, 2010. (Cited on page 87.)

[Schäpers 2000] B. Schäpers, M. Feldmann, T. Ackemann and W. Lange. *Interaction of Localized Structures in an Optical Pattern-Forming System.* Physical Review Letters, vol. 85, page 748, July 2000. (Cited on page 9.)

[Segel 1969] L. Segel. *Distant side-walls cause slow amplitude modulation of cellular convection.* J. Fluid Mech., vol. 38, page 203, 1969. (Cited on page 4.)

[Silberberg 1990] Y. Silberberg. *Collapse of optical pulses.* Optics Letters, vol. 15, page 1282, 1990. (Cited on page 7.)

[Slowinski 2010] P. Slowinski, B. Krauskopf and S. M. Wieczorek. Solution structure and dynamics of a semiconductor laser subject to feedback from two external filters. 2010. (Cited on page 39.)

[Slowinski 2014] P. Slowinski, B. Krauskopf and S. M. Wieczorek. *Mode structure of a semiconductor laser with feedback from two external filters.* In Discrete and continuous dynamical systems, . 2014. (Cited on page 39.)

[Sondermann 2003] M. Sondermann, M. Weinkath, T. Ackemann, J. Mulet and S. Balle. *Two-frequency emission and polarization dynamics at lasing threshold in vertical-cavity surface-emitting lasers.* Physical Review A, vol. 68, page 033822, 2003. (Cited on page 36.)

[Soto-Crespo 1997] J.M. Soto-Crespo, N.N. Akhmediev and Afanasjev V.V. *Pulse solutions of the cubic-quintic complex Ginzburgh Landau equation in the case of normal dispersion.* Physical Review E, vol. 55, page 4783, 1997. (Cited on page 29.)

[Soto-Crespo 2001] J.M. Soto-Crespo, N.N. Akhmediev and G. Town. *Interrelation between various branches of stable solitons in dissipative systems : conjecture*

for stability criterion. Optics Communicatons, vol. 199, pages 283–293, 2001. (Cited on pages 29 and 30.)

[Sukow 2012] D.W. Sukow, T.Gilfillan, B. Pope, M. S. Torre, A. Gavrielides and C. Masoller. *Relaxation and square-wave oscillations in a semiconductor laser with polarization rotated optical feedback.* Physical Review A, vol. 86, page 033818, 2012. (Cited on page 38.)

[Swift 1977] J. Swift and P.C. Hohenberg. *Hydrodynamic fluctuations at the convective instability.* Physical Review A, vol. 15, page 319, 1977. (Cited on page 4.)

[Takagi 2004] K. Takagi, A. Shirai, Y. Tatsuoka, C. Watatani, T. Aoyagi T. Ota T. Takiguchi, T. Nishimura and N. Tomita. *10 Gb/s uncooled direct modulated 1.3 μm Al- GaInAs MQW DFB laser diodes,.* IEEE Photonics Technology Letters, vol. 16, pages 2415–2417, 2004. (Cited on page 12.)

[Tang 2008] D. Y. Tang, H. Zhang, L. M. Zhao and X. Wu. *Observation of High-Order Polarization-Locked Vector Solitons in a Fiber Laser.* Physical Review Letter, vol. 101, page 153904, 2008. (Cited on page 18.)

[Tanguy 2006] Y. Tanguy, T. Ackemann and R. Jager. *Characteristics of bistable localized emission states in broad-area vertical-cavity surface-emitting lasers with frequency-selective feedback.* Physical Review A, vol. 74, page 053824, 2006. (Cited on page 23.)

[Tanguy 2008a] Y. Tanguy, T. Ackemann, W. J. Firth and R. Jäger. *Realization of a Semiconductor-Based Cavity Soliton Laser.* Physical Review Letters, vol. 100, page 013907, Jan 2008. (Cited on page 23.)

[Tanguy 2008b] Y. Tanguy, N. Radwell, T. Ackemann and R. Jäger. *Characteristics of cavity solitons and drifting excitations in broad-area vertical-cavity surface-emitting lasers with frequency-selective feedback.* Physical Review A, vol. 78, page 023810, Aug 2008. (Cited on page 23.)

[Thompson 1972] G. H. B. Thompson. *A Theory for filamentation in semiconductor lasers including the dependence of dielectric constant on injected carrier density.* Opto-electronics, vol. 4, pages 257–310, 1972. (Cited on page 44.)

[Tlidi 1994] M. Tlidi, Paul Mandel and R. Lefever. *Localized structures and localized patterns in optical bistability.* Physical Review Letters, vol. 73, pages 640–643, Aug 1994. (Cited on pages 9 and 10.)

[Tlidi 2010] M. Tlidi and L. Gelens. *High-order dispersion stabilizes dark dissipative solitons in all-fiber cavities.* Optics Letters, vol. 35, page 306, 2010. (Cited on page 63.)

[Tlidi 2013] M. Tlidi, L. Bahloul, L. Cherbi, A. Hariz and S. Coulibaly. *Drift of dark cavity solitons in a photonic-crystal fiber resonator.* Physical Review A, vol. 88, page 035802, 2013. (Cited on page 63.)

[Tsuzuki 2003] K. Tsuzuki, T. Ishibashi, T. Ito, S. Oku, Y. Shibata, R. Iga, Y. Kondo and Y. Tohmori. *A 40 Gbit/s InP-based n-i-n mach-zehnder modulator with a π-voltage of 2.2 V.* Electronics Letters, vol. 39, pages 1464–1466, 2003. (Cited on page 13.)

[Tucker 1985] Rodney S. Tucker. *High-Speed Modulation of Semiconducor Lasers.* Journal of Lightwave Technology, vol. LT-3, page 1180, 1985. (Cited on page 12.)

[Tucker 2005] Rodney S. Tucker, Pei-Cheng Ku and Constance J. Chang-Hasnain. *Slow-Light Optical Buffers: Capabilities and Fundamental Limitations.* Journal of Lightwave Technology, vol. 23, page 4046, 2005. (Cited on pages 14 and 16.)

[Turconi 2013] M. Turconi, M. Giudici and S. Barland. *Drift-induced excitable localized states.* Physical Review Letter, vol. 111, page 233901, 2013. (Cited on page 26.)

[Turing 1952] A. M. Turing. *The chemical basis of morphogenesis.* Philos. Trans. R. Soc. London, vol. 237, page 37, 1952. (Cited on page 3.)

[Uenoyama 1990] T. Uenoyama and L.J. Sham. *Carrier relaxation and luminiscence polarization in quantum wells.* Physical Review B, vol. 42, pages 7114–7123, 1990. (Cited on page 37.)

[Umbanhowar 1996] P.B. Umbanhowar, F. Melo and L. Harry. *Localized excitations in a vertically vibrated granular layer.* Nature, vol. 382, pages 793–796, 1996. (Cited on pages 8 and 9.)

[Veretonov 2000] N. A. Veretonov, A. G. Vladimirov, N. A. Kaliteevskii, N. N. Rosanov, S.V. Fedorov and A. N. Shatsev. *Conditions for the existence of Laser Bullets.* Optics and spectroscopy, vol. 89, page 380, 2000. (Cited on page 25.)

[Virte 2013] Martin Virte, Krassimir Panajotov, Hugo Thienpont and Marc Sciamanna. *Deterministic polarization chaos from a laser diode.* Nature Photonics, vol. 7, pages 60–65, 2013. (Cited on page 36.)

[Virte 2014] M. Virte, M. Sciamanna, E. Mercier and K. Panajotov. *Bistability of time-periodic polarization dynamics in a free-running VCSEL.* Optics Express, vol. 22, pages 6772–6777, 2014. (Cited on page 36.)

[Vladimirov 1999] A. G. Vladimirov, S. V. Fedorov, N. A. Kaliteevskii, G.V. Khodova and N.N. Rosanov. *Numerical investigation of laser localized structures.* Journal of Optics B, vol. 1, pages 101–106, 1999. (Cited on pages 17, 24 and 25.)

[Vladimirov 2005] A. G. Vladimirov and D. Turaev. *Model for passive mode locking in semiconductor lasers.* Physical Review A, vol. 72, page 033808, 2005. (Cited on pages 28, 76 and 77.)

[Wabnitz 2009] S. Wabnitz. *Cross-Polarization Modulation Domain Wall Solitons for WDM Signals in Birefringent Optical Fibers.* IEEE Photonics Technology Letter, vol. 21, page 875, 2009. (Cited on page 18.)

[Wilcox 2008] Wilcox, K. G., Mihoubi, Z., Daniell, G. J., S. Elsmere, A. Quarterman, I. Farrer, D. A. Ritchie and A. Tropper. *Ultrafast optical stark mode-locked semiconductor laser.* Optics Letters, vol. 33, pages 2797–2799, 2008. (Cited on page 27.)

[Wilcox 2013] K. G. Wilcox, A. C. Tropper, H. E. Beere, D. A. Ritchie, B. Kunert, B. Heinen and W. Stolz. *4.35 kw peak power femtosecond pulse mode-locked vecsel for supercontinuum generation.* Optics Express, vol. 21, pages 1599–1605, 2013. (Cited on page 43.)

[Williams 1948] F.C. Williams and T. Kilburn. *Electronic Digital Computers.* Nature, vol. 162, page 4117, Sept. 1948. (Cited on page 15.)

[Williams 1997] Q. L. Williams, J. Garcia-Ojalvo and R. Roy. *Fast intracavity polarization dynamics of an erbium-doped fiber ring laser: Inclusion of stochastic effects.* Physical Review A, vol. 55, page 2376, 1997. (Cited on pages 18 and 34.)

[Wright 2007] M. W. Wright and J. Kovalik. *A Fiber-Based Master Oscillator Power Amplifier Laser Transmitter for Optical Communications.* IPN Progress Report, vol. 42, page 171, 2007. (Cited on page 14.)

[Zakharov 1972] V. E. Zakharov and A. B. Shabat. *Exact theory of two-dimensional self-focusing and one-dimensional self-modulation of waves in nonlinear media.* Sov. Phys. JETP, vol. 34, page 62, 1972. (Cited on page 8.)

[Zakharov 2009] V.E. Zakharov and L.A. Ostrovsky. *Modulation instability: The beginning.* Physica D: nonlinear phenomena, vol. 238, pages 540–548, 2009. (Cited on pages 4 and 5.)

[Zhang 2008] H. Zhang, D. Y. Tang, L. M. Zhao and N. Xiang. *Coherent energy exchange between components of a vector soliton in fiber lasers.* Optics Express, vol. 16, page 12618, 2008. (Cited on page 34.)

[Zhang 2009] H. Zhang, D. Y. Tang, L. M. Zhao and X. Wu. *Observation of polarization domain wall solitons in weakly birefringent cavity fiber lasers.* Physical Review B, vol. 80, page 052302, 2009. (Cited on pages 18 and 34.)

[Zhang 2011] Han Zhang, Dingyuan Tang, Luming Zhao, Qiaoliang Bao and Kian Ping Loh. *Vector dissipative solitons in graphene mode locked fiber*

lasers. Optics Communications, vol. 284, pages 619–624, 2011. (Cited on pages 18, 33 and 34.)

[Zhao 2009] L. M. Zhao, 1 D. Y. Tang, X. Wu, H. Zhang and H. Y. Tam. *Coexistence of polarization-locked and polarization-rotating vector solitons in a fiber laser with SESAM*. Optics Letters, vol. 34, page 3059, 2009. (Cited on pages 18, 33 and 34.)